Federal Agency and Organization Element to Which Report is Submitted	Office of Fossil Energy U.S. Department of Energy National Energy Technology Laboratory
Federal Grant or Other Identifying Number Assigned by Agency	DE-FE0031526
Project Title	Economic Extraction, Recovery and Upgrading of Rare Earth Elements from Coal-Based Resources
PD/PI Name, Title and Contact Information (e-mail address and phone number)	Dr. Michael L. Free Department of Metallurgical Engineering University of Utah 135 S. 1460 E. Room 412 Salt Lake City, UT 84112 Phone: 801-585-9798 Email: michael.free@utah.edu
Name of Submitting Official, Title, and Contact Information (e-mail address and phone number), if other than PD/PI	Dr. Michael L. Free Department of Metallurgical Engineering University of Utah 135 S. 1460 E. Room 412 Salt Lake City, UT 84112 Phone: 801-585-9798 Email: michael.free@utah.edu
Submission Date	March 27, 2020
DUNS Number	009095365
Recipient Organization (Name and Address)	University of Utah Office of Sponsored Projects 1471 East Federal Way Salt Lake City, Utah 84102-1821 Phone: 801-581-4913
Project/Grant Period (Start Date, End Date)	11/16/2017 to 12/31//2019
Reporting Period End Date	December 31, 2019
Report Term or Frequency (annual, semi-annual, quarterly, other)	Final
Signature of Submitting Official (electronic signatures are acceptable)	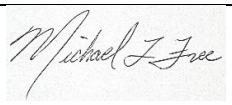

Economic Extraction, Recovery, and Upgrading of Rare Earth Elements from Coal-Based Resources

Project Final Report

Award Information

Prime Sponsor: US Department of Energy
Lead Institution: University of Utah
Lead Principle Investigator: Michael Free
Virginia Tech Principle Investigator: Aaron Noble
Virginia Tech Co-Investigators: Gerald H. Luttrell (retired)
Federal Award Number: DE-FE0031526
Solicitation Number: DE-FOA-0001718

Report Authors

University of Utah:
Landon Allen
Zongliang Zhang
Parshant Sarswat, PhD
Michael L. Free, PhD

Virginia Tech:
Morgen Leake
Daejin Kim, PhD
Aaron Noble, PhD
Gerald H. Luttrell, PhD

ACCOMPLISHMENTS

a) Project Goals

The overall objective of this project is to produce a rare earth elements product with greater than 8% rare earth elements from coal-based resources using an economically viable and environmentally benign processing methodology. The objective of the coal processing work will be to acquire appropriate coal feed and produce a viable clean coal product, a concentrated REE feed stream, and a pyrite stream (where available) that can be used to enhance leaching. The objective of the bio-oxidation portion of the project is to utilize bacteria to oxidize sulfide minerals and ferrous ions to ferric ions to accelerate leaching and remove the sulfides to prevent future acid mine drainage and related liabilities. The objective of the solution conditioning work is to remove iron and control leaching solution conditions to facilitate extraction of REEs without significant thorium extraction. The objective of the column leaching work is to engineer/model and simulate heap leaching to demonstrate low-cost extraction of REEs from coal-based resources. The objective of the solvent extraction work is to selectively extract and recover through controlled stripping of REEs that are solubilized through leaching. The objective of the precipitation portion of the project is to recover the REEs from the solvent extraction stripping solutions and dry them to achieve the final product of rare earth elements that is > 8 % REEs. The objective of the technical, economic, and environmental analysis is to determine the overall viability of the processing approach that is demonstrated in this project.

This project encompasses a range of technologies that are currently in industrial practice that are applied and engineered to produce rare earth element product from coal feed sources. The potential sources include large coal feed resources in active coal mines in addition to coal waste. This technology involves the utilization of advanced coal processing technology that can be used to deliver clean coal for the market as well as rare-earth-element-bearing non-coal rock that is of the correct size for heap leaching applications in addition to providing concentrated sulfide minerals (for mid to high sulfur coals) for cleaner coal and for enhanced bio-oxidation to accelerate leaching of REEs from the non-coal rock. The removal of the sulfide minerals cleans the coal, accelerates subsequent REEs extraction, and it removes the future potential for most acid-rock drainage. (For low sulfur coals some pyrite may be purchased if needed.) The processing method also utilizes bio-oxidation to enhance ferric ion production to enhance leaching, while also consuming the sulfide mineral and its associated environmental liability. The project includes a technical, economic, and environmental analysis to facilitate an appropriate assessment of commercial viability for this processing technology.

Table of Contents

Task 1: Project Management

The project PIs have utilized their extensive project management experience and skills, combined with a well-developed project completion plan with 33 specific tasks divided and organized amongst 5 task groups, to accomplish the project objective. the PIs have work with DOE to establish a formal project management plan at the beginning of the project. The project PIs have managed a large number of projects and the associated students and staff members who have worked on their projects. This project is of relatively short duration, so detailed and experienced project management throughout the project are critical to its success, and this team has used their experience and skills to accomplish the project tasks. The other key aspect to project management is the detailed plan that was developed, which guided the leadership team as they manage the project. Interim Accomplishment Reports have been submitted as requested by DOE.

Task 2: Sample Acquisition and Characterization

2.1 Acquire Coal Ore Samples

Key Findings

- Six unique field samples from four sites were identified and collected for further testing and evaluation. Preliminary data indicated that all four samples meet the 300 ppm TREE feedstock qualification limit

Detailed Results

The project team initially identified four separate coal refuse samples that meet the 300 ppm TREE feedstock qualification limit. All samples were collected using automated cross belt samplers while following all appropriate ASTM protocols. In total, eleven 55-gallon barrels of coal refuse were collected as the sources for this study and delivered to the Virginia Tech Mining and Minerals Engineering research facility. These 11 barrels represent six unique material types from four different mines in three states. **Error! Reference source not found.** provides a s ummary of the sampled material with county-level identifying information. Two of the plants, site "C" and site "D" process coal from multiple sources, and as such, the sub-samples for this study (i.e. sample "1" and "2") represent different coal blends that were processed on different days.

Table 2 - 1: Coal refuse samples acquired from four industrial plants

Sample Code	County	State	Sampled Quantity
CR-A	Nicholas County	West Virginia	2 barrels
CR-B	Green County	Pennsylvania	1 barrel
CR-C1	Dickenson County	Virginia	2 barrels
CR-C2	Dickenson County	Virginia	2 barrels
CR-D1	Wise County	Virginia	2 barrels
CR-D2	Wise County	Virginia	2 barrels

(CR: coarse refuse, A-D: site code, #: multiple samples from the same site)

After receiving the samples at the Virginia Tech research facility, all samples were prepared using a standardized crushing, splitting, and screening process as depicted in Figure 2 - 1. Samples occupying multiple barrels (i.e. all but CR-B) were first homogenized, and, each sample was then crushed to minus 1 inch using a laboratory jaw crusher (Morse Bros. Machinery Company, Denver, CO, Figure 2 - 2(a)). Some samples had a notable fraction of elongated material that was re-crushed several times to produce a more uniform size. Figure 2 - 3 shows each coal refuse sample before and after the jaw crushing step.

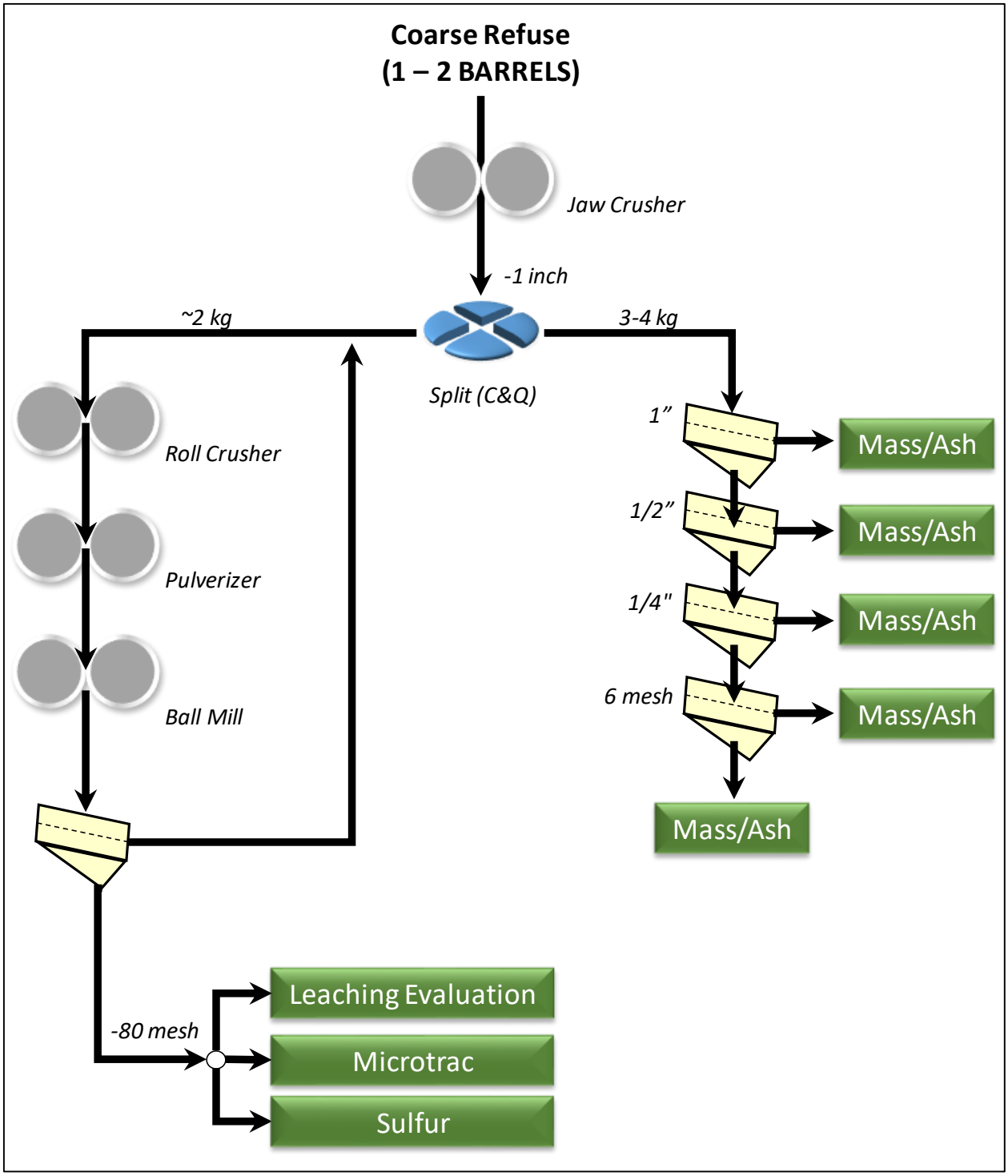

Figure 2 - 1: Flow chart of the comminution process of coal refuse samples

Figure 2 - 2: Pictures of (a) a jaw crusher, (b) a roll crusher, (c) a pulverizer, (d) a grinding mill, (e) a RO-TAP® test sieve shaker, and (f) a silent sifter.

Following the initial crushing, several representative splits of each sample were obtained for preliminary testing and characterization, while the remaining minus 1-inch material was sealed and stored. The representative splits were obtained by repeatedly coning and quartering each barrel sized sample. Coning and quartering was conducted by first pouring the material into a conical heap on a clean tarp. Next, the material was divided into four quarters by a flat separator. Two opposite corners were combined, while the other two corners were set aside. This process was repeated several times until approximately one bucket of sample was obtained.

One representative split of each sample (approximately 3 – 4 kg) was used for size and ash-by-size analysis. Ash was determined using a LECO 701, and the sieves sizes used in the size analysis included: 1", ½", ¼", and 6 mesh. Screening was conducted using a Silent Sifter (Gilson Company, Inc., Figure 2 - 2(f)).

A second representative split (approximately 2 kg) was staged crushed and ground in sequence to produce a minus 80 mesh product suitable for sulfur analysis and leaching tests. The staged crushing and grinding process included: (1) a laboratory roll crusher (Sturtevant Laboratory Roll, Sturtevant Mill Co., Figure 2 - 2(b)), (2) a laboratory pulverizer (Bico Inc., Figure 2 - 2 (c)), and (3) a laboratory ball grinding mill (QCG Systems LLC, Figure 2 - 2(d)).

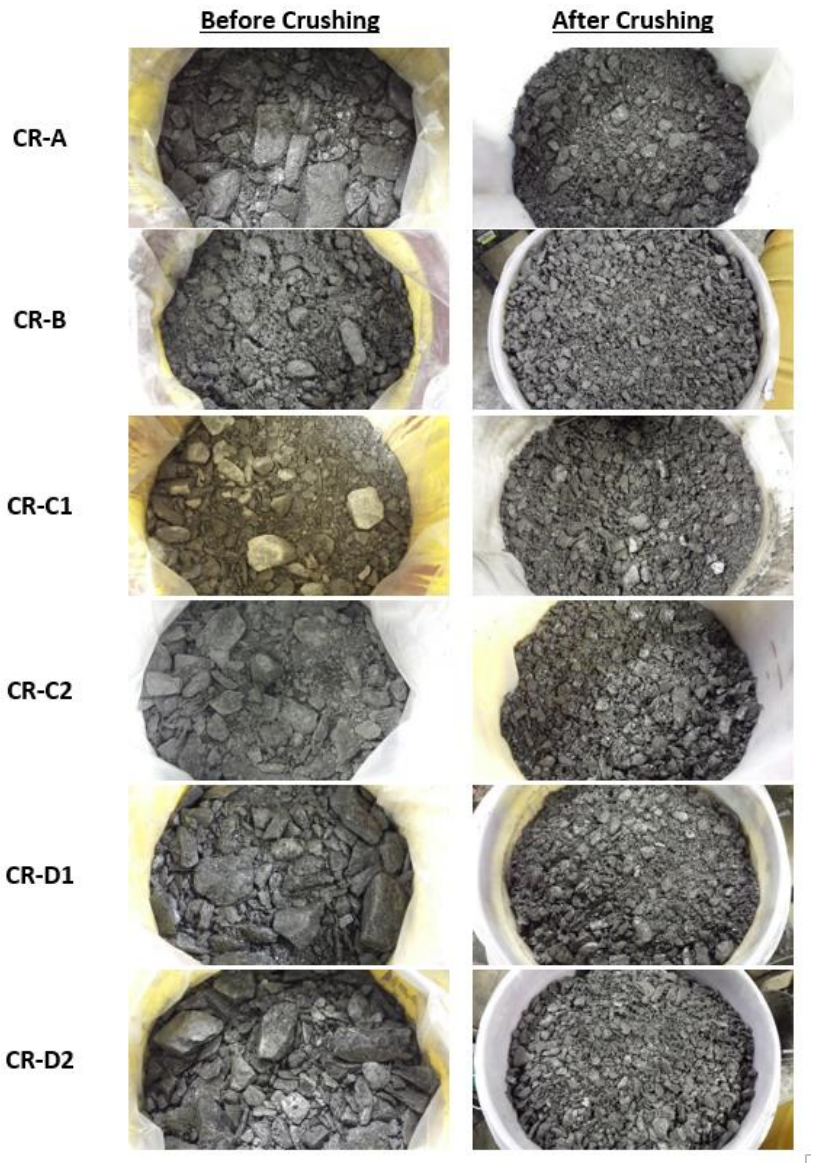

Figure 2 - 3: Coal refuse samples before and after crushing.

After the stage crushing and grinding, the material was screened at 80 mesh using a RO-TAP® test sieve shaker (Haver Tyler Corporation, Figure 2 - 2(e)) or with a Silent Sifter to produce a fine sample suitable for leaching tests. Approximately, 2 kg of each sample was delivered to University of Utah for REE analysis and preliminary leaching tests. Size distributions of this material are shown in Figure 2 - 4. Sulfur analyses were conducted by Precision Testing Laboratory Inc. (Daniels, WV). As an example of the size reduction, Figure 2 - 5 shows the pictures of CR-D2 sample taken after each stage of the comminution process.

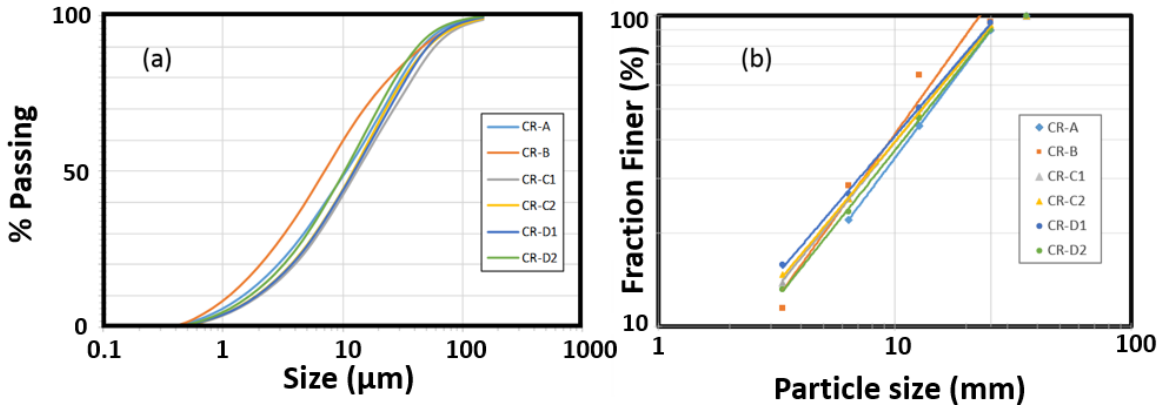

Figure 2 - 4: (a). Size distribution data for the fine (-80 mesh) samples delivered to the university of Utah; (b) Gates-Gaudin-Schuhmann plot for coal refuse samples.

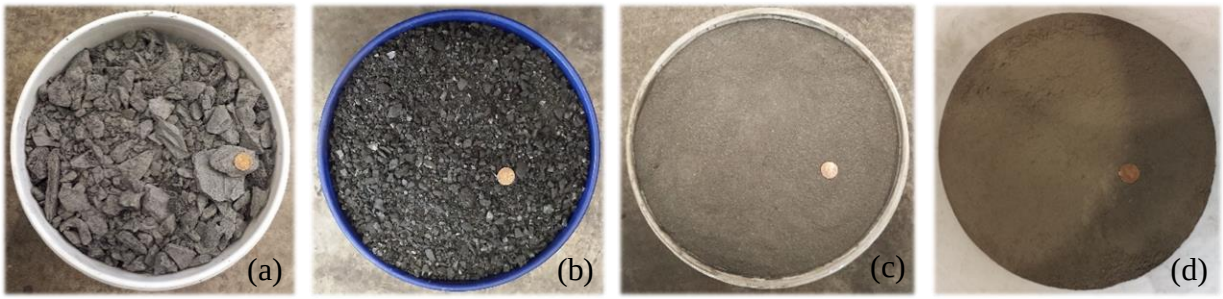

Figure 2 - 5: Pictures of CR-D2 sample after being processed with (a) a jaw crusher, (b) a roll crusher, (c) a pulverizer/grinding mill, and (d) a sieve shaker.

2.2 Characterize Samples

Key Findings

- Size analysis showed that all samples have a similar size distribution with little variability in the GGS parameters.
- Primary mineral constituents of the samples include silica, iwakite, illite, siderite, and pyrite in one sample.
- A sodium peroxide fusion method resulted in the greatest TREE concentrations for the CR head samples, compared to hydrofluoric and reverse aqua regia digestions.

Detailed Results

2.2.1 Size, ash, and sulfur analysis**Error! Reference source not found.** summarizes the s ize, ash, and moisture data for each of the 6 samples. The size distributions are also presented graphically in Figure 2 - 6. The data shows that the ash content is very high for all samples, varying from 83.9% (CR-B) to 89.7% (CR-C1, CR-D2). Likewise, the ash content does not vary

considerably between size classes of individual samples. All samples are very low sulfur (<0.4%) with the exception of CR-B, which is 3.86% sulfur. Overall, this data validates the objectives of the sampling program, which were to obtain high ash coarse refuse samples and a variety of sulfur contents.

Table 2 - 2: Sample Characterization Summary

	Sample											
	CR-A		CR-B		CR-C1		CR-C2		CR-D1		CR-D2	
Size Class	Mass (%)	Ash (%)	Mass (%)	Ash (%)	Mass (%)	Ash (%)	Mass (%)	Ash (%)	Mass (%)	Ash (%)	Mass (%)	Ash (%)
+ 1”	10.1%	87.0%	4.1%	86.6%	8.2%	91.5%	6.3%	90.9%	4.6%	88.6%	10.2%	90.2%
½ x 1”	45.6%	87.3%	31.2%	83.9%	41.4%	90.2%	45.5%	89.5%	44.9%	89.9%	42.9%	91.4%
¼ x ½”	22.2%	86.6%	36.2%	83.8%	24.6%	89.7%	22.5%	82.0%	23.8%	89.0%	23.5%	88.8%
6 mesh x ¼”	14.6%	86.6%	17.0%	84.1%	12.0%	89.2%	11.0%	81.8%	10.9%	88.4%	10.3%	88.0%
-6 mesh	7.4%	86.4%	11.4%	83.2%	13.8%	87.6%	14.7%	78.9%	15.8%	87.2%	13.1%	86.6%
TOTAL	100%	87.0%	100%	83.9%	100%	89.7%	100%	85.5%	100%	89.0%	100%	89.7%
Moisture	1.67%		1.85%		2.71%		1.72%		0.87%		1.01%	
Sulfur	0.12%		3.86%		0.37%		0.14%		0.31%		0.29%	

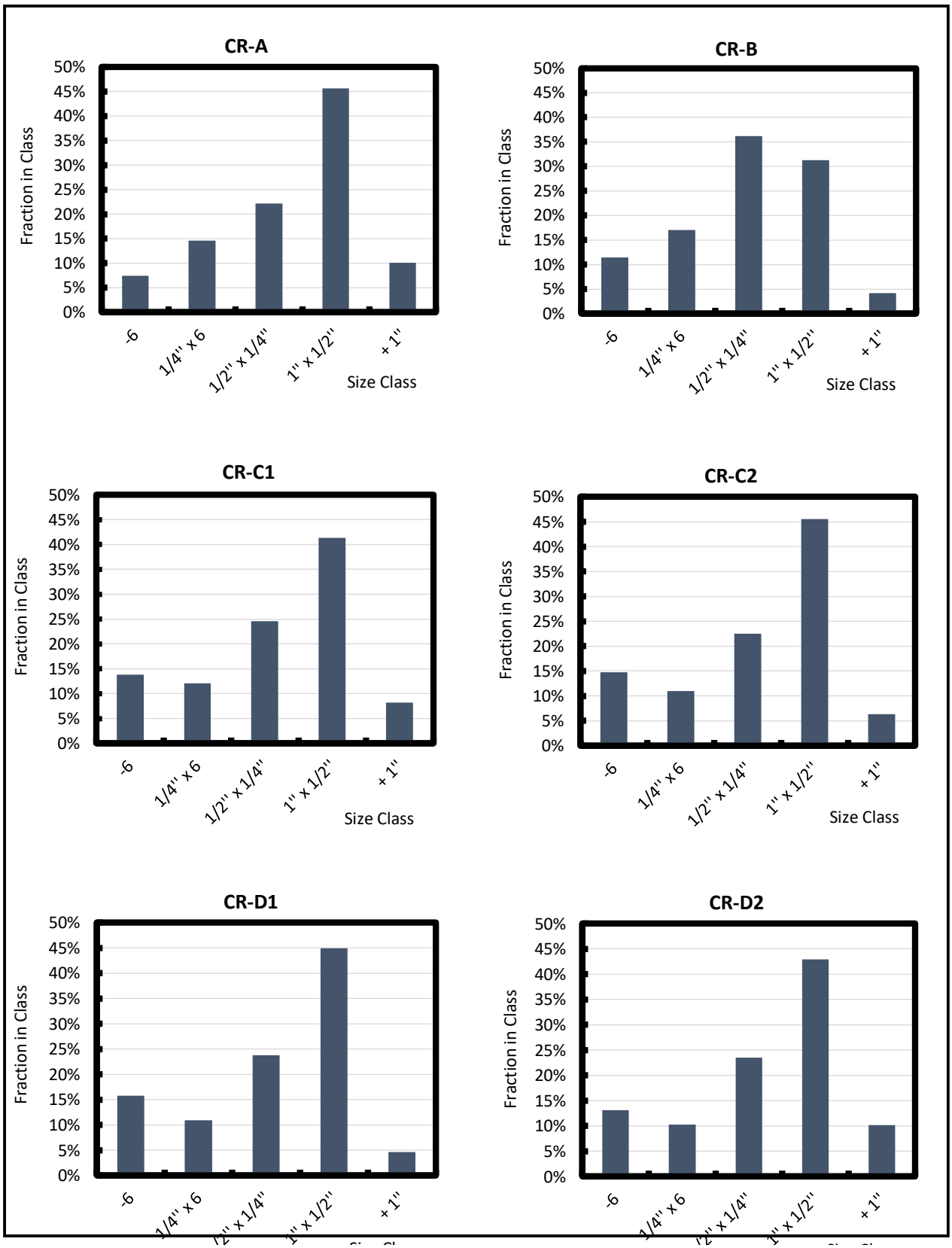

Figure 2 - 6: Fractional size distribution of coal refuse samples

2.2.2. SEM imaging

Figure 2 - 7 shows the SEM images of coal refuse samples with different magnification (x1000, x2500, x5000, and x10000). All the coarse refuse samples (CR-A, CR-B, CR-C1, CR-C2, CR-D1, and CR-D2) have similar crystallographic structures; however, the pyrite sample has a unique micromorphological structure as shown in Figure 2 - 8. Several SEM images of the pyrite show a spherical framboidal structure which consists of densely packed euhedral microcrystallites. These SEM images clearly demonstrate the presence of framboidal pyrite in the desulfurization reject sample.

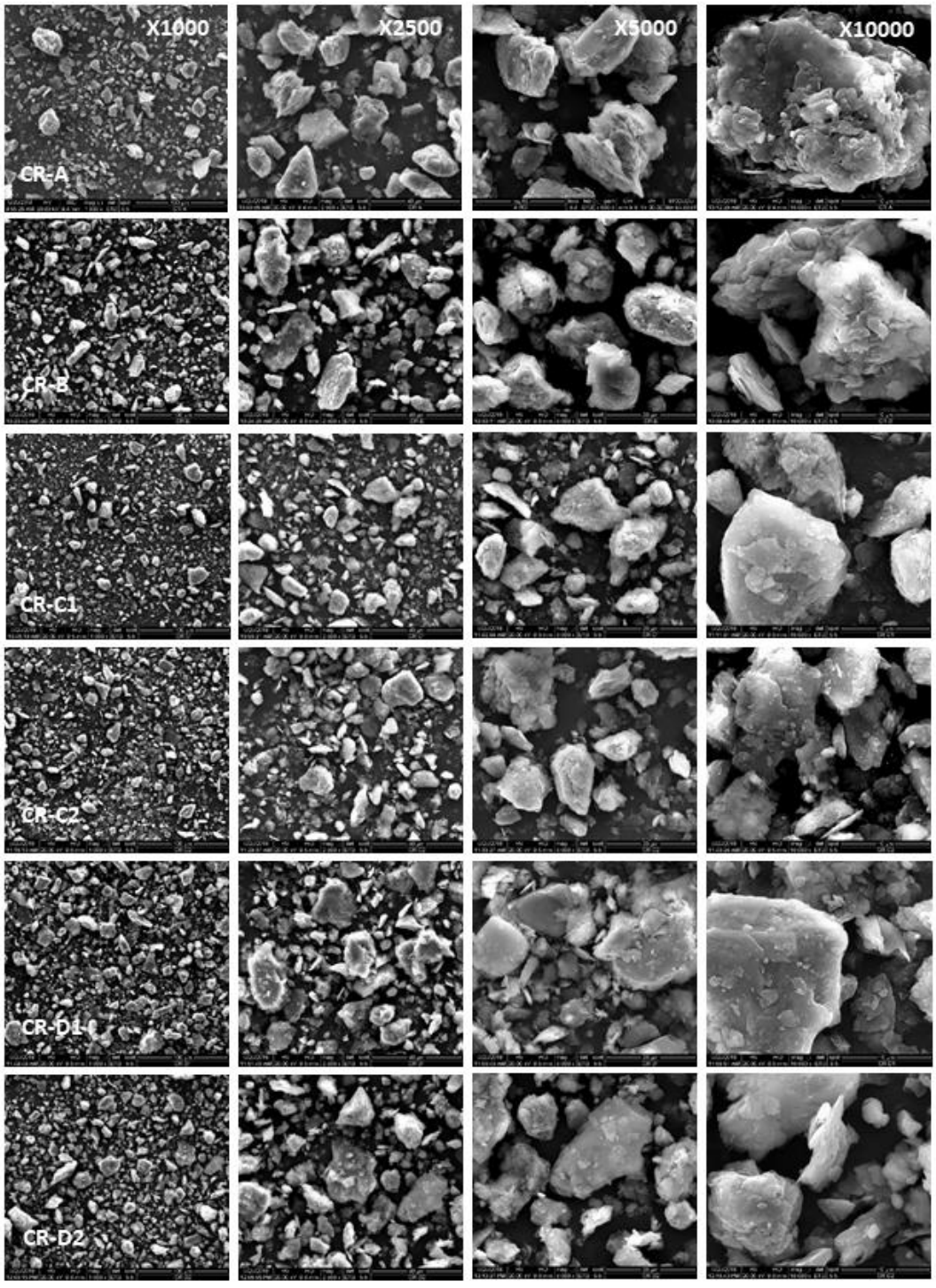

Figure 2 - 7: SEM images of coal refuge samples at different magnifications (x1000, 2500, 5000, 10000)

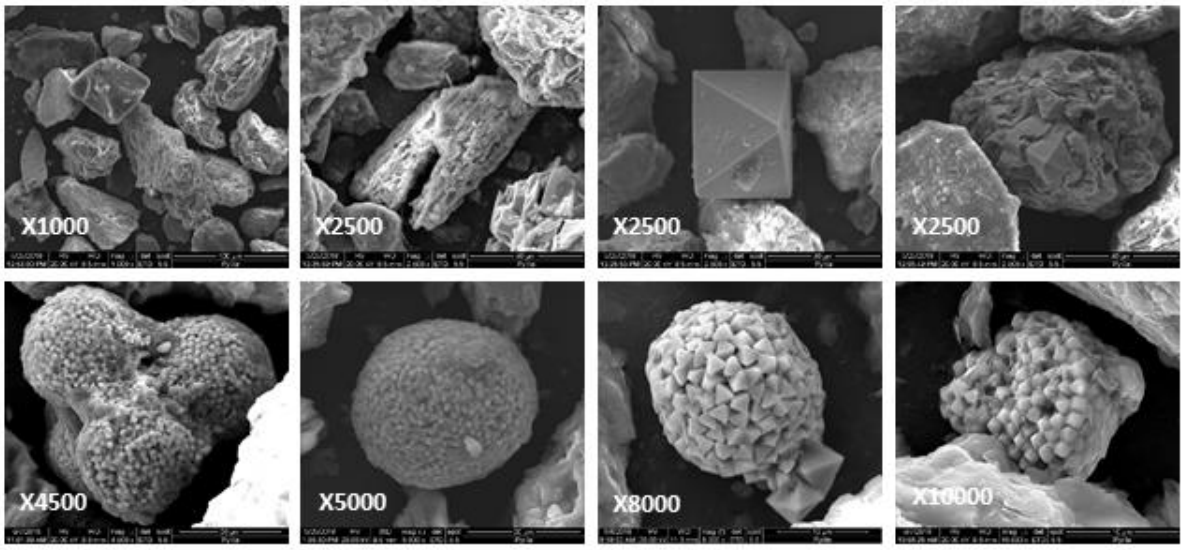

Figure 2 - 8: SEM images of pyrite samples at different magnifications

2.2.3 SEM-EDS mapping

The elemental composition of each coal refuse sample was analyzed by SEM-EDS. Figure 2 - 9 shows the resulting EDS mapping image (a) and spectrum (b) of CR-A sample. It should be noted that the peaks at 2.123 and 2.838 keV in the figure are from the sputter coating of Au and Pd, rather than the actual test specimen. An inset in Figure 2 - 9(b) shows the weight percentage of each element observed in CR-A by SEM-EDS. This data shows that CR-A is primarily composed of silicon oxide and aluminum oxide. Fe is present in the sample with a low concentration of 3.58%. While Figure 2 - 9 shows a complete elemental map of the entire image, Figure 2 - 10 shows point analysis of specific particles to better show the range of elemental concentrations.

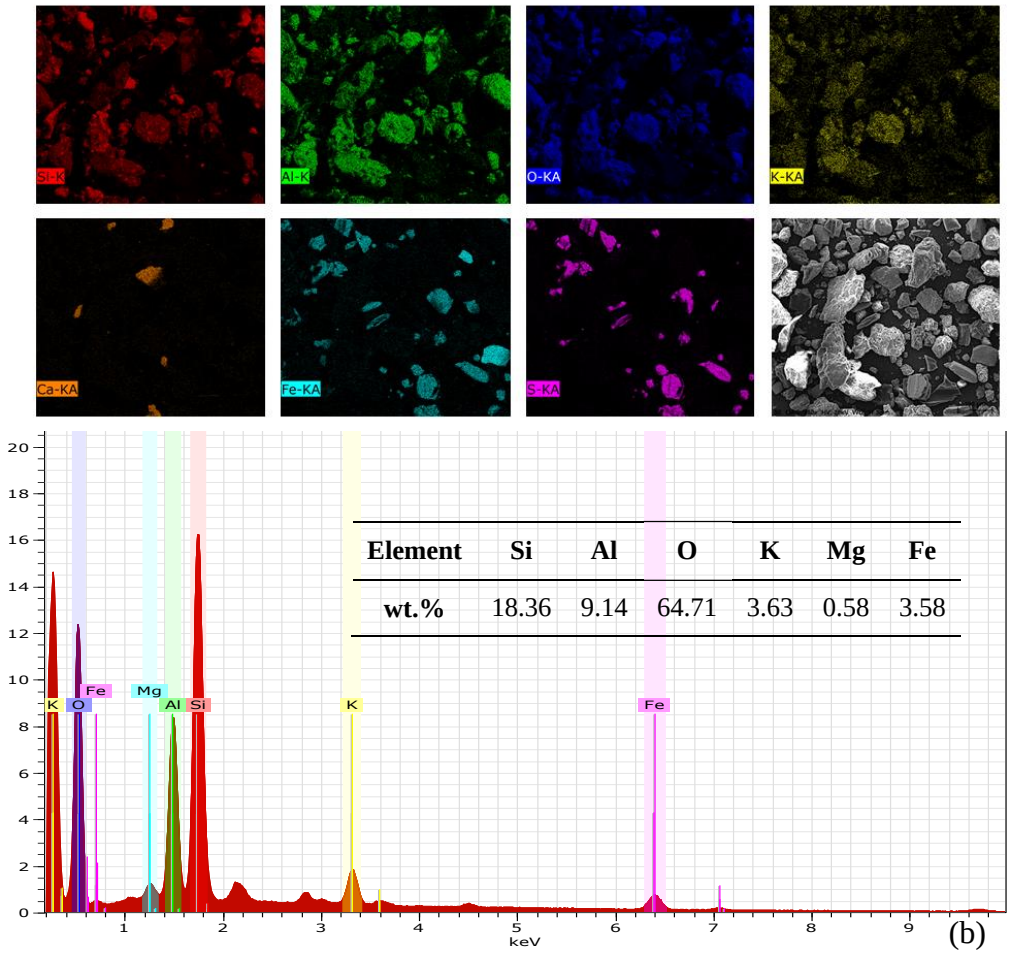

Element	Si	Al	O	K	Mg	Fe
wt.%	18.36	9.14	64.71	3.63	0.58	3.58

Figure 2 - 9: (a) SEM-EDS mapping images and (b) spectrum of CR-A

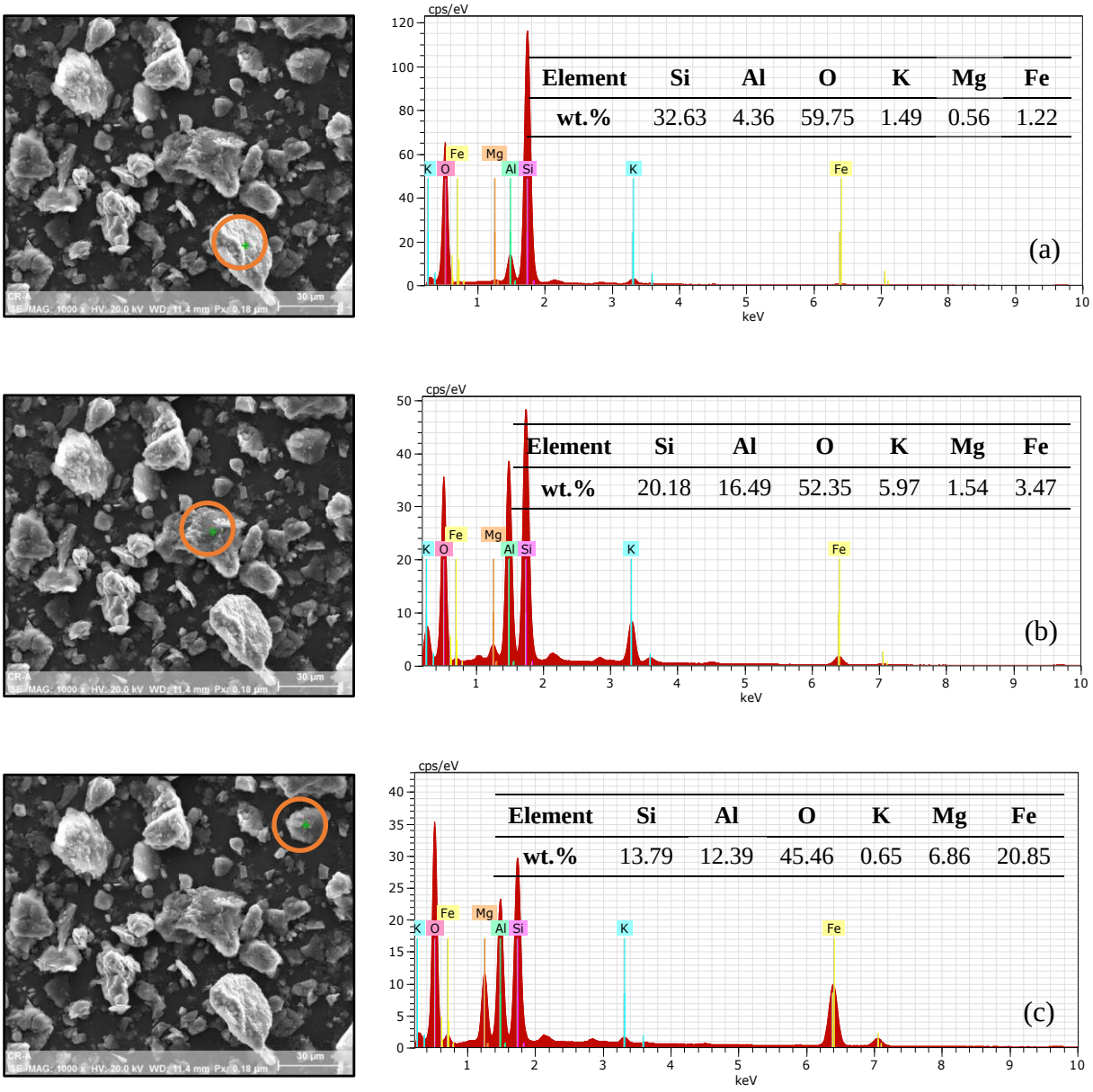

Figure 2 - 10: EDS point analysis of CR-A at the different specimens

Figure 2 - 11 to Figure 2 - 15 show the SEM-EDS analysis for the other coal refuse samples. Notably, the EDS spectra for CR-B (Figure 2 - 11) shows a moderate amount of sulfur (4.73 wt%), which agrees well with the sulfur values in **Error! Reference source not found.**. T he elemental composition and morphology of the remaining samples are similar to that of the CR-A, showing no or little evidence of sulfur/pyrite in the samples. By contrast, SEM-EDS analysis of the desulfurization reject sample shows a high sulfur content of 8.39 wt% (Figure 2 - 16). Moreover, Figure 2 - 17 shows that the iron and sulfur are largely contained in the framboidal structure, with the point analysis of the framboid itself (Figure 2 - 17 (c)) showing a very high sulfur content of 40.87 wt%. Table 2 - 3 lists the areal elemental compositions (as obtained by SEM-EDS) of each coal refuse sample for comparison.

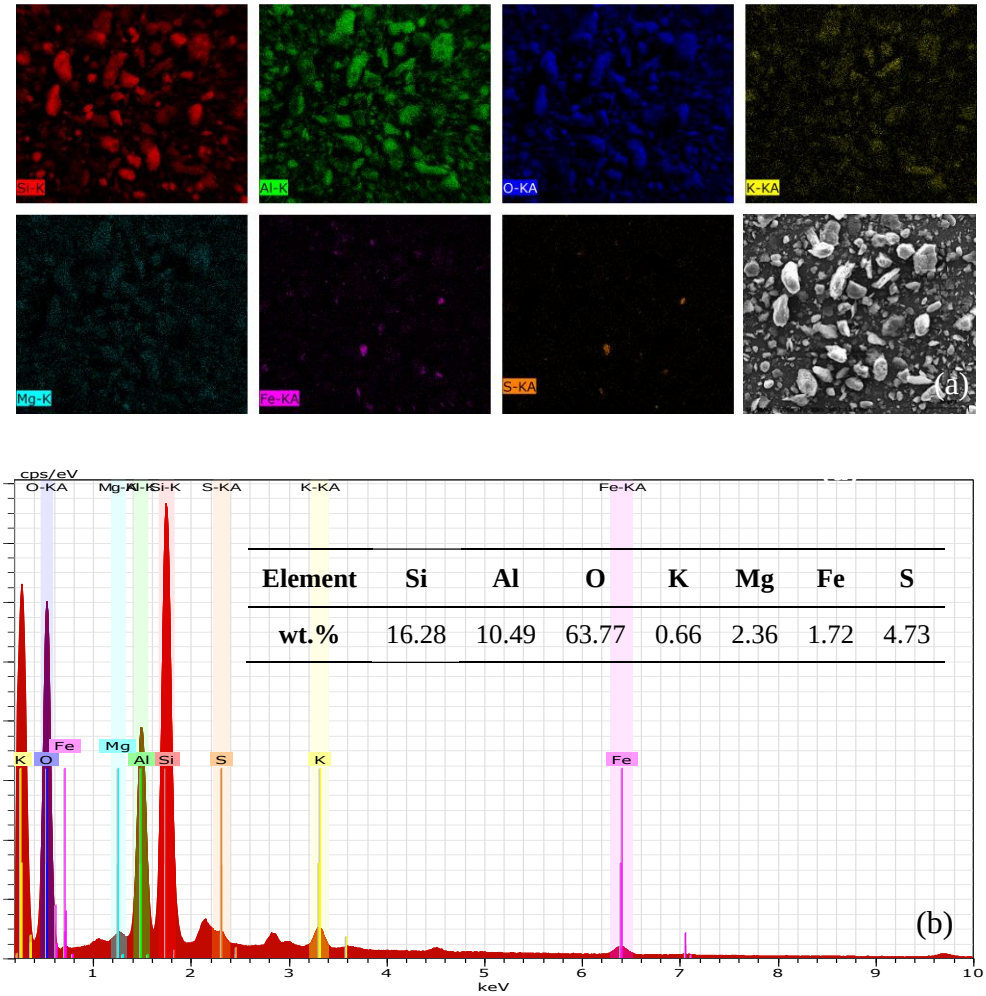

Figure 2 - 11: (a) SEM-EDS mapping images and (b) EDS spectrum of CR-B

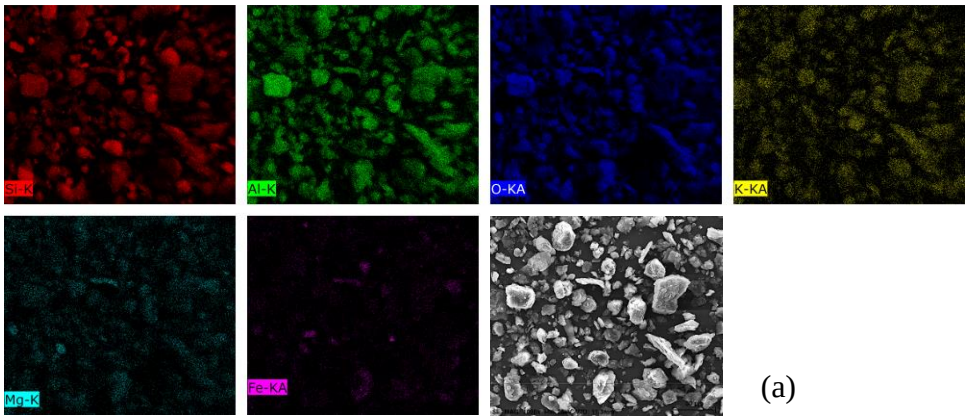

(a)

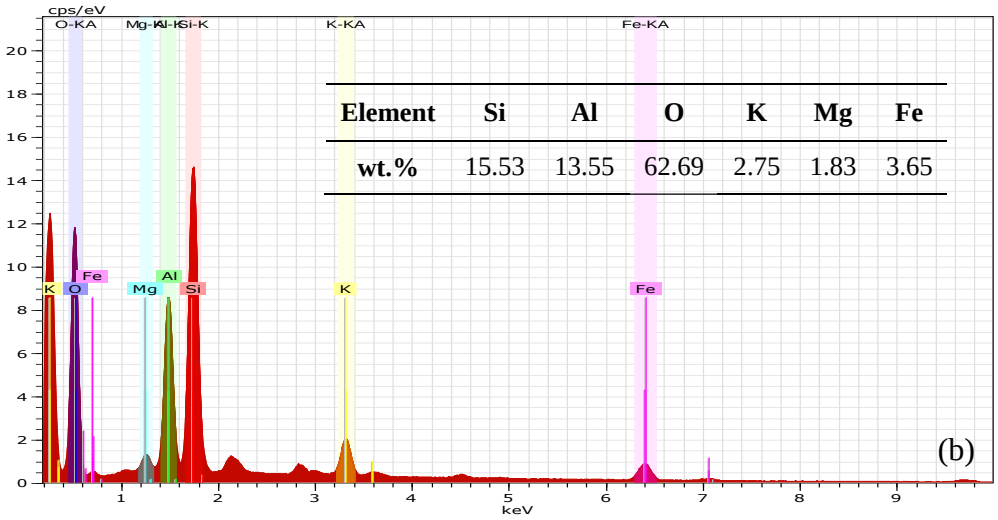

Element	Si	Al	O	K	Mg	Fe
wt.%	15.53	13.55	62.69	2.75	1.83	3.65

(b)

Figure 2 - 12: (a) SEM-EDS mapping images and (b) EDS spectrum of CR-C1

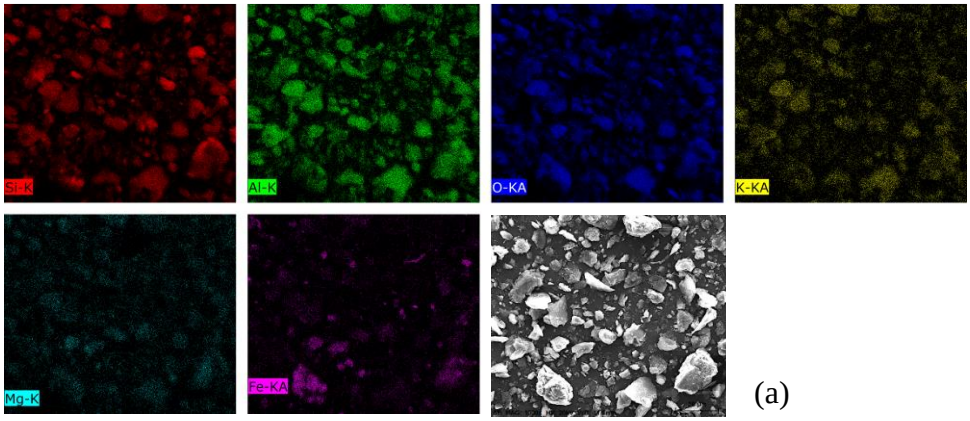

(a)

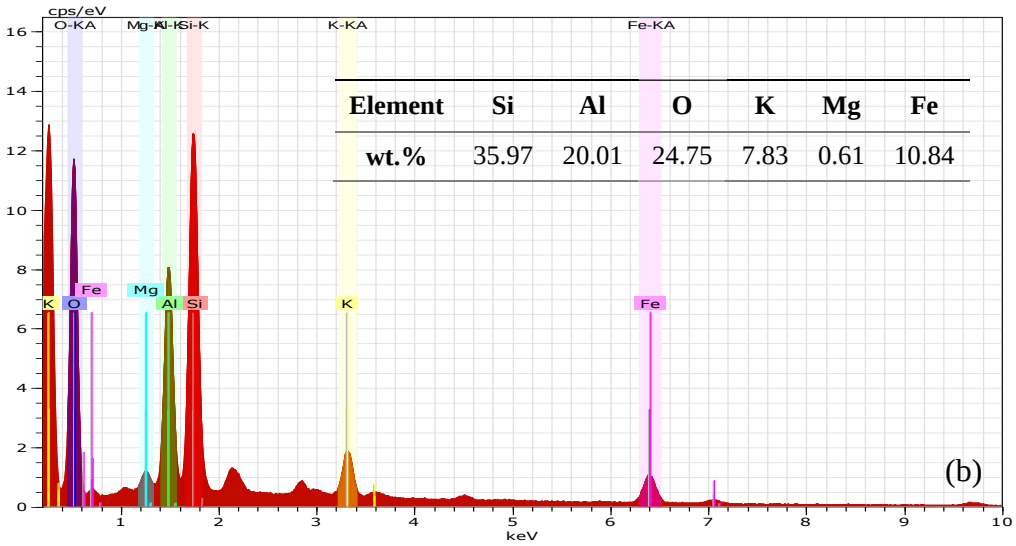

Element	Si	Al	O	K	Mg	Fe
wt.%	35.97	20.01	24.75	7.83	0.61	10.84

Figure 2 - 13: (a) SEM-EDS mapping images and (b) EDS spectrum of CR-C2

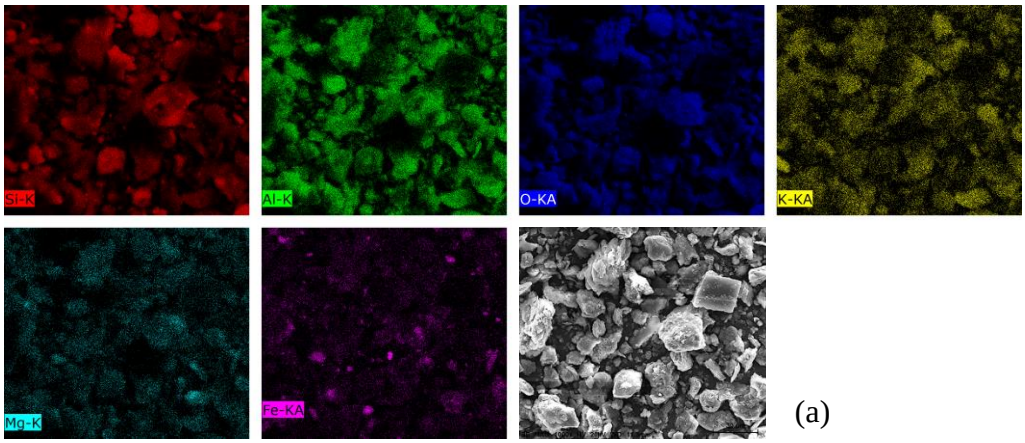

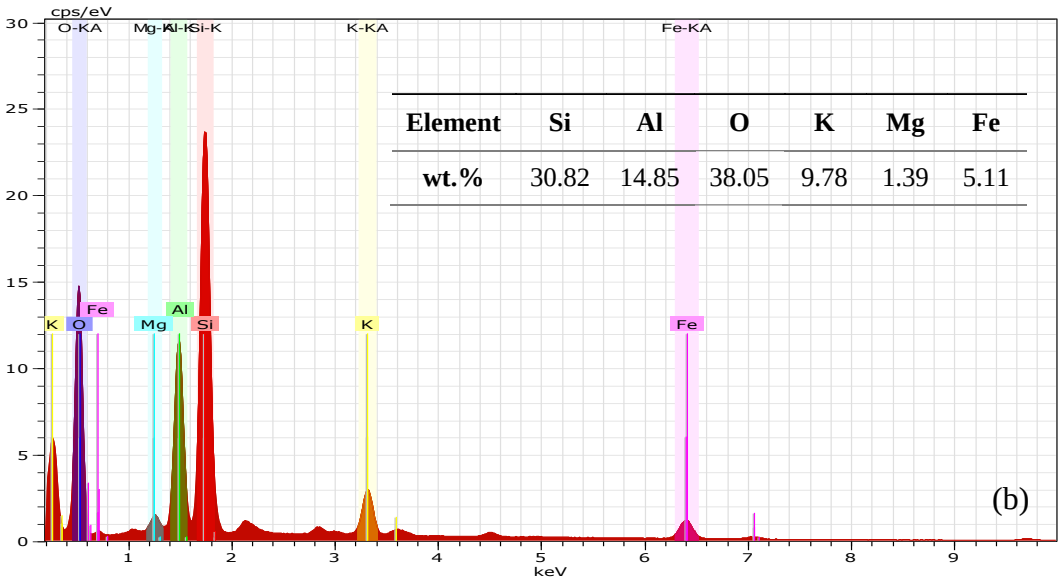

Figure 2 - 14: (a) SEM-EDS mapping images and (b) EDS spectrum of CR-D1

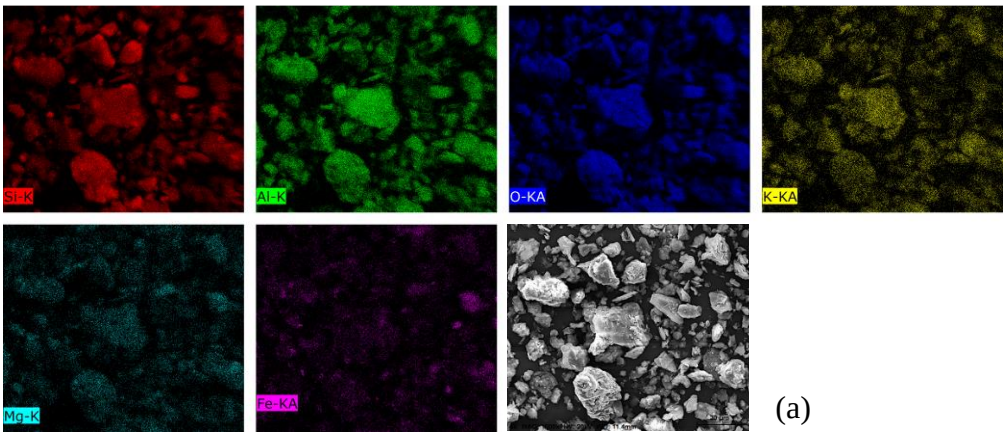

(a)

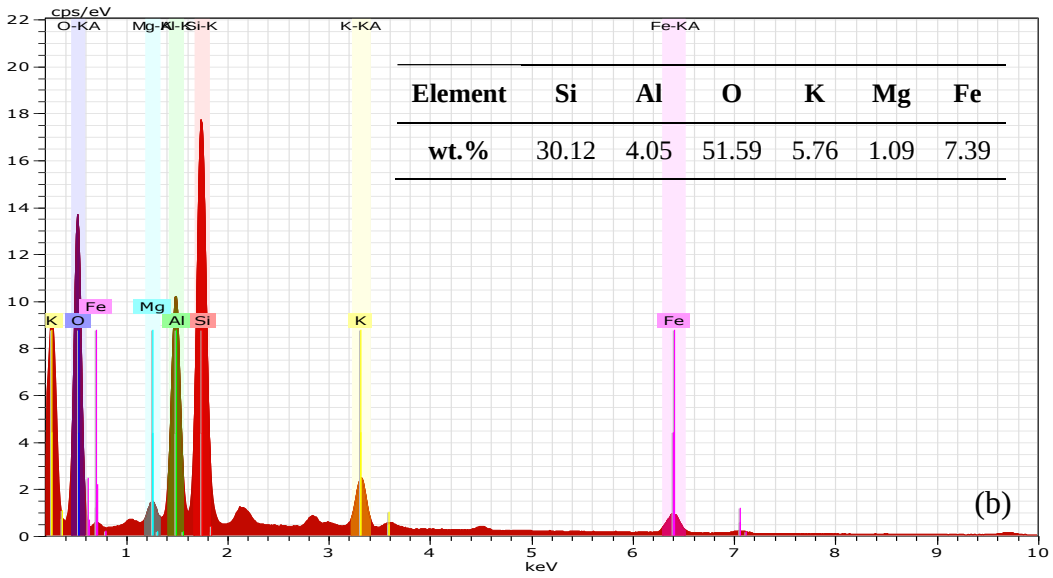

Element	Si	Al	O	K	Mg	Fe
wt.%	30.12	4.05	51.59	5.76	1.09	7.39

(b)

Figure 2 - 15: (a) SEM-EDS mapping images and (b) EDS spectrum of CR-D2

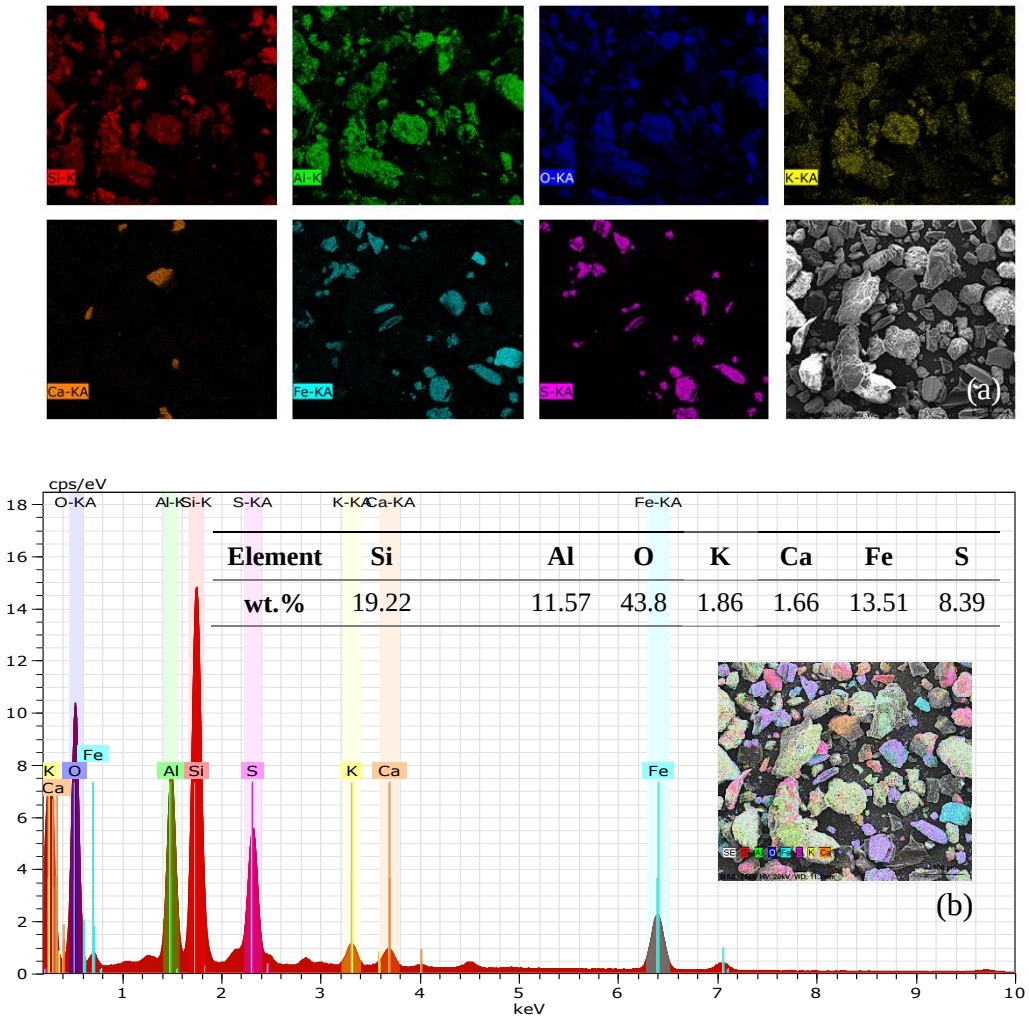

Figure 2 - 16: (a) SEM-EDS mapping images and (b) EDS spectrum of Pyrite

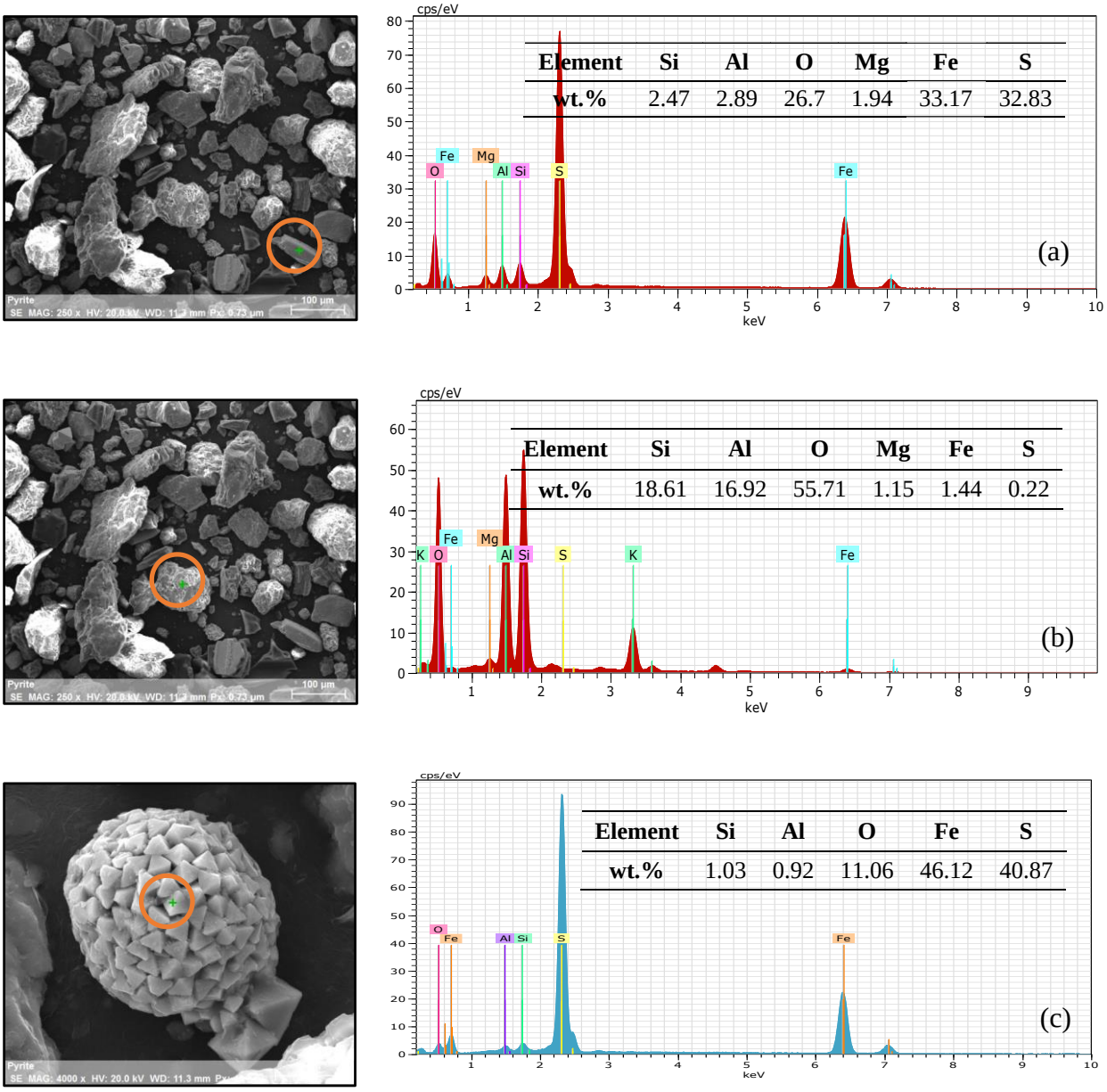

Figure 2 - 17: EDS point analysis of Pyrite in different specimens

Table 2 - 3: Elemental composition of the 7 different coal refuse samples as obtained by SEM-EDS

	Si	Al	O	K	Mg	Fe	S	Ca
CR-A	18.36	9.14	64.71	3.63	0.58	3.58		
CR-B	16.28	10.49	63.77	0.66	2.36	1.72	4.73	
CR-C1	15.53	13.55	62.69	2.75	1.83	3.65		
CR-C2	35.97	20.01	24.75	7.83	0.61	10.84		
CR-D1	30.82	14.85	38.05	9.78	1.39	5.11		
CR-D2	30.12	4.05	51.59	5.76	1.09	7.39		
Pyrite	19.22	11.57	43.8	1.86		13.51	8.39	1.66

2.2.4 X-Ray diffraction

Further characterization of coal refuse samples was carried out by x-ray diffraction for phase identification and crystal structure determination. Figure 2 - 18 shows the XRD patterns for all the coal refuse samples. Specifically, CR-A, C1, C2, D1, and D2 displayed almost identical XRD patterns as shown in Figure 2 - 19(a), whereas the XRD pattern of CR-B deviated from the patterns of the other coal refuses as illustrated in Figure 2 - 19 (b). The XRD spectrum of the pyrite sample includes several distinctive peaks compared to other patterns as shown in Figure 2 - 19 (c). Figure 2 - 20 presents the crystalline phases found in CR-A, using a database of x-ray powder diffraction patterns maintained by the International Center for Diffraction Data. According to this data, CR-A primarily consists of quartz low, iwakiite, brindleyite, dysprosium, silicon oxide, nitride, etc. The chemical formula and crystal structure of those phases are described in Table 2 - 4. A higher score in the table indicates a higher match with the possible phase identification. The phase identification of CR-B is shown in Figure 2 - 21 and Table 2 - 5. The major components of CR-B are quartz low, kaolinite, ammonioalunite, and nickel sulfate hydrate, which have different crystal structures such as hexagonal, anorthic, and tetragonal. CR-C1 and CR-C2 show the same phase identification including quartz low, iwakiite, nimesite, and aluminum lanthanum magnesium, as displayed in Figure 2 - 22, Figure 2 - 23 and Table 2 - 6, Table 2 - 7, respectively. Likewise, both CR-D1 and CR-D2 are primarily composed of quartz low, iwakiite, nimesite, and yttrium silicon oxide nitride, as shown in Figure 2 - 24, Figure 2 - 25 and Table 2 - 8, Table 2 - 9, respectively. The phases of the pyrite sample detected by the XRD pattern analysis were quartz, pyrite, kaolinite-montmorillonite, and calcium yttrium silicate, as indicated in Figure 2 - 26 and Table 2 - 10.

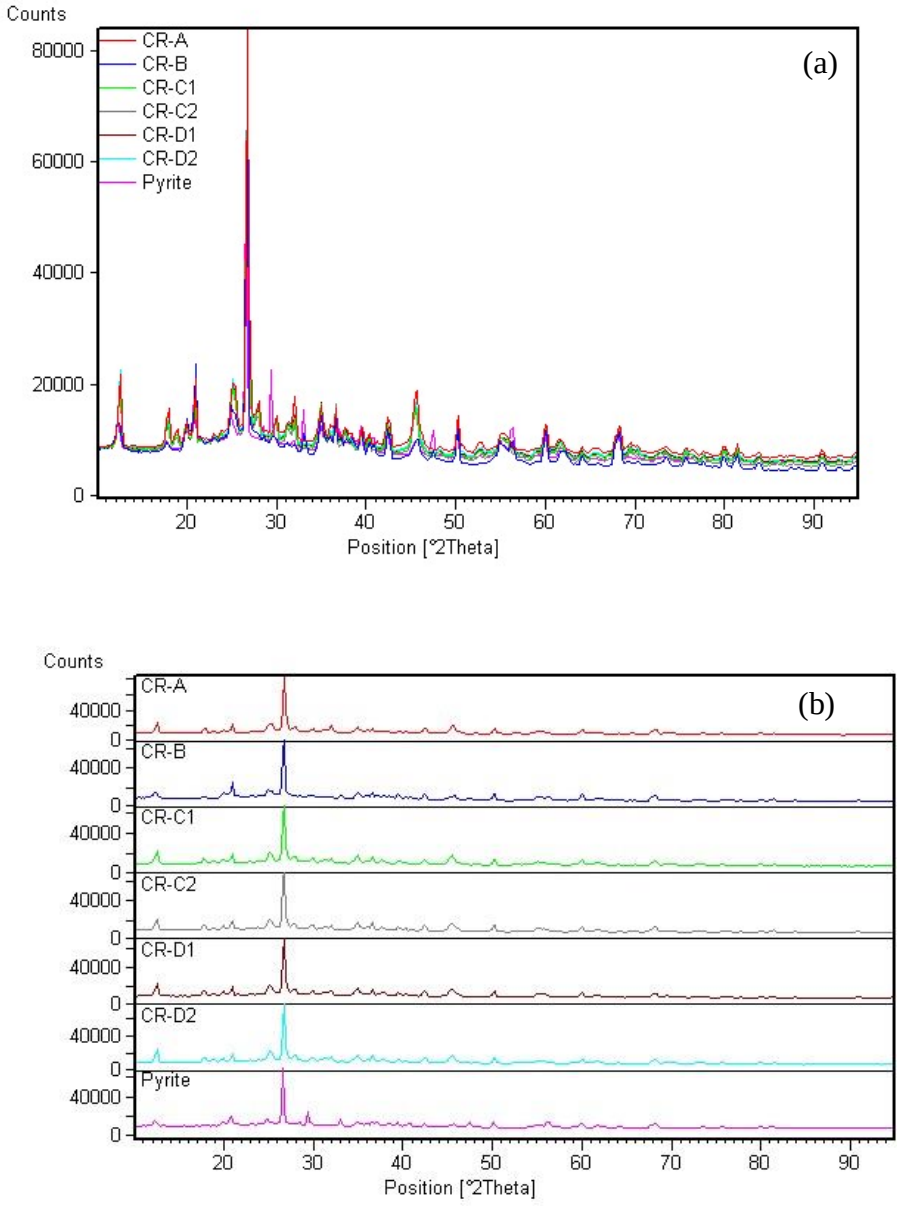

Figure 2 - 18: Comparison of XRD patterns for all coal refuse samples

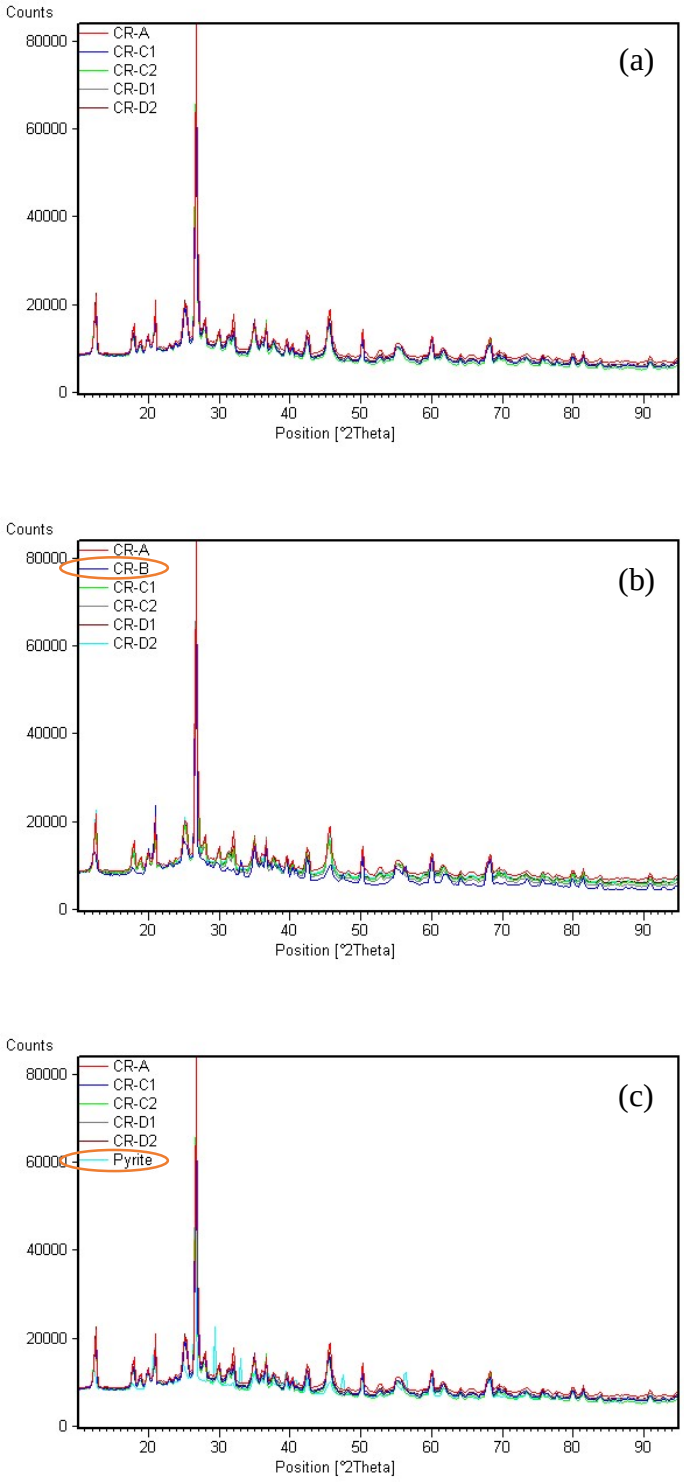

Figure 2 - 19: XRD patterns of (a) CR-A, C1, C2, D1, D2; with (b) CR-B; with (c) Pyrite

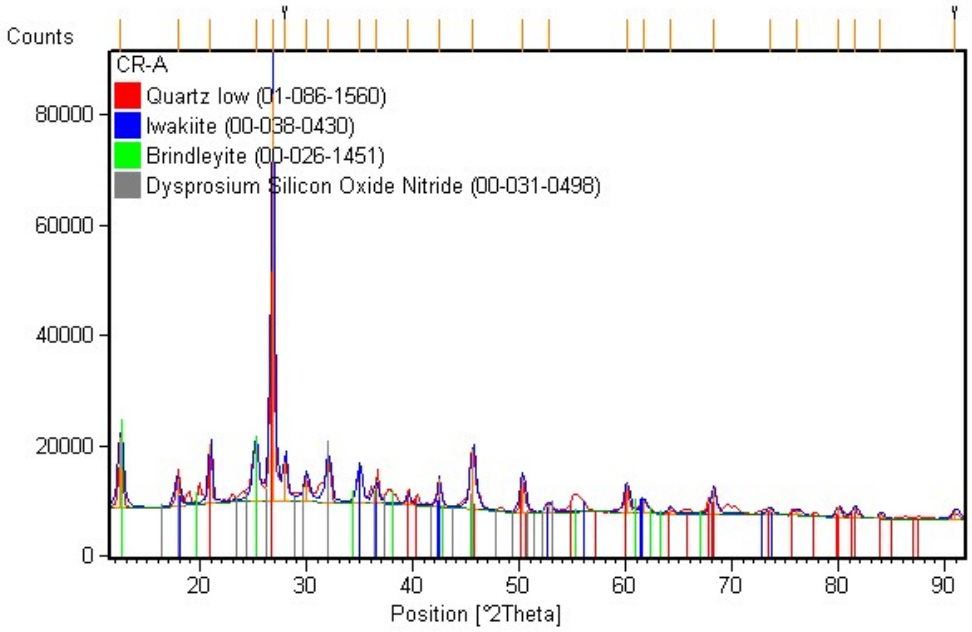

Figure 2 - 20: Identification of XRD phase for CR-A

Table 2 - 4: Phase and crystal structure of CR-A

Compound Name	**Chemical Formula**	**Crystal**	**Score**
Quartz low	SiO_2	Hexagonal	65
Iwakiite	$MnFe_2O_4$	Tetragonal	46
Brindleyite	$(Ni_2Al)(SiAl)O_5(OH)_4$	Unknown	43
Dysprosium Silicon Oxide Nitride	$Dy_2Si_3N_4O_3$	Unknown	38

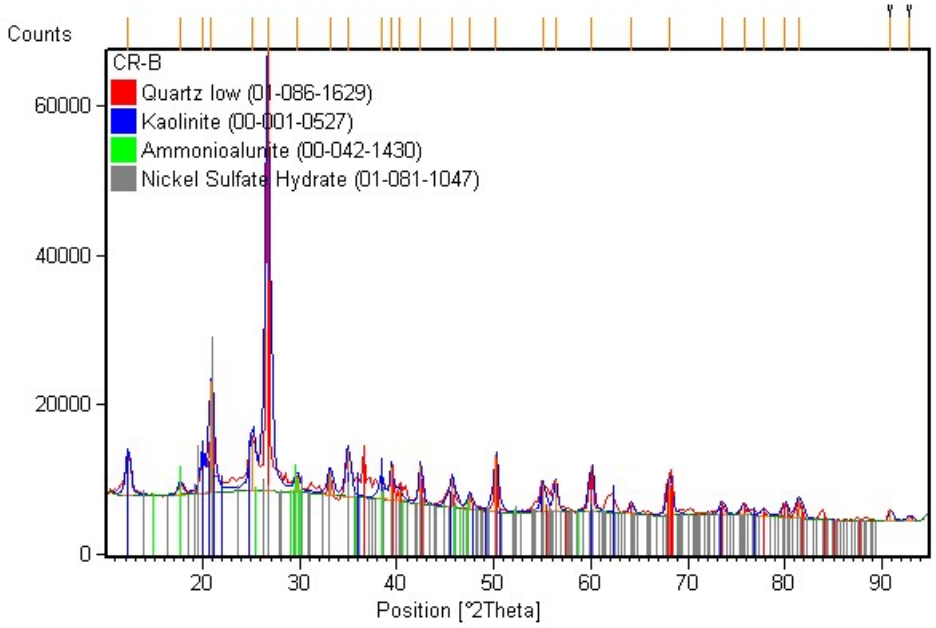

Figure 2 - 21: Identification of XRD phase for CR-B

Table 2 - 5: Phase and crystal structure of CR-B

Compound Name	**Chemical Formula**	**Crystal**	**Score**
Quartz low	SiO_2	Hexagonal	74
Kaolinite	$Al_2Si_2O_5(OH)_4$	Anorthic	52
Ammonioalunite	$NH_4Al_3(SO_4)_2(OH)_6$	Hexagonal	40
Nickel Sulfate Hydrate	$Ni(SO_4)(H_2O)_6$	Tetragonal	27

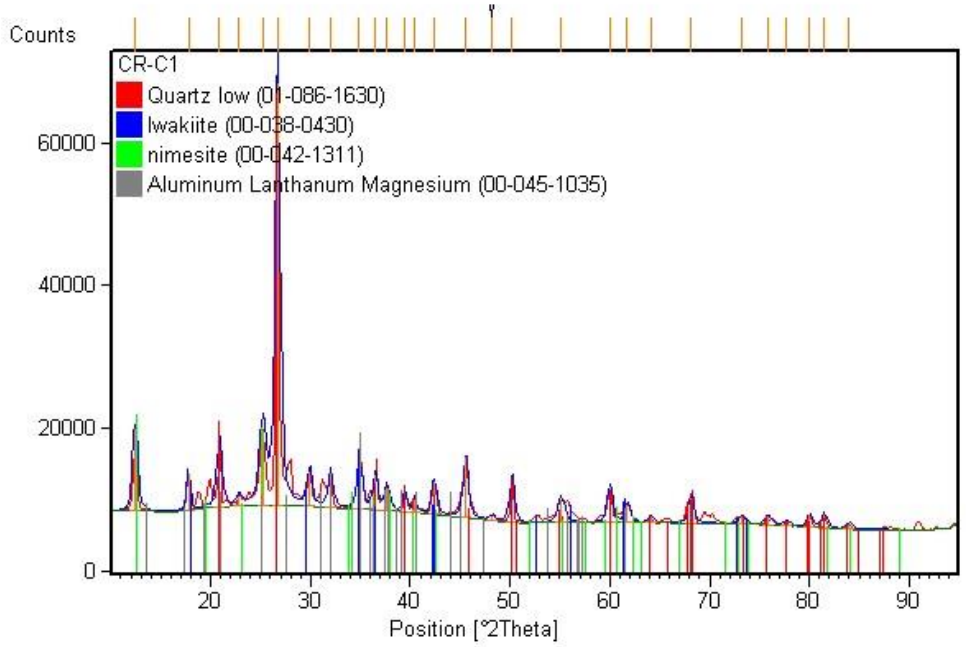

Figure 2 - 22: Identification of XRD phase for CR-C1

Table 2 - 6: Phase and crystal structure of CR-C1

Compound Name	**Chemical Formula**	**Crystal**	**Score**
Quartz low	SiO_2	Hexagonal	70
Iwakiite	$MnFe_2O_4$	Tetragonal	48
Nimesite	$(Ni_2Al)(AlSi)O_5(OH)_4$	Hexagonal	44
Aluminum Lanthanum Magnesium	$Al_2La_{0.15}Mg_{0.85}$	Unknown	22

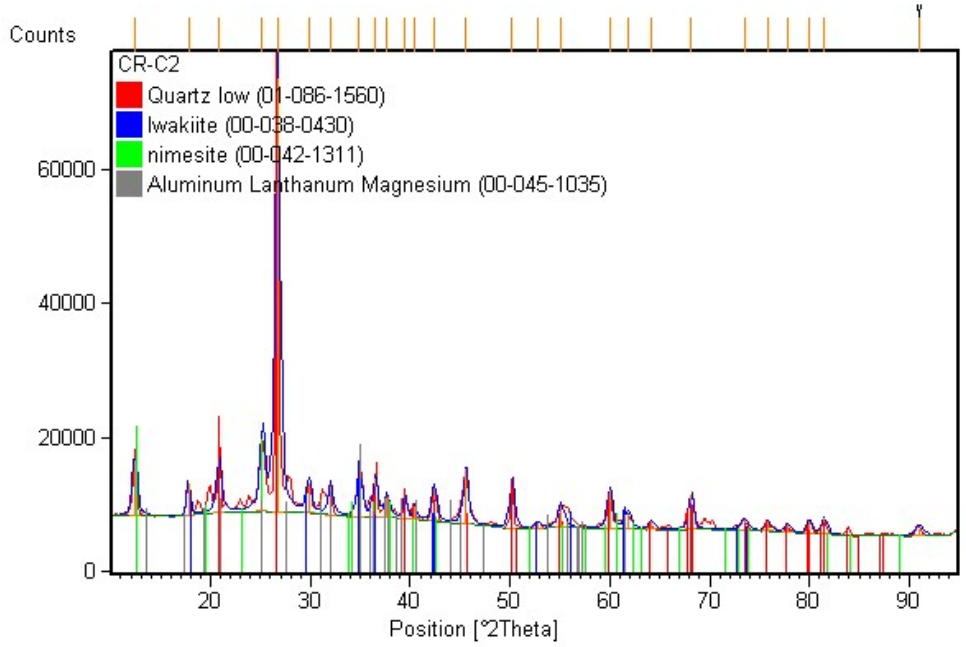

Figure 2 - 23: Identification of XRD phase for CR-C2

Table 2 - 7: Phase and crystal structure of CR-C2

Compound Name	**Chemical Formula**	**Crystal**	**Score**
Quartz low	SiO_2	Hexagonal	75
Iwakiite	$MnFe_2O_4$	Tetragonal	48
Nimesite	$(Ni_2Al)(AlSi)O_5(OH)_4$	Hexagonal	45
Aluminum Lanthanum Magnesium	$Al_2La_{0.15}Mg_{0.85}$	Unknown	21

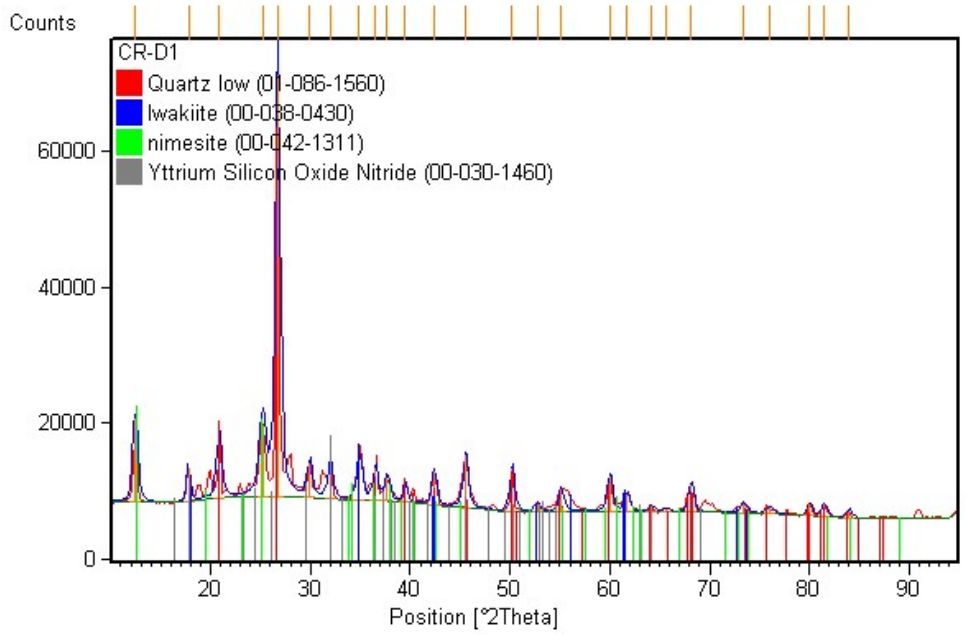

Figure 2 - 24: Identification of XRD phase for CR-D1

Table 2 - 8: Phase and crystal structure of CR-D1

Compound Name	**Chemical Formula**	**Crystal**	**Score**
Quartz low	SiO_2	Hexagonal	71
Iwakiite	$MnFe_2O_4$	Tetragonal	52
Nimesite	$(Ni_2Al)(AlSi)O_5(OH)_4$	Hexagonal	45
Yttrium Silicon Oxide Nitride	$Y_2Si_3N_4O_3$	Tetragonal	38

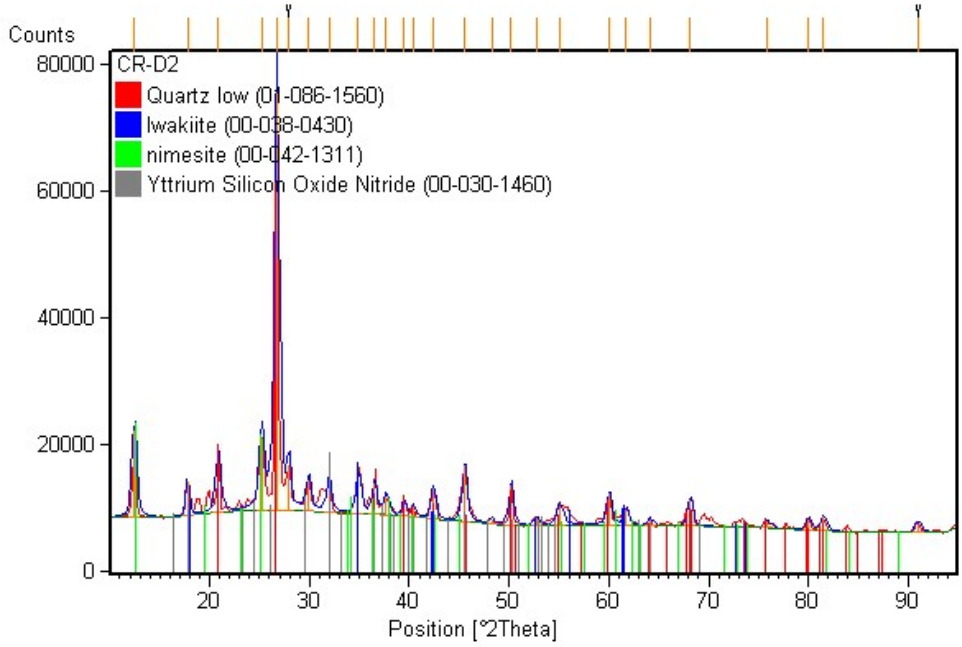

Figure 2 - 25: Identification of XRD phase for CR-D2

Table 2 - 9: Phase and crystal structure of CR-D2

Compound Name	**Chemical Formula**	**Crystal**	**Score**
Quartz low	SiO_2	Hexagonal	68
Iwakiite	$MnFe_2O_4$	Tetragonal	51
Nimesite	$(Ni_2Al)(AlSi)O_5(OH)_4$	Hexagonal	45
Yttrium Silicon Oxide Nitride	$Y_2Si_3N_4O_3$	Tetragonal	39

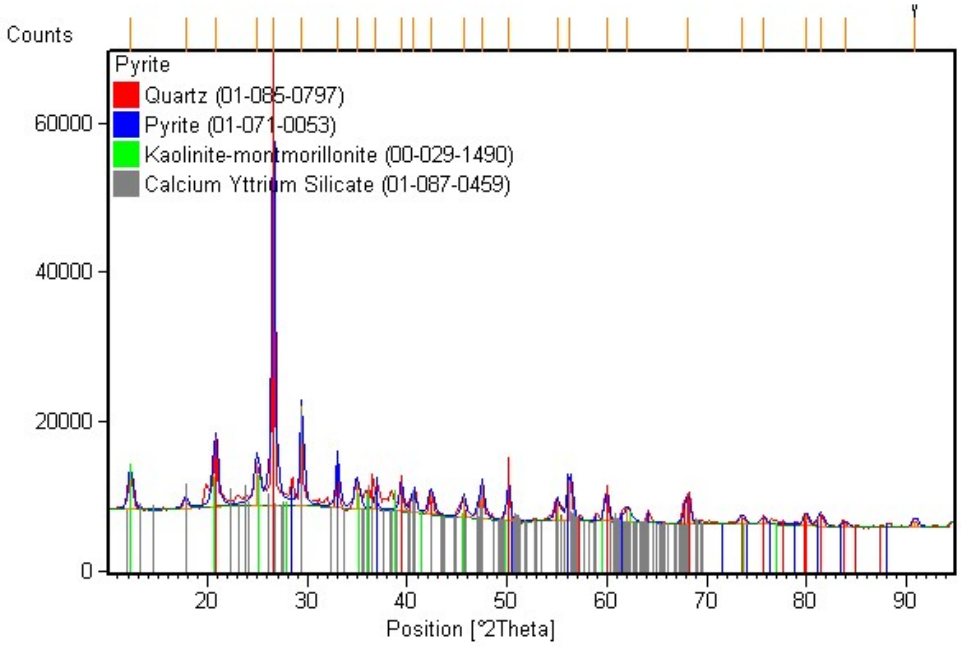

Figure 2 - 26: Identification of XRD phase for pyrite

Table 2 - 10: Phase and crystal structure of pyrite

Compound Name	**Chemical Formula**	**Crystal**	**Score**
Quartz	SiO_2	Hexagonal	77
Pyrite	FeS_2	Cubic	44
Kaolinite-montmorillonite	$Na_{0.3}Al_4Si_6O_{15}(OH)_6 \cdot 4H_2O$	Unknown	43
Calcium Yttrium Silicate	$Ca_3Y_2(Si_3O_9)_2$	Monoclinic	32

2.2.5 X-Ray fluorescence

An X-ray fluorescence (XRF) scanner (Niton^{TM} XL2 GOLD, Thermo Scientific) was used to determine the bulk elemental concentration of various species. Each coal refuse sample was first ground to 25 μm, and then pressed into a pellet using a laboratory pellet press at 9 metric tons of pressure. Table 2 - 11 shows the results of XRF analysis with 7 different samples. The predominant elements of the coal refuse samples are Si, Al, Fe, and K. Only CR-B and Pyrite samples showed high sulfur contents of 3.88 and 9.58 wt.%, respectively, which are similar to the aerial values obtained from SEM-EDS analysis in Figure 2 - 11 and Figure 2 - 16. Other elements such as Ba, Sn, Nb, Zr, Sr, Rb, Bi, As, W, Ta, Hf, Ni, and V were detected by XRF at a weight percent of less than 0.1. Table 2 - 12 presents the XRF results after ashing the coal refuse samples. Compared to the values before ashing, the amount of sulfur dropped significantly in the CR-B and Pyrite samples. The weight loss of sulfur was about 60-70%, which is attributed to the volatilization of sulfur during the ashing process at a high temperature of 700 ^{o}C. Nevertheless, the XRF data for sulfur on the pre-ashed samples agrees well with the total sulfur analysis presented in the prior report. This result indicates that the Niton XRF is suitable to sulfur content in processed samples.

Table 2 - 11: XRF analysis of coal refuse samples (wt.%)

Sample	Si	Al	Fe	S	K	Ca	Ti	Mn
CR-A	32.00	15.11	6.87	0.31	3.09	0.17	0.75	0.1
CR-B	33.74	15.63	4.76	3.88	1.70	0.66	1.12	0.02
CR-C1	33.30	16.18	5.92	0.42	3.48	0.09	0.56	0.07
CR-C2	32.99	14.71	4.91	0.38	3.13	0.24	0.75	0.05
CR-D1	33.34	15.98	6.11	0.45	3.32	0.07	0.64	0.08
CR-D2	33.03	15.63	6.18	0.45	3.31	0.10	0.68	0.09
Pyrite	27.32	15.56	9.16	9.58	1.27	2.65	0.53	0.02

Table 2 - 12: XRF analysis of coal refuse ashes (wt.%)

Sample	Si	Al	Fe	S	K	Ca	Ti	Mn
CR-A	34.61	17.73	7.77	0.71	3.44	0.21	0.79	0.16
CR-B	37.53	19.76	7.03	1.43	1.9	0.65	1.13	0.03
CR-C1	34.90	17.83	6.38	0.93	3.64	0.12	0.63	0.07
CR-C2	36.93	18.77	5.76	0.62	3.55	0.26	0.89	0.07
CR-D1	35.78	18.53	6.93	0.71	0.62	0.10	0.73	0.09
CR-D2	35.71	18.40	7.03	0.95	3.64	0.13	0.66	0.09
Pyrite	30.67	19.61	13.99	2.85	1.33	2.20	0.60	0.02

2.2.6 Digestion and ICP-MS

A microwave digestion technique was developed and used in the analysis of total REE content. Several acid mixtures were evaluated for the microwave digestions including HNO_3, HCl, aqua regia, reverse aqua regia, H_3PO_4(20%)+HNO_3, H_2SO_4(20%)+HNO_3, and H_2O_2(20%)+HNO_3. During the method development, a 25 mg sample of ground CR-A material (<25 μm) was added in a digestion vessel followed by the addition of 12 ml acid mixture. After loading the vessels, the microwave unit (Multiwave Go, Anton Paar) was ramped to 185^o C within 15 min followed by a hold time of 20 min. The vessels were then cooled down to 70^o C and the resulting solution was diluted with DI water to achieve a 2% acid solution for ICP-MS analysis. The digestions were not complete and solid residues remained in all the cases. Table 2 - 13 shows the concentration of REEs in the CR-A detected by the ICP-MS analysis. It was found that REEs such as Ce, La, Nd, and Y were present at the concentration of 1 to 6 ppm in the CR-A and other REEs such as Sc, Pr, Dy, Sm, and Gd were also identified with low concentration of less than 1 ppm. Among all the acid solutions, the mixture of H_2SO_4(20%)+HNO_3 has shown the highest extraction of REEs in the CR-A. Further work is needed to determine if this incomplete digestion is suitable for assays.

Table 2 - 13: REE concentrations in CR-A with different digestion solutions (ppm)

Sample	Ce	La	Nd	Y	Sc	Pr	Dy	Sm	Gd
HNO_3	5.25	2.58	2.39	1.66	0.51	0.64	0.34	0.47	0.43
HCl	5.91	2.9	2.65	1.83	0.77	0.72	0.37	0.51	0.47
Aqua Regia	4.13	2.06	1.89	1.07	0.43	0.51	0.22	0.36	0.31
Reverse AR	3.96	1.96	1.81	1.14	0.5	0.48	0.23	0.35	0.31
H_3PO_4+HNO_3	3.49	1.69	1.59	1.01	0.3	0.42	0.21	0.32	0.29
H_2SO_4+HNO_3	6.79	3.31	3.06	1.8	1.01	0.82	0.39	0.59	0.51
H_2O_2+HNO_3	5.94	2.91	2.68	1.78	0.87	0.72	0.36	0.52	0.45

With those digestions, there were suspected issues involving dilution of the digestion solutions and interpretation of the results from the lab. All the CR head samples were then subjected to another digestion experiment using reverse aqua regia. For each CR head sample, approximately 25 mg was digested in 12 mL of reverse aqua regia solution and then analyzed for REE content by ICP-MS analysis. Table 2 - 14 shows the total and individual REE concentrations for the 5 CR head samples. CR-D2 contains the highest TREE concentration while CR-B has the lowest. Figure 2 - 27 shows the TREE concentration versus ash content on both whole mass and whole ash bases. Chondrite normalized individual REE concentrations are shown in Figure 2 - 28. All CR head samples are relatively similar in REE concentrations, with CR-D2 containing the greatest concentration.

Table 2 - 14: REE concentrations for coarse refuse head samples determined by ICP-MS

Sample	**TREE** **ppm**	Sc ppm	Y ppm	La ppm	Ce ppm	Pr ppm	Nd ppm	Sm ppm	Eu ppm	Gd ppm	Tb ppm	Dy ppm	Ho ppm	Er ppm	Tm ppm	Yb ppm	Lu ppm
CR-B	**199.79**	14.18	16.37	36.27	69.12	8.29	33.38	6.43	1.26	5.18	0.76	4.06	0.74	1.86	0.25	1.44	0.20
CR-C1	**232.57**	12.03	21.06	42.69	79.85	9.91	40.20	7.56	1.40	6.08	0.91	4.97	0.93	2.41	0.34	1.97	0.27
CR-C2	**227.90**	11.13	21.46	41.61	78.11	9.59	39.31	7.51	1.37	6.01	0.91	5.03	0.93	2.38	0.33	1.94	0.27
CR-D1	**247.52**	12.15	23.03	45.06	84.33	10.54	43.18	8.30	1.52	6.64	1.00	5.46	1.01	2.57	0.37	2.08	0.29
CR-D2	**250.98**	13.09	23.92	45.40	84.47	10.49	43.79	8.42	1.55	6.66	1.02	5.55	1.05	2.70	0.38	2.19	0.31

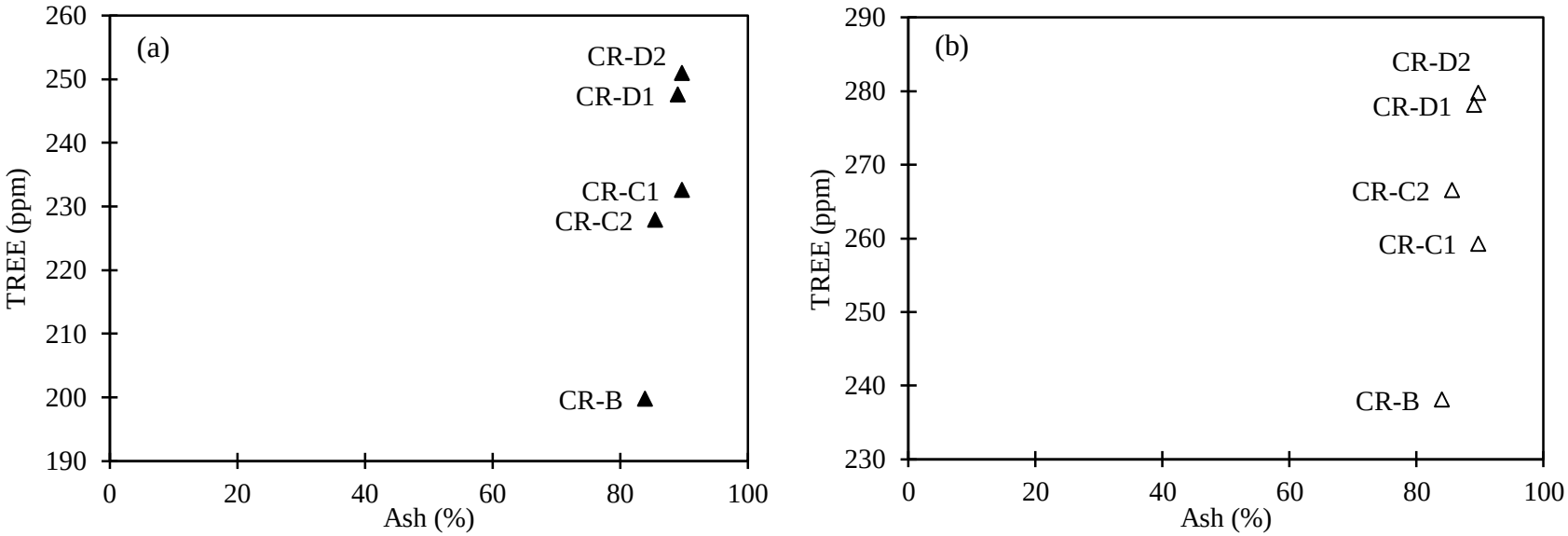

Figure 2 - 27: TREE vs. Ash content for CR head samples on whole sample basis (a) and ash basis (b)

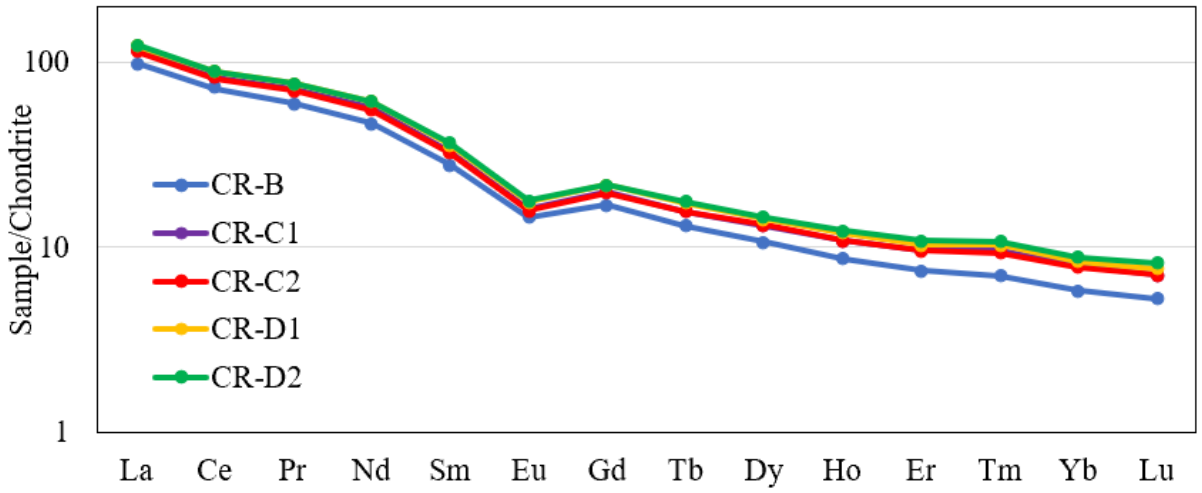

Figure 2 - 28: Chondrite normalized REE concentrations in coarse refuse head samples

Initial REE analysis on CR samples had been conducted using a reverse aqua regia microwave digestion method prior to ICP-MS analysis. To evaluate other methods of trace elemental analysis preparation, the head samples (CR-A, CR-B, CR-C1, CR-C2, CR-D1, CR-D2, CR-E) were sent to two independent laboratories for alternative sample preparation methods for trace elemental analysis. In this comparison, an additional coarse refuse sample from a West Virginia prep plant was included (CR-E).

One lab performed a hydrofluoric (HF) acid digestion, while the other utilized a sodium peroxide fusion. The TREE content measured from each preparation method are compared to the reverse aqua regia method the team has been using in Figure 2 - 29. LREE, HREE, and Scandium values are compared in Figure 2 - 30 – Figure 2 - 32, respectively. CR-E was not prepared using the reverse aqua regia digestion but is compared between the HF digestion and sodium peroxide fusion methods.

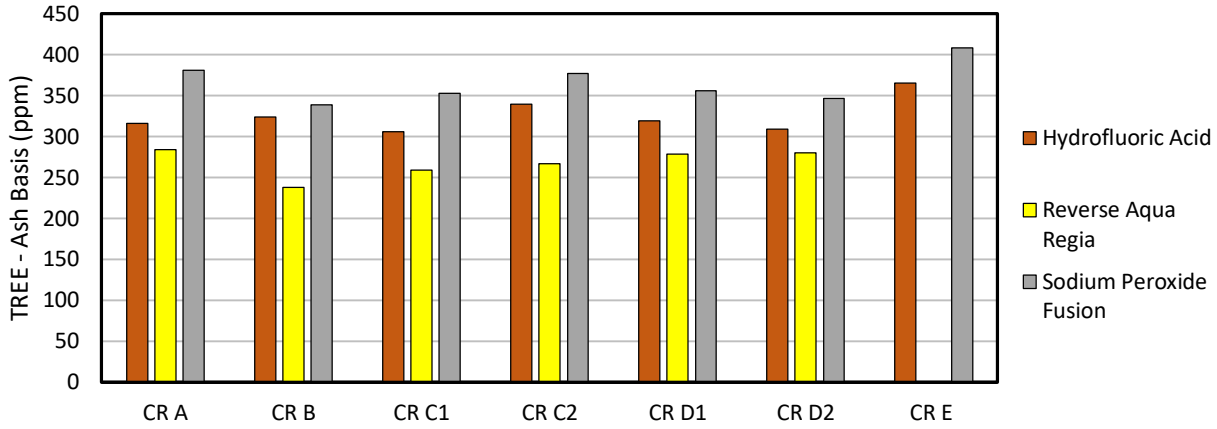

Figure 2 - 29: Trace elemental analysis sample preparation method comparison, TREE (ash basis)

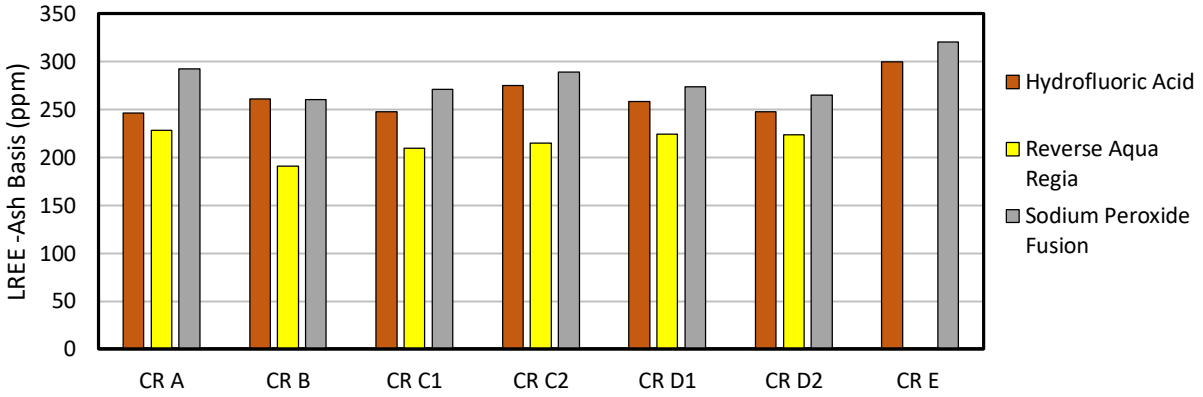

Figure 2 - 30: Trace elemental analysis sample preparation comparison, LREE (Ce-Gd) (ash basis)

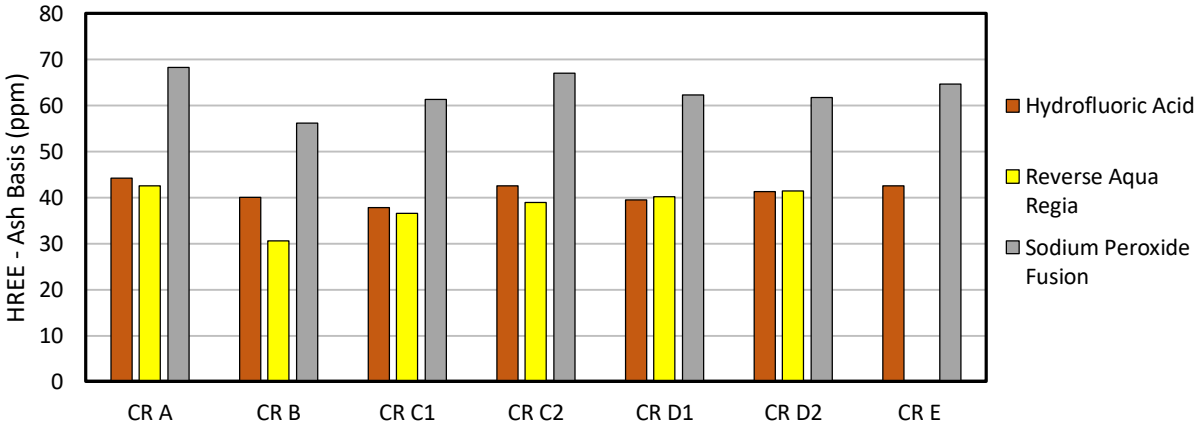

Figure 2 - 31: Trace elemental analysis sample preparation method comparison, HREE (Tb-Lu, Y) (ash basis)

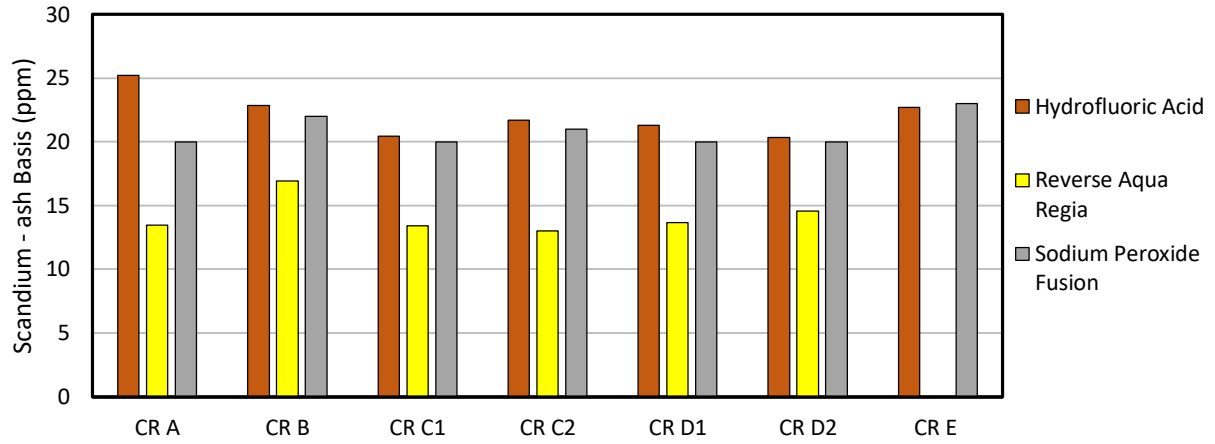

Figure 2 - 32: Trace elemental analysis sample preparation method comparison, Scandium (ash basis)

The sodium peroxide fusion method resulted in the highest TREE concentrations across all samples. This outcome was also the case for HREE and LREE values, however the sodium peroxide fusion method appeared to perform much better for HREEs than the other methods when compared to the difference in LREEs between methods. Interestingly, the HF digestion resulted in higher Scandium content for all samples except CR-E. The reverse aqua regia digestion resulted in the lowest concentrations for every scenario, except for CR-D2, where it provided a slightly higher HREE content.

Table 2 - 15 – Table 2 - 17 provide the individual REE values for each method. Table 2 - 18 – Table 2 - 20 show a direct comparison of percent change in individual REE values between each method. For most REEs the HF acid digestion resulted in higher concentrations than reverse aqua regia. The sodium peroxide fusion method outperformed the reverse aqua regia digestion for every REE in each sample. Some REEs had greater concentrations from the sodium peroxide fusion than HF such as Y, La, Ce, Dy, Ho, Tm, and Yb. Other REEs such as Pr through Gd appeared in lower concentrations from the sodium peroxide fusion than the HF digestion.

Table 2 - 15: REE content for CR head samples prepared by hydrofluoric acid digestion (ppm)

(ppm)	Sc	Y	La	Ce	Pr	Nd	Sm	Eu	Gd	Tb	Dy	Ho	Er	Tm	Yb	Lu	**TREE (Ash Basis)**	dry ash %
CR A	25.22	26.65	54.86	92.68	15.87	56.40	13.59	2.10	10.70		6.21	1.33	4.79	0.55	3.88	0.81	**315.7**	87.00
CR B	22.88	23.49	51.29	117.08	15.07	52.67	12.38	2.03	10.56	1.06	4.89	0.77	4.55	0.52	3.67	1.04	**324.0**	83.90
CR C1	20.45	22.76	52.04	103.11	15.21	53.04	12.36	1.99	9.70		5.18	0.94	4.18	0.55	3.46	0.70	**305.7**	89.70
CR C2	21.69	25.14	57.30	118.08	16.16	57.83	12.88	2.15	10.55		6.27	1.63	4.87	0.60	3.57	0.50	**339.2**	85.50
CR D1	21.28	23.57	55.70	105.87	15.96	55.47	13.12	2.03	9.97		5.95	1.18	4.41		3.53	0.79	**318.8**	89.00
CR D2	20.36	23.79	52.65	100.22	15.77	54.35	12.89	2.00	9.62	0.90	6.01	1.08	4.45	0.58	3.61	0.90	**309.2**	89.70
CR E	22.70	25.39	61.22	137.47	17.26	59.05	12.81	2.19	9.87		6.89	1.46	4.74	0.53	3.51		**365.1**	88.67

Table 2 - 16: REE content for CR head samples prepared by reverse aqua regia digestion (ppm)

(ppm)	Sc	Y	La	Ce	Pr	Nd	Sm	Eu	Gd	Tb	Dy	Ho	Er	Tm	Yb	Lu	**TREE (Ash Basis)**	dry ash %
CR A	13.49	27.36	51.05	97.66	12.02	48.72	9.39	1.75	7.70	1.19	6.40	1.19	3.06	0.43	2.52	0.35	**284.28**	87.00
CR B	16.91	19.51	43.23	82.38	9.88	39.78	7.67	1.50	6.18	0.90	4.84	0.88	2.21	0.30	1.72	0.24	**238.13**	83.90
CR C1	13.41	23.48	47.59	89.02	11.04	44.82	8.43	1.57	6.78	1.01	5.54	1.04	2.69	0.38	2.19	0.30	**259.28**	89.70
CR C2	13.02	25.09	48.67	91.35	11.22	45.98	8.78	1.60	7.03	1.06	5.88	1.09	2.79	0.39	2.27	0.31	**266.54**	85.50
CR D1	13.65	25.88	50.63	94.76	11.84	48.51	9.32	1.70	7.46	1.13	6.14	1.13	2.89	0.41	2.34	0.33	**278.12**	89.00
CR D2	14.59	26.66	50.61	94.17	11.70	48.81	9.38	1.73	7.42	1.14	6.19	1.17	3.01	0.42	2.44	0.35	**279.80**	89.70

Table 2 - 17: REE content for CR head samples prepared by sodium peroxide fusion (ppm)

(ppm)	Sc	Y	La	Ce	Pr	Nd	Sm	Eu	Gd	Tb	Dy	Ho	Er	Tm	Yb	Lu	**TREE (Ash Basis)**	dry ash %
CR A	20.00	45.80	64.00	132.00	16.05	58.00	10.90	2.16	9.35	1.46	8.57	1.73	4.79	0.70	4.50	0.74	**380.75**	87.00
CR B	22.00	37.50	58.60	119.00	13.87	49.40	9.80	1.87	7.72	1.24	7.03	1.42	3.89	0.61	3.80	0.62	**338.37**	83.90

CR C1	20.00	40.80	59.50	121.00	14.87	55.10	10.40	1.89	8.41	1.35	7.62	1.60	4.45	0.67	4.10	0.68	**352.44**	89.70
CR C2	21.00	44.70	63.90	130.00	15.84	57.40	11.00	2.05	9.02	1.43	8.48	1.71	4.77	0.71	4.50	0.71	**377.22**	85.50
CR D1	20.00	41.50	60.60	123.00	14.88	54.70	10.20	1.93	8.53	1.36	8.06	1.64	4.32	0.65	4.10	0.66	**356.13**	89.00
CR D2	20.00	41.50	58.50	118.00	14.67	53.30	10.20	1.88	8.49	1.30	7.64	1.59	4.30	0.65	4.10	0.67	**346.79**	89.70
CR E	23.00	42.50	72.20	144.00	17.49	63.80	11.40	2.17	9.34	1.47	8.38	1.71	4.71	0.70	4.50	0.70	**408.07**	88.67

Table 2 - 18: Percent change in REE values between hydrofluoric acid and reverse aqua regia digestions

(% Change)	Sc	Y	La	Ce	Pr	Nd	Sm	Eu	Gd	Tb	Dy	Ho	Er	Tm	Yb	Lu	**TREE (Ash Basis)**
CR A	86.95	-2.58	7.47	-5.10	32.10	15.78	44.66	19.93	38.89		-3.02	12.56	56.52	27.85	53.99	128.26	11.03
CR B	35.34	20.41	18.66	42.11	52.64	32.40	61.48	34.95	70.99	17.69	0.88	-12.30	105.58	75.86	113.62	336.14	36.05
CR C1	52.45	-3.07	9.36	15.83	37.71	18.34	46.61	27.40	43.04		-6.49	-9.42	55.71	44.68	57.86	136.74	17.89
CR C2	66.65	0.18	17.72	29.26	44.08	25.78	46.69	33.79	49.96		6.69	49.20	74.86	53.22	57.02	58.98	27.26
CR D1	55.89	-8.90	10.00	11.73	34.77	14.35	40.66	19.12	33.69		-3.04	4.18	52.50		51.14	139.91	14.64
CR D2	39.52	-10.77	4.04	6.42	34.80	11.34	37.41	15.61	29.63	-21.16	-2.91	-7.90	47.89	37.46	48.01	156.49	10.50

Table 2 - 19: Percent change in REE values between reverse aqua regia acid digestion and sodium peroxide fusion

(% Change)	Sc	Y	La	Ce	Pr	Nd	Sm	Eu	Gd	Tb	Dy	Ho	Er	Tm	Yb	Lu	**TREE (Ash Basis)**
CR A	-32.56	-40.26	-20.23	-26.01	-25.13	-16.01	-13.82	-18.81	-17.62	-18.47	-25.31	-31.46	-36.07	-38.99	-43.97	-52.11	-25.34
CR B	-23.15	-47.98	-26.23	-30.77	-28.80	-19.47	-21.77	-19.75	-19.97	-27.04	-31.12	-37.97	-43.09	-51.35	-54.74	-61.40	-29.63
CR C1	-32.93	-42.46	-20.02	-26.43	-25.73	-18.66	-18.96	-17.18	-19.39	-24.93	-27.29	-35.25	-39.62	-43.53	-46.53	-56.28	-26.43
CR C2	-38.02	-43.86	-23.83	-29.73	-29.19	-19.90	-20.18	-21.74	-22.03	-25.85	-30.65	-36.09	-41.60	-44.98	-49.47	-56.12	-29.34
CR D1	-31.75	-37.65	-16.45	-22.96	-20.42	-11.31	-8.58	-11.68	-12.57	-17.22	-23.87	-31.07	-33.12	-36.70	-42.98	-49.99	-21.91
CR D2	-27.04	-35.75	-13.49	-20.19	-20.26	-8.42	-8.00	-8.16	-12.58	-12.37	-19.00	-26.40	-30.00	-35.21	-40.46	-47.73	-19.32

Table 2 - 20: Percent change in REE values between sodium peroxide fusion and hydrofluoric acid digestion

(% Change)	Sc	Y	La	Ce	Pr	Nd	Sm	Eu	Gd	Tb	Dy	Ho	Er	Tm	Yb	Lu	**TREE (Ash Basis)**

CR A	-20.69	71.84	16.65	42.43	1.10	2.84	-19.79	2.70	-12.60		38.04	29.62	-0.06	28.20	15.90	-8.52	20.62
CR B	-3.85	59.67	14.24	1.64	-7.98	-6.21	-20.84	-7.66	-26.92	16.46	43.90	83.83	-14.53	16.88	3.42	-40.60	4.45
CR C1	-2.20	79.29	14.33	17.35	-2.24	3.88	-15.83	-5.22	-13.27		47.08	70.50	6.36	22.39	18.48	-3.38	15.30
CR C2	-3.19	77.81	11.53	10.09	-1.99	-0.75	-14.59	-4.50	-14.48		35.15	4.87	-2.07	18.62	26.03	43.33	11.20
CR D1	-6.01	76.04	8.81	16.18	-6.76	-1.39	-22.24	-4.95	-14.44		35.48	39.26	-1.95		16.05	-16.65	11.70
CR D2	-1.76	74.43	11.10	17.74	-6.97	-1.93	-20.89	-5.81	-11.75	44.73	27.16	47.52	-3.39	12.29	13.49	-25.41	12.16
CR E	1.34	67.39	17.94	4.75	1.31	8.05	-10.98	-0.84	-5.35		21.63	17.21	-0.67	32.87	28.37		11.78

2.3 Identify Comminution Size Range

Key Findings

- Size distribution parameters confirm that all crushed samples have similar distribution patterns.

Detailed Results

Since the efficiency and kinetics of heap leaching are strongly dependent on the ore particle size and subsequently the hydraulic conductivity, Virginia Tech researchers carefully assessed and worked with University of Utah researchers to determine the material particle size for the various coal product streams feeding the general coarse refuse material. The size distribution of the fine (-80 mesh) samples delivered to the University of Utah were analyzed using a laser particle size analyzer (Mircrotrac). Results from these analyses are shown in Figure 2 - 4 (a) and confirm that the material is very fine with 95% passing 70 microns in most cases.

The coarse sizing distribution data (-1 inch) was further assessed using the Gates-Gaudin-Schuhmann (GGS) equation, which is given by Eq. (2-1):

$$P = 100\left(\frac{X}{K}\right)^{\alpha} \qquad (2\text{-}1)$$

where P is the cumulative undersize in percentage, X the particle size, K the apparent (theoretical) top size obtained by extrapolation, and α the distribution coefficient. In this formulation, K and α are fitting parameters that can be found by a linear fit of log (P) versus log (X). Figure 2 - 4 (b) shows the size data as a GGS plot, and

Table 2 - 21 summarizes the GGS parameters along with other indicative measures of size, such as the mass mean and various passing sizes (P95, P80, and P50).

This data confirms that all samples have a similar size distribution with little variability in the GGS parameters. Nevertheless, these parameters can be used in the future to specify the screen sizes needed to produce a desired particle size distribution optimized for heap leaching.

Table 2 - 21: Mass mean size, P95, P80, P50, α, and K values of coal refuse samples

	CR-A	CR-B	CR-C1	CR-C2	CR-D1	CR-D2
Mass Mean Size (mm)	14.05	11.08	12.89	12.86	12.37	13.58
P95 (mm)	30.73	25.04	29.48	27.60	25.30	30.74
P80 (mm)	22.65	18.94	21.77	21.58	21.06	22.49
P50 (mm)	14.31	10.13	12.58	13.21	12.58	13.62
α	1.01	1.06	0.94	0.91	0.89	0.96
K (mm)	28.28	22.84	27.16	27.72	27.13	28.38

2.4 Evaluate Separation Parameters

Key Findings

- X-ray sorting has the capacity to produce a high yield, REE-enriched product, along with an iron-enriched (pyrite if present) fraction and a middling ash carbon fraction.
- On a whole mass basis, the green sub samples from the x-ray sorting process (i.e. high-ash, low-iron) have the highest TREE concentrations. On a whole ash basis, the orange sub samples (i.e. low-ash) contain the greatest TREE concentrations.
- A standard coal flotation showed ability to enrich REE-bearing material in a tailings product.

Detailed Results

2.4.1 Preliminary Pre-Concentration Trials

In addition to the detailed characterization work, efforts focused on identifying a low-cost strategy to separate both the pyrite and the REE-enriched rock fractions from the low-REE carbonaceous material. By rejecting barren or otherwise useless material early in the overall process, the efficiency of downstream unit reactions, such as the bioreactor or the actual heap leach, will be dramatically improved. While numerous separation technologies may be suitable for this task, the approach employed in the current quarter utilized a dual-scan x-ray ore sorter. This technology uses x-rays to classify individual particles according to mean atomic number in real time. While this classification cannot detect the dilute REE components, it can successfully distinguish coal, rock, and pyrite materials. The unit used for the current testing is a prototype pilot-scale system marketed by Mineral Separation Technologies Inc, under the trade name, DriJet^{TM} (Figure 2 - 33).

Figure 2 - 33: Pilot-Scale DriJetTM x-ray sorter

In the DriJet^{TM} unit, the x-ray scanner is positioned at the end of a conveyor belt. As material leaves the belt, the scanner classifies the particles in flight and within milliseconds, the processer decides whether to retain or reject the particle, based on the user's desired settings. If a particle is selected for rejection, air jets at the end of the belt are initiated to divert the particle trajectory to a separate product bin. This unit operates at a very high capacity as is extremely efficient at separating different particle types.

To augment the DriJet^{TM} production unit, an x-ray "baggage" scanner (Smiths Heimann) was used to analyze feed and product samples off line (Figure 2 - 34 (a)). This scanner (like those used in airport security checkpoints) produces photographic images of scanned material and color codes the images based on the x-ray attenuation (i.e. mean atomic number) of individual particles. For the refuse samples analyzed in this testing campaign, orange corresponds to carbonaceous material, green corresponds to clay and silicates, and blue corresponds to iron or pyrite. The color coding corresponds well to the classification algorithm used in the DriJet^{TM} production unit, and the color contrast between individual particles is indicative of the separation potential that can be

achieved in production runs. Altogether, the baggage scanner is a good diagnostic tool that supplements the actual Drijet™ unit.

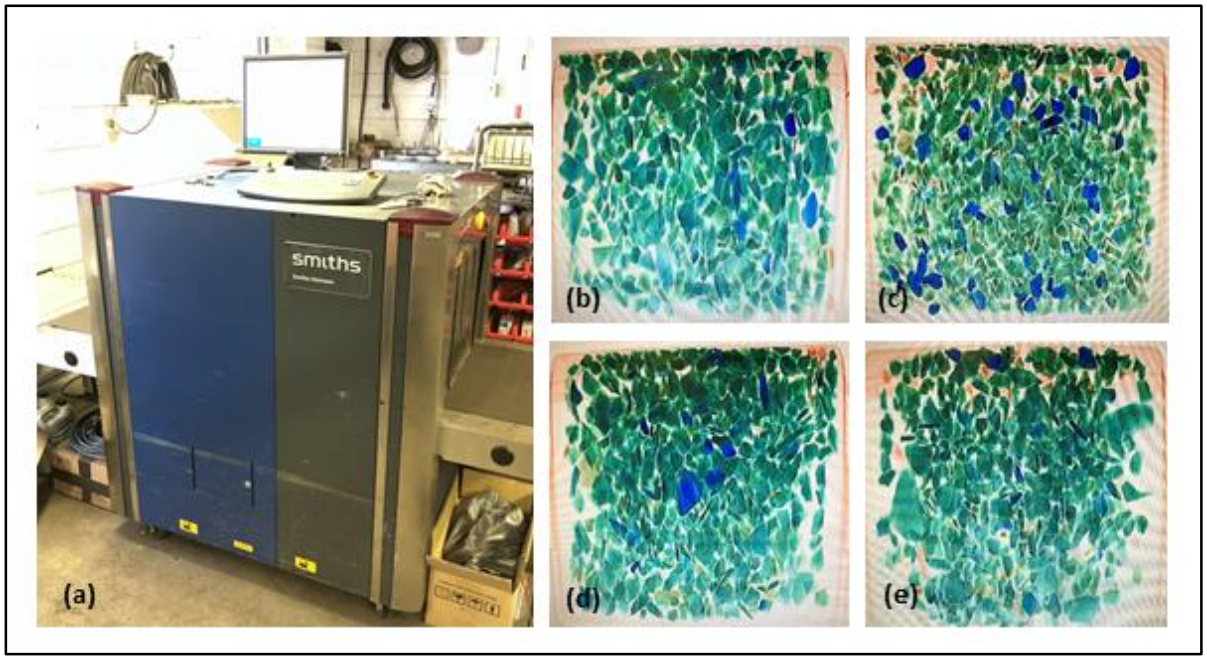

Figure 2 - 34: (a) x-ray scanner, and x-ray images of (b) CR-A, (c) CR-B, (d) CR-C1, and (e) CR-D1.

Figure 2 - 34 (b-e) shows the x-ray scans of the various CR feed materials. As shown here, CR-A, CR-C, and CR-D are almost entirely composed of green particles, with a very low population of orange and blue particles. This result is expected as earlier characterization work showed that all these particular samples have high ash and low sulfur. Alternatively, the x-ray scan of CR-B shows a moderate contrast between green and blue, suggesting that pyrite can be selectively separated in the production unit.

Based on this finding, two separation tests were conducted: (1) an "ideal" test where the baggage scanner was used along with "hand picking" to create a sample of pure blue and pure green particles; and (2) an actual production run with the DriJet™. Reject and clean samples from both tests were retained and analyzed using the XRF unit described above. The results of these tests show both the maximum separation potential that can achieved using x-ray sorting as well as a typical result under normal (i.e. non-optimized) operation. The x-ray scans of the resultant products are shown in Figure 2 - 35, and the XRF analysis is shown in Table 2 - 22. While the technique does show that the x-ray sorting can successfully reject pyrite, the production tests were not as effective as the ideal separation. In the ideal separation, the sulfur content was reduced to 2.05% in the rock product and increased to nearly 40% in the pyrite product (for reference, pure pyrite is 53% sulfur). However, in the actual production run, the sulfur content was increased to only 15% in the pyrite product. Since the DriJet™ is typically operated to separate coal from rock (rather than pyrite from rock) further optimization may be needed to approach the ideal result.

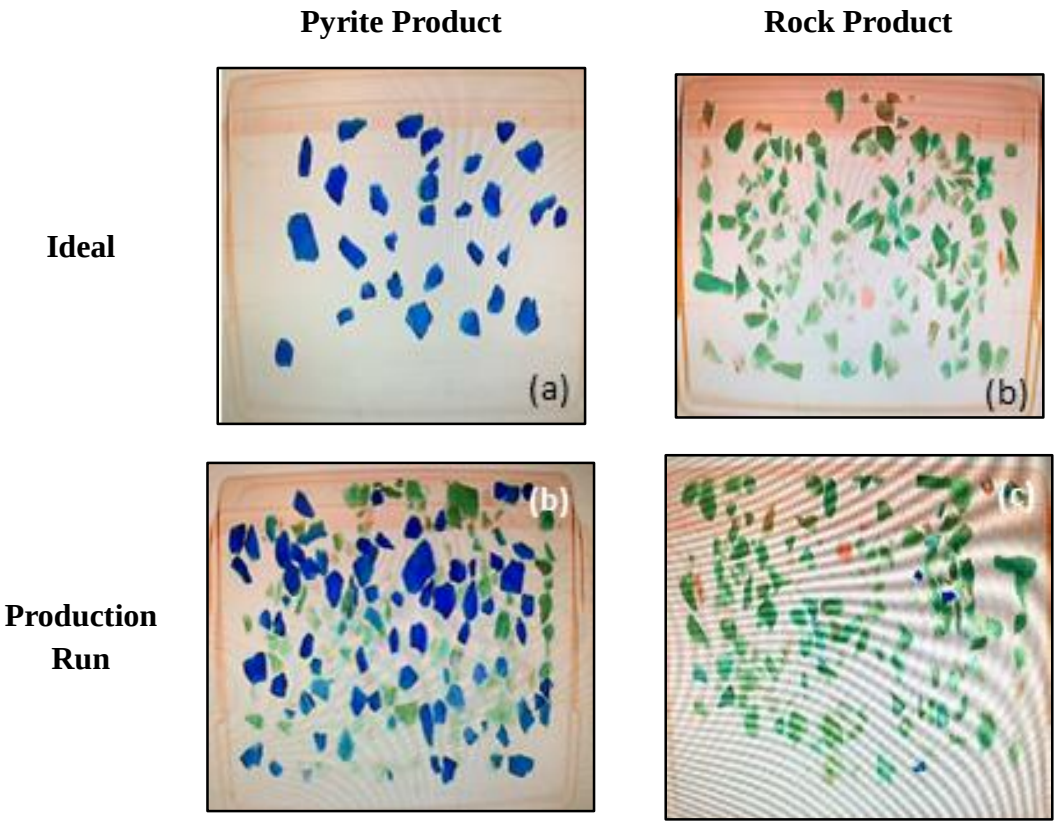

Figure 2 - 35: Results from CR-B sorting tests.

Table 2 - 22: XRF comparative analysis of x-ray sorted CR-B samples (wt. %)

CR-B Sample	Si	Al	Fe	S	K	Ca	Ti	Mn
DriJet Rock Product	1.53	1.53	9.77	11.06	1.53	0.05	0.96	LOD
DriJet Pyrite Product	1.30	1.30	14.35	15.43	1.30	0.22	0.72	0.02
Ideal Rock Product	1.40	1.40	2.30	2.05	1.40	0.05	0.98	0.02
Ideal Pyrite Product	0.49	0.49	30.94	39.86	0.49	.	0.26	.

2.4.2 Sorting of 5 CR Samples

Following the results of the preliminary x-ray sorting, approximately 5-10 lbs of each CR sample (CR-B, CR-C1, CR-C2, CR-D1, CR-D2) from each sample were hand sorted using the x-ray baggage scanner. The x-ray scanner clearly differentiates three colors: blue, orange, and green, based on the mean atomic number determined from x-ray attenuation. These three splits (collectively denoted BOG splits) represent the distinct materials that can be isolated using the production-scale sorting equipment. Blue typically signifies the presence of heavier minerals (e.g. pyrite), green represents primarily silica bearing minerals, and orange indicates carbonaceous material. BOG products were created by starting with a representative feed and visually inspecting the x-ray scans. The most apparent particles of each color were picked out and scanned again to confirm consistency of the samples. Figure 2 - 36 shows an initial scan of a CR-B feed sample, as well as a hand-picked blue product of CR-B to illustrate the selection of colors from the initial sample. The green product consistently corresponded to the highest mass fraction of the feed (approximately 75%), while the blue product made up a much smaller fraction, and the orange product constituted the smallest fraction. This distribution is expected as the coarse refuse sample is a high-ash, low carbon bearing byproduct of the coal cleaning process.

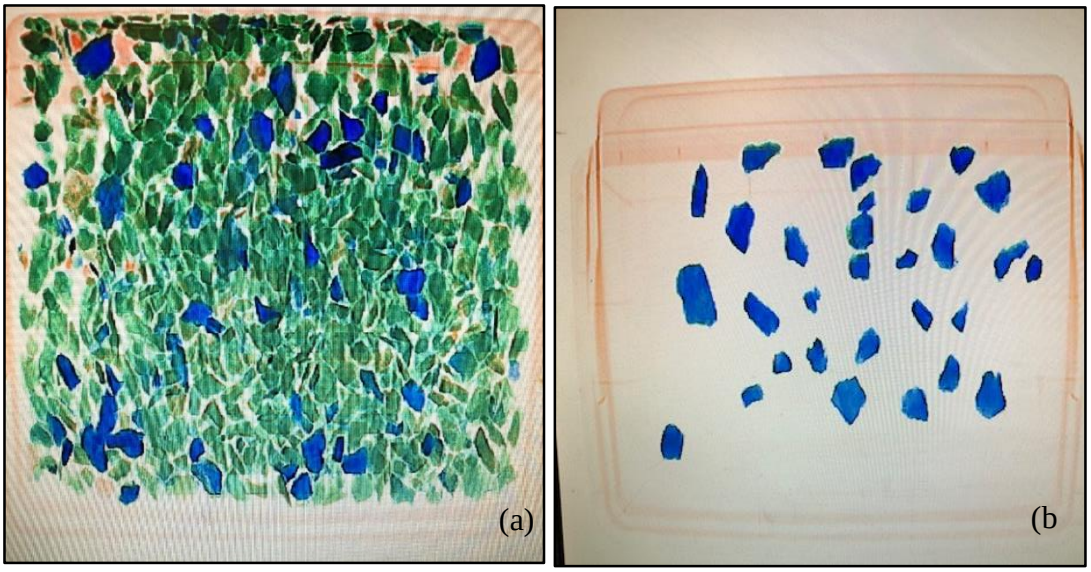

Figure 2 - 36: X-ray scans of (a) CR-B "feed" material and (b) hand-picked blue product

After hand sorting, the BOG products were analyzed for ash using a LECO thermogravimetric analyzer and major metal content using a Niton XL2 GOLD handheld XRF analyzer. For the XRF analysis, the sorted samples were first crushed to minus 80 mesh and then pelletized using a laboratory pellet press at 9 metric tons of pressure. Figure 2 - 37 shows the three pelletized BOG products of CR-B. These images indicate that the orange product has the darkest color owing to the high carbon content. Data from the ash and XRF analysis is shown in Table 2 - 23. This data confirms the separation occurring between the three products. For all

samples, the orange material consistently has the lowest ash value, ranging from a low of 41% in CR-D1 to a high of 56% in CR-C1. These values are often 20 to 30% lower than the medium ash blue samples and 30 to 40% lower than the high ash green samples. Likewise, the XRF data shows that the blue samples are typically concentrated in iron bearing minerals. For example, the iron content for the blue samples ranges from a low of 16.5% in CR-B to a high of 21.6% in CR-D1. Alternatively, the orange and green samples typically average only 3% to 5% iron. Lastly, the green samples typically contain the highest ash fraction and also contain elevated concentrations of aluminum and silica.

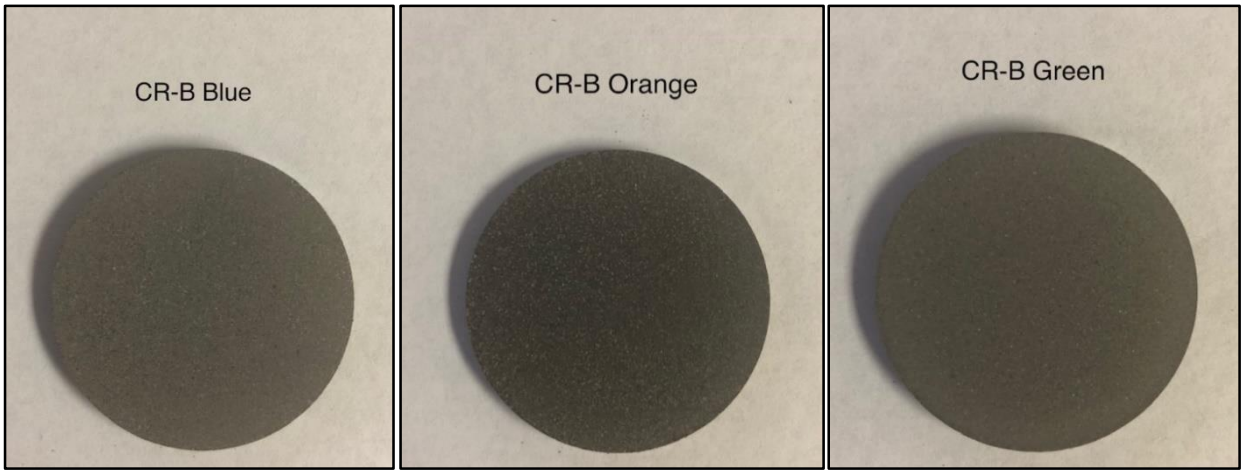

Figure 2 - 37: Pelletized CR-B BOG products

Table 2 - 23: Bulk elemental composition and ash content of BOG samples

	Fe	Ti	K	Al	Si	S	Mg	Ca	Ash
CR-B									
Blue	16.49	0.51	1.36	11.64	18.44	18.99	1.67	1.08	65.64
Green	3.11	1.08	1.48	13.14	30.76	2.85	1.04	0.93	84.20
Orange	3.98	1.44	1.33	10.95	26.00	4.89	0.77	0.28	54.54
CR-C1									
Blue	19.01	0.34	2.30	13.26	22.69	3.97	2.07	0.67	83.77
Green	5.56	0.65	3.15	14.93	32.81	0.63	2.01	0.17	92.93
Orange	3.93	1.24	2.19	11.79	26.22	1.70	0.69	0.11	55.86
CR-C2									
Blue	16.57	0.51	2.61	13.79	26.17	1.45	1.86	0.58	86.48
Green	6.21	0.80	3.38	16.15	35.10	0.44	1.65	0.07	93.27
Orange	2.97	1.30	1.14	7.26	21.95	1.52	0.63	0.35	48.38
CR-D1									
Blue	21.57	0.34	2.08	12.43	21.56	2.68	1.64	1.58	82.68
Green	5.43	0.56	3.27	14.92	32.95	0.26	1.86	0.04	93.28
Orange	5.40	1.16	1.85	11.46	22.81	2.62	0.73	0.39	41.51
CR-D2									
Blue	19.89	0.38	2.18	12.40	23.24	1.03	2.02	0.99	83.59
Green	6.10	0.61	3.38	15.65	33.99	0.25	1.69	0.11	93.73
Orange	9.06	1.10	2.47	13.28	25.83	2.56	1.71	0.37	52.34

To further characterize the materials comprising the BOG samples, each sub-sample was subjected to XRD for phase identification and determination of crystal structure. Figure 2 - 38 – Figure 2 - 42 show the XRD patterns for the BOG products, while Table 2 - 24 – Table 2 - 28 provide the corresponding phase identification generated by the XRD software. The score provided in these phase identification tables indicates the likelihood of a match with the possible phase identification; a higher score indicating a higher likelihood. The XRD data from all samples indicates that the mineralogy of the orange and green splits are largely coincident and typically include quartz, kaolinite, muscovite, and illite. The blue samples often contain many of these same constituents (particularly quartz); however, they also contain an iron-bearing species, either pyrite (FeS_2), for the case of CR-B, or siderite ($FeCO_3$) for the other sample species. This data aligns well with the XRF results (Table 2 – 23) showing that all blue splits have high iron content, but CR-B is the only sample with a similarly elevated sulfur content. This result suggests that the presence of iron (rather than the presence of pyrite) dictates the classification in the blue sub-sample.

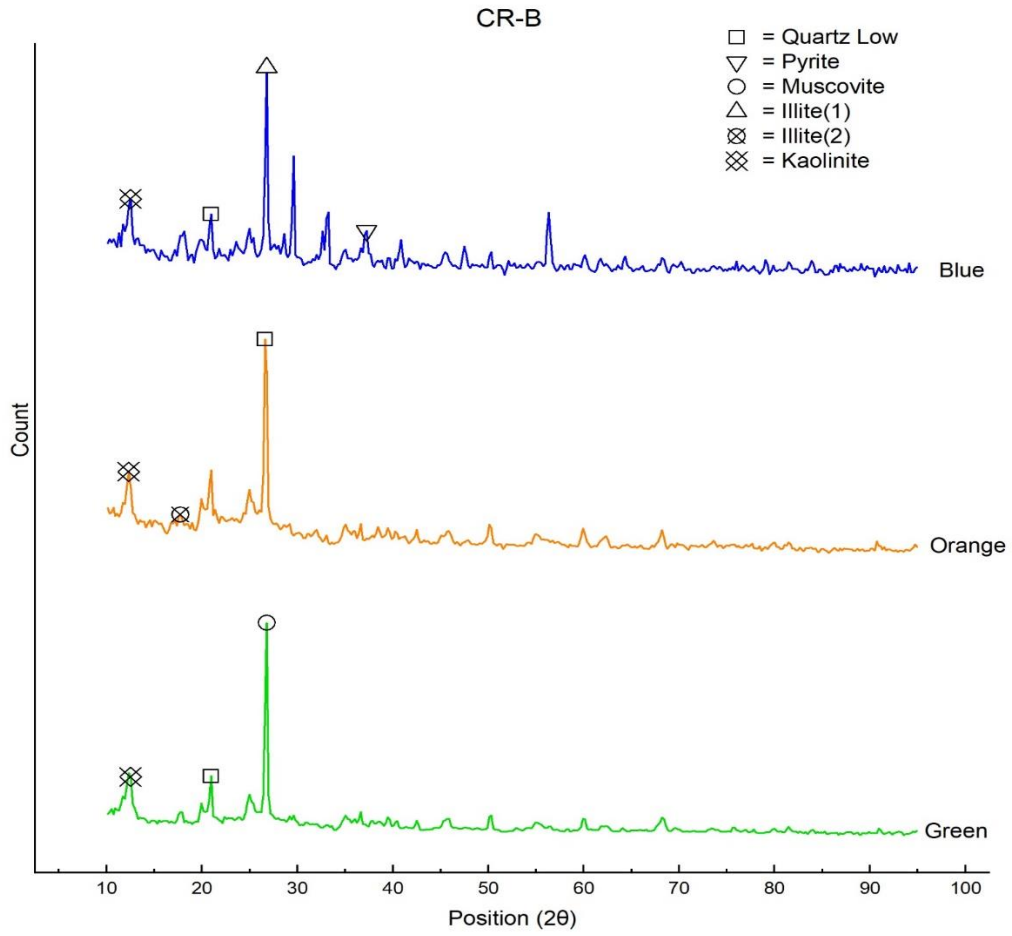

Figure 2 - 38: XRD patterns and phase identification of CR-B BOG samples

Table 2 - 24: Phase and crystal structure of CR-B

Compound Name	**Chemical Formula**	**Crystal**	**Score**		
			Blue	**Orange**	**Green**
Quartz low	SiO_2	Hexagonal	32	55	64
Pyrite	FeS_2	Cubic	28	--	--
Muscovite	$(K,Na)(Al,Mg,Fe)_2 (Si_{3.1} Al_{0.9})O_{10}(OH)_2$	Hexagonal	--	--	25
Illite (1)	$(K,H_3O)Al_2Si_3AlO_{10}(OH)_2$	Monoclinic	19	--	--
Illite (2)	$Al_2(SiAl)_4O_{10}(OH)_2$	Monoclinic	--	38	--
Kaolinite	$Al_2 Si_2 O_5 (OH)_4$	Monoclinic	--	24	39

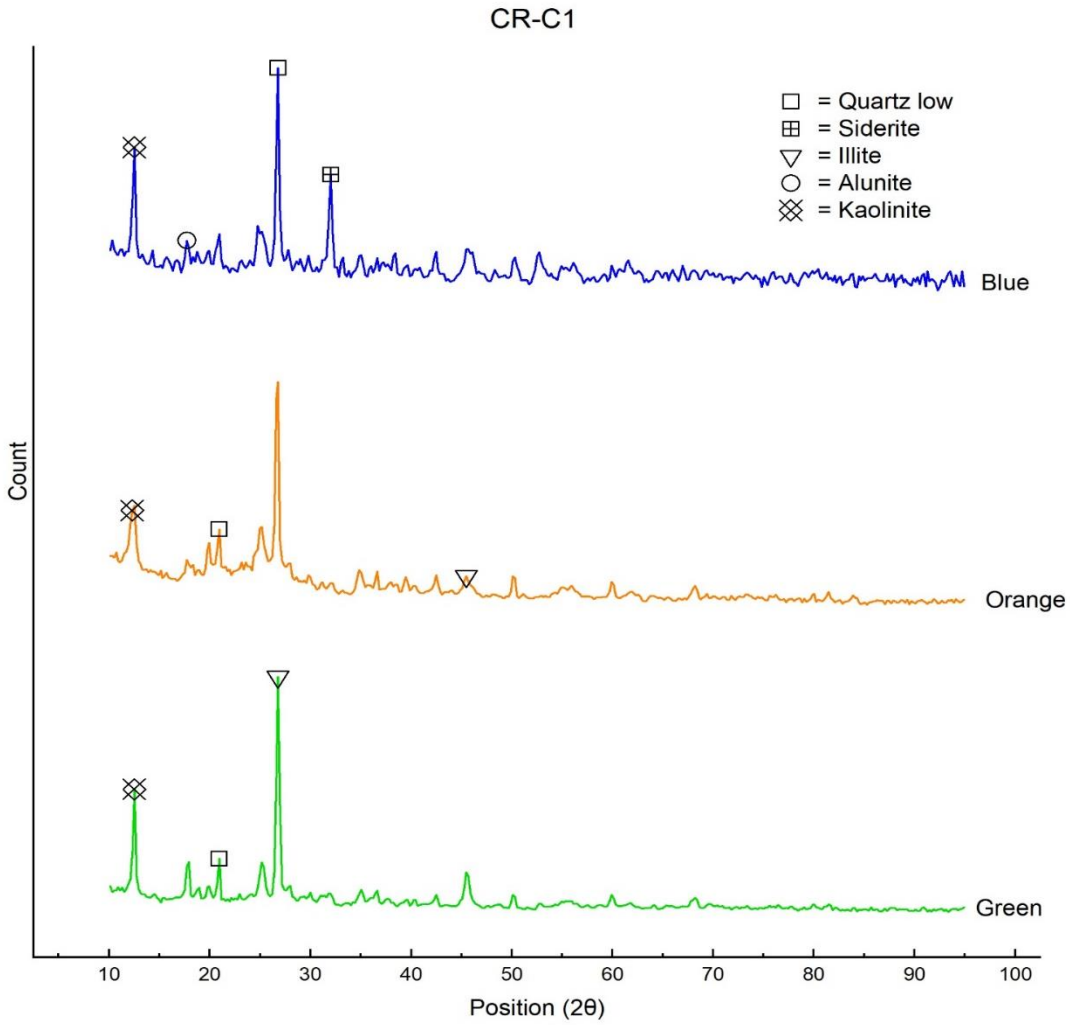

Figure 2 - 39: XRD patterns and phase identification of CR-C1 BOG samples

Table 2 - 25: Phase and crystal structure of CR-C1

Compound Name	Chemical Formula	Crystal	Score		
			Blue	Orange	Green
Quartz low	SiO_2	Hexagonal	27	60	45
Siderite	$FeCO_3$	Rhombohedral	28	--	--
Illite	$(K,H_3O)Al_2Si_3AlO_{10}(OH)_2$	Monoclinic	--	34	34
Alunite	$K\ (Al_3(SO_4)_2(OH)_6\ )$	Rhombohedral	10	--	--
Kaolinite	$Al_2Si_2O_5(OH)_4$	Monoclinic	18	28	22

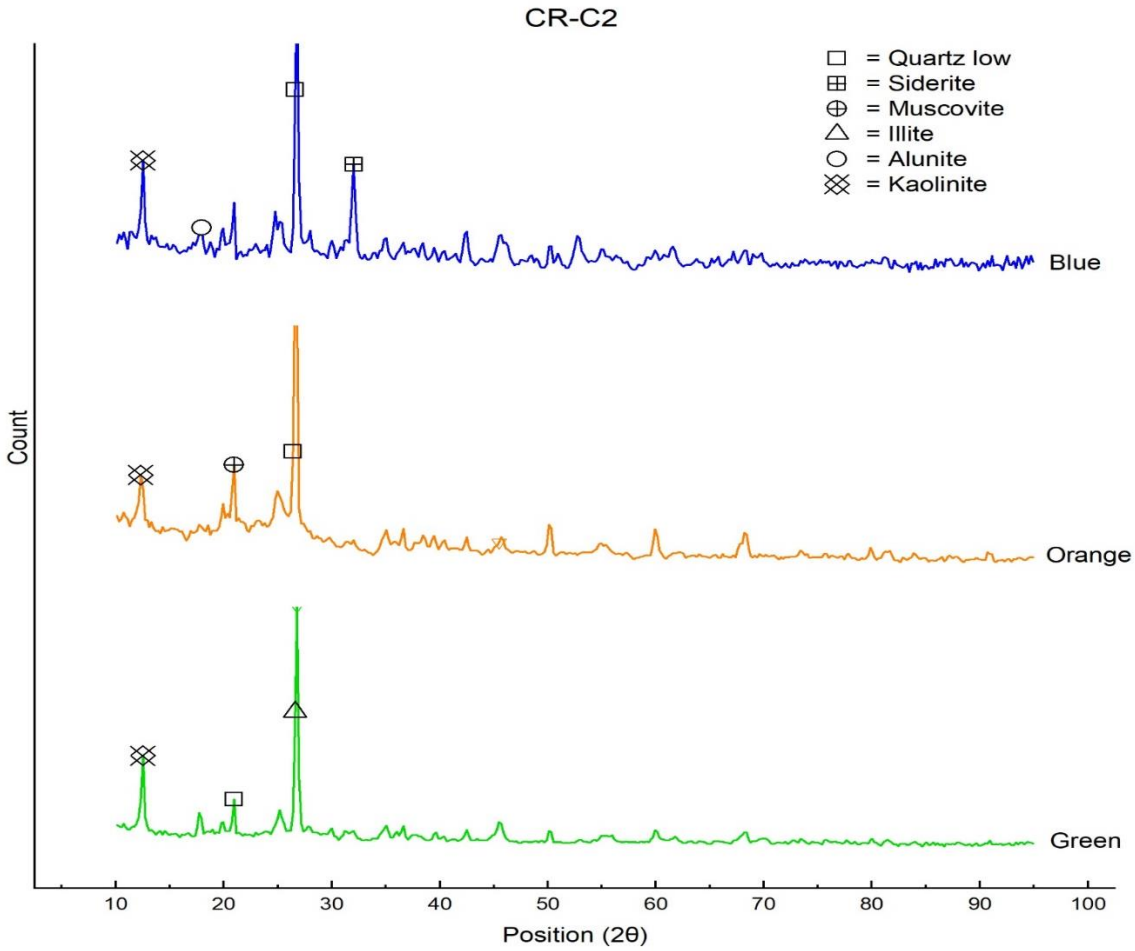

Figure 2 - 40: XRD patterns and phase identification of CR-C2 BOG samples

Table 2 - 26: Phase and crystal structure of CR-C2

Compound Name	Chemical Formula	Crystal	Score		
			Blue	Orange	Green
Quartz low	SiO_2	Hexagonal	33	67	48
Siderite	$FeCO_3$	Rhombohedral	31	--	--
Muscovite	$KAl_3Si_3O_{10}(OH)_2$	Hexagonal	--	16	--
Illite	$(K,H_3O)Al_2Si_3AlO_{10}(OH)_2$	Monoclinic	--	--	36
Alunite	$K\ (Al_3(SO_4)_2(OH)_6\ )$	Rhombohedral	12	--	--
Kaolinite	$Al_2Si_2O_5(OH)_4$	Monoclinic	22	32	32

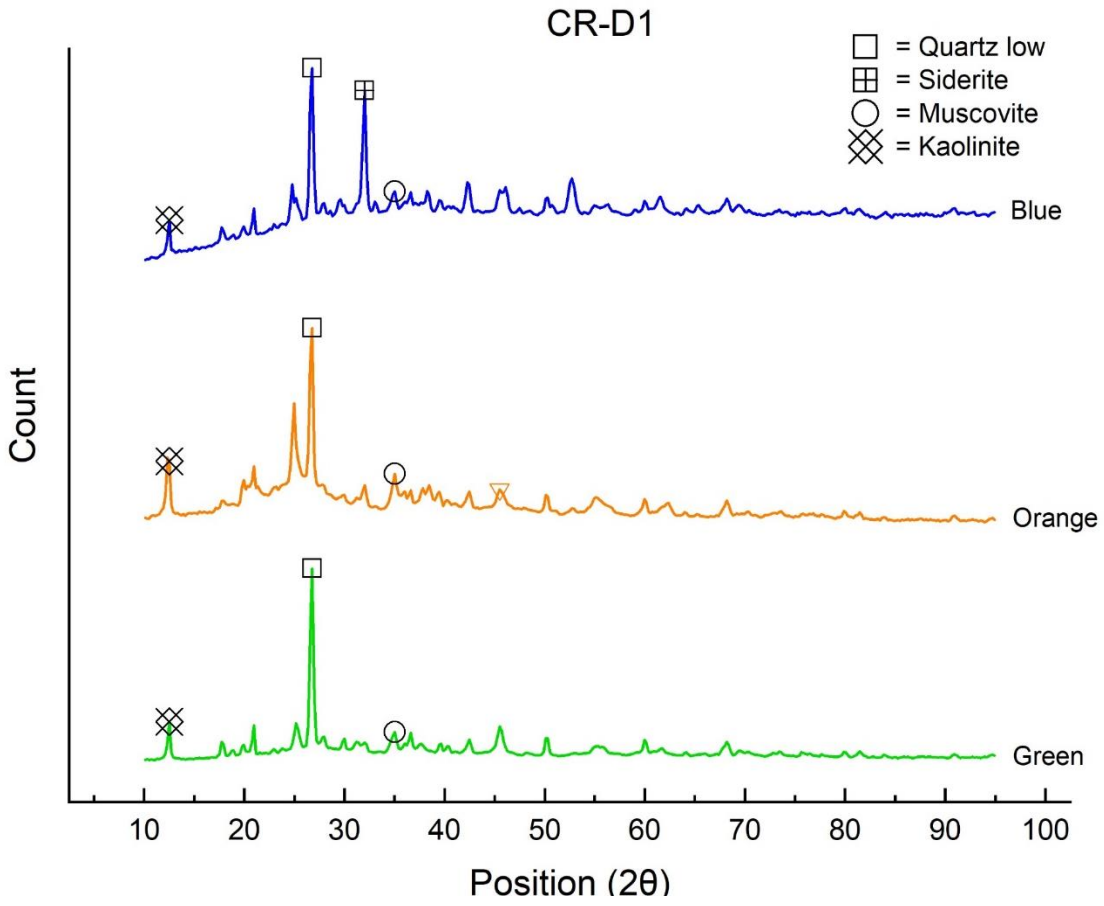

Figure 2 - 41: XRD patterns and phase identification of CR-D1 BOG samples

Table 2 - 27: Phase and crystal structure of CR-D1

Compound Name	Chemical Formula	Crystal	Score		
			Blue	Orange	Green
Quartz low	SiO_2	Hexagonal	48	64	62
Siderite	$FeCO_3$	Rhombohedral	44	--	--
Muscovite	$H_2KAl_3(SiO_4)_3$	Monoclinic	27	45	43
Kaolinite	$Al_2Si_2O_5(OH)_4$	Monoclinic	26	59	30

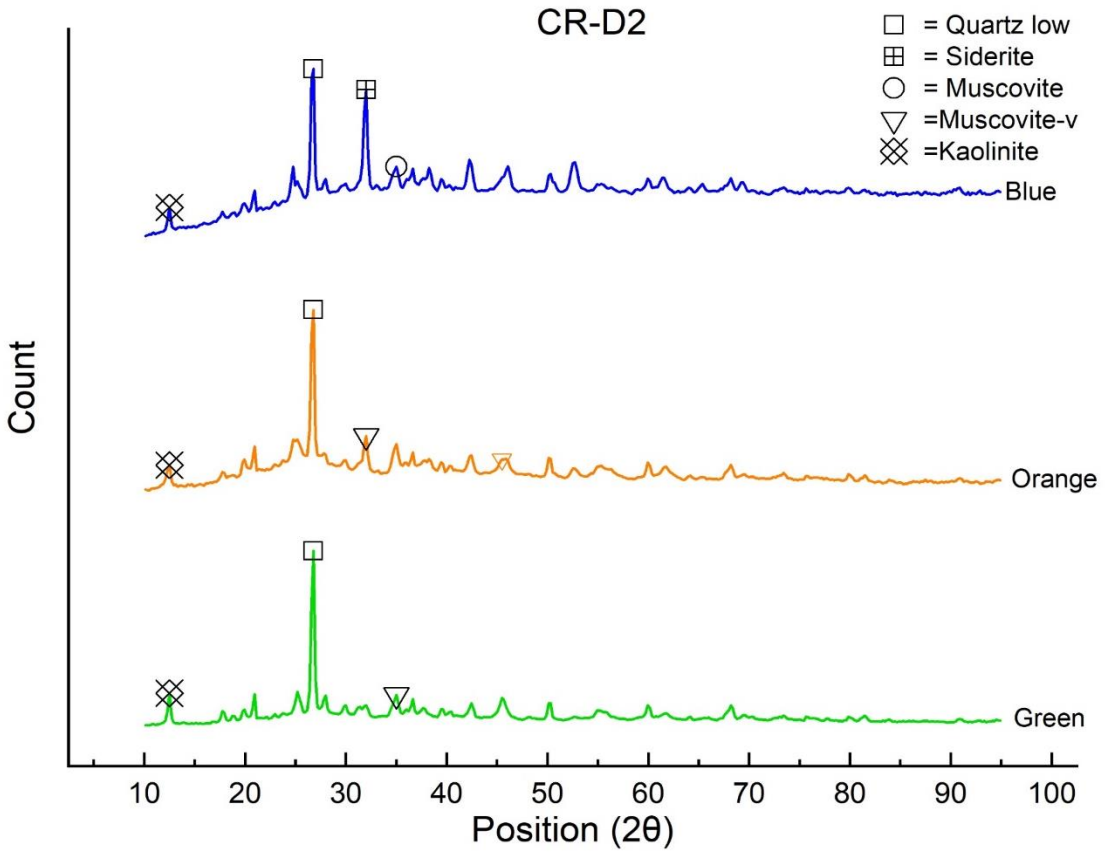

Figure 2 - 42: XRD patterns and phase identification of CR-D2 BOG samples

Table 2 - 28: Phase and crystal structure of CR-D2

Compound Name	Chemical Formula	Crystal	Score		
			Blue	Orange	Green
Quartz low	SiO_2	Hexagonal	54	64	67
Siderite	$FeCO_3$	Rhombohedral	54	--	--
Muscovite	$KAl_2(Si_3Al)O_{10}(OH)_2$	Monoclinic	29	--	--
Muscovite-vanadian	$K(Al\ V)_2(SiAl)_4O_{10}(OH)_2$	Monoclinic	--	37	41
Kaolinite	$Al_2Si_2O_5(OH)_4$	Monoclinic	24	44	30

For REE analysis, splits from the BOG sub samples were homogenized and screened to minus 80 mesh for microwave digestion. Approximately 50 mg of each sub sample was digested in a 12 mL reverse aqua regia solution in preparation for trace elemental analysis by ICP-MS. Table 2 - 29 shows the element-by-element concentration of each REE for the various splits, while Table 2 - 30 shows the total rare earth element (TREE) concentrations alongside the major elemental analysis found via XRF. Based on these results, the green sub samples contain the highest TREE concentration among the BOG products for each coarse refuse sample. The orange sub samples are more TREE-enriched than the blue sub samples in CR-B, CR-C1, and CR-D1, while the opposite is true for CR-C2 and CR-D2. Figure 2 - 43 shows a graphical comparison of the TREE content in the head samples and the x-ray sorted products.

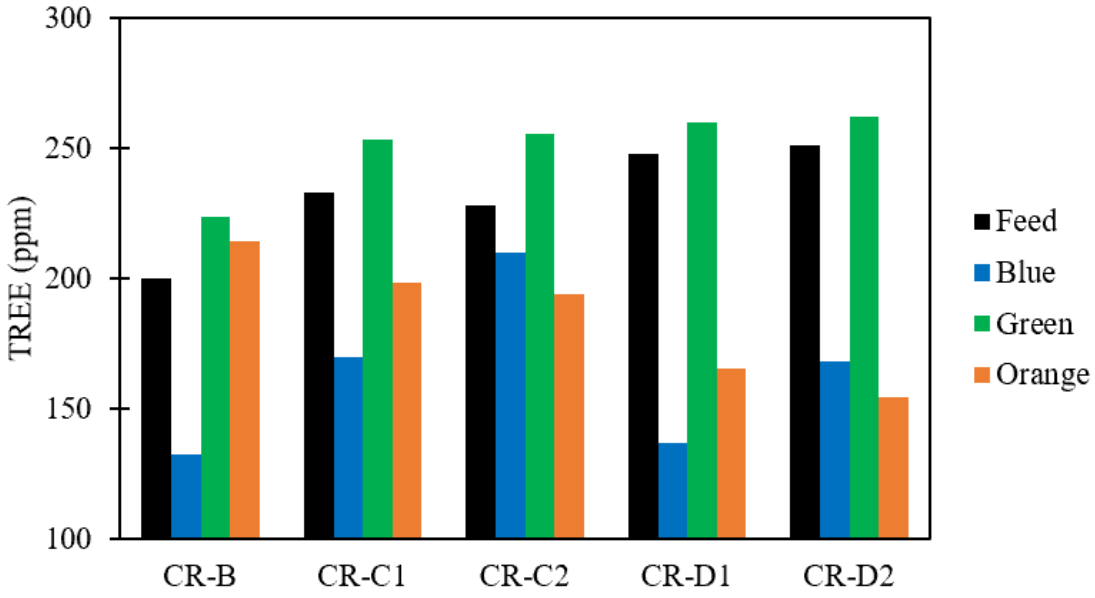

Figure 2 - 43: Comparison of CR head samples and their corresponding x-ray sorted products

Table 2 - 29: REE concentration in BOG sub samples (whole mass basis)

Sample	Sc ppm	Y ppm	La ppm	Ce ppm	Pr ppm	Nd ppm	Sm ppm	Eu ppm	Gd ppm	Tb ppm	Dy ppm	Ho ppm	Er ppm	Tm ppm	Yb ppm	Lu ppm	Th ppm	U ppm
CR-B																		
Blue	8.84	13.80	19.99	44.74	5.54	21.85	5.00	1.00	4.38	0.59	3.11	0.55	1.38	0.19	1.10	0.16	6.55	1.68
Green	16.52	19.88	37.77	78.84	9.26	35.54	7.31	1.47	6.16	0.85	4.52	0.82	2.12	0.28	1.69	0.24	12.84	2.03
Orange	12.27	17.15	34.56	78.68	9.26	36.40	7.92	1.58	6.49	0.85	4.23	0.73	1.89	0.24	1.47	0.21	9.80	2.53
CR-C1																		
Blue	13.78	23.87	24.73	52.48	6.32	24.47	5.64	1.21	5.65	0.84	4.74	0.90	2.46	0.33	2.08	0.30	7.57	1.47
Green	14.26	23.78	44.52	90.21	10.88	41.11	8.18	1.55	6.70	0.93	5.10	0.95	2.50	0.33	2.04	0.29	12.46	1.91
Orange	12.52	20.51	33.32	69.07	8.13	30.87	6.42	1.26	5.51	0.78	4.37	0.79	2.17	0.30	1.86	0.26	11.24	2.46
CR-C2																		
Blue	14.77	26.24	32.38	68.25	8.16	31.96	6.88	1.42	6.50	0.92	5.23	0.99	2.69	0.36	2.34	0.35	8.48	1.41
Green	12.98	26.00	44.26	90.24	10.77	41.48	8.08	1.52	6.89	0.98	5.35	1.00	2.67	0.36	2.21	0.31	12.24	1.93
Orange	10.32	20.52	33.37	69.49	8.06	30.05	6.11	1.13	5.16	0.74	4.12	0.75	2.03	0.27	1.68	0.24	12.92	2.49
CR-D1																		
Blue	10.09	20.50	19.24	41.67	5.03	20.15	4.58	0.95	4.68	0.68	4.00	0.76	2.11	0.29	1.82	0.26	6.06	1.26
Green	13.02	23.21	46.19	94.71	11.34	43.40	8.17	1.51	6.60	0.91	4.97	0.90	2.43	0.33	1.95	0.28	11.98	1.82
Orange	9.69	18.04	28.32	58.87	6.69	24.31	5.02	0.96	4.44	0.66	3.81	0.71	1.79	0.25	1.49	0.21	16.74	4.11
CR-D2																		
Blue	13.28	26.22	23.25	50.81	5.98	23.72	5.46	1.13	5.62	0.84	5.04	0.96	2.72	0.38	2.38	0.35	7.21	1.62
Green	13.66	25.70	45.40	93.10	11.14	42.94	8.36	1.56	6.92	0.97	5.43	1.00	2.76	0.37	2.24	0.32	12.31	2.15
Orange	9.33	17.24	25.42	53.26	6.23	23.67	4.89	0.96	4.42	0.65	3.73	0.68	1.85	0.26	1.57	0.22	9.77	3.48

Table 2 - 30: Major elemental composition, Ash, and total rare earth concentration in coarse refuse BOG sub samples

Sample	Fe %	Ti %	K %	Al %	Si %	S %	Mg %	Ca %	Ash %	Comb. %	TREE ppm
CR-B											
Blue	16.49	0.51	1.36	11.64	18.44	18.99	1.67	1.08	65.64	34.36	132.21
Green	3.11	1.08	1.48	13.14	30.76	2.85	1.04	0.93	84.20	15.80	223.26
Orange	3.98	1.44	1.33	10.95	26.00	4.89	0.77	0.28	54.54	45.46	213.93
CR-C1											
Blue	19.01	0.34	2.30	13.26	22.69	3.97	2.07	0.67	83.77	16.23	169.80
Green	5.56	0.65	3.15	14.93	32.81	0.63	2.01	0.17	92.93	7.07	253.32
Orange	3.93	1.24	2.19	11.79	26.22	1.70	0.69	0.11	55.86	44.14	198.14
CR-C2											
Blue	16.57	0.51	2.61	13.79	26.17	1.45	1.86	0.58	86.48	13.52	209.47
Green	6.21	0.80	3.38	16.15	35.10	0.44	1.65	0.07	93.27	6.73	255.11
Orange	2.97	1.30	1.14	7.26	21.95	1.52	0.63	0.35	48.38	51.62	194.03
CR-D1											
Blue	21.57	0.34	2.08	12.43	21.56	2.68	1.64	1.58	82.68	17.32	136.80
Green	5.43	0.56	3.27	14.92	32.95	0.26	1.86	0.04	93.28	6.72	259.93
Orange	5.40	1.16	1.85	11.46	22.81	2.62	0.73	0.39	41.51	58.49	165.24
CR-D2											
Blue	19.89	0.38	2.18	12.40	23.24	1.03	2.02	0.99	83.59	16.41	168.14
Green	6.10	0.61	3.38	15.65	33.99	0.25	1.69	0.11	93.73	6.27	261.86
Orange	9.06	1.10	2.47	13.28	25.83	2.56	1.71	0.37	52.34	47.66	154.40

Table 2 - 31 shows the ash percent and TREE concentrations on both whole mass and ash basis for all the BOG sub samples as a single population. On an ash basis, the orange sub samples contain the greatest TREE concentration, with CR-C2 orange exceeding 400 ppm. It should be noted that while this enrichment is favorable, the mass yield of the orange sub sample from x-ray sorting is very small for these high-ash coarse refuse samples. Figure 2 - 44 graphically shows the comparison of TREE content on whole ash vs. whole mass basis, and Figure 2 - 45 displays TREE concentration compared to major elements found in the samples (Fe, Si, Ti, K, Al, S, Mg, Ca). On a whole mass basis, TREE concentration is slightly positively correlated with ash content; however, the strongest correlation with respect to the major elements is a positive trend between Si and TREE for the entire population of data points.

Table 2 - 31: Ash and TREE content for BOG sub samples on whole mass and whole ash basis

Sample	Ash %	TREE Whole Mass (ppm)	TREE Whole Ash(ppm)
CR-B			
Blue	65.64	132.21	201.42
Green	84.20	223.26	265.16
Orange	54.54	213.93	392.24
CR-C1			
Blue	83.77	169.80	202.70
Green	92.93	253.32	272.60
Orange	55.86	198.14	354.71
CR-C2			
Blue	86.48	209.47	242.21
Green	93.27	255.11	273.51
Orange	48.38	194.03	401.06
CR-D1			
Blue	82.68	136.80	165.46
Green	93.28	259.93	278.65
Orange	41.51	165.24	398.07
CR-D2			
Blue	83.59	168.14	201.15
Green	93.73	261.86	279.37
Orange	52.34	154.40	294.99

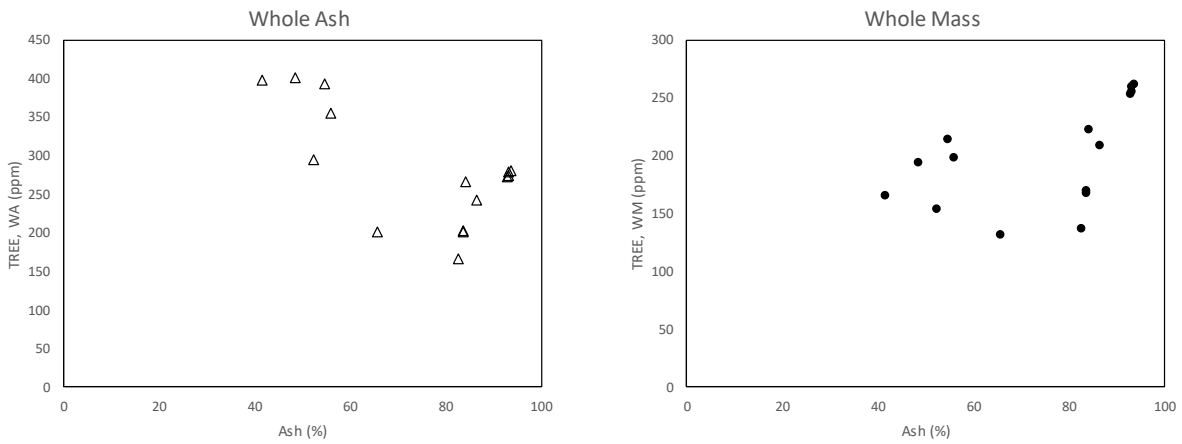

Figure 2 - 44: TREE vs ash content for BOG sub samples on whole mass and whole ash bases

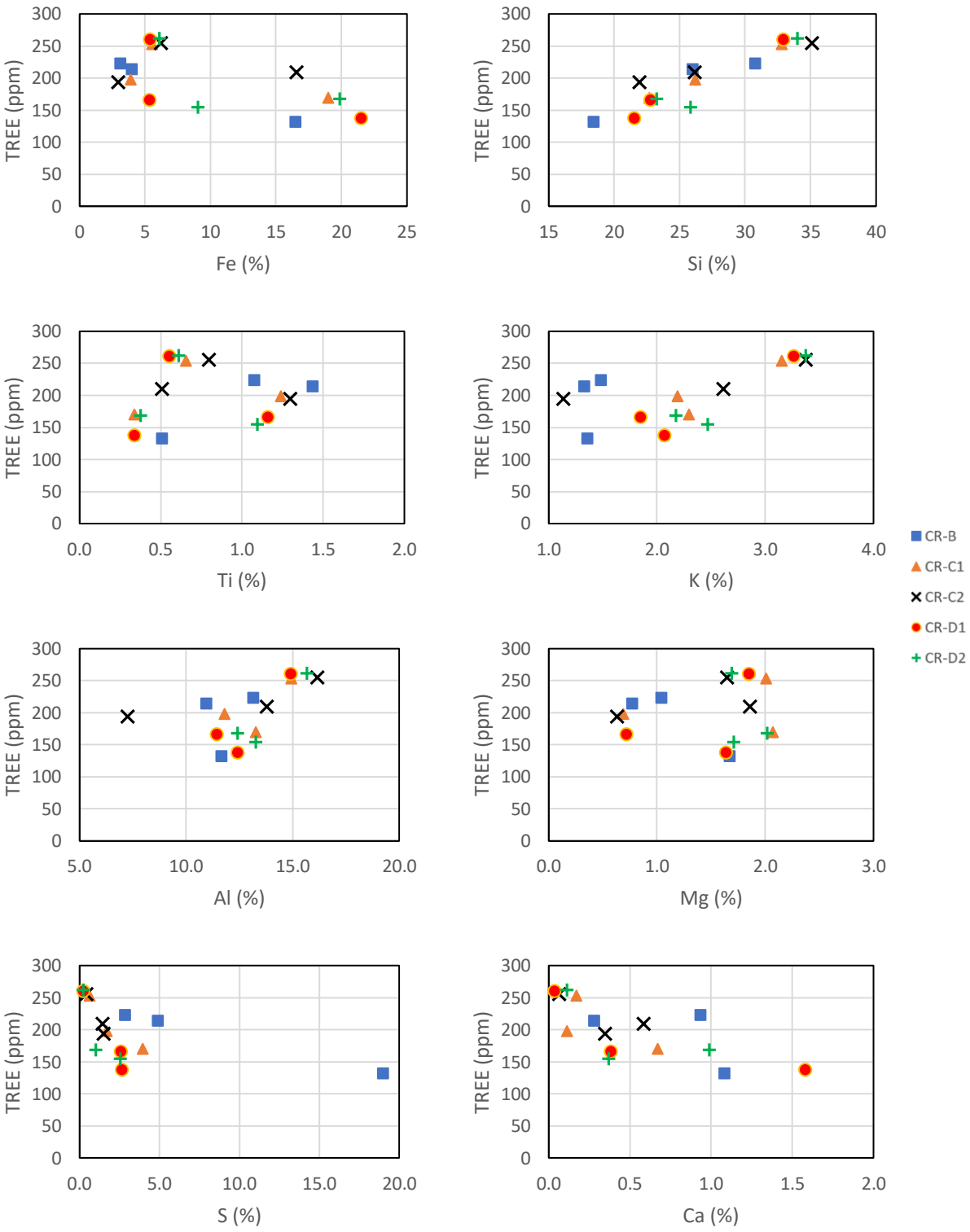

Figure 2 - 45: Whole mass comparison of TREE concentration (ppm) to major compositional elements

The major element versus REE data as well as the TREE versus ash data in indicate that each individual sample does not follow the overall trend seen in the bulk data set. For example, the TREE content in CR-B, CR-C1, and CR-D1 decreases and then increases with increasing ash content, while the TREE content in CR-D2 first decreases and then increases with increasing silica content. Figure 2 - 46 illustrates the ranges of TREE values found in each sub sample color group, meaning the green box and whisker plot is generated by the TREE values of the green sub sample of each coarse refuse sample.

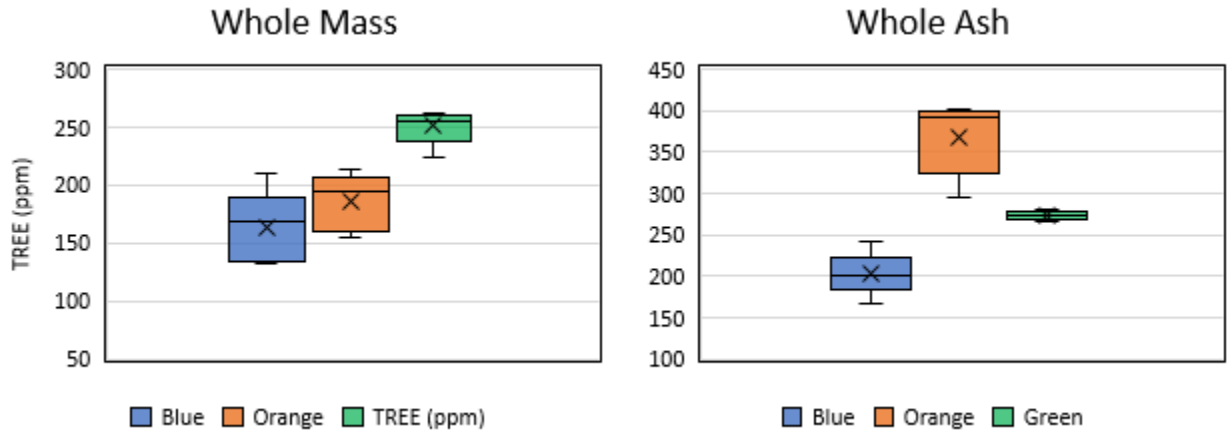

Figure 2 - 46: Ranges of TREE concentrations for BOG sub samples on whole mass and whole ash bases for all coarse refuse samples

Individual rare earth element concentrations are shown as a distribution of the total REE content for each BOG sample in

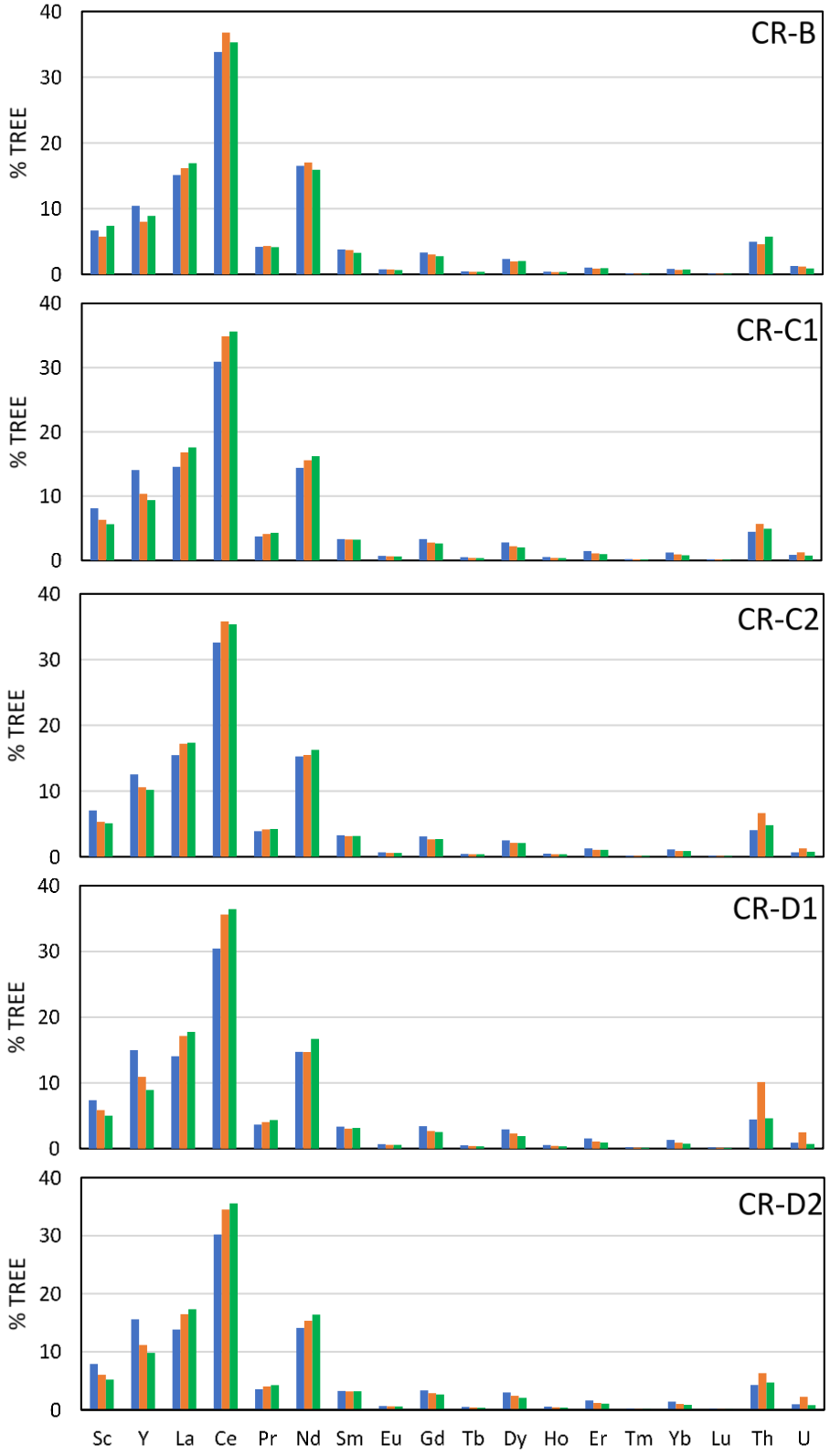

Figure 2 - 47. As expected, Ce is the most abundant REE, making up approximately 30-35% of the TREE content for all sub samples. La, Nd, Y, Sc, and Th were the next most concentrated,

ranging from 5-15% TREE. The rest of the elements in the spectrum each made up less than 5% TREE in the sub samples. Figure 2 - 48 shows the chondrite-normalized REE concentration in the BOG sub samples for each coarse refuse sample. Chondritic meteor REE abundance values reported by Taylor and McLennan (1985) were used to normalize the REE concentrations. The chondrite normalized values appear to be very similar to other reported chondrite normalized REE values, with the green sub samples maintaining the highest abundance of REEs.

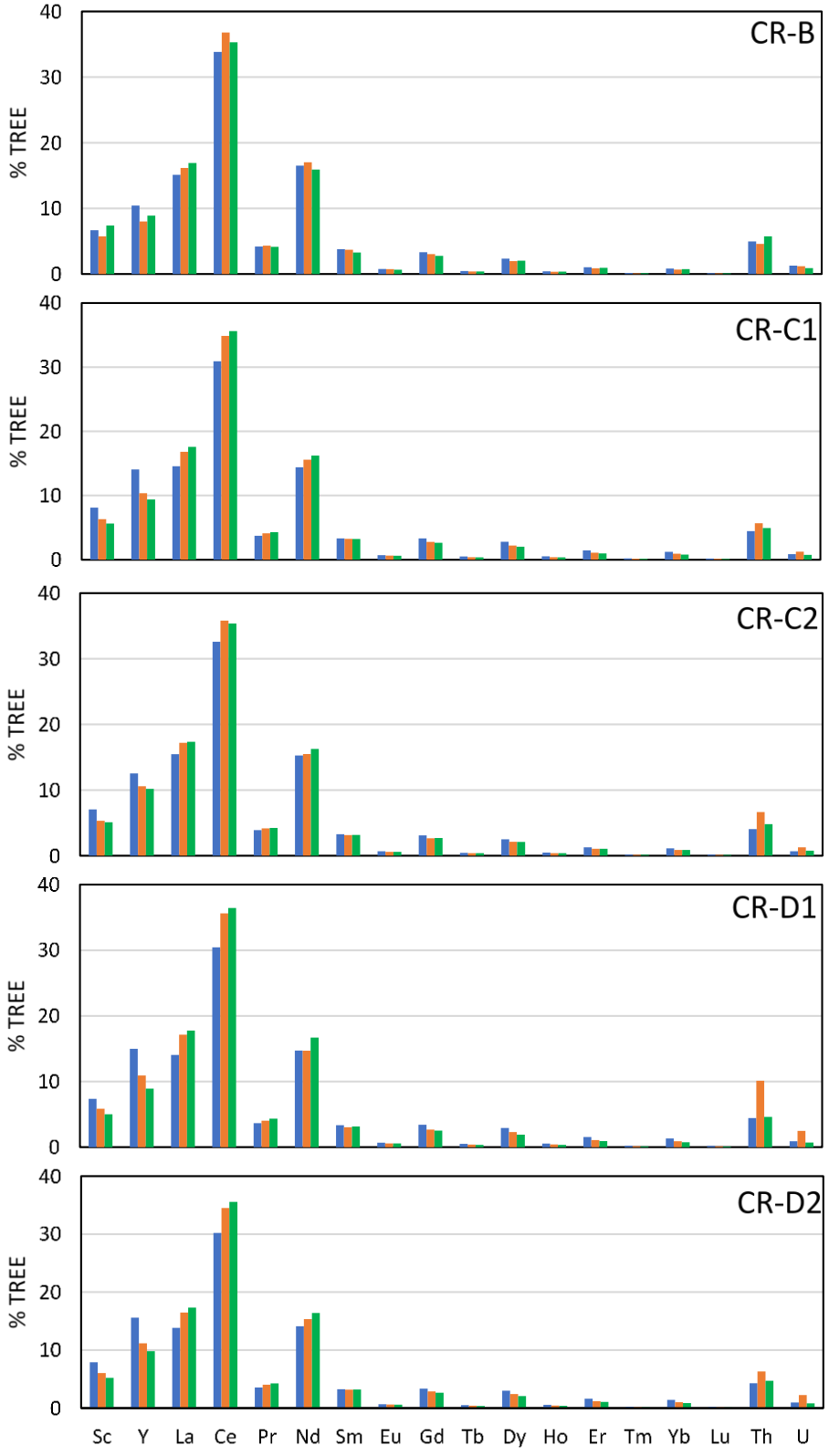

Figure 2 - 47: REE distribution as part of TREE for coarse refuse BOG sub samples

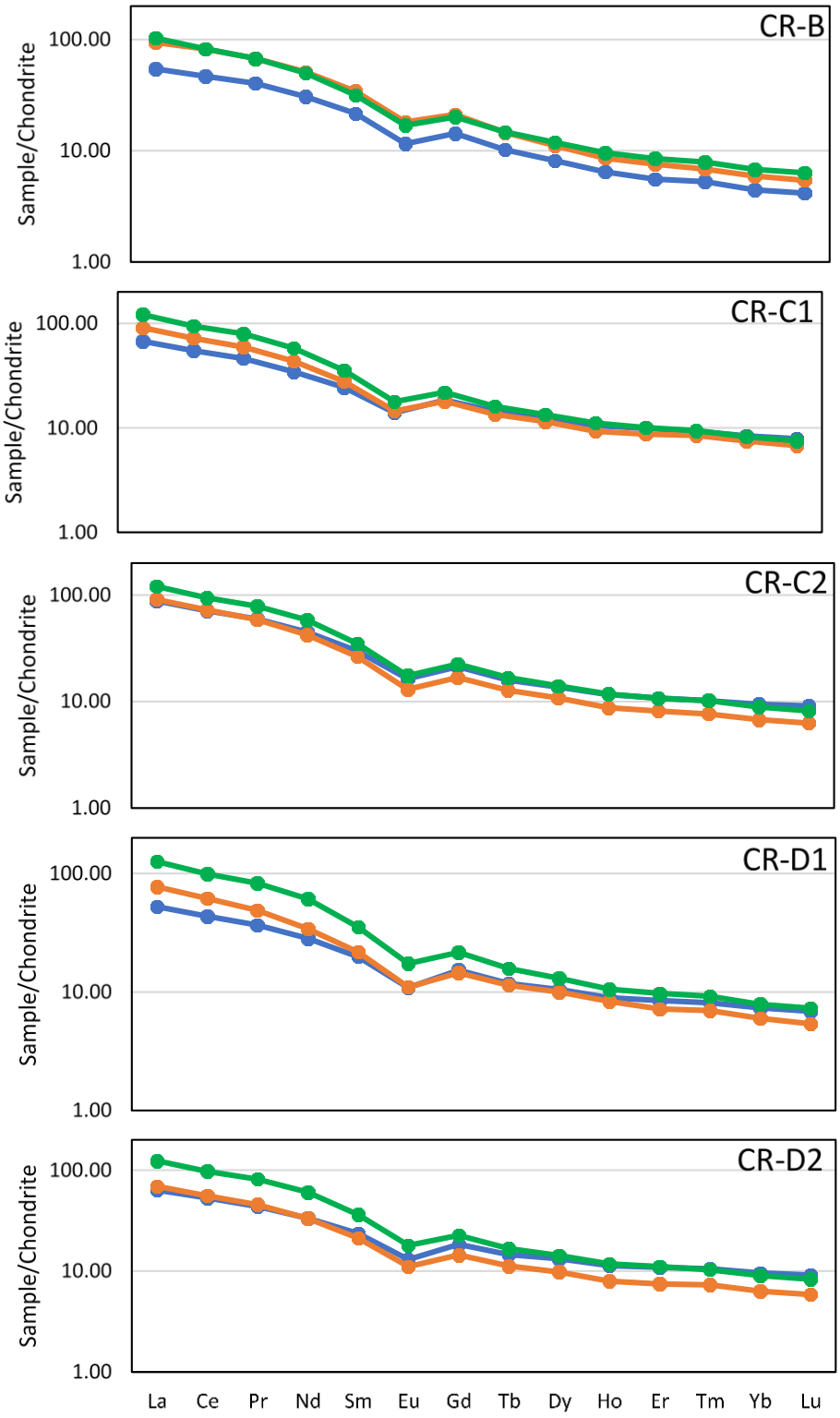

Figure 2 - 48: Chondrite normalized curves of REE concentration in coarse refuse BOG sub samples

While these results do provide insight on how the REEs are partitioning between the BOG splits, it should be noted that a definitive digestion method for the coarse refuse and BOG sub samples has not been established. Varying material properties in the samples subjected to digestion may lead to varying performance of the digestion. For example, a higher ash green product may digest more completely in reverse aqua regia than the low ash orange product. For consistency, the same acid solution (reverse aqua regia) has been used for all samples for the data collected to date. Going forward however, variable digestion parameters will be compared for similar and dissimilar samples to develop more specific digestion methods for varying samples.

In addition to ICP-MS analysis, the coarse refuse BOG sub samples were analyzed by SEM-EDS using a FEI Quanta 600 FEG environmental SEM to determine the morphology and grain features of the sample splits. Minus 80 mesh samples of each BOG sub sample were prepared for SEM-EDS analysis. Each sample was first attached to a conductive tape and then coated with a platinum/palladium sputter coating. Figure 2 - 49 –

Figure 2 - 53 show backscatter images captured with the microscope of each BOG sub sample at 100x, 200x, 1000x, and 3000x magnification. These backscatter images are formed by electrons deflected off the sample surface, and higher atomic weights deflect more electrons. In the images, a higher number of deflected electrons is represented by brighter objects, so heavier elements will appear brighter in backscatter images. Samples with higher variability in composition (such as those around 50% ash) will tend to show a larger color contrast in the backscatter image. This observation was confirmed in the current study, as the low-ash, orange sub samples showed the greatest color contrast, owing to the mix of coal and silica present in the sample. Alternatively, the higher-ash green and blue sub samples appear more homogenous in the backscatter image, as they are composed of mostly heavier ash material and less combustibles.

EDS point analysis and mapping were then used to identify the composition of different particles in the samples. The electron beam that performs the point analysis measures a volume of approximately 1 cubic micron on the sample surface and provides wt.% data for the elements contained in that point. The mapping feature of the microscope scans the surface of the sample for an element/s designated by the user, continuously picking points and labeling each point with a color indicating the detected element. This process paints the sample surface with a color coding for elemental composition. These analysis tools were used primarily in this effort to investigate the presence of pyrite in the blue sub samples. As a result, the point analysis selectively targeted bright particles in the backscatter image.

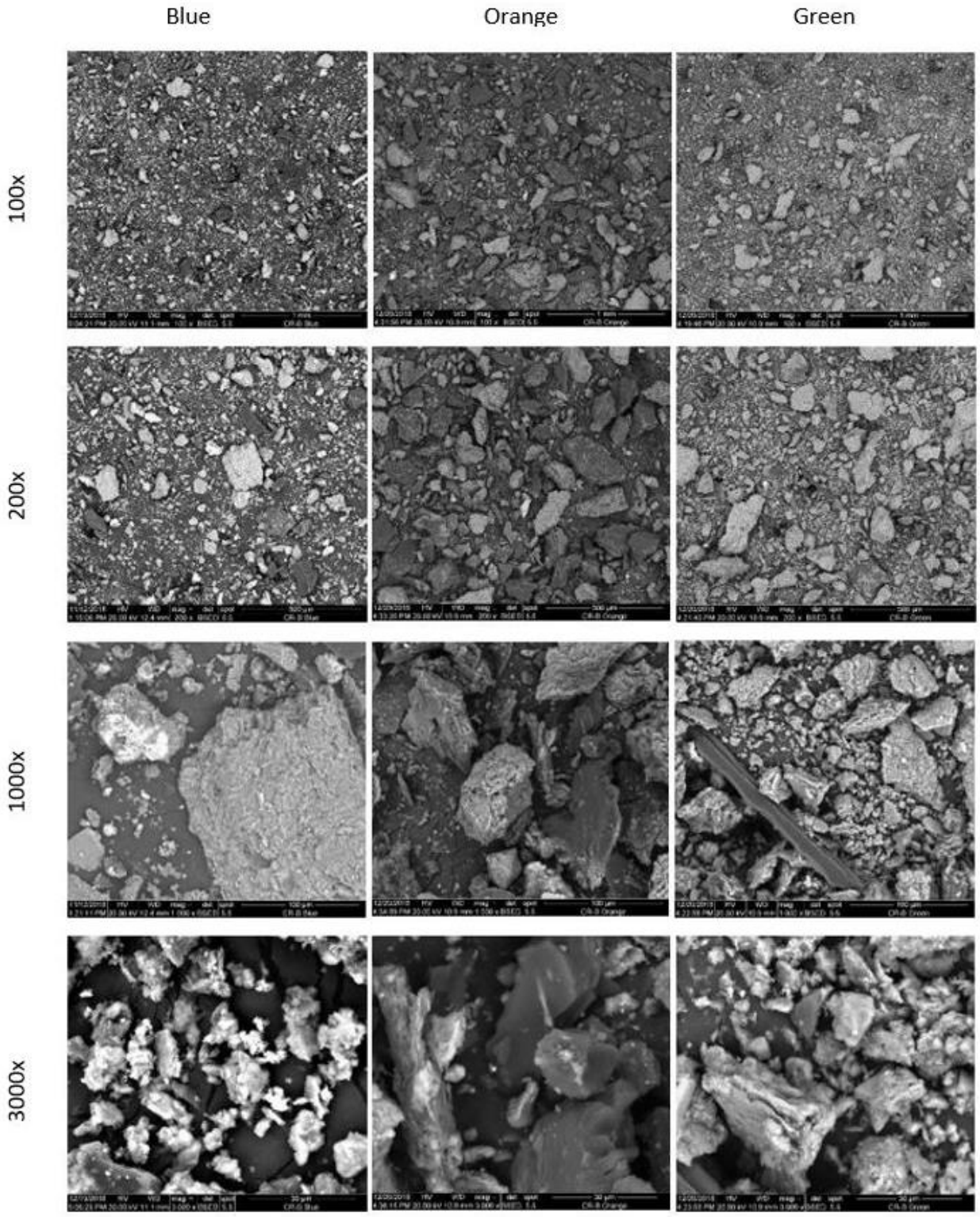

Figure 2 - 49: CR-B backscatter images of BOG sub samples at 100x, 200x, 1Kx, 3Kx

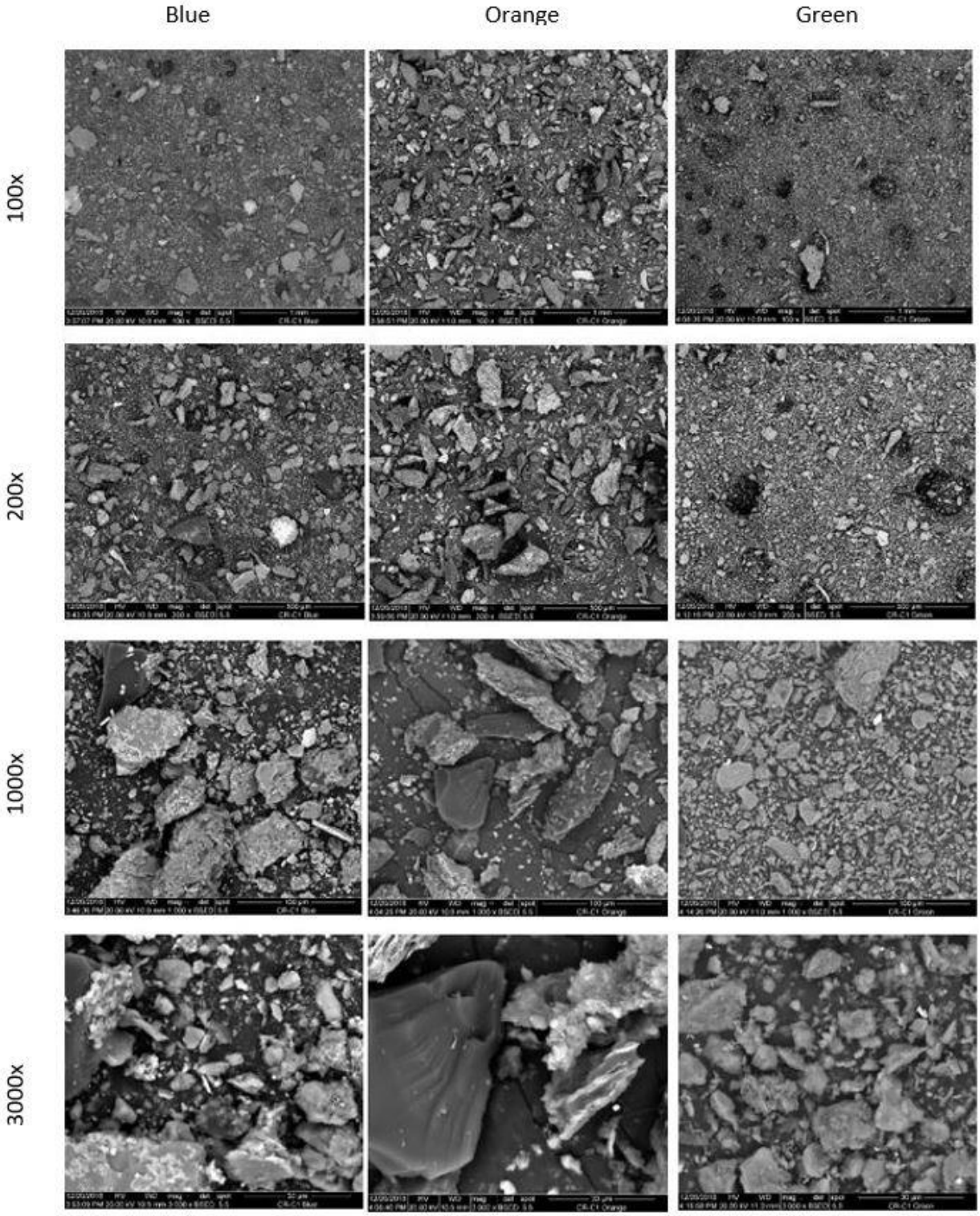

Figure 2 - 50: CR-C1 backscatter images of BOG sub samples at 100x, 200x, 1Kx, 3Kx

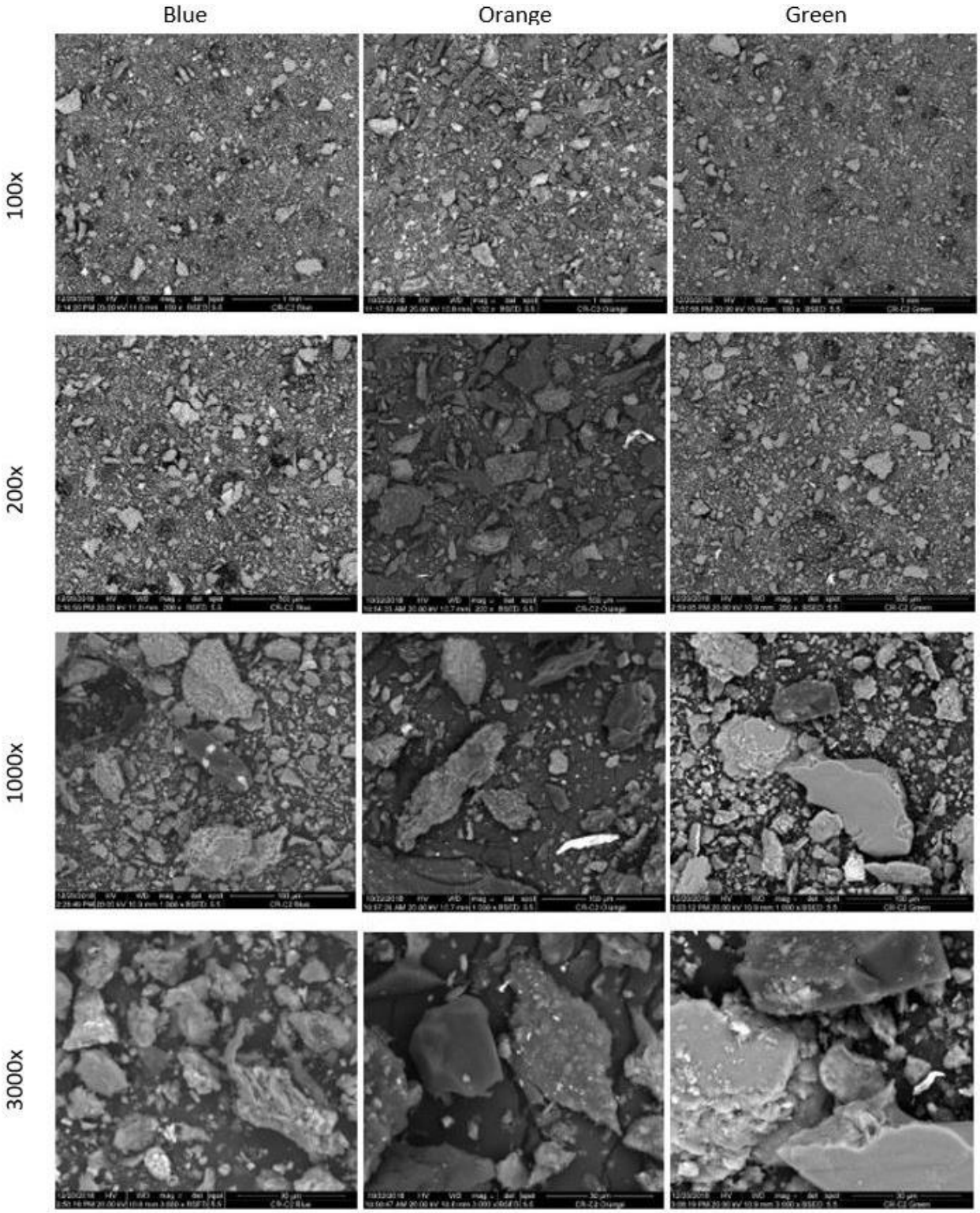

Figure 2 - 51: CR-C2 backscatter images of BOG sub samples at 100x, 200x, 1Kx, 3Kx

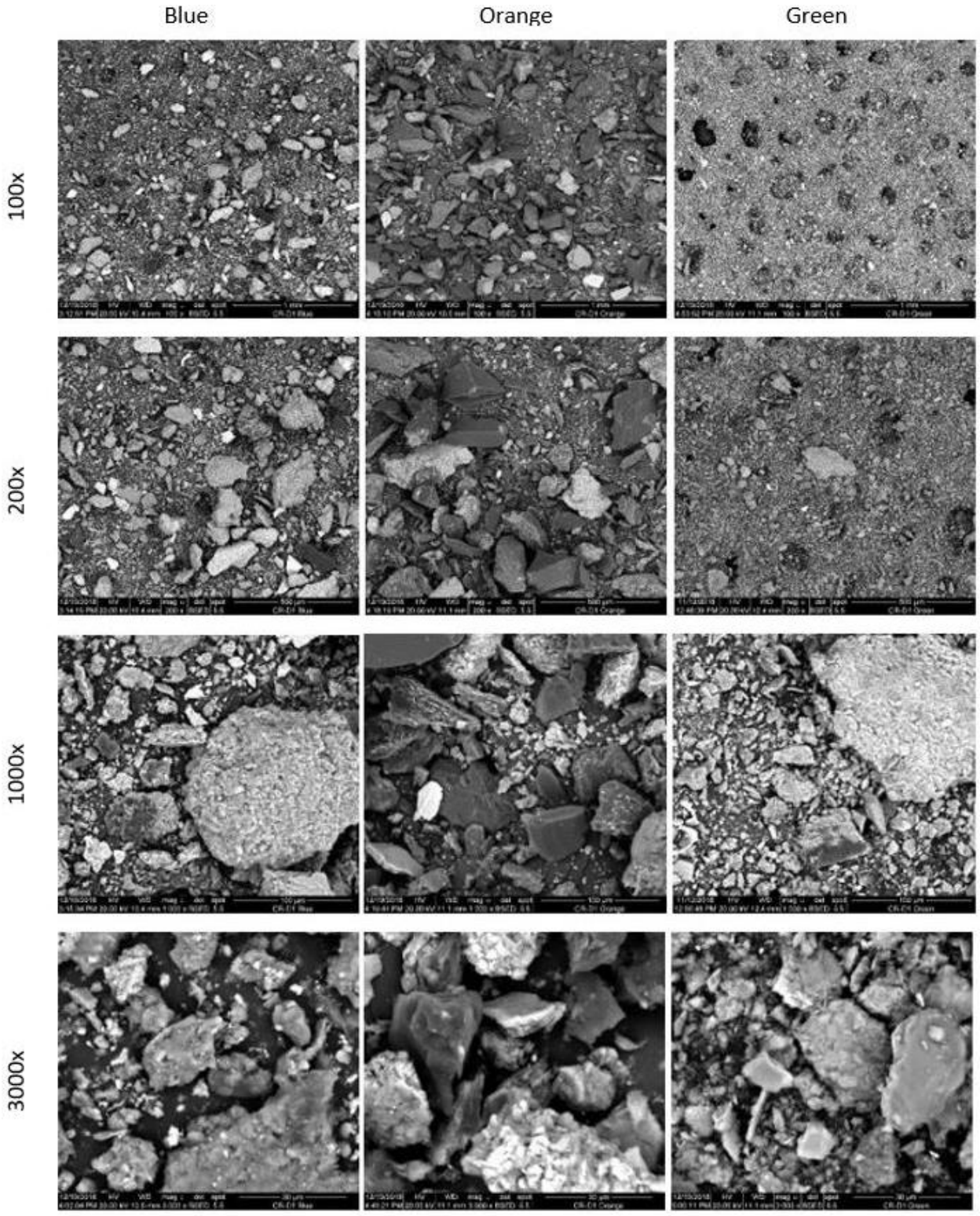

Figure 2 - 52: CR-D1 backscatter images of BOG sub samples at 100x, 200x, 1Kx, 3Kx

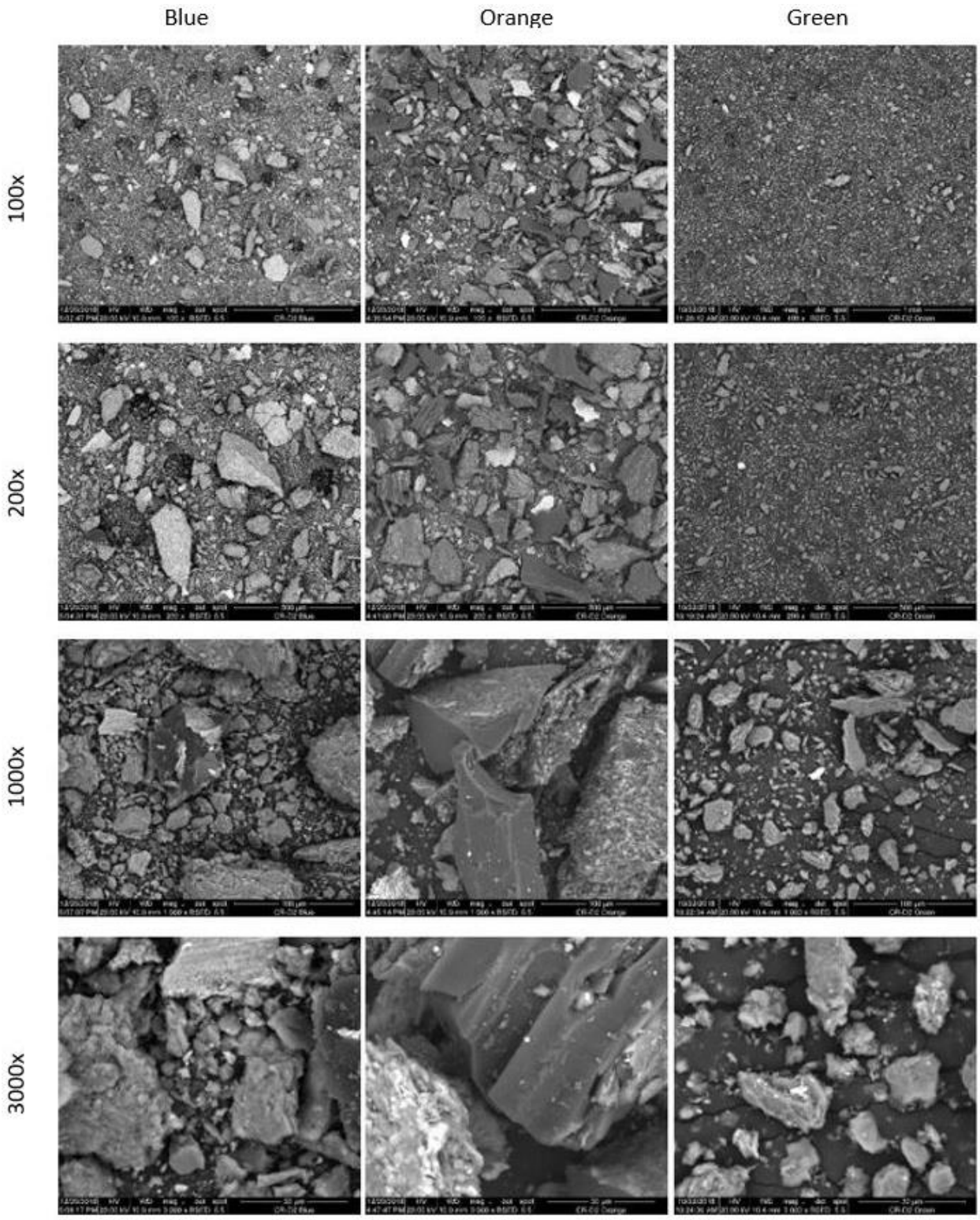

Figure 2 - 53: CR-D2 backscatter images of BOG sub samples at 100x, 200x, 1Kx, 3Kx

A notable find of the SEM-EDS analysis was an EDS point analysis of CR-D1 Orange that detected cerium and lanthanum in a coal particle. Figure 2 - 54**Error! Reference source not found.** shows the spectrum analysis of the point and surrounding points to compare. The adjacent bright point is some form of barium and sulfide according to the spectrum analysis, but previous XRD analysis did not detect any minerals in CR-D1 containing barium. All the coarse refuse BOG sub samples are archived and may be subjected to SEM-EDS analysis at any point necessary for more details or exploration.

Finally, small specimens that appeared foreign to the BOG sub sample compositions had been noticed in several sample images. The objects were different in structure and composition than the rest of the particles in the sample, so an EDS point analysis was performed on the unknown object. Figure 2 - 55 shows the foreign objects and the associated spectrum analysis. It has been assumed that these objects are iron shavings from the grinding plates used in the comminution and homogenization of these coarse refuse BOG sub samples.

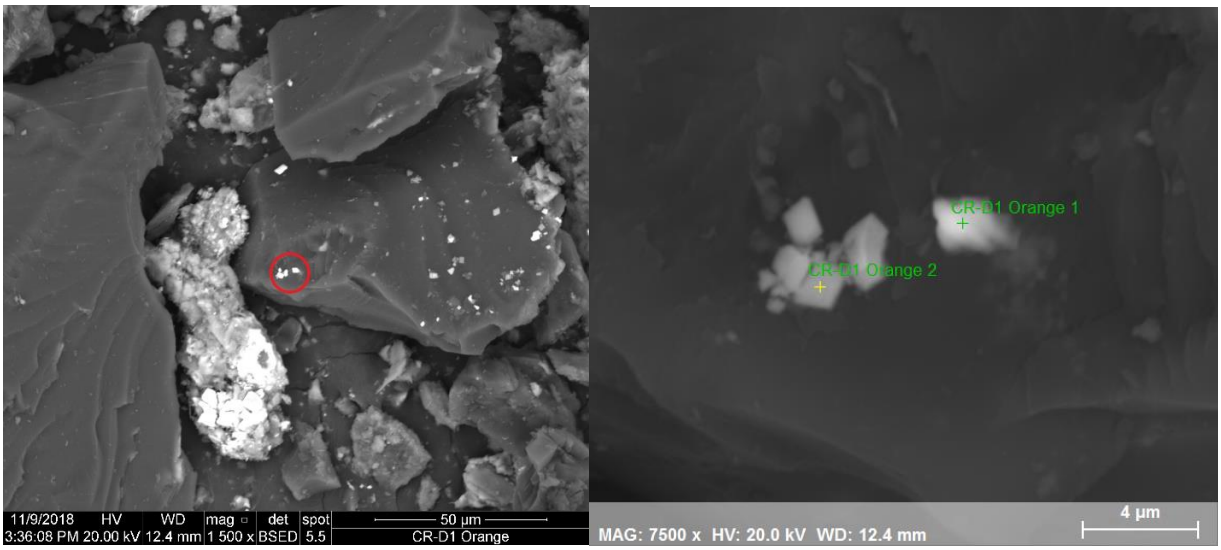

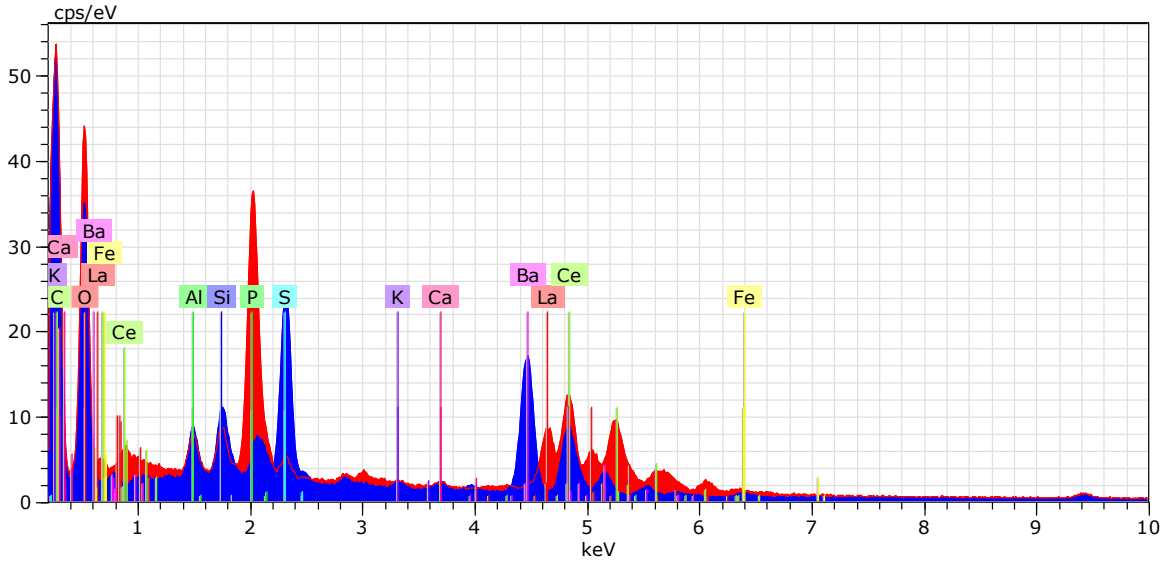

Element (wt. %)	C	O	Al	Si	P	S	K	Ca	Fe	Ba	La	Ce
CR-D1 Orange 1	60.05	33.4	0.51	0.42	2.88	0.15	--	--	--	--	0.98	1.62
CR-D1 Orange 2	44.35	44.57	1.54	1.58	--	3.95	0.05	0.1	0.19	3.67	--	--

Figure 2 - 54: Ce and La detection by EDS point analysis in a coal particle of CR-D1 Orange

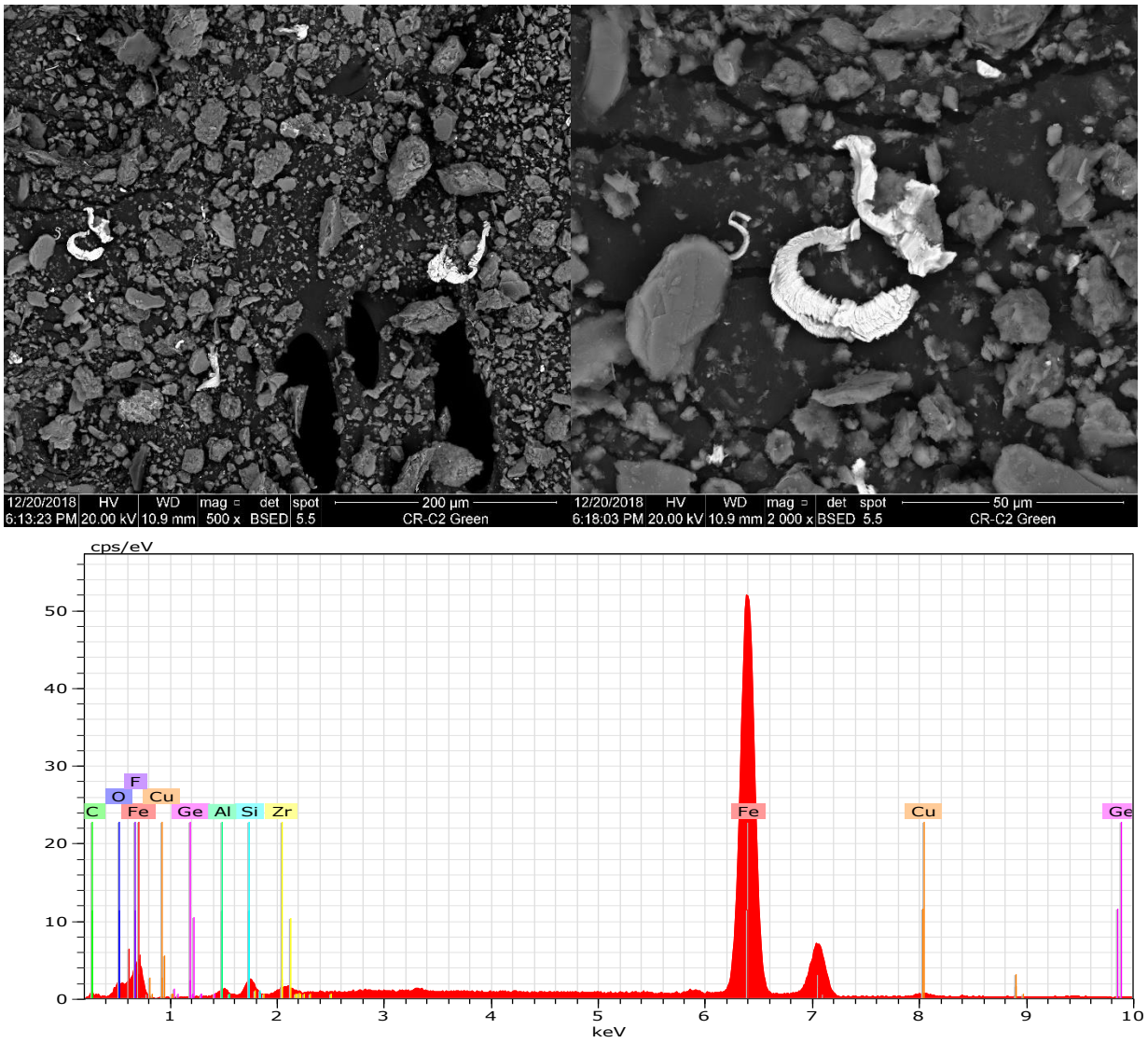

Figure 2 - 55: Iron shavings in CR-C2 Green from grinding plate on mill used in sample preparation

2.5 Evaluate Pyrite Separation

In this project, the potential to separate pyrite away from the coarse coal refuse was examined from two perspectives: 1) creating a pyrite enriched product to feed the bioreactor for an internal acid source and avoid purchasing costly acid and 2) separating pyrite from the heap leach feed material to avoid issues associated with nuisance pyrite in the heap. These two perspectives guided the experimental work conducted under this task.

Key Findings

- Through x-ray sorting, size classification, and density separation, an approximately 40% sulfur material can be produced from a feed material containing only 4-5% sulfur.
- Pyrite framboids have been found in both the high-ash and low-ash x-ray sorted sub samples. This finding could complicate efforts to concentrate pyrite through density or flotation methods alone. Additionally, pyrite can be identified in most of the sub samples but the abundance of pyrite in CR-B Blue far surpasses all others.
- This product is derived from a byproduct stream in an REE-concentrating process, so two favorable material streams can be produced by a single separation process.
- The XRF results showing higher sulfur content in CR-B and CR-B-b have been supported by greater acid producing potential observed in a simple static leaching trial of blue x-ray sorted products
- Progressions in the development of density separation and flotation methods led to a minor improvement in attainable sulfur concentration, with an increase to 10% S in a float fraction of a 1.65 SG separation, and over 8% in a single stage flotation as opposed to 8% in the previous quarter from a two-stage flotation. Neither surpassed the almost 18% S achieved by x-ray hand sorting.
- Sulfur may be depleted from the heap leach feed by gravity separation in a size class suitable for spiral concentration; however, this step will need to be considered against the comminution required for a high yield of material to be processed.

Detailed Results

2.5.1 Pyrite separation from the head samples

2.5.1.1 Coarse separation

As previously discussed, the coarse refuse was subjected to x-ray sorting. One of the products of this separation contained enriched heavy mineral content, generally iron bearing and either pyrite or siderite. The heavy mineral products of x-ray sorting were analyzed for pyrite concentration.

Figure 2 - 56 to Figure 2 - 62 show EDS point and mapping analyses for various blue sub samples to compare and differentiate the sources of iron and sulfur in the x-ray sorted coarse refuse samples. Figure 2 - 56 shows a 1500x view of CR-D2 Blue. Three objects are analyzed in this figure showing two different iron sources, most likely pyrite and siderite based on the assay data.

This result agrees with previous XRD analysis, which showed pyrite and siderite as the predominant iron bearing minerals.

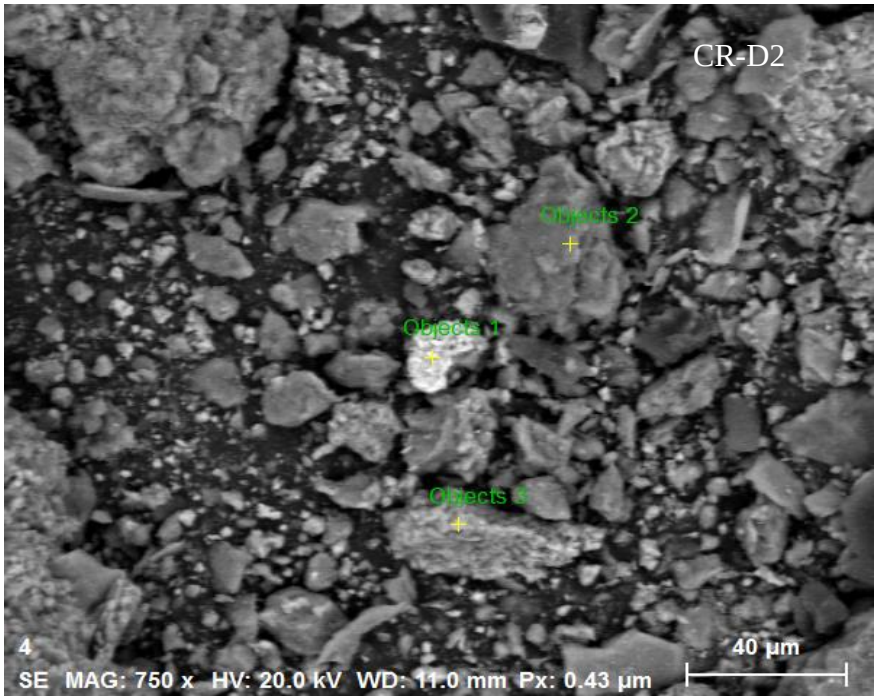

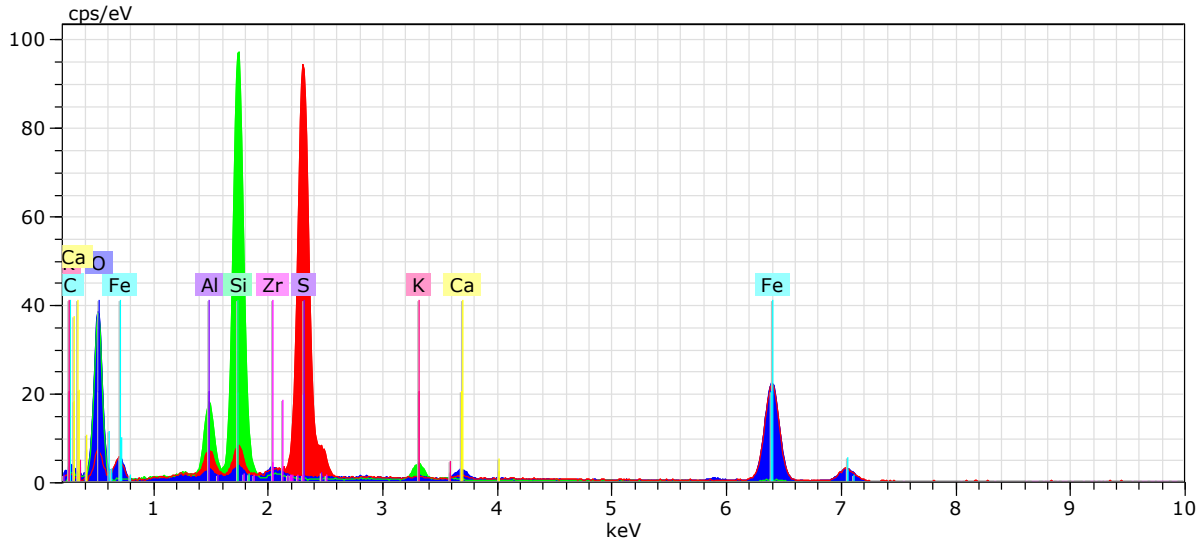

Element (wt. %)	C	O	Al	Si	S	K	Ca	Fe	Ge	Zr	Pd
Object 1	12.19	14.64	2.5	2.12	34.97	--	--	37.53	--	--	--
Object 2	7.64	41.25	4.54	25.13	--	2.06	--	0.8	--	--	--
Object 3	--	47.53	0.68	0.75	--	--	1.73	47.25	1.63	1.85	0.64

Figure 2 - 56: Multipoint spectra analysis of CR-D2 Blue at 1500x mag.

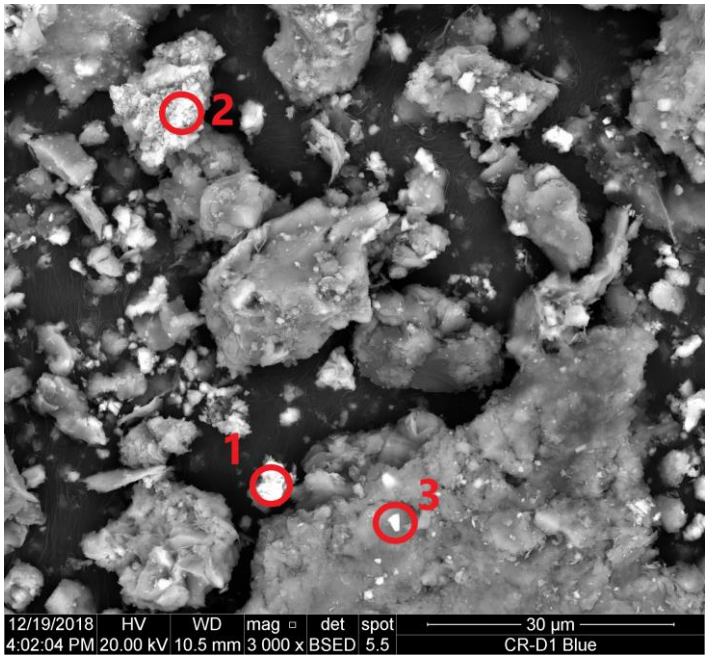

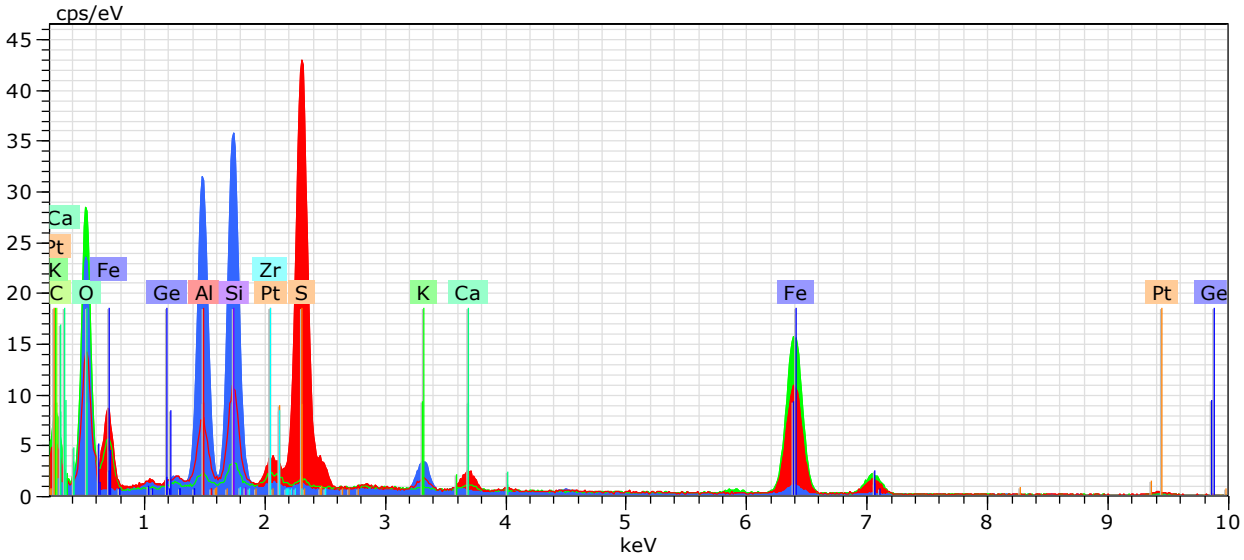

Element (wt. %)	C	O	Na	Mg	Al	Si	S	K	Ca	Fe	Ge	Br	Zr	Pt
Object 1	6.86	35.79	1.22	0.75	4.18	4.77	24.25	0.89	1.87	27.89	1.89	--	--	3.36
Object 2	26.82	53.32	--	--	--	0.64	--	--	--	35.58	1.23	--	0.86	--
Object 3	9.65	52.59	--	--	8.64	22.28	--	2.64	--	2.55	--	16.71	--	--

Figure 2 - 57: Multipoint spectra analysis of CR-D1 Blue at 3000x mag.

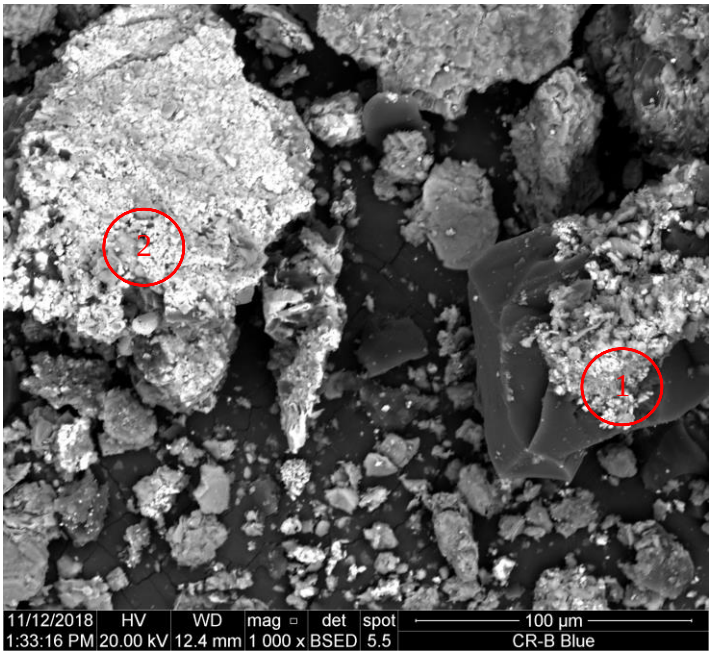

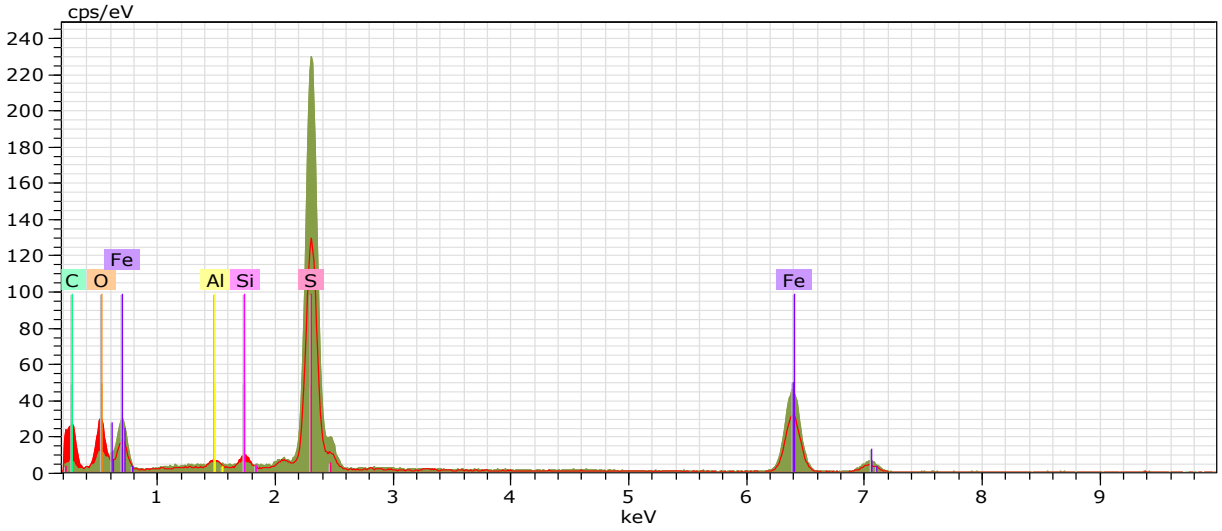

Figure

Element (wt. %)	C	O	Al	Si	S	Fe
Object 1	27.76	31.86	1.14	1.24	25.37	26.19
Object 2	21.83	10.92	--	--	34.21	37.15

Figure 2 - 58: Pyrite associated with coal and silica gangue in CR-B Blue at 1000x mag.

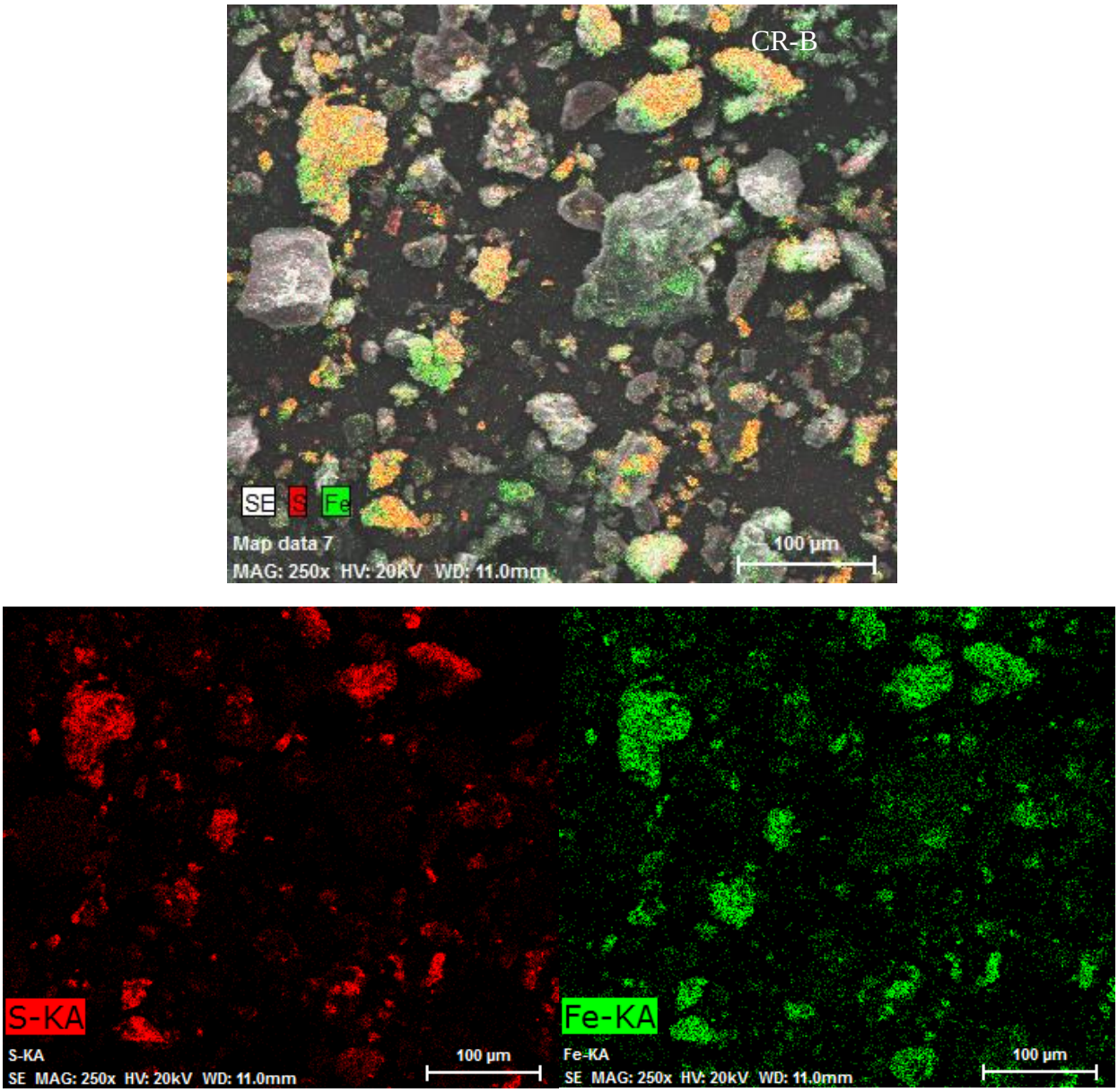

Figure 2 - 59: Spectrum mapping of pyrite in CR-B Blue at 500x mag.

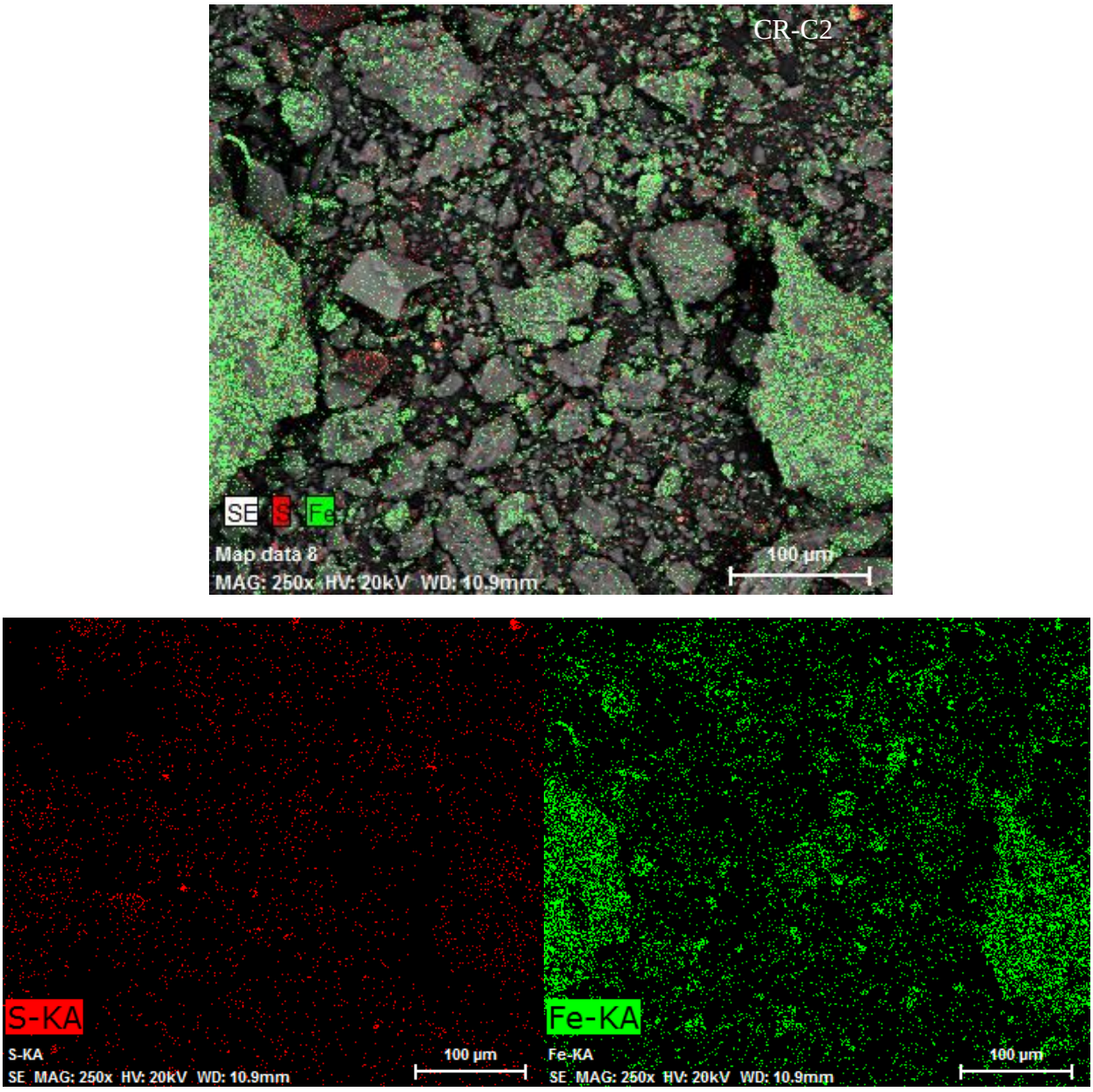

Figure 2 - 60: Spectrum mapping of pyrite in CR-C2 Blue at 500x mag.

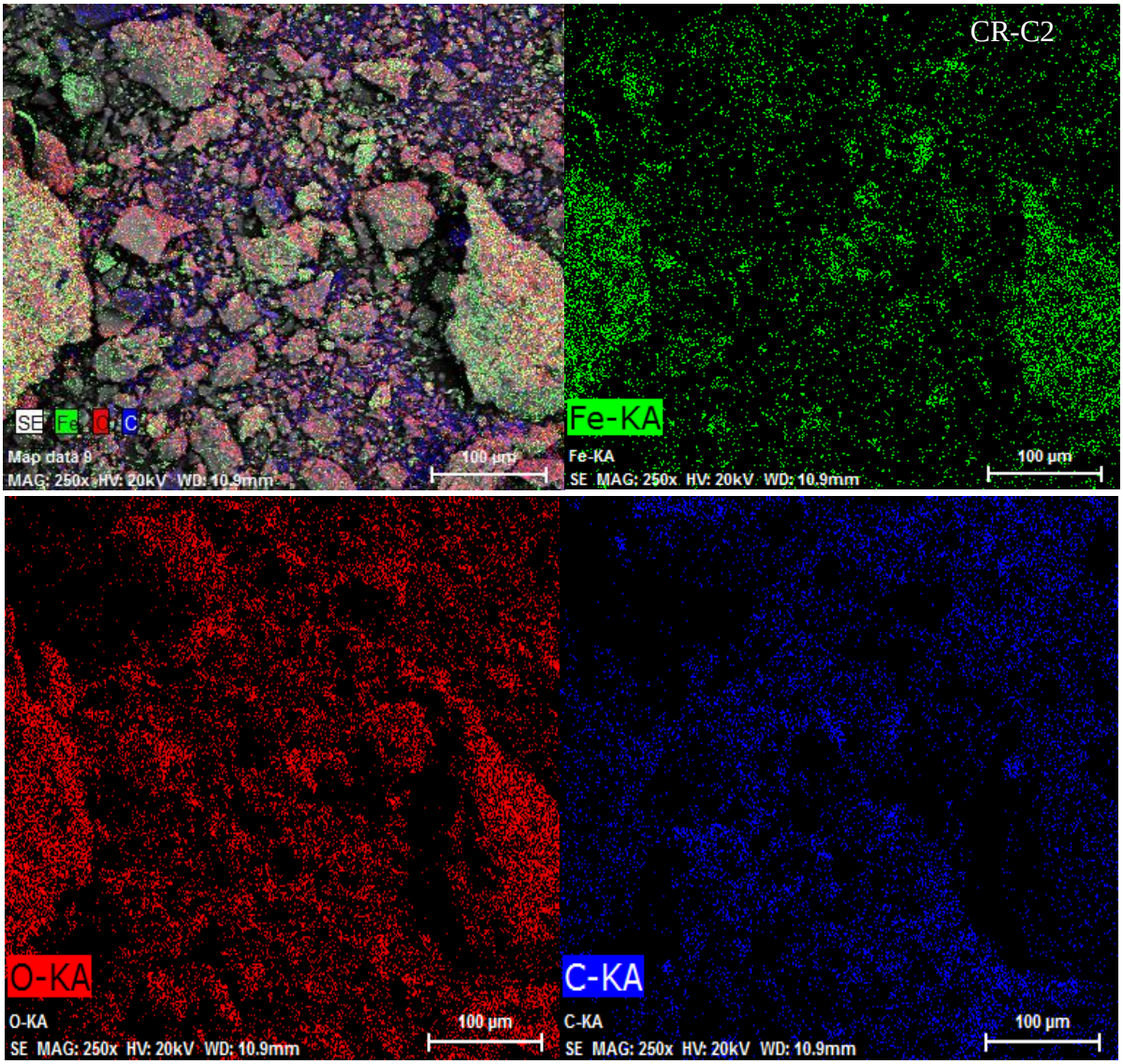

Figure 2 - 61: Spectrum mapping of iron bearing species in CR-C2 Blue at 500x mag.

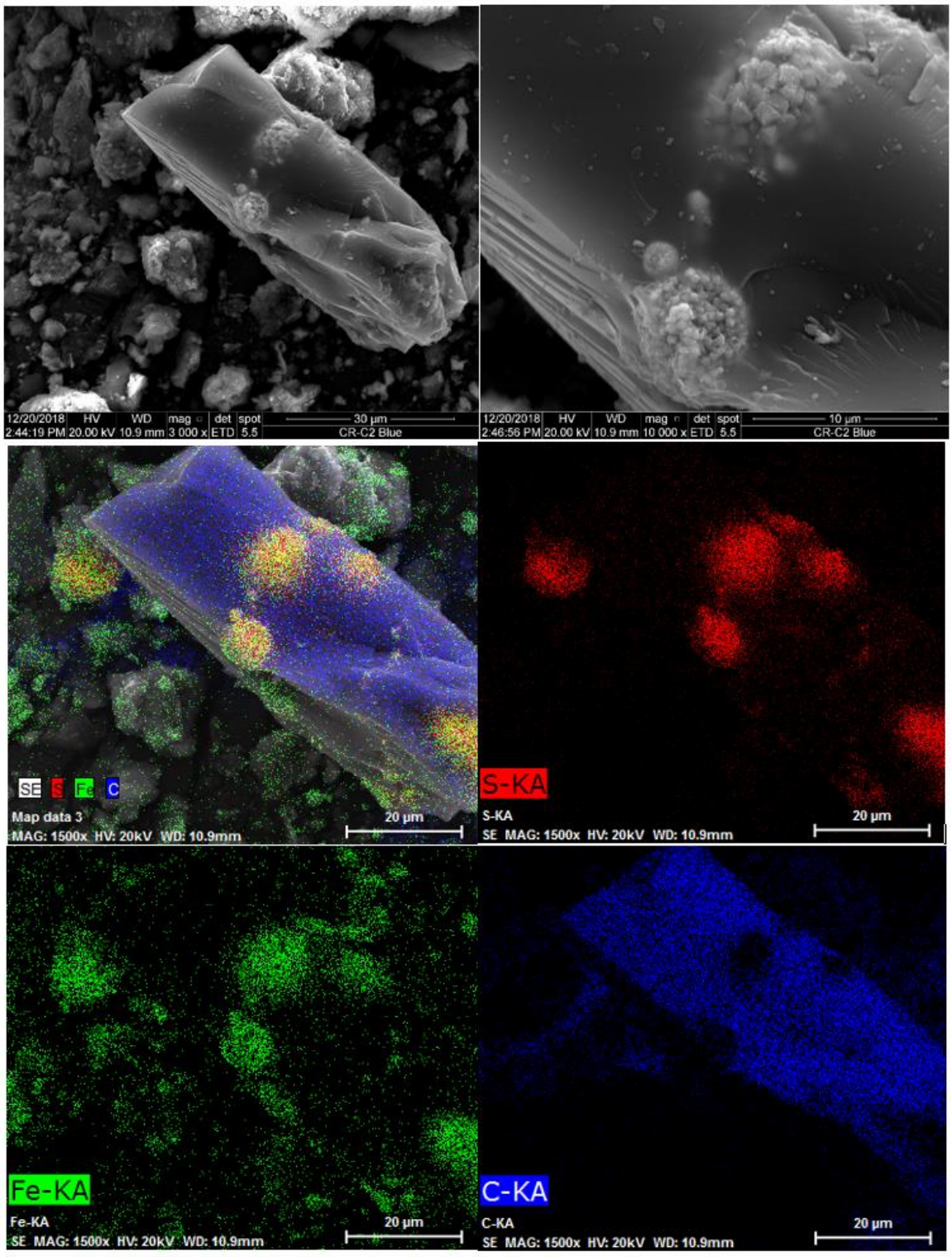

Figure 2 - 62: Backscatter images and spectrum mapping of pyrite in a coal particle of CR-C2 Blue

While the prior characterization studies have shown that CR-B has the greatest concentration of pyrite, the current SEM-EDS data suggests that pyrite is still present in the other CR samples, though only in trace amounts. For example, Figure 2 - 57, shows a multipoint EDS analysis of CR-D1 Blue at 3000x magnification. Three bright points were selected for spectra analysis which showed that one of the points is most likely pyrite, while the other similar spots may are likely to be siderite and muscovite or kaolinite, based on the spectra assays. Similarly, Figure Figure 2 - 58 shows multipoint EDS analysis of CR-B Blue at 1000x magnification. The significance of this image is that pyrite is visibly associated with both silica/ash material and coal simultaneously.

Figure 2 - 59 and Figure 2 - 60 compare small areas at 500x magnification on the surfaces of CR-B Blue and CR-C2 Blue, respectively. The EDS mapping reveals the locations where chosen elements are detectable, in this case either iron and sulfur or iron, carbon, and oxygen. It is clear in Figure 2 - 59 where iron and sulfur points are concentrated together and where they are not. In Figure 2 - 60, iron and sulfur are not concentrated together as they are in CR-B Blue while Figure 2 - 61 shows iron, oxygen, and some carbon concentrated together which could be siderite.

Pyrite framboids are also found in some of the samples, such as CR-C2 Blue which has revealed the presence of framboids locked in gangue and coal material (Figure 2 - 62). The association of pyrite with both combustible and ash material may make density separations or flotations of pyrite enriched material more challenging, however continuing optimization of those methods will provide more insight.

2.5.1.2 Fine separation

Preliminary fine pyrite separations were evaluated using a laboratory-scale test spiral (Figure 2 - 63). Efforts focused on assembling and troubleshooting the equipment and as a result, only a single test run was complete. For this test, a representative sample of as-received CR-B was ground and sized to 0.15mm x 1mm to produce an ideal feed for the spiral concentrator. Figure 2 - 64 provides the size distribution of the feed material, confirming the desired size limits.

During the tests, the material was continuously mixed in a bucket with water to create a feed slurry with approximately 25% by mass. This slurry was then pumped to the spiral, and the product was collected into two buckets. For this preliminary run, the splitter was set approximately at the middle of the material stream. The material stream on the spiral is shown in Figure 2 - 65, with a color difference visible from the outside to the inside of the stream. Samples from the feed, concentrate, and tailings streams were then split and subjected to ash and XRF analysis. These results are shown in Table 2 - 32. The XRF data shows a slight percent increase in sulfur, iron, and ash in the concentrate and a decrease in all three in the tailings. With the splitter placed in the middle of the stream, almost 75% of the total mass reported to the concentrate which led to approximately 80% recoveries of the total iron and sulfur mass in the feed. In addition, some mass was lost during the test, which precluded a more thorough mass balance.

Figure 2 - 63: Spiral concentrator and feed setup

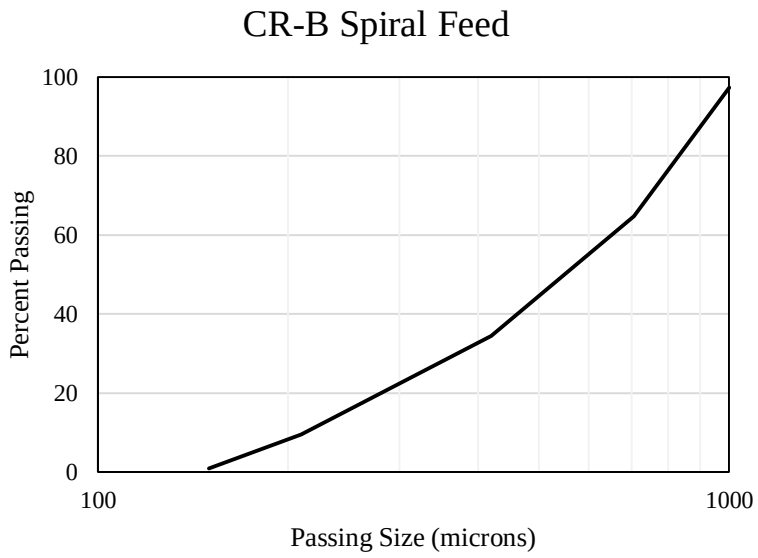

Figure 2 - 64: Spiral Concentration feed material size distribution

Figure 2 - 65: CR-B stream in spiral concentrator

Table 2 - 32: CR-B spiral concentration feed and product characterization

	Sulfur (%)	Iron (%)	Ash (%)
Feed	6.51	6.17	80.90
Conc.	6.87	6.71	84.24
Tail.	4.35	5.28	73.27

To improve on the preliminary spiral concentration, CR-B was subjected to a simple density cut. A heavy liquid solution with a specific gravity of 1.65 was created using lithium metatunsgtate and deionized water. Figure 2 - 66 shows the float-sink test setup with the sample just introduced to the vessel. The float and sink products were recovered after ample separating time was allowed, and then filtered and dried in an oven at 60°C. The dried samples were analyzed for ash using a LECO thermogravimetric analyzer and major metal content using a Niton XL2 GOLD handheld XRF analyzer. Prior to XRF analysis, the samples were pelletized using a laboratory pellet press at 9 metric tons of pressure.

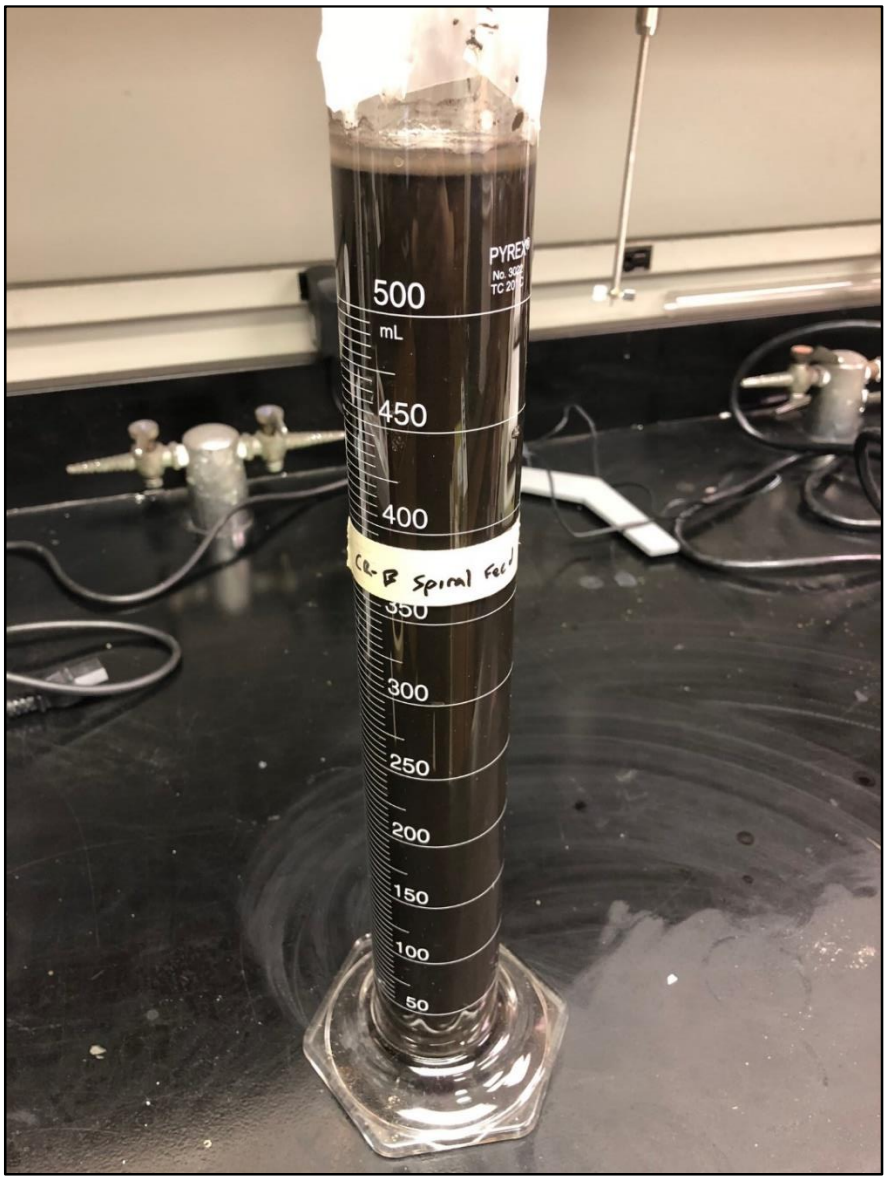

Figure 2 - 66: 1.65 SG float-sink separation of CR-B spiral feed

The float-sink test feed, sink, and float pellets are shown in Figure 2 - 67. Table 2 - 33 provides the balanced mass values for the feed and recovered products, along with the ash and major metal content. A very small fraction of the feed mass reported to the float product but resulted in the highest sulfur concentration of 10% while the sulfur content decreased in the sink product. Interestingly, the XRF results show iron concentration changing oppositely from the sulfur concentration. Approximately 50 mg of each material was digested in a 12 mL solution of aqua regia for ICP-MS analysis. The ICP-MS results are displayed in Table 2 - 34. The REE values in the sink and float products were both lower than the feed concentrations, which may indicate some error in the processing of the products.

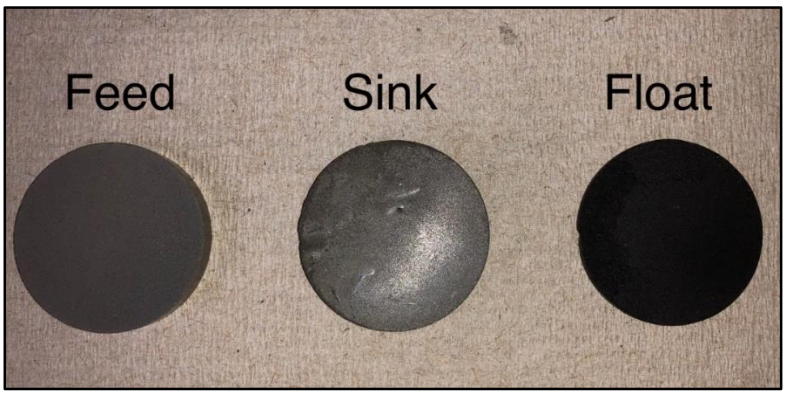

Figure 2 - 67: Pelletized feed, sink, and float fractions for density separation of CR-B spiral feed at 1.65 SG

Table 2 - 33: Mass, ash, and major elemental composition of CR-B spiral feed, float and sink fractions at 1.65 SG

CR-B Spiral Feed	Mass g	Ash %	Fe %	Ti %	K %	Al %	Si %	S %	Mg %	Ca %
Feed	50.08	81.23	4.88	0.66	1.00	9.29	23.29	5.65	--	0.20
Float	3.41	18.16	4.09	1.09	0.77	3.93	9.18	10.26	--	0.39
Sink	46.68	85.83	4.94	0.63	1.01	9.68	24.32	5.31	0.76	0.18

Table 2 - 34: Measured REE concentrations for feed and products of 1.65 SG density separation of CR-B obtained by ICP-MS

CR-B 1.65 SG Cut	**TREE ppm**	Sc ppm	Y ppm	La ppm	Ce ppm	Pr ppm	Nd ppm	Sm ppm	Eu ppm	Gd ppm	Tb ppm	Dy ppm	Ho ppm	Er ppm	Tm ppm	Yb ppm	Lu ppm
Feed	**203.48**	13.78	16.90	36.15	74.25	8.78	32.51	6.18	1.29	5.26	0.63	3.54	0.67	1.75	0.23	1.39	0.19
1.65 SG Float	**86.86**	10.26	11.95	12.38	25.61	3.10	11.77	2.51	0.59	2.59	0.38	2.39	0.48	1.36	0.18	1.15	0.17
1.65 SG Sink	**172.24**	11.20	13.39	31.08	63.68	7.50	27.90	5.35	1.09	4.39	0.53	2.82	0.54	1.40	0.18	1.06	0.15

2.5.1.3 Ultrafine separation

Pyrite is a common iron sulfide and can be rendered hydrophobic using a xanthate collector at high pH. Once hydrophobic, pyrite can be readily separated from other hydrophilic gangue minerals, including shales, clays, and silica. To evaluate the concentration of pyrite from ultrafine process streams, flotation was conducted on a sample of fine refuse (thickener underflow) recovered from site B (sample ID: FR-B). The material has a nominal size of -250 microns and is approximately 49% ash. This testing campaign evaluated two potential flowsheets: one which included a preliminary coal flotation step prior to xanthate flotation and a second which evaluated the xanthate flotation without a prior coal recovery step. All tests were conducted in a laboratory-scale Denver flotation cell (Figure 2 - 68). In the coal flotation step stage, the FR-B feed material was floated in a 2L cell using 0.75 lb/ton kerosene as the collector and two drops of MIBC as a frother. In the xanthate stage, a solution of potassium amyl xanthate was used as the collector at a dosage of 3.9 lb/ton, along with 2 drops of MIBC as the frother. Following typical sulfide flotation guidelines, a pH of 11 was maintained for the xanthate flotation.

Figure 2 - 68: Laboratory scale Denver flotation cell

In the first test series, the two-stage flotation process was applied, whereby coal was removed in the first stage, and the xanthate flotation was conducted on both the concentrate and the tailings. Alternatively, the second test series applied the xanthate flotation process directly to the as-received FR-B sample without prior coal removal. Figure 2 - 69 and Figure 2 - 70 show flowsheet representations of two-stage flotation circuits as well as the experimental data acquired during testing.

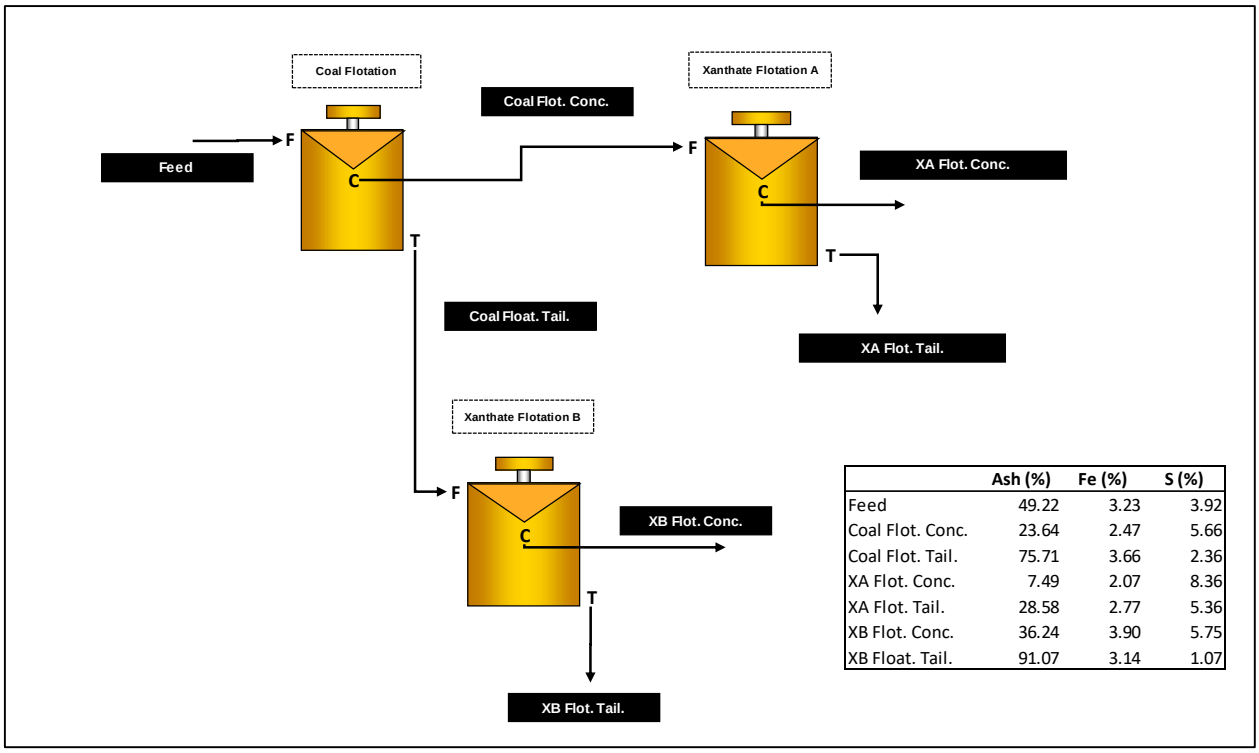

	Ash (%)	Fe (%)	S (%)
Feed	49.22	3.23	3.92
Coal Flot. Conc.	23.64	2.47	5.66
Coal Flot. Tail.	75.71	3.66	2.36
XA Flot. Conc.	7.49	2.07	8.36
XA Flot. Tail.	28.58	2.77	5.36
XB Flot. Conc.	36.24	3.90	5.75
XB Float. Tail.	91.07	3.14	1.07

Figure 2 - 69: Flowsheet Representation of two-stage pyrite flotation circuit

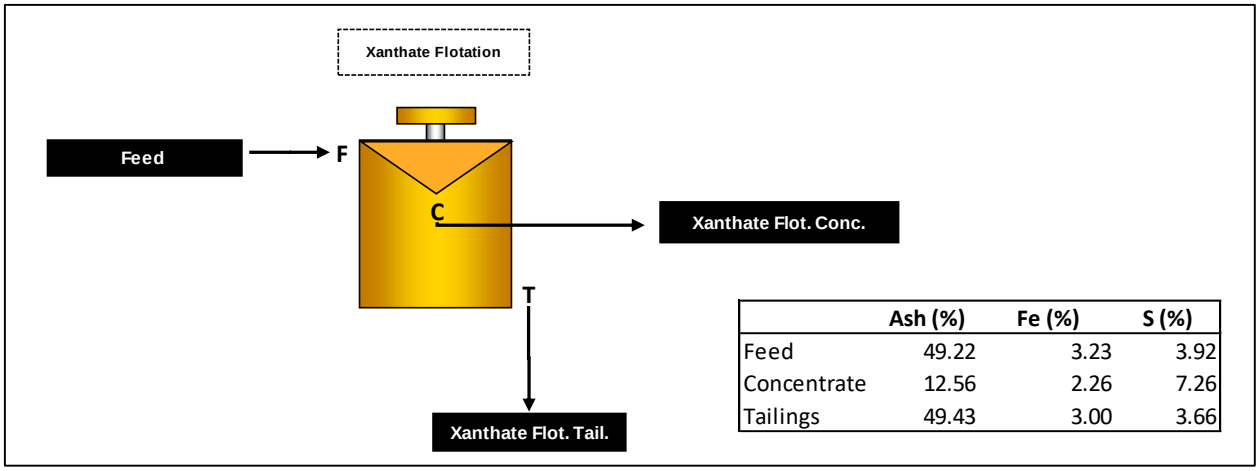

	Ash (%)	Fe (%)	S (%)
Feed	49.22	3.23	3.92
Concentrate	12.56	2.26	7.26
Tailings	49.43	3.00	3.66

Figure 2 - 70: Flowsheet representation of a single-stage pyrite flotation

These results indicate that flotation has some promise to improve sulfur concentration when using xanthate as a collector. In the two stage circuit, the sulfur largely followed the clean coal, with the coal flotation concentrate having a sulfur concentration of 5.56% versus a tailings concentration of 2.35%. This result is somewhat expected, as pyrite can be mildly hydrophobic, even without xanthate collector. The second stage of xanthate flotation was then able to further increase the overall concentration of sulfur up to 8.36%, a notable improvement from the initial feed concentration of 3.92%. Unfortunately, the tailings from the coal removal step were largely depleted of pyrite, and the xanthate flotation was unsuccessful in concentrating that material. Interestingly, the direct flotation using a single xanthate flotation stage was also successful, producing a sulfur concentration 7.26%, once again a notable improvement from the initial feed concentration of 3.92%.

A flotation release analysis was also performed on FR-B to further evaluate the possibility of using a flotation process to concentrate pyrite or REE-enriched material. A sample of FR-B was screened to minus 250 microns to simulate the plant reject after coal recovery. Approximately 250 g of the sample was introduced into a 2L Denver flotation cell with tap water. Kerosene was used as a collector and dosed at 0.75 lb/ton, while 2 drops of MIBC were used as a frother. Once the flotation began, the float product was collected in time increments of 0-30, 30-60, 60-90, 90-120, and 120-240 seconds. All the material remaining in the cell after 240 seconds of flotation made up the sink product. The products were all filtered and dried for ash analysis in a LECO thermogravimetric analyzer and major metal analysis by a Nitron XL2 GOLD handheld XRF analyzer. The pellets of the FR-B feed, sink product, and 30 second float product are shown in Figure 2 - 71.

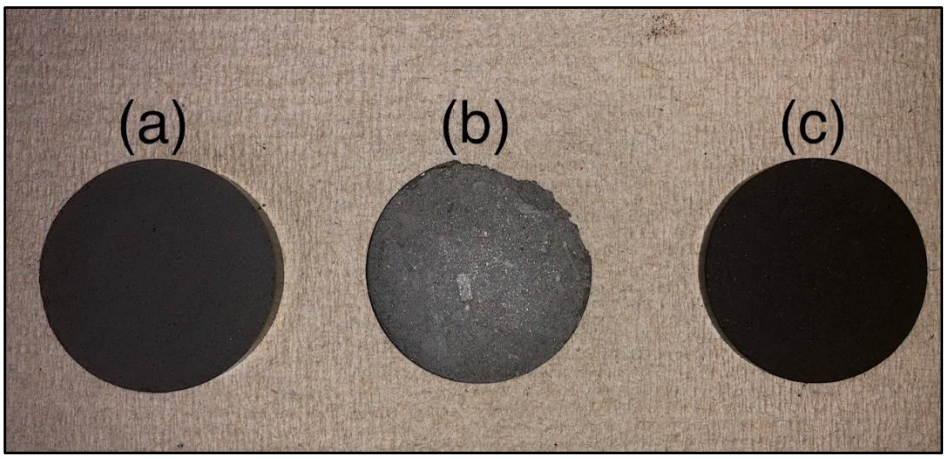

Figure 2 - 71: Pelletized FR-B release analysis feed, sink, and 30 sec float fractions

Table 2 - 35 provides the balanced mass, ash, and major metal content for the products of the release analysis. The float products all had higher sulfur contents than the feed or sink material. There was no significant change in iron content among the products with the exception of a slight increase in the 60-90 second float time period, which also has the highest sulfur content. This data shows that the sulfur mostly floated with the clean coal, which could be from the sulfur associated with the coal or from pyrite that is mildly hydrophobic by itself. Approximately 50 mg of each product was digested in a 12 mL solution of reverse aqua regia for ICP-MS analysis. The measured REE concentrations of the release products are shown in Table 2 - 36. The balanced mass, ash, and TREE content for the flotation fractions is provided in Table 2 - 37. The sink fraction of the flotation appears to have higher TREE content than the feed, and a high mass yield. Figure 2 - 72 graphically depicts the TREE content in each flotation fraction.

Table 2 - 35: Mass, ash, and major elemental composition of FR-B release analysis feed, float. fractions, and sink fraction

Intervals	**Mass**	**Ash**	**Fe**	**Ti**	**K**	**Al**	**Si**	**S**	**Mg**	**Ca**
Sec.	**g**	**%**	**%**	**%**	**%**	**%**	**%**	**%**	**%**	**%**
Feed	250.24	49.90	2.64	0.97	1.21	7.12	20.32	3.93	0.49	1.00
30	29.43	18.53	2.66	1.00	1.05	4.24	11.74	6.59		0.86
60	16.74	20.22	2.57	0.95	0.95	4.12	12.29	6.05	0.55	0.84
90	8.80	18.12	3.39	1.19	1.32	5.96	14.98	8.24		1.04
120	16.41	26.48	2.62	0.94	1.13	5.19	14.78	5.81		0.90
240	40.25	32.76	2.64	0.92	0.98	4.86	15.68	4.87	0.56	0.97
Tails	138.61	69.91	2.59	0.98	1.34	9.05	25.45	2.34	0.75	1.06

Table 2 - 36: Measured REE concentrations for feed and products of flotation release analysis of FR-B obtained from ICP-MS

FR-B Flot. Fractions	**TREE ppm**	Sc ppm	Y ppm	La ppm	Ce ppm	Pr ppm	Nd ppm	Sm ppm	Eu ppm	Gd ppm	Tb ppm	Dy ppm	Ho ppm	Er ppm	Tm ppm	Yb ppm	Lu ppm
Feed	**129.93**	8.65	12.01	23.37	46.68	5.44	20.21	3.79	0.80	3.21	0.41	2.36	0.46	1.23	0.16	1.01	0.14
30 Sec	**69.48**	5.10	7.34	11.83	23.89	2.82	10.62	2.04	0.45	1.84	0.24	1.43	0.27	0.77	0.10	0.64	0.09
60 Sec	**67.89**	4.67	7.09	11.59	23.52	2.81	10.42	2.07	0.43	1.82	0.25	1.42	0.27	0.75	0.10	0.61	0.08
90 Sec	**61.19**	4.36	6.56	10.39	21.04	2.48	9.38	1.82	0.38	1.64	0.21	1.26	0.25	0.69	0.09	0.57	0.09
120 Sec	**83.44**	5.84	8.33	14.52	29.26	3.47	12.82	2.45	0.53	2.15	0.28	1.64	0.33	0.88	0.11	0.73	0.09
240 Sec	**93.65**	6.03	9.22	16.41	33.23	3.89	14.67	2.78	0.59	2.42	0.32	1.80	0.35	0.94	0.13	0.76	0.11
Sink	**175.76**	11.73	14.29	31.93	64.59	7.66	27.92	5.30	1.11	4.37	0.52	2.89	0.55	1.41	0.19	1.12	0.16

Table 2 - 37: Balanced mass, ash, and TREE content of FR-B release analysis

FR-B Float Fractions	Mass g	Ash %	TREE ppm
Feed	249.88	49.35	130.45
30 Sec	31.39	18.55	69.47
60 Sec	17.22	20.23	67.88
90 Sec	9.08	18.13	61.17
120 Sec	16.84	26.48	83.42
240 Sec	42.18	32.78	93.58
Tailings	133.16	70.65	175.27

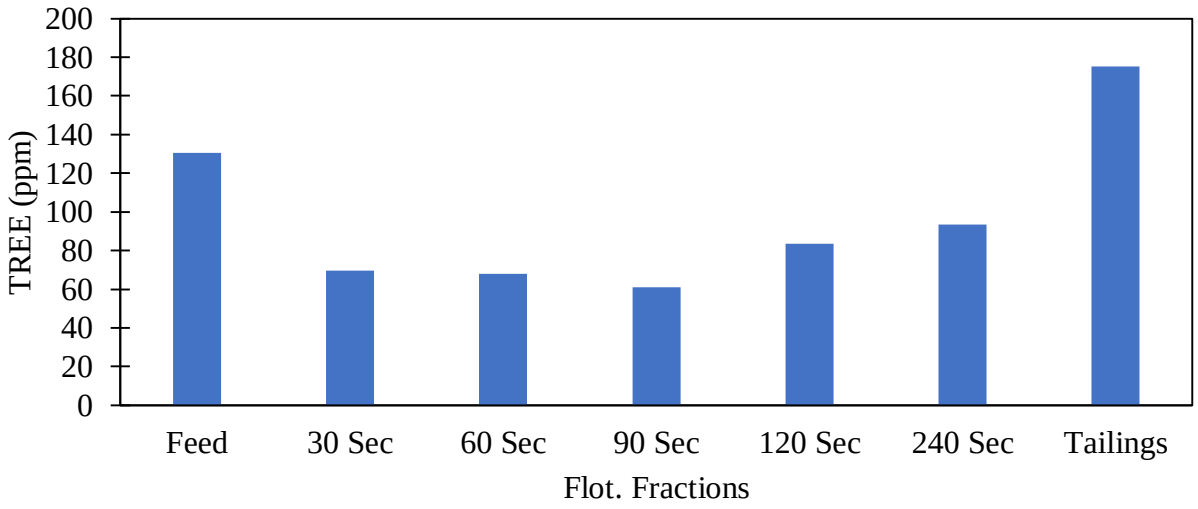

Figure 2 - 72: TREE content of FR-B flotation fractions

2.5.2 Pyrite separation from the coarse sorted product

Continued efforts to produce a pyrite enriched product focused on further processing of the coarse pyrite product from x-ray sorting. The sorted product was subjected to size, density, and magnetic analyses for potential process development.

2.5.2.1 Size analysis

The x-ray sorted material (2x0.5") was passed through a Sturtevant laboratory roll crusher and Bico pulverizer to approximately minus 3 mm. Using US standard mesh 8-inch sieves and a Gilson Silent Sifter sieve shaker, the sample was separated into 4 size classes: +1 mm, 1x0.6 mm, 0.6x0.15 mm, and -0.15mm. The particle size distribution for the CR-B-blue sample is shown in Figure 2 - 73. Splits were taken from each size class to be ground and homogenized in an agate mortar and pestle (Figure 2 - 74) for TGA and XRF analysis. TGA analysis was performed with a LECO TGA 701 and XRF measurements were taken with a Niton XL2 Goldd handheld XRF analyzer.

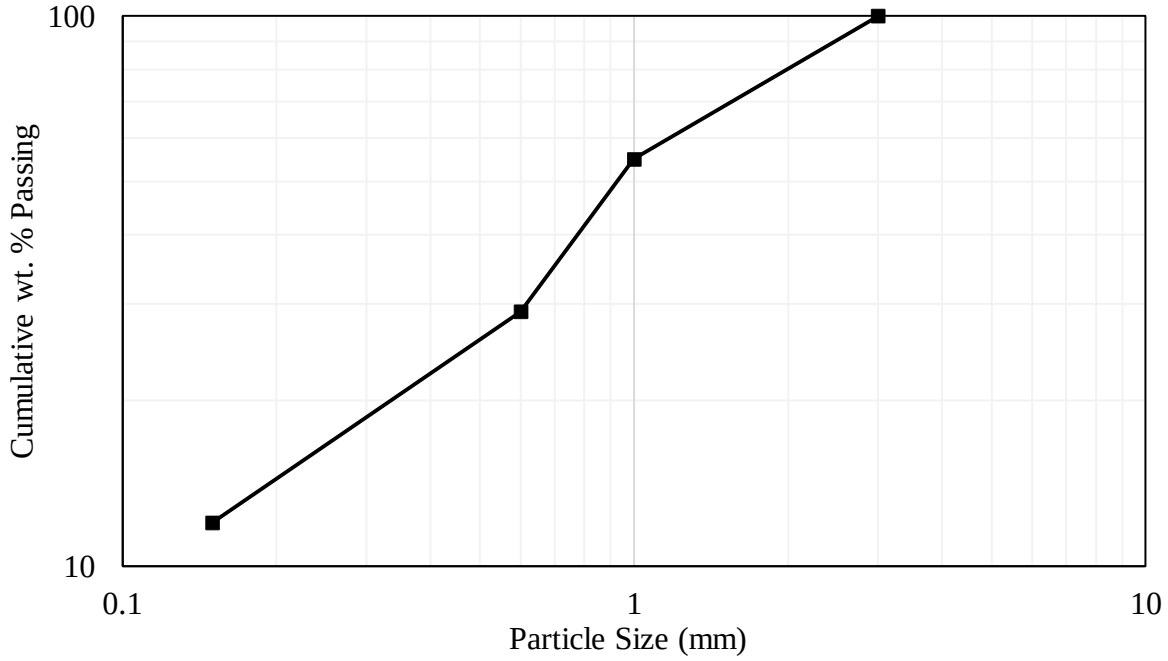

Figure 2 - 73: Particle size distribution of crushed CR-B-blue

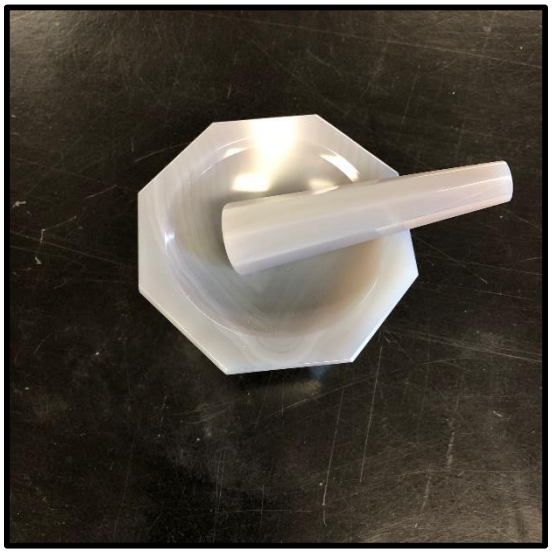

Figure 2 - 74: Agate mortar and pestle used to prepare samples for pelletizing for XRF

Table 2 - 38 provides the XRF readings of the CR-B-blue feed and size products. Sulfur content in each size class was greater than the 19% reported in previous quarters; therefore, the sample was re-homogenized and re-analyzed by XRF. The new sulfur value for CR-B-blue used for these trials was approximately 25%. Table 2 - 39 shows the balanced mass, ash, and sulfur values by feed and size class. Slight differences in measured and balanced values are a result of the balancing method and variability in XRF measurements, even with repeated readings taken per sample. The differences in sulfur content of the crushed CR-B-blue product were small, but a slight trend of decreasing sulfur content with particle size can be observed in Figure 2 - 75.

Table 2 - 38: Major elemental composition of CR-B-blue size fractions measured by XRF analysis

CR-B Blue Size Classes (mm)	Fe (%)	Ti (%)	K (%)	Al (%)	Si (%)	S (%)	Mg (%)	Ca (%)
Feed	20.51	0.45	0.88	10.18	14.23	24.82	1.52	1.29
+1	21.72	0.44	0.74	10.41	14.01	27.26	--	0.89
-1/+0.6	20.63	0.45	0.71	9.13	12.55	26.16	--	1.46
-0.6/+0.15	18.86	0.48	0.85	9.23	13.50	23.52	1.52	1.53
-0.15	17.93	0.41	0.91	7.99	12.96	22.21	1.14	0.99

Table 2 - 39: Balanced mass, ash, and sulfur content of the CR-B-blue size classes

Size Class (mm)	Mass in Class (%)	Ind. Ash (%)	Ind. Sulfur (%)	Sulfur Distribution (%)
1	45.08	65.92	26.9	47.58
1 x 0.6	25.50	63.78	25.97	25.98
0.6 x 0.15	17.42	63.16	23.41	16.01
-0.15	12.00	62.97	22.14	10.43
Feed	25.48	64.54.	25.48	100

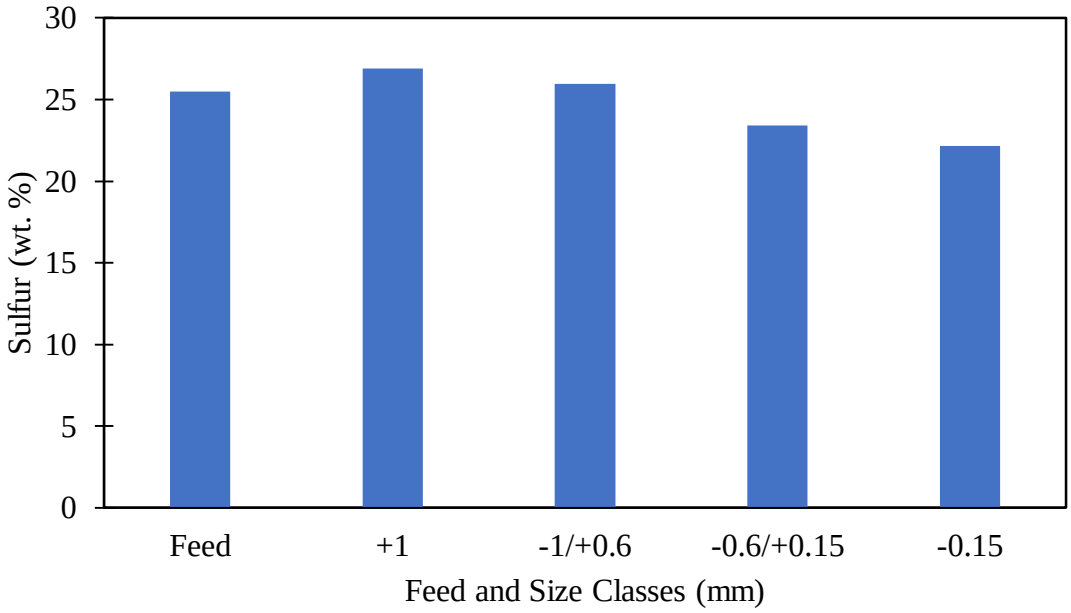

Figure 2 - 75: Sulfur Content (wt. %) of size fractions of CR-B-blue determined by XRF

The highest distribution and grade of sulfur were in the coarsest size fraction. Almost half of the sulfur content is recovered in the +1 mm size fraction and at the highest grade of approximately 27%. If the cut point is moved to lighter densities, the total sulfur increases but the overall grade of the concentrate decreases.

2.5.2.2 Density concentration

To further concentrate pyrite from the x-ray sorted product stream, a 1x0.15 mm size fraction of CR-B-blue was subjected to a float-sink test to produce 4 density fractions: +2.95, 2.4-2.95, 1.8-2.4, and -1.8 SG. The 1x0.6 and 0.6x0.15 mm size fractions were re-homogenized to create a size fraction suitable for spiral concentration.

The float-sink test was performed using lithium meta-tungstate as the heavy liquid to create three dense medium baths in lab beakers: 2.95, 2.4, and 1.8 SG. The feed sample was deslimed before being introduced to the 2.95 SG bath first. The material was given time to separate, and then the float fraction was recovered and fed to the 2.4 SG bath. This process was repeated for the final bath, creating four SG classes. Material near the SG of each bath was decanted with the float fractions. The samples were rinsed of any heavy liquid residue and dried and weighed in a nitrogen atmosphere. A representative split from each density fraction was ground in the agate mortar and pestle for XRF analysis. Figure 2 - 76 shows the float-sink separations and the pellets created for XRF analysis.

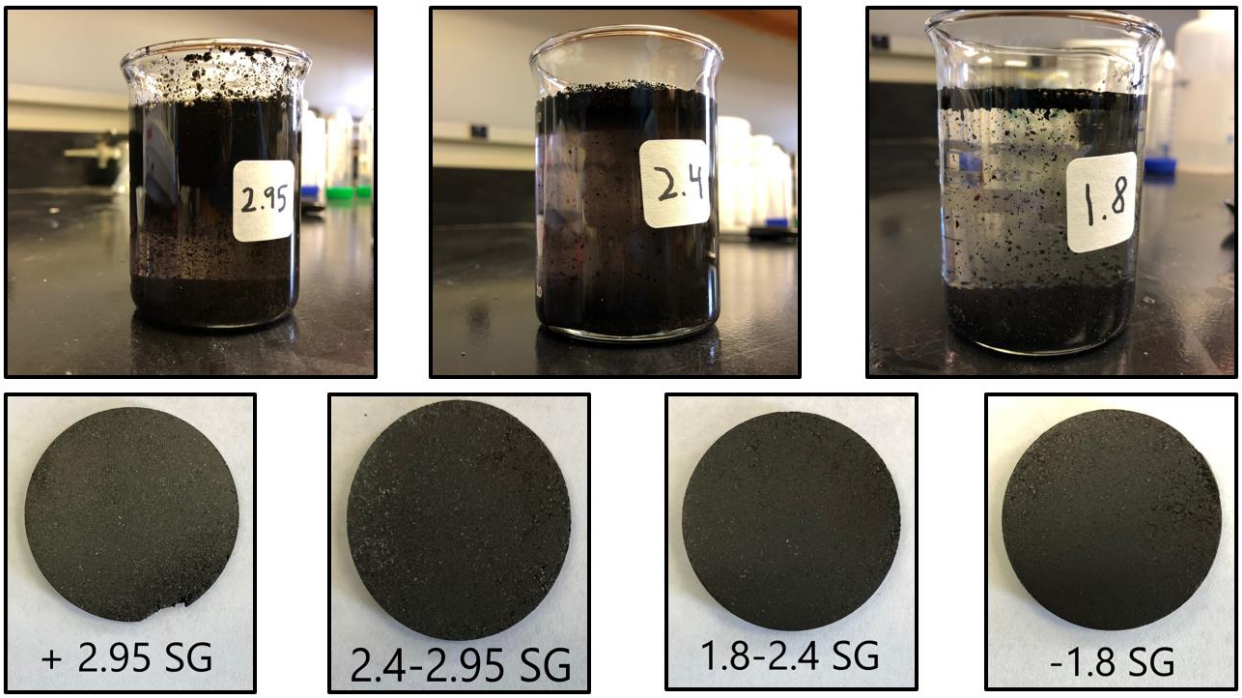

Figure 2 - 76: SG Baths and pellets of density fractions analyzed by XRF

Table 2 - 40 shows the measured major element concentrations determined by XRF. Table 2 - 41 contains the balanced mass, ash, and sulfur content for the 1x0.15 mm feed and four density products. The sulfur content of each density class is shown in Figure 2 - 77. The +2.95-density fraction contained the highest sulfur concentration and accounted for over half of the mass of the feed sample. The +2.95 SG fraction accounts for almost 70% of the sulfur in the sample and has a grade of almost 40%. Stepping down to the next lightest cut-point, the recovery increases to 85%,

but the grade decreases down to 30%, only slightly higher than the balanced feed grade for this trial.

Table 2 - 40: Major elemental composition of CR-B-blue 1x0.15mm density fractions measured by XRF analysis

CR-B Blue 0.15x1 mm	Fe (%)	Ti (%)	K (%)	Al (%)	Si (%)	S (%)	Mg (%)	Ca (%)
Feed	19.13	0.55	0.78	9.22	13.28	25.37	1.23	1.83
-1.8	12.23	0.51	0.49	2.74	5.87	18.66	LOD	0.49
1.8-2.4	13.85	0.56	0.45	6.15	11.47	24.22	0.99	1.39
2.4-2.95	11.34	0.60	1.09	10.80	18.98	18.28	LOD	2.61
+2.95	31.85	0.16	0.24	7.38	6.75	42.87	LOD	0.17

Table 2 - 41: Balanced mass, ash, and sulfur content for 4 density classes of 1 x 0.15 mm CR-B-blue

Density Class (S.G.)	Mass in Class (%)	Ind. Ash (%)	Ind. Sulfur (%)	Sulfur Distribution (%)
-1.8	2.31	25.87	18.53	4.59
1.8-2.4	3.88	56.79	23.85	9.91
2.4-2.95	9.79	75.15	17.74	18.58
2.95	16.48	66.14	37.93	66.92
Feed	32.46	64.87	28.78	100

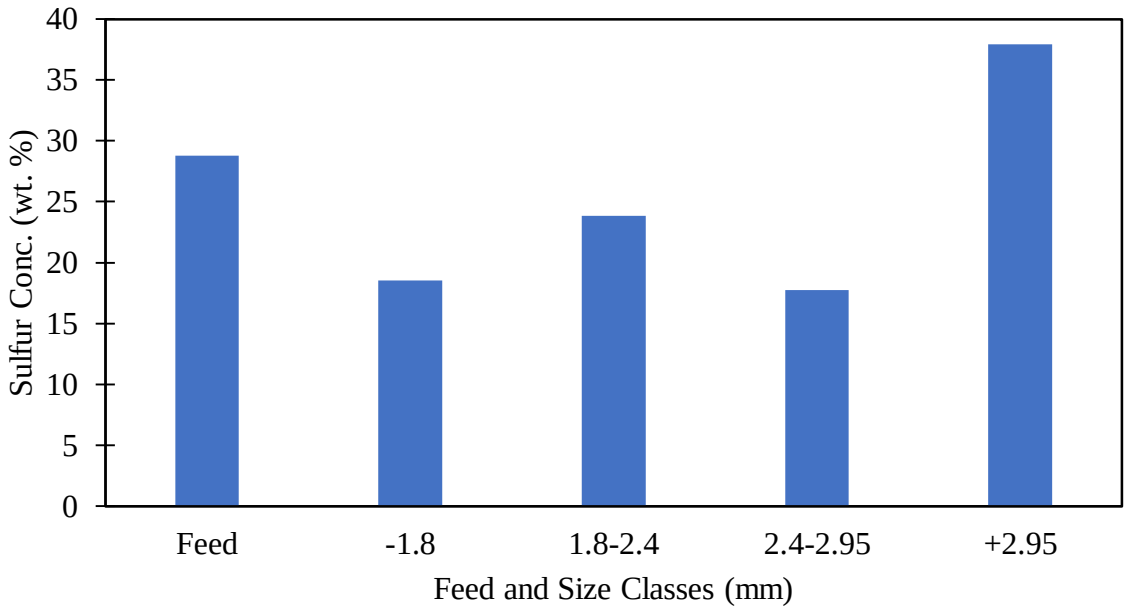

Figure 2 - 77: Sulfur content (wt. %) in density fractions of the 1x0.15mm size fraction of CR-B-blue

2.5.2.3 Magnetic separation

In addition to size and density analysis of sulfur distribution, the team wanted to investigate the potential magnetic susceptibility of pyrite in the sample. This effort was conducted using the -0.15 mm size fraction of CR-B-blue. A powerful, handheld rare earth magnet was used in these separation trials (Figure 2 - 78). The -0.15 mm material was weighed and spread out in a vessel. The magnet was passed through the entirety of the sample to collect any magnetic material possible. This process is illustrated in Figure 2 - 79. After the magnetic material was removed, the remaining sample in the vessel was weighed and a split was taken to be pelletized for XRF analysis. This process was repeated four times with the products re-homogenized between each trial. The same feed assay was used for each trial.

Figure 2 - 78: RE magnet used for separation trials of -0.15 mm CR-B-blue

Figure 2 - 79: (a) CR-B-blue (-0.15 mm) spread in vessel for magnetic separation and (b) magnetic material recovered by passing the magnet through the sample

Table 2 - 42 shows the measured XRF results for the major elemental composition of the tailings of each separation trial. No significant changes can be observed from the feed to the tailings assays for any of the major elements. The measured feed and tailings assays were used to calculate the concentrate assays due to the small concentrate mass. From the calculated assays, sulfur recovery and rejection were also calculated for each trial. Table 2 - 43 shows these measured and calculated data. The sulfur concentration data is also depicted graphically in Figure 2 - 80. In each trial, the sulfur recovery is very low and mirrors the overall mass yields for the separation. It appears material was only separated in these trials, with no observable concentration.

Table 2 - 42: Major elemental composition of magnetic separation tailings determined by XRF

CR-B Blue -0.15 mm	Fe (%)	Ti (%)	K (%)	Al (%)	Si (%)	S (%)	Mg (%)	Ca (%)
Feed	18.63	0.46	0.97	8.55	13.75	23.13	--	0.04
Run 1 Tails	18.27	0.41	0.96	8.64	13.65	23.12	--	1.03
Run 2 Tails	18.23	0.41	0.95	9.08	13.81	23.15	1.42	1.02
Run 3 Tails	18.23	0.42	0.91	8.56	13.41	23.10	1.23	1.03
Run 4 Tails	18.60	0.44	0.96	9.16	13.88	23.53	1.69	1.07

Table 2 - 43: Measured sulfur concentrations of the magnetic separation feed and tailings with calculated concentrate sulfur %, recovery, and rejection

Trial	Feed Sulfur (%)	Tail S (%)	Mass Yield (%)	Conc S (%)	S Recovery (%)	S Rejection (%)
1	23.13	23.12	4.25	23.34	4.48	95.52
2	23.13	23.15	3.29	22.68	3.23	96.77
3	23.13	23.10	3.50	23.85	3.60	96.40
4	23.13	23.53	3.11	10.80	1.45	98.55

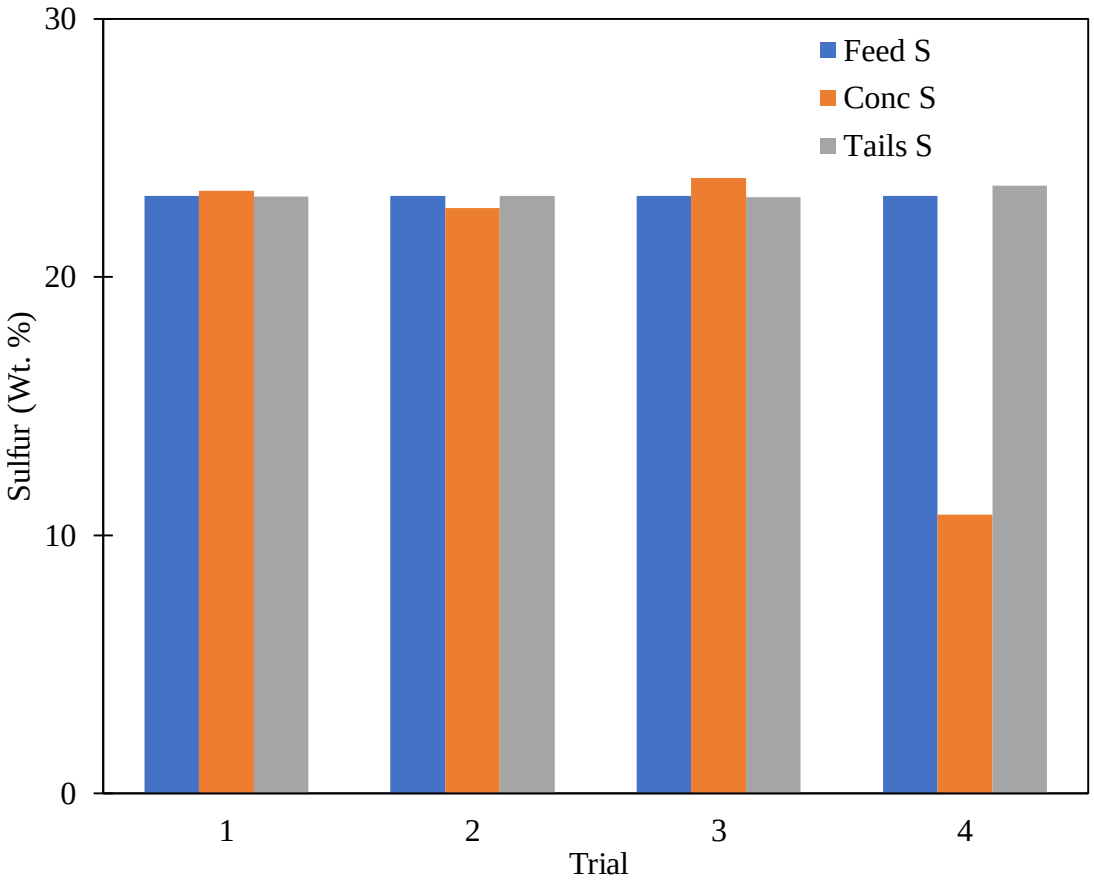

Figure 2 - 80: Sulfur concentrations of feed, concentrate, and tailings from magnetic separation trials

2.5.2.4 Flowsheet development

A flowsheet was developed to illustrate these sulfur concentration trials. Figure 2 - 81 depicts the process beginning with the CR-B head sample. Sulfur concentrations are shown throughout the flowsheet in a material balance format. For each concentration method, the feed assays were analyzed immediately pre-testing, which is why some values such as the float-sink feed assay do not match exactly with the assays of the product from the subsequent concentration method. The highest sulfur product from the flowsheet was the +2.95 SG fraction of the float-sink trials. The XRF measurement for sulfur in this product indicated 42% sulfur, but this value is slightly lower (37%) in the flowsheet after mass balancing. Size fractionation only showed slight concentration of sulfur in the coarser size ranges, and magnetic separation efforts did not yield any significant concentration of sulfur.

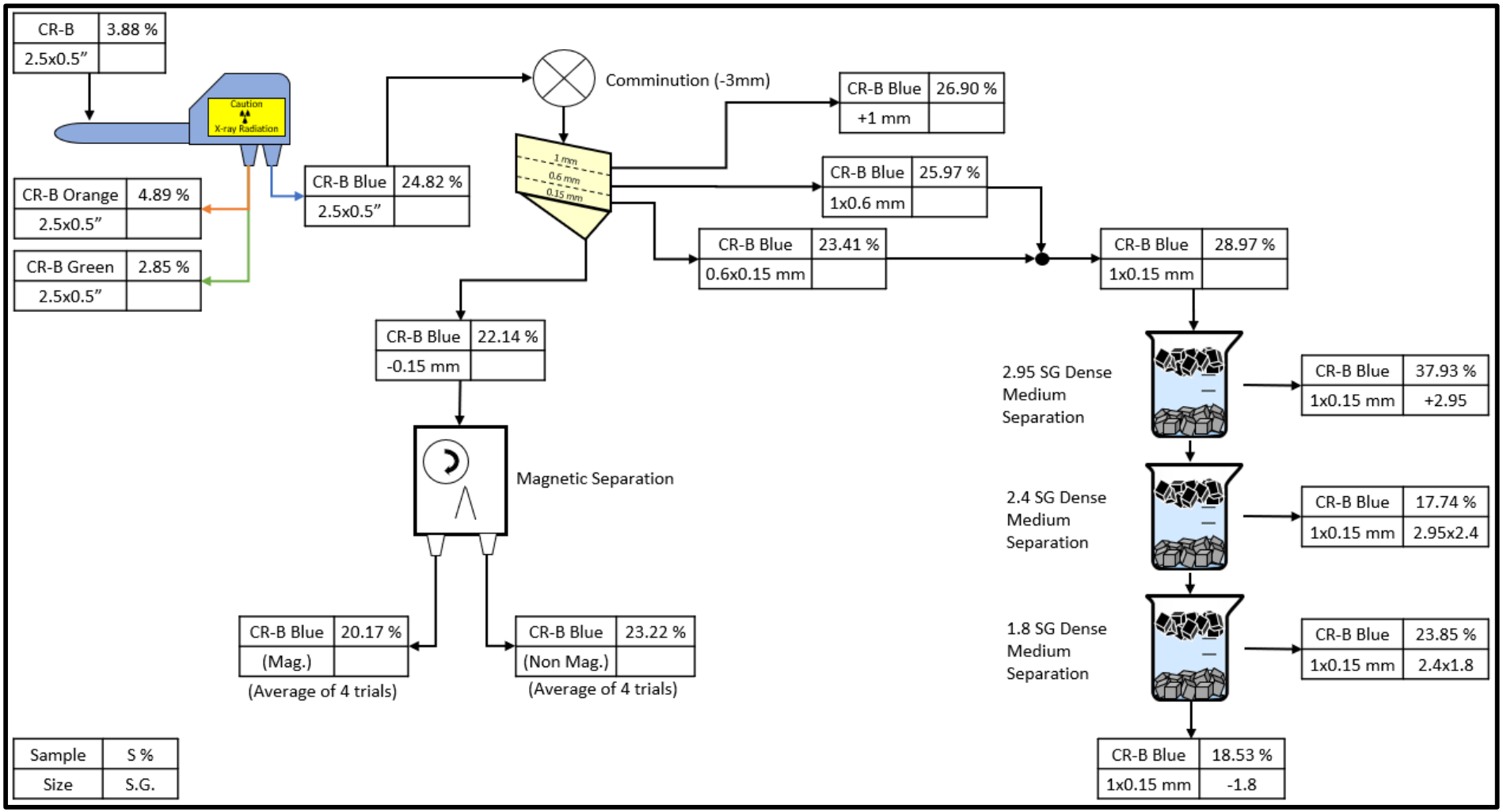

Figure 2 - 81: Process flowsheet for concentrating sulfur in CR-B

2.5.3 Pyrite separation from the sorted heap feed material

In addition to creating a desirable pyrite material for acid production, another goal of pyrite separation was to rid the heap leach feed material of nuisance pyrite. The REE-enriched sorter product CR-B-green (i.e. heap leach feed) was evaluated for sulfur depletion. Limiting the sulfur content in the heap leach feed has notable advantages, as low sulfur content can mitigate uncontrolled acid "hot spots," increase heap stability, and improve long term environmental outcomes.

Four representative splits were taken from the x-ray sorted green product, CR-B-g. One split was retained without further processing, while the other three splits were crushed using a 2-lb sledgehammer to passing ¾", ½", and ¼", respectively. The splits were then sized using US standard sieves and a Gilson Silent Sifter sieve shaker.

Table 2 - 44 – Table 2 - 47 show the balanced mass, ash, and sulfur values for size classes within each split, while Figure 2 - 82 and Figure 2 - 83 depict the ash and sulfur values, respectively. The data shows relatively consistent ash values across size classes but suggests the sulfur partitions towards the finer classes. Table 2 - 48 – Table 2 - 51 show major metal content for the size classes of each split. Sulfur and major metal content were determined using a Niton XL2 Goldd XRF analyzer.

To further evaluate the potential for pyrite removal from the heap feed, the 1 x 0.15 mm size classes of the crushed splits were subjected to a density concentration at 2.95 SG. This laboratory process was selected to simulate a simple heavy mineral spiral. Figure 2 - 84 shows the float-sink separation of each crushed split. The sink portion has a very small yield. Table 2 - 52 – Table 2 - 54 provide the masses and sulfur content for the feed, float, and sink fractions. Due to the very small mass of the sink fraction, the mass and sulfur values for those fractions were back calculated based on the recovered float fraction mass and XRF readings. From the XRF readings and calculations, it appears that some pyrite can be further removed from the heap feed material at a high SG cut-point, depending on the desired amount of comminution applied to the heap feed material.

Table 2 - 44: Mass, ash, and sulfur content in size classes of CR-B-g

Uncrushed CR-B-g	Mass ret. (g)	Ash in Class (%)	Sulfur in Class (%)
Feed	629.29	79.97	3.62
+3/4"	136.73	86.87	1.51
3/4 x 1/2"	226.20	68.86	4.05
1/2 x 1/4"	149.29	86.41	3.94
1/4" x 1 mm	73.79	87.59	3.29
-1 mm	43.28	81.10	7.57

Table 2 - 45: Mass, ash, and sulfur content in size classes of CR-B-g crushed to minus 3/4"

Passing ¾” CR-B-g	Mass ret. (g)	Ash in Class (%)	Sulfur in Class (%)
Feed	634.52	82.80	3.53
3/4 x 1/2"	320.39	81.60	3.95
1/2 x 1/4"	194.15	84.22	2.12
1/4" x 1 mm	77.12	85.78	2.98
1 mm x 0.15 mm	27.96	79.54	7.18
- 0.15 mm	14.91	80.63	9.06

Table 2 - 46: Mass, ash, and sulfur content in size classes of CR-B-g crushed to minus 1/2"

Passing ½” CR-B-g	Mass ret. (g)	Ash in Class (%)	Sulfur in Class (%)
Feed	489.55	80.63	3.82
1/2 x 1/4"	302.64	79.69	3.35
1/4" x 1 mm	145.62	82.88	3.68
1 mm x 0.15 mm	29.02	79.88	7.16
- 0.15 mm	12.26	78.86	8.99

Table 2 - 47: Mass, ash, and sulfur content in size classes of CR-B-g crushed to minus 1/4"

Passing 1/4 CR-B-g	Mass ret. (g)	Ash in Class (%)	Sulfur in Class (%)
Feed	658.63	81.67	3.78
1/2 x 1/4"	192.84	81.93	3.84
1/4" x 1 mm	344.79	82.29	3.11
1 mm x 0.15 mm	93.62	79.56	5.08
- 0.15 mm	27.37	79.14	7.26

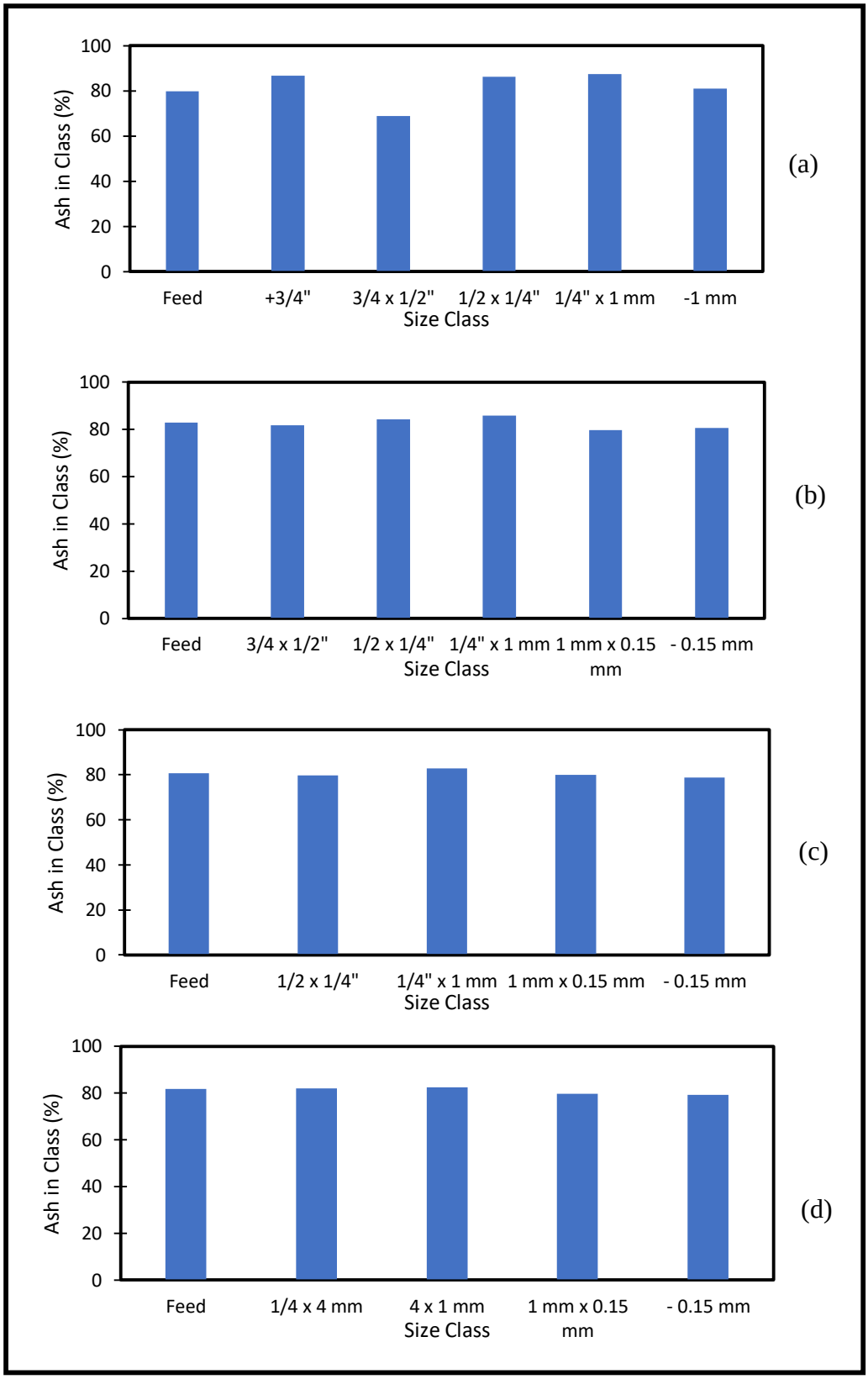

Figure 2 - 82: Ash distribution in splits of crushed CR-B-g: (a) uncrushed, (b) passing 3/4", (c) passing 1/2", (d) passing 1/4"

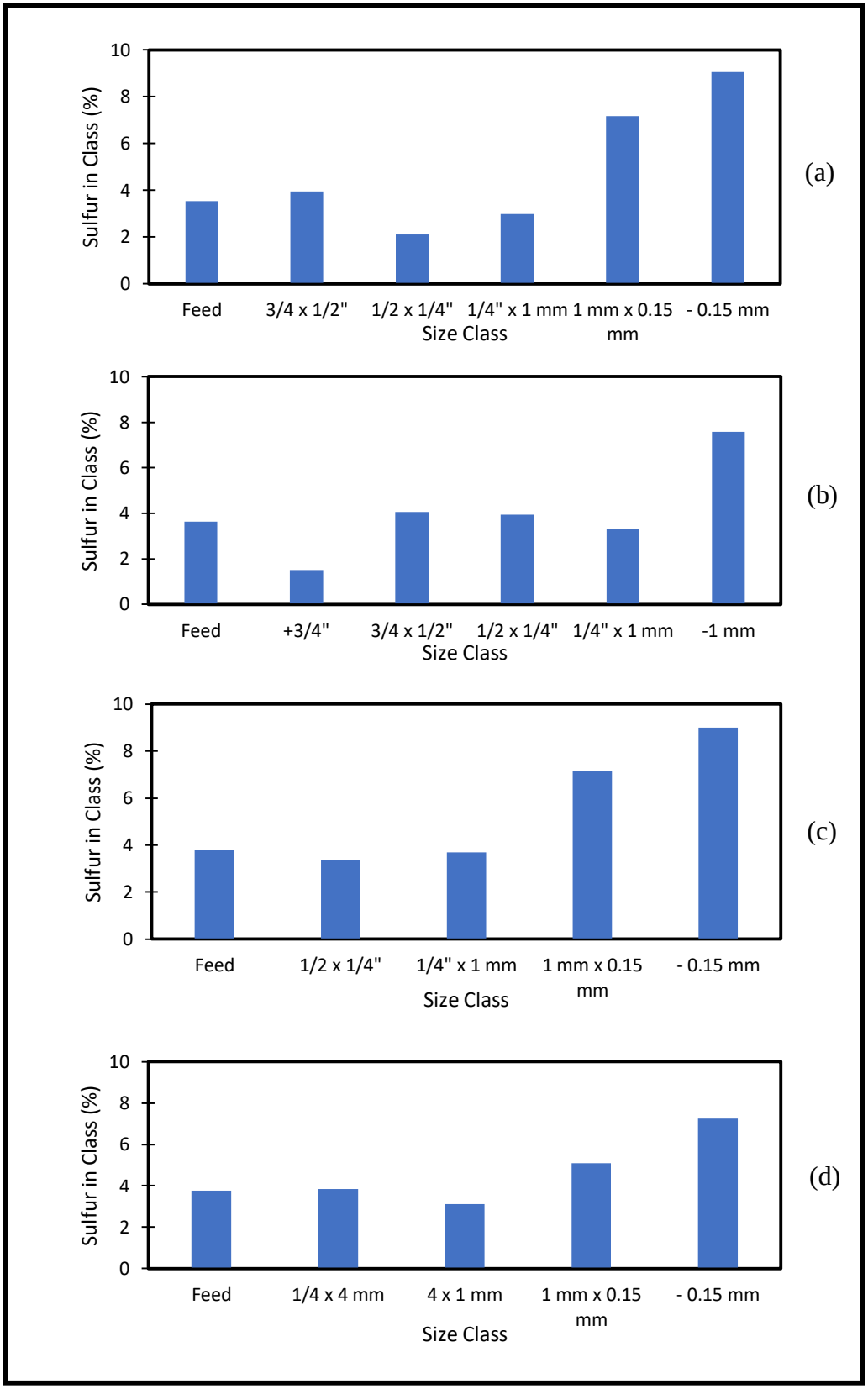

Figure 2 - 83: Sulfur distribution in splits of crushed CR-B-g: (a) uncrushed, (b) passing 3/4", (c) passing 1/2", (d) passing 1/4"

Table 2 - 48: Major metal content of uncrushed CR-B-g

Size Class	Fe (%)	Ti (%)	K (%)	Al (%)	Si (%)	Mg (%)	Ca (%)
+3/4	2.36	1.25	1.76	15.20	33.84	1.08	LOD
3/4x1/2	4.38	1.20	1.30	12.03	28.10	0.65	LOD
1/2x1/4	4.25	1.13	1.54	15.40	32.47	1.00	0.49
1/4x1mm	3.71	1.21	1.87	16.31	34.12	1.05	0.22
-1mm	7.32	0.95	1.67	13.31	26.55	1.13	1.30

Table 2 - 49: Major metal content of CR-B-g crushed to passing 3/4"

Size Class	Fe (%)	Ti (%)	K (%)	Al (%)	Si (%)	Mg (%)	Ca (%)
3/4 x 1/2"	5.46	1.10	1.43	13.98	30.05	0.85	0.81
1/2 x 1/4"	2.49	1.32	1.59	13.97	33.07	0.94	0.54
1/4" x 1 mm	3.35	1.24	1.73	14.69	32.56	0.88	0.40
1 mm x 0.15 mm	6.85	0.94	1.54	12.26	25.92	1.00	0.82
- 0.15 mm	7.75	0.84	1.56	10.68	22.82	0.78	1.91

Table 2 - 50: Major metal content of CR-B-g crushed to passing 1/2"

Size Class	Fe (%)	Ti (%)	K (%)	Al (%)	Si (%)	Mg (%)	Ca (%)
1/2 x 1/4"	6.00	1.10	1.37	14.88	30.46	0.82	0.07
1/4" x 1 mm	4.47	1.14	1.57	15.03	32.11	0.82	0.23
1 mm x 0.15 mm	6.89	0.99	1.52	13.30	27.21	0.95	0.64
- 0.15 mm	7.76	0.78	1.55	11.73	23.65	0.94	1.46

Table 2 - 51: Major metal content of CR-B-g crushed to passing 1/4"

Size Class	Fe (%)	Ti (%)	K (%)	Al (%)	Si (%)	Mg (%)	Ca (%)
1/4 x 4 mm	4.61	1.19	1.43	13.68	30.46	1.02	LOD
4 x 1 mm	4.20	1.16	1.44	13.47	30.25	0.65	0.14
1 mm x 0.15 mm	5.47	1.09	1.44	13.18	28.66	0.91	0.30
- 0.15 mm	6.35	0.94	1.46	11.77	25.36	0.79	0.86

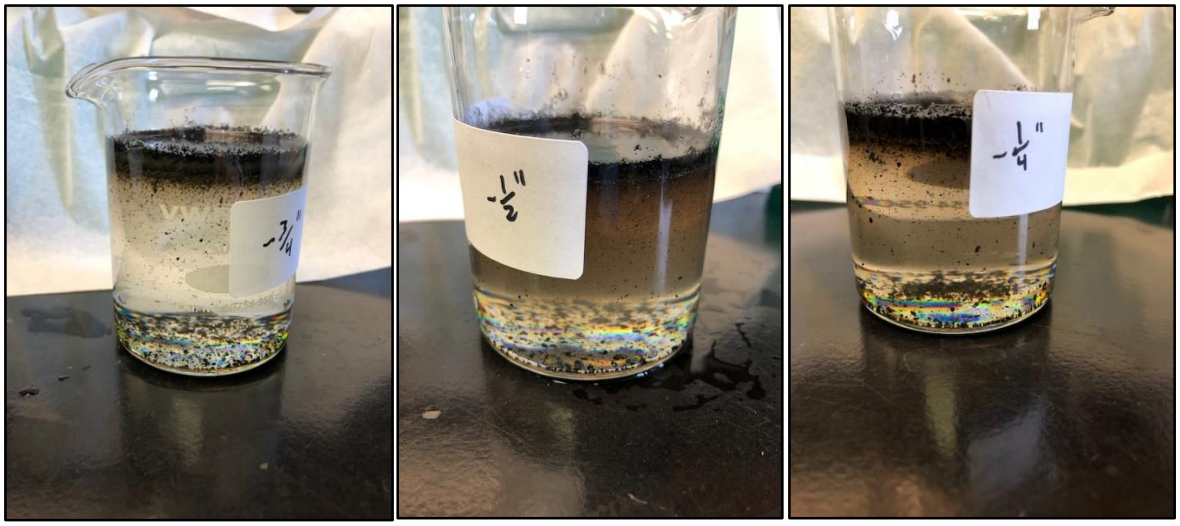

Figure 2 - 84: Density separations of 1x0.15 mm material from crushed CR-B-g samples at 2.95 S.G.

Table 2 - 52: Mass and sulfur content of feed, float, and sink fractions of 2.95 S.G. density separation (*calculated)

CR-B-g -3/4”	Mass (g)	S (%)
Feed	6.87	7.38
Float	6.62	4.35
Sink*	0.25	88.32

Table 2 - 53: Mass and sulfur content of feed, float, and sink fractions of 2.95 S.G. density separation (*calculated)

CR-B-g -1/2"	Mass (g)	S (%)
Feed	4.60	7.56
Float	4.13	3.95
Sink*	0.48	38.74

Table 2 - 54: Mass and sulfur content of feed, float, and sink fractions of 2.95 S.G. density separation (*calculated)

CR-B-g -1/4"	Mass (g)	S (%)
Feed	6.44	5.59
Float	6.08	3.84
Sink*	0.36	35.10

Task 3: Leaching

3.1 Small Column Leaching Tests

Leaching tests were performed using small, 4cm D x 30cm L, columns through which a volume of about 450 ml is recirculated. The general setup of the experiments is as shown in Figure 3 - 1. 650 grams of coal waste was used in each column and leachate was applied in the center of the column and distributed using a cloth to ensure even distribution of flow over the entire cross-section of the column. Table 3 - 1 provides the conditions for this series of small column leaching tests that are designed to determine the overall effects of ferric sulfate concentration, pH, and flowrate. The pH of each test was adjusted using sulfuric acid.

Table 3-1: Test parameter matrix for small column leaching tests

Test	Ferric Sulfate	Flowrate	pH
1	5 g/L	4.5 mL/hr	1.8
2	20 g/L	12 mL/hr	1.8
3	5 g/L	12 mL/hr	1.8
4	20 g/L	4.5 mL/hr	1.8
5	5 g/L	4.5 mL/hr	1.2
6	20 g/L	12 mL/hr	1.2
7	5 g/L	12 mL/hr	1.2
8	20 g/L	4.5 mL/hr	1.2

Figure 3 - 1: View of small column leaching test set up with mounted columns and associated pumps and tubing along with the solution reservoirs.

The results are presented in Table 3 - 2 and 3 - 3.

Table 3 – 2: Comparison of the concentration (ppm) of selected elements in the leached solution analysis from small column 14-day leaching tests based on the conditions in Table 3 - 1

Column	Sc	Y	La	Ce	Pr	Nd	Sm	Eu
1	1.26	4.81	1.38	4.80	0.66	3.45	1.12	0.30
2	2.08	4.27	1.36	4.09	0.54	2.68	0.94	0.23
3	1.20	5.20	1.63	5.64	0.79	4.16	1.35	0.35
4	0.93	2.60	0.80	2.55	0.32	1.43	0.54	0.14
5	0.26	1.03	0.21	0.70	0.11	0.53	0.21	0.04
6	0.24	0.94	0.21	0.69	0.09	0.40	0.15	0.03
7	0.86	3.29	0.74	2.71	0.51	2.03	0.86	0.15
8	0.69	2.67	0.47	1.86	1.67	3.46	2.54	0.12

Table 3 - 3: Comparison of the concentration (ppm) of selected elements (part 2) in the leached solution analysis from small column 14-day leaching tests based on the conditions in Table 3 - 1

Column	Gd	Tb	Dy	Ho	Er	Lu	Yb	Tm
1	1.69	0.23	1.46	0.23	0.64	0.07	0.54	0.08
2	1.19	0.18	0.96	0.20	0.46	0.07	0.35	0.05
3	2.00	0.30	1.69	0.28	0.73	0.08	0.61	0.09
4	0.71	0.11	0.75	0.11	0.36	0.03	0.25	0.04
5	0.23	0.03	0.22	0.03	0.09	0.01	0.05	0
6	0.19	0.03	0.27	0.03	0.08	0.01	0.06	0
7	0.72	0.11	0.95	0.12	0.53	0.04	0.25	0
8	0.66	0.09	2.10	0.10	2.22	0.03	0.21	0

The relative extraction percentages of the rare earth elements from columns 1-8 are presented in Figures 3 - 2 to 3 - 9.

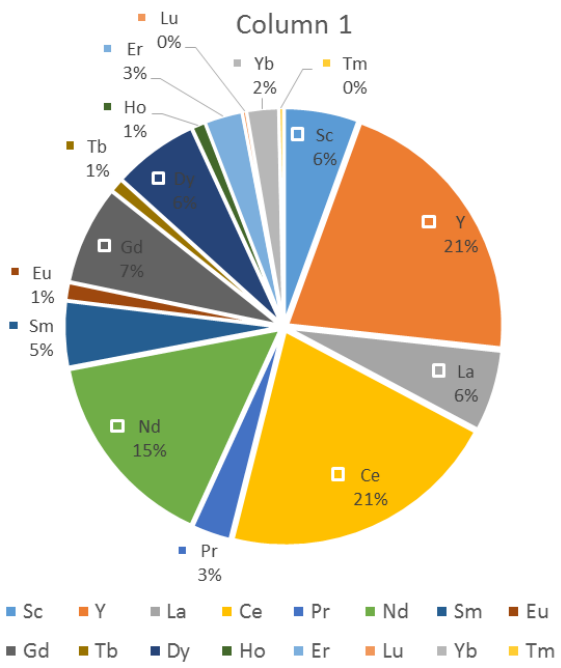

Figure 3 – 2: A pie chart showing % distribution of different rare earth elements (obtained after leaching in small columns) for small column 1.

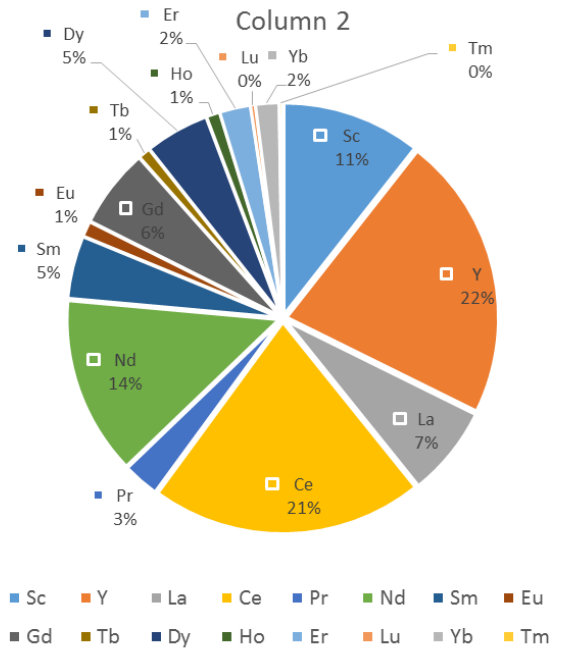

Figure 3 – 3: A pie chart showing % distribution of different rare earth elements (obtained after leaching in small columns) for small column 2.

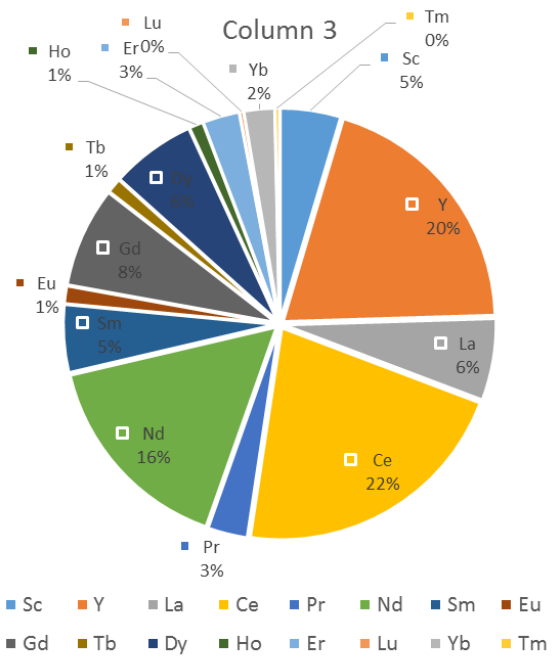

Figure 3 – 4: A pie chart showing % distribution of different rare earth elements (obtained after leaching in small columns) for small column 3.

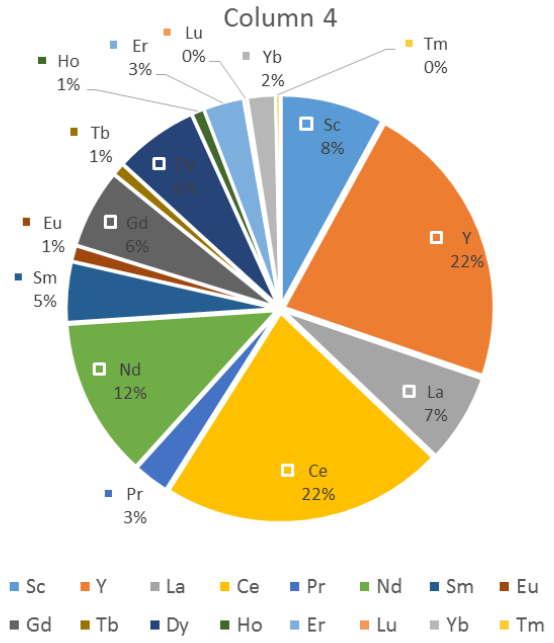

Figure 3 – 5: A pie chart showing % distribution of different rare earth elements (obtained after leaching in small columns) for small column 4.

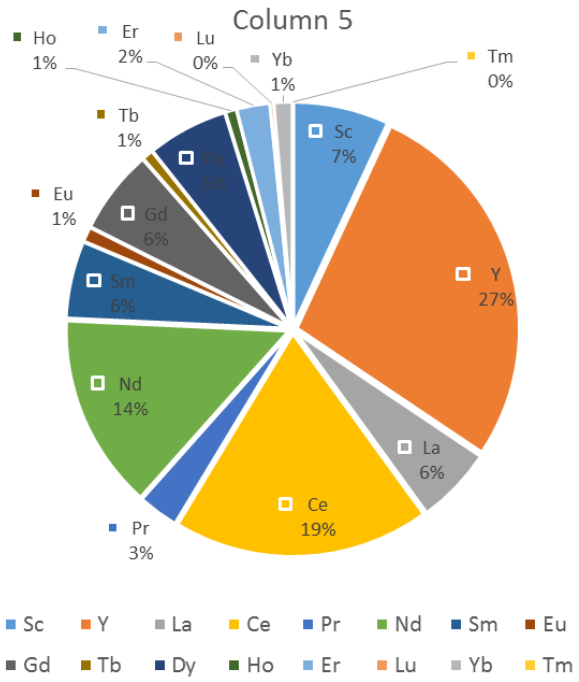

Figure 3 – 6: A pie chart showing % distribution of different rare earth elements (obtained after leaching in small columns) for small column 5.

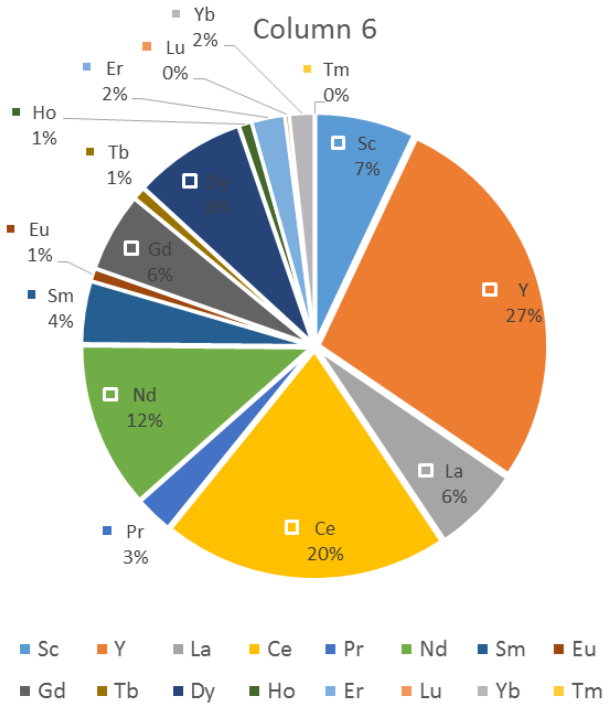

Figure 3 – 7: A pie chart showing % distribution of different rare earth elements (obtained after leaching in small columns) for small column 6.

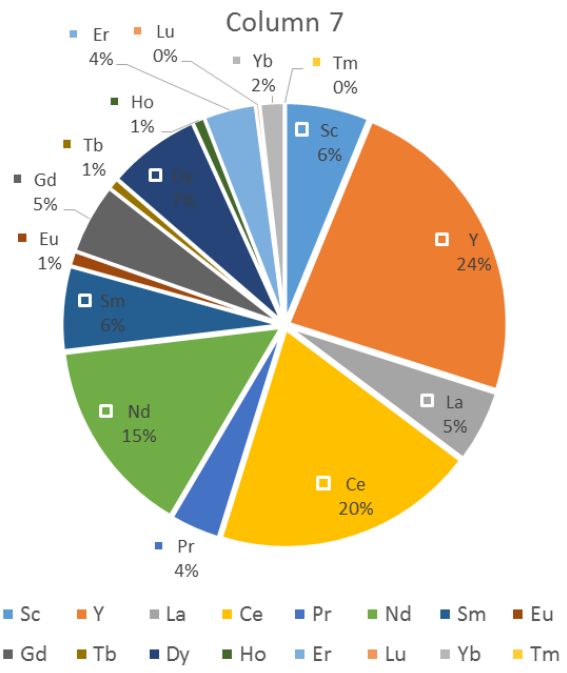

Figure 3 – 8: A pie chart showing % distribution of different rare earth elements (obtained after leaching in small columns) for small column 7.

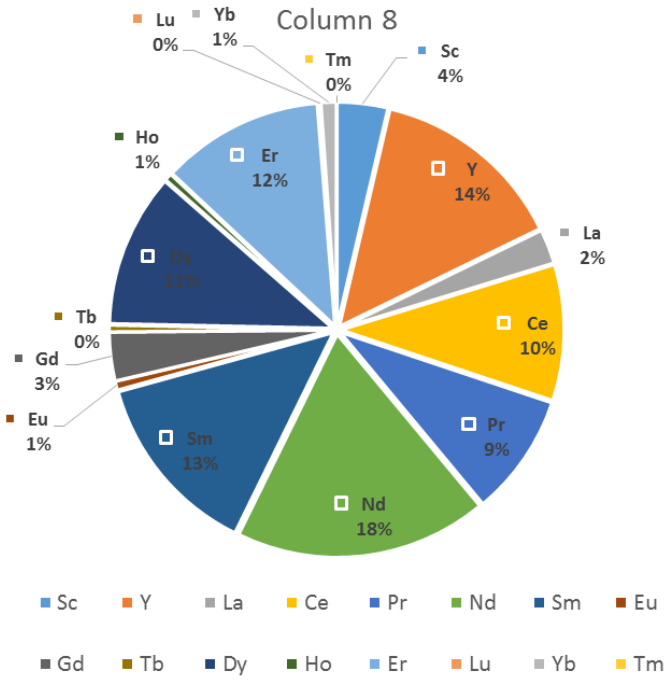

Figure 3 – 9: A pie chart showing % distribution of different rare earth elements (obtained after leaching in small columns) for small column 8.

The sum of the rare earth elements for the small column leaching tests is summarized in Table 3 - 4.

Table 3 – 4: Value of total rare earth element content in small column leaching solutions (ppm) after 14 days of leaching

Column	Total REE
1	21.31
2	17.44
3	24.73
4	10.66
5	3.48
6	3.16
7	12.97
8	18.17

The small column leaching tests were designed using a statistical design of experiments approach with a high and low level for three factors. The statistical design matrix is shown in Table 3 – 5.

Table 3 – 5: Comparison of relative weighting of factors (high = +, low = -) in factorial design analysis matrix for the small column experiments

Run	**A**	**B**	**C**	*AB*	*AC*	*BC*	*ABC*	**Observation**
1	-	-	-	+	+	+	-	$\mathbf{Y_1}$
2	+	-	-	-	-	+	+	$\mathbf{Y_2}$
3	-	+	-	-	+	-	+	$\mathbf{Y_3}$
4	+	+	-	+	-	-	-	$\mathbf{Y_4}$
5	-	-	+	+	-	-	+	$\mathbf{Y_5}$
6	+	-	+	-	+	-	-	$\mathbf{Y_6}$
7	-	+	+	-	-	+	-	$\mathbf{Y_7}$
8	+	+	+	+	+	+	+	$\mathbf{Y_8}$

In which factor A is the ferric sulfate concentration with high and low levels of 20 and 5 grams of ferric sulfate heptahydrate per liter of solution. Factor B is the flow rate with high and low flow rate levels of 12 and 4.5 ml/hour. Factor C is the pH with high and low levels of 1.8 and 1.2. The effects of AB, AC, BC, and ABC are the combinations of the factors. The analysis of the effects of each factor on the resulting extraction is performed using the following equations:

$$(A) = \frac{-Y_1 + Y_2 - Y_3 + Y_4 - Y_5 + Y_6 - Y_7 + Y_8}{4} \quad (1)$$

$$(B) = \frac{-Y_1 - Y_2 + Y_3 + Y_4 - Y_5 - Y_6 + Y_7 + Y_8}{4} \quad (2)$$

$$(C) = \frac{-Y_1 - Y_2 - Y_3 - Y_4 + Y_5 + Y_6 + Y_7 + Y_8}{4} \quad (3)$$

$$(AB) = \frac{+Y_1 - Y_2 - Y_3 + Y_4 + Y_5 - Y_6 - Y_7 + Y_8}{4} \quad (4)$$

$$(AC) = \frac{+Y_1 - Y_2 + Y_3 - Y_4 - Y_5 + Y_6 - Y_7 + Y_8}{4} \quad (5)$$

$$(BC) = \frac{+Y_1 + Y_2 - Y_3 - Y_4 - Y_5 - Y_6 + Y_7 + Y_8}{4} \quad (6)$$

$$(ABC) = \frac{-Y_1 + Y_2 + Y_3 - Y_4 + Y_5 - Y_6 - Y_7 + Y_8}{4} \quad (7)$$

$$mean = \frac{Y_1 + Y_2 + Y_3 + Y_4 + Y_5 + Y_6 + Y_7 + Y_8}{8} \quad (8)$$

Using these equations to analyze the data from the small columns leads to the following analysis of the effects of the factors.

Table 3 – 6: Comparison of factors and outcome result effects for the small column test data shown in Tables 3 - 4 and 3 - 5

Factor	Effect
A (Fe3+)	-3.26
B (flow rate)	5.29
C (pH)	-9.09
AB	-1.17
AC	5.70
BC	6.97
ABC	3.93
Mean	13.99

Positive values in Table 3 – 6 indicate that increasing the value had a positive effect on rare earth elements extraction. Conversely, negative values in Table 3 – 6 indicate that increasing the value had a negative effect on rare earth elements extraction. The magnitude of the value indicates the magnitude of the effect on the extraction. Thus, the conclusion is that the increased ferric ion concentration had a small negative effect on the extraction, increasing flow rate had a modest positive effect on extraction, increasing pH had a negative effect on extraction, the combination of ferric ion concentration and flow rate had no significant effect, increasing both ferric ion concentration and pH had a positive effect, increasing flow rate and pH had a positive effect, and increasing all three parameters had a very small positive impact.

Based on the information from the small column leaching tests, conditions for large (8-inch diameter, 5 ft tall) columns were determined.

3.2 Large column leaching tests

The PIs and team performed large column leaching tests. Four columns were simultaneously leached using different operating conditions. Each column was approximately 6 ft. tall and 8 inches in diameter. Each column was filled with ~ 50 kg of CR-D1 crushed sample. The bottom portion of the column was filled with glass frit (up to 3 inch of column length) in order to hold the coal waste and to allow uniform circulation of leaching solution without any settling and associated collection problems near the bottom. The flow rate of leaching solution was ~ 500 ml/day. The upper portion (~ 8 inch from top) of the column was also kept unfilled. A fabric filter was also placed to keep the coal refuse samples intact in the center portion. The schematic diagrams of the columns as well as images of actual columns and supply vessels are shown in Figures 3 - 10 and 3 - 11. Altogether four large columns were leached and the details of these columns are as follows:

1. Column 1: Bacterial leaching solution prepared using 9k medium was circulated continuously. In this case solution is collected, biooxidized in an air-sparged bioreactor with a 4-day residence time at 35^{o}C, then sent back again for leaching. Initial Eh of solution was ~ 680 mV and after 20 days it was ~ 480 mV (see Figure 3). The drop in Eh reflects the low level of ferric ions in the solution due to reduction of ferric ions during column leaching and subsequent precipitation. Figure 3 - 12 shows the Eh reduction trend with respect to time.

2. Column 2: In this column also, bacterial leaching solution prepared using 9k medium in an air-sparged bioreactor with a 4-day residence time at 35^{o}C that was fed to the leaching column. However, in this case the solution is not recycled to the column. In this case after circulation through column, the solution is collected in one vessel. The feed solution was maintained at a pH of 1.5.

3. Column 3: In this column bacterial leaching solution was used from an air-sparged bioreactor with a 4-day residence time at 35^{o}C that was fed a pyrite enriched solids feed material. The pyrite allowed the bacteria to generate acid for leaching so no acid

supplement was needed. The solution fed to the bioreactor had constituents listed in Table 3 - 7.

Table 3 - 7: details of the bacterial leaching solution

Name of the salt/species	Concentration
Potassium Sulfate	0.88 g/l
Ammonium Sulfate	0.9 g/l
Potassium Phosphate	0.25 g/l
Magnesium Sulfate	0.5 g/l
Pyrite from Mine sites	100 g/l
Sulfuric Acid	Added up to pH 1.5

4. Column 4: In this column 20g/l ferric sulfate solution was recirculated. In this case no 9k media was used. In order to adjust Eh, hydrogen peroxide was used. Initial Eh was ~ 600 mV and pH was ~ 1.5. pH was maintained through sulfuric acid addition. This is a control test for the chemical oxidation and leaching without bacteria. Hydrogen peroxide was added throughout the test to maintain the solution at approximately 600 mV with respect to a silver/silver chloride reference Redox electrode.

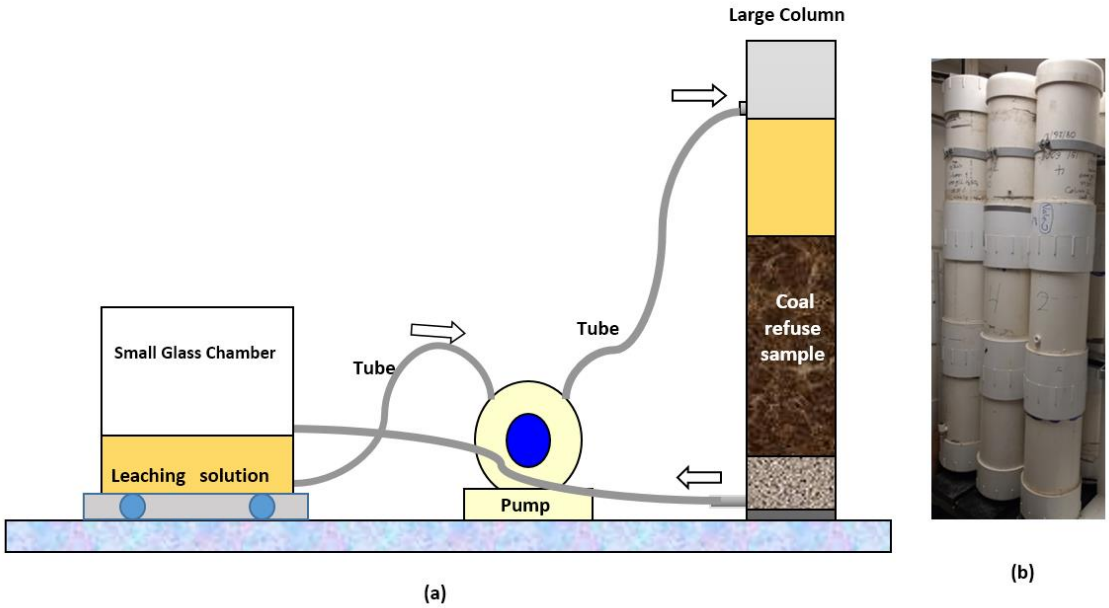

Figure 3 - 10: A schematic diagram showing leaching of coal waste using the large column (a); and (b) picture of actual columns used for leaching. In this case leaching solution is continuously recycled through column as used for Column 1.

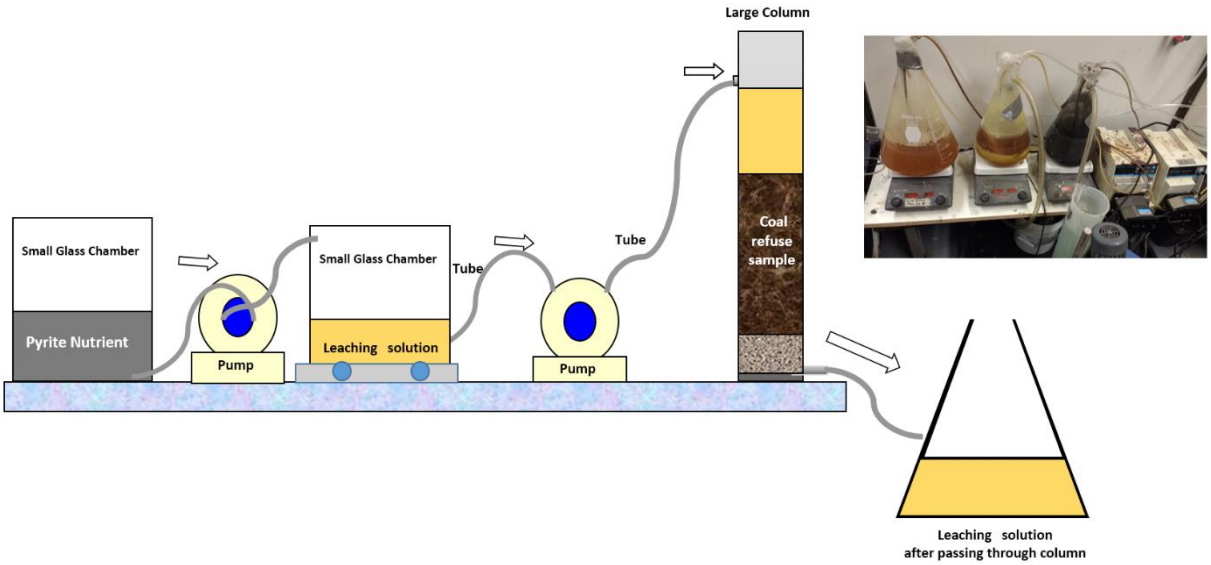

Figure 3 - 11: A schematic diagram showing leaching of coal waste using the large column following the scenario for Column 3.

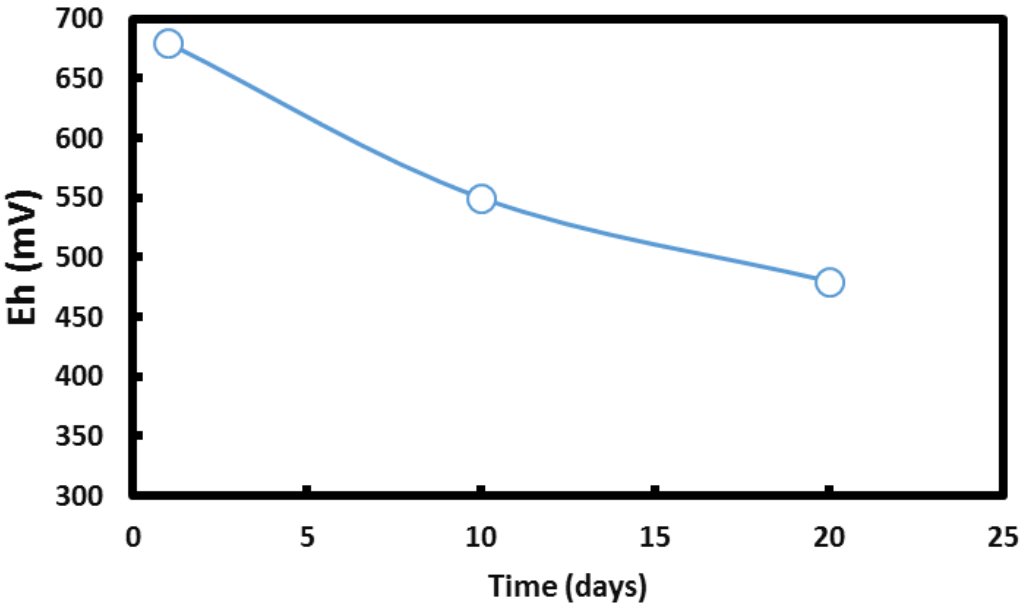

Figure 3 - 12: Eh vs. time graph for the solution that was used in continuously recycling large column test.

Tables 3 - 8 and 3 - 9 show the results from the first two weeks of leaching in the large columns.

Table 3 - 8: Comparison of the concentration (ppm) of selected elements in the leached solution analysis from large column leaching tests after two weeks of leaching based on the conditions described in the beginning of this section

Column	Sc	Y	La	Ce	Pr	Nd	Sm	Eu
1	3.98	10.6	1.50	5.75	0.80	4.27	1.69	0.45
2	2.20	6.56	1.05	3.92	0.60	3.34	1.22	0.32
3	0.78	3.05	0.48	1.93	0.30	1.67	0.61	0.15
4	0.50	1.61	0.37	1.33	0.20	1.06	0.36	0.11

Table 3 - 9: Comparison of the concentration (ppm) of selected elements (part 2) in the leached solution analysis from large column leaching tests after two weeks of leaching based on the conditions described in the beginning of this section

Column	Gd	Tb	Dy	Ho	Er	Lu	Yb	Tm
1	2.44	0.44	2.58	0.45	1.24	0.15	1.09	0.16
2	1.65	0.28	1.54	0.29	0.81	0.12	0.71	0.11
3	0.89	0.15	0.82	0.16	0.43	0.07	0.39	0.06
4	0.56	0.10	0.50	0.09	0.27	0.04	0.24	0.04

The relative percentages of the individual rare earth elements are presented in Figures 3 - 13 to 3 - 16.

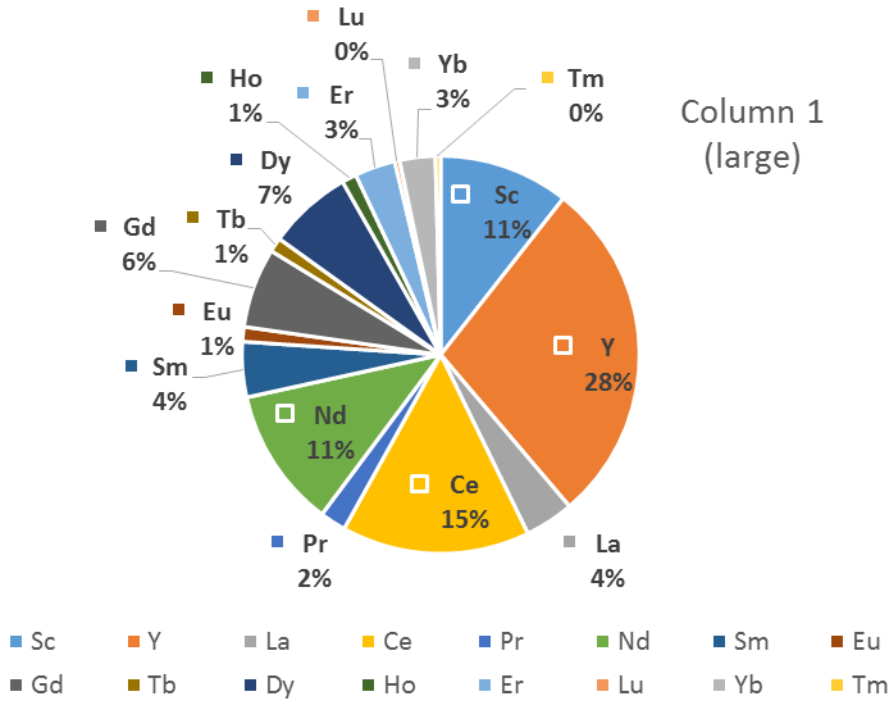

Figure 3 - 13: A pie chart showing % distribution of different rare earth elements obtained after leaching in large column 1 for two weeks.

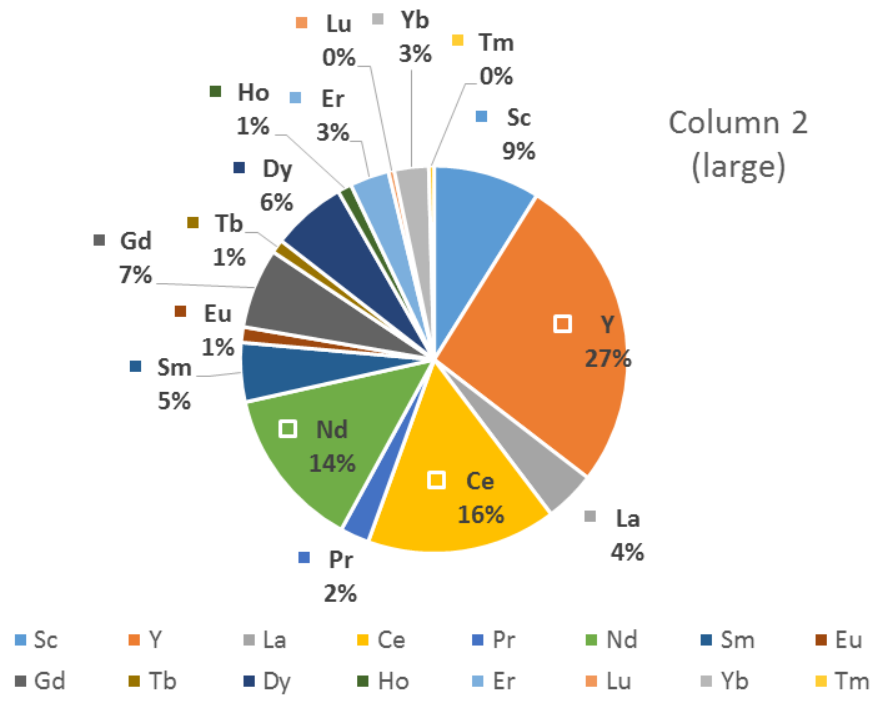

Figure 3 - 14: A pie chart showing % distribution of different rare earth elements obtained after leaching in large column 2 for two weeks.

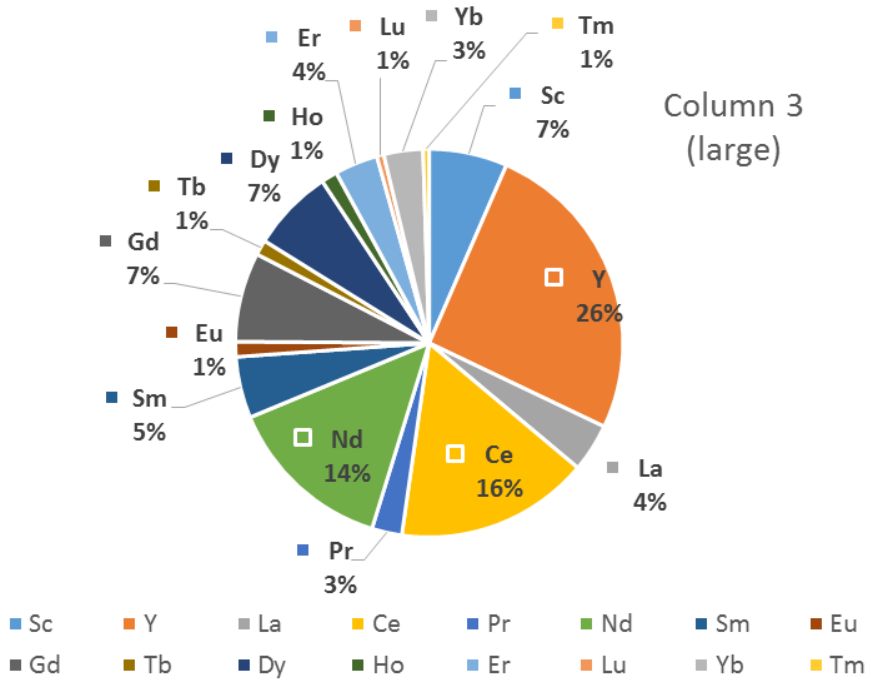

Figure 3 - 15: A pie chart showing % distribution of different rare earth elements obtained after leaching in large column 3 for two weeks.

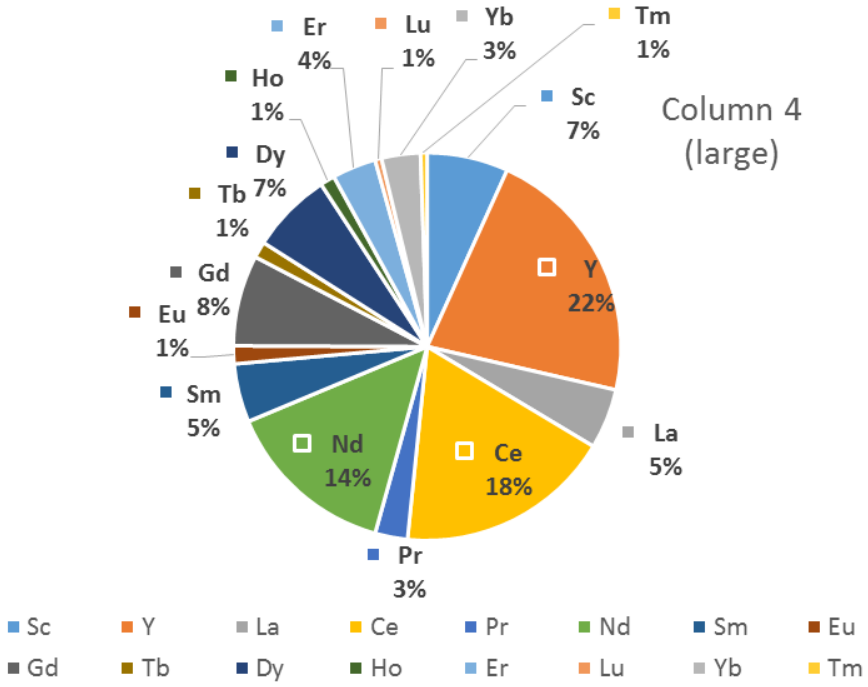

Figure 3 - 16: A pie chart showing % distribution of different rare earth elements obtained after leaching in large column 4 for two weeks.

The relative distribution of REEs in the column leaching solutions after approximately 90 days is presented in Figures 3 - 17 to 3 - 20. It is important to note that scandium, which is the most economically important of the elements to be recovered is leached into solution in proportions that are at least as high as the baseline concentration proportion. In other words, scandium is leached at least as well as or better than the other elements evaluated. Other more valuable REEs such as Y, Nb, and Dy are also leached as well as or better than other REEs.

The cumulative total of REEs extracted from the coal waste as a function of time for the large columns 1-4 are presented in Figures 3 - 21 to 3 - 36. It should be noted that due to the recirculation of solution through Columns 1 and 4, the accumulation of leached iron caused some precipitation to occur, which also seems to correlate with reduced available REEs in solution in Columns 1 and 4. Due to the precipitation in these columns, fresh solutions were periodically introduced in order minimize precipitation and the loss of REEs in solution. Columns 2 and 3 are more representative of biooxidation enhanced leaching. Column 2 had iron sulfate added to feed solution to help grow bacteria and generate ferric ions and acid for leaching in a separate reactor that had a residence time of approximately 4 days before the solution was added to the large column for leaching. Column 3 had pyrite enriched (7 % pyrite) coal waste to provide a low-cost, readily available material for feeding bacteria to allow them to produce ferric ions and acid for leaching. The pyrite enriched waste was biooxidized in a separate reactor with a residence time of approximately 4 days prior to feeding the resulting slurry to the large column (3). Column 3 is the most representative column for commercial implementation of this process because the pyrite

is readily available in most coal operations, and its use as a bioreactor feed material for acid and ferric ion generation for leaching also mitigates subsequent acid mine drainage by removing the sulfide through biooxidation.

The overall accumulation of REEs in leaching solutions approaches an overall recovery of around 10 % after 90 days.

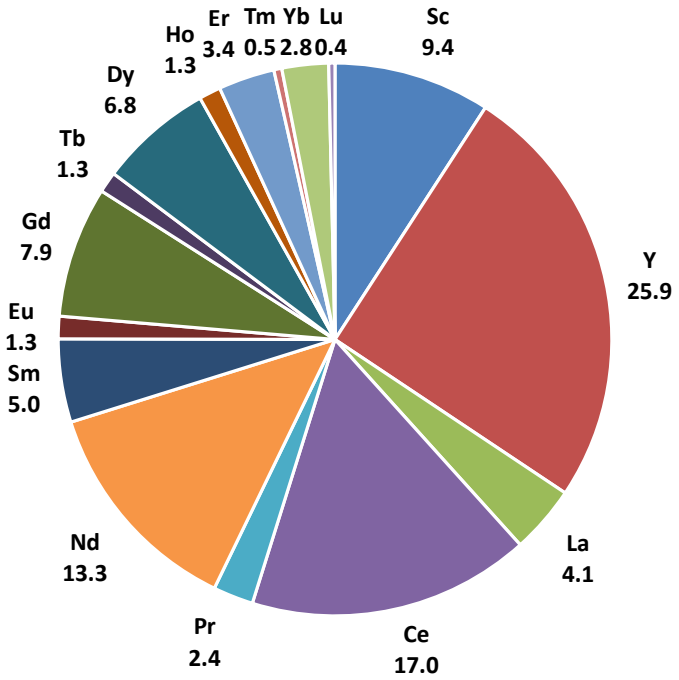

Figure 3 - 17: A pie chart showing the cumulative distribution (%) of different rare earth elements obtained after leaching in large column 1 at the end of 90 days.

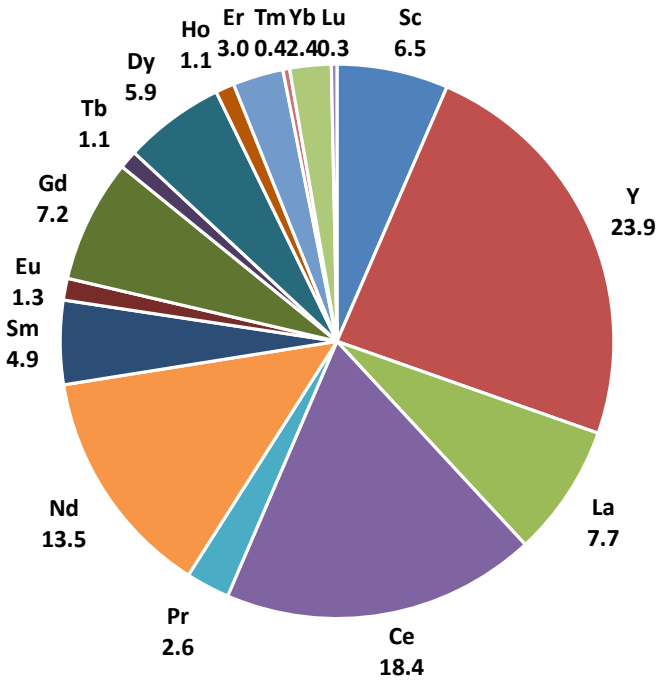

Figure 3 - 18: - A pie chart showing the cumulative distribution (%) of different rare earth elements obtained after leaching in large column 2 at the end of 90 days.

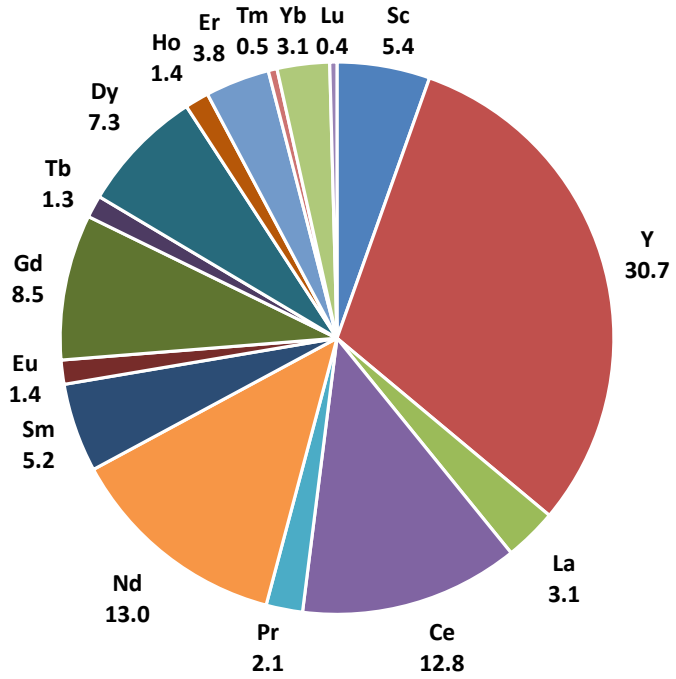

Figure 3 - 19: A pie chart showing the cumulative distribution (%) of different rare earth elements obtained after leaching in large column 3 at the end of 90 days.

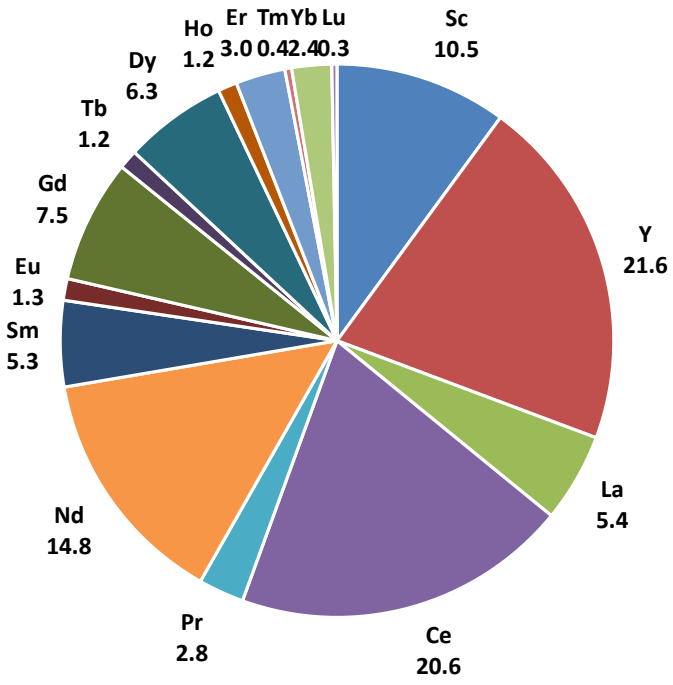

Figure 3 - 20: A pie chart showing the cumulative distribution (%) of different rare earth elements obtained after leaching in large column 4 at the end of 84 days.

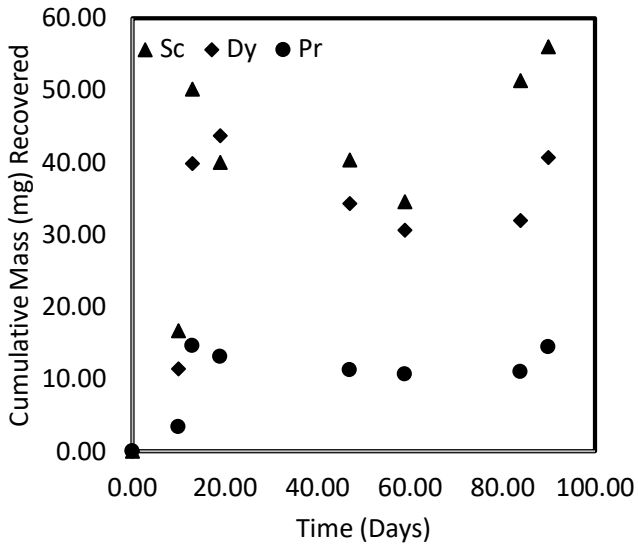

Figure 3 - 21: Column 1 leaching data in terms of cumulative mass recovered in leaching solution versus time for the elements shown based on leaching solution analysis. Note that between 13 and 84 days there was some precipitation of species that removed some of the REEs from the recovered solution. After 84 days a fresh solution was prepared and the recovered mass increased.

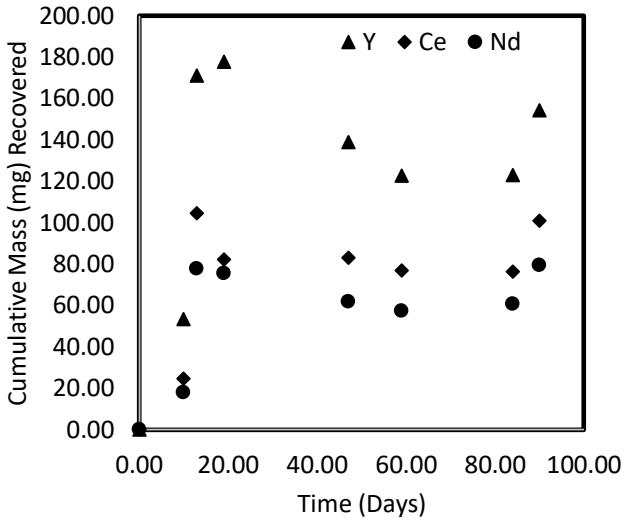

Figure 3 - 22: Column 1 leaching data in terms of cumulative mass recovered in leaching solution versus time for the elements shown based on leaching solution analysis. Note that between 13 and 84 days there was some precipitation of species that removed some of the REEs from the recovered solution. After 84 days a fresh solution was prepared and the recovered mass increased.

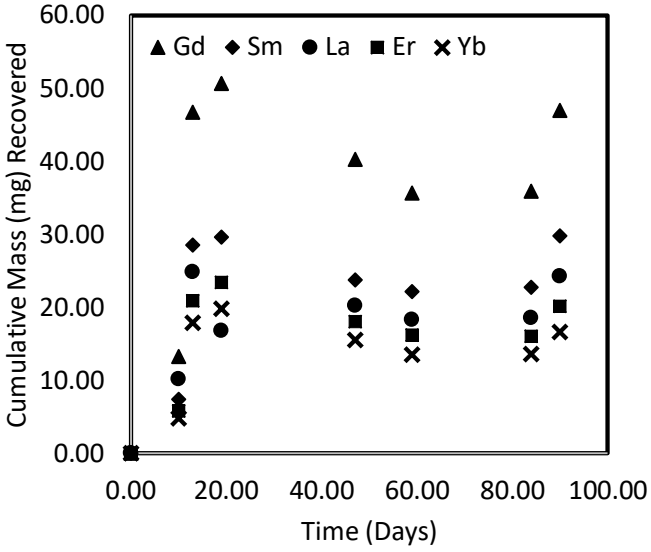

Figure 3 - 23: Column 1 leaching data in terms of cumulative mass recovered in leaching solution versus time for the elements shown based on leaching solution analysis. Note that between 13 and 84 days there was some precipitation of species that removed some of the REEs from the recovered solution. After 84 days a fresh solution was prepared and the recovered mass increased.

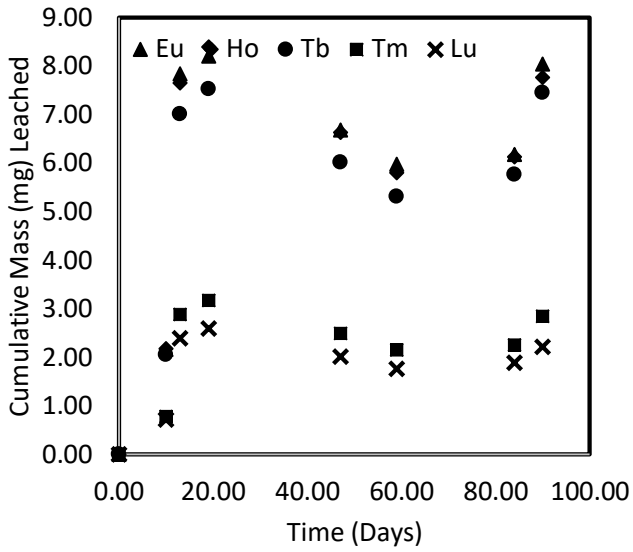

Figure 3 - 24: Column 1 leaching data in terms of cumulative mass recovered in leaching solution versus time for the elements shown based on leaching solution analysis. Note that between 13 and 84 days there was some precipitation of species that removed some of the REEs from the recovered solution. After 84 days a fresh solution was prepared and the recovered mass increased.

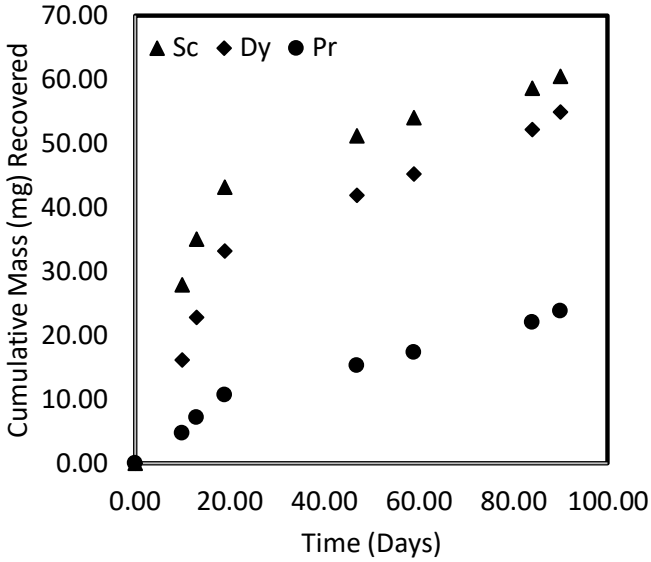

Figure 3 - 25: Column 2 leaching data in terms of cumulative mass recovered in leaching solution versus time for the elements shown based on leaching solution analysis.

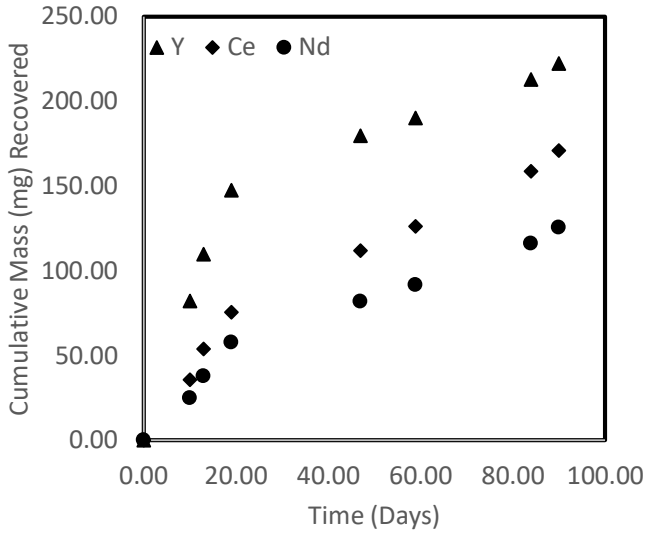

Figure 3 - 26: Column 2 leaching data in terms of cumulative mass recovered in leaching solution versus time for the elements shown based on leaching solution analysis.

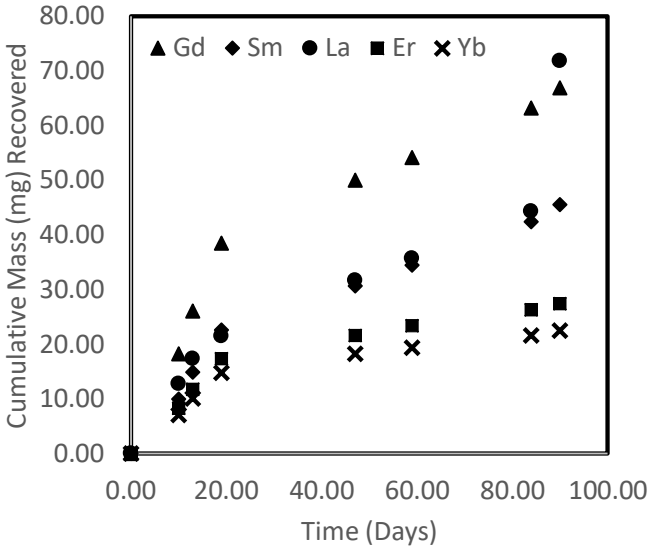

Figure 3 - 27: Column 2 leaching data in terms of cumulative mass recovered in leaching solution versus time for the elements shown based on leaching solution analysis.

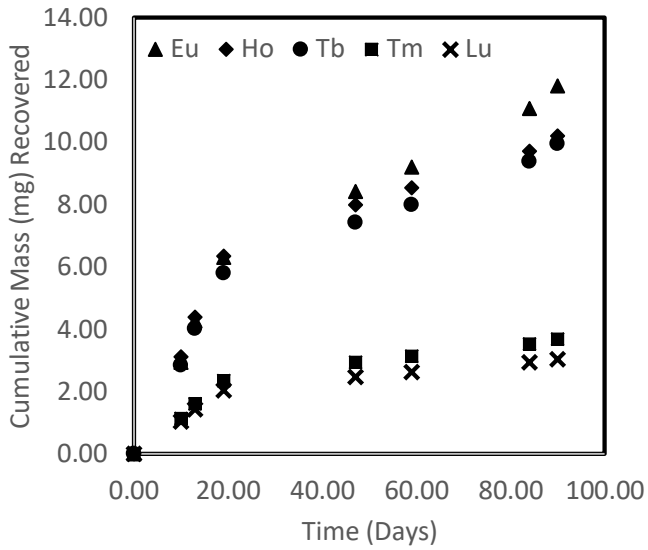

Figure 3 - 28: Column 2 leaching data in terms of cumulative mass recovered in leaching solution versus time for the elements shown based on leaching solution analysis.

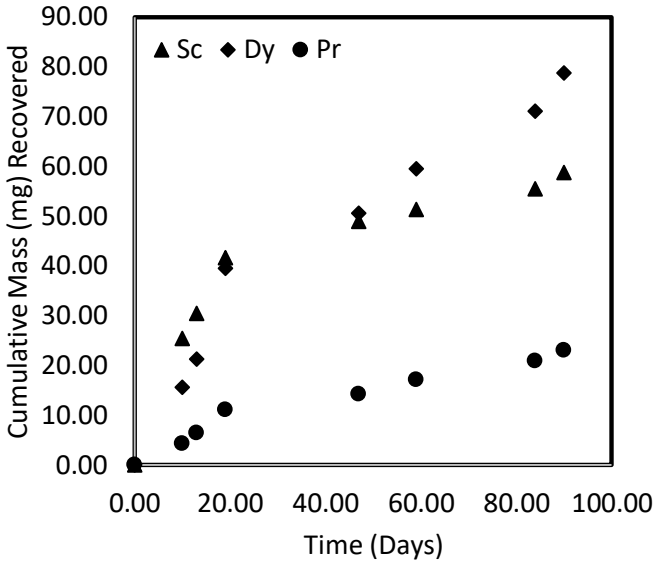

Figure 3 - 29: Column 3 leaching data in terms of cumulative mass recovered in leaching solution versus time for the elements shown based on leaching solution analysis.

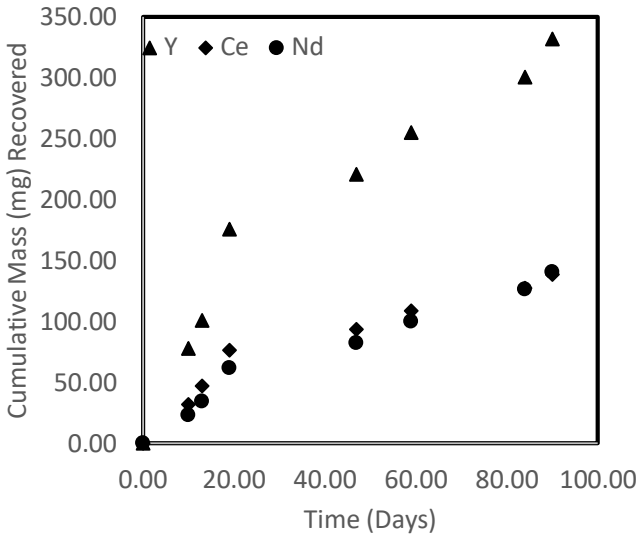

Figure 3 - 30: Column 3 leaching data in terms of cumulative mass recovered in leaching solution versus time for the elements shown based on leaching solution analysis.

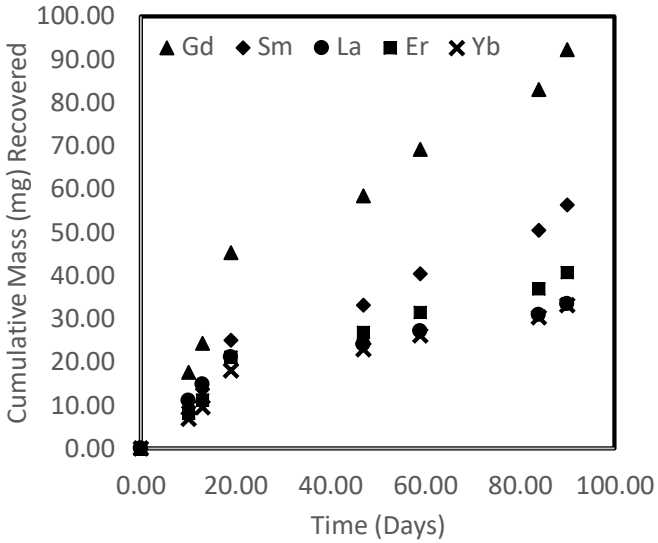

Figure 3 - 31: Column 3 leaching data in terms of cumulative mass recovered in leaching solution versus time for the elements shown based on leaching solution analysis.

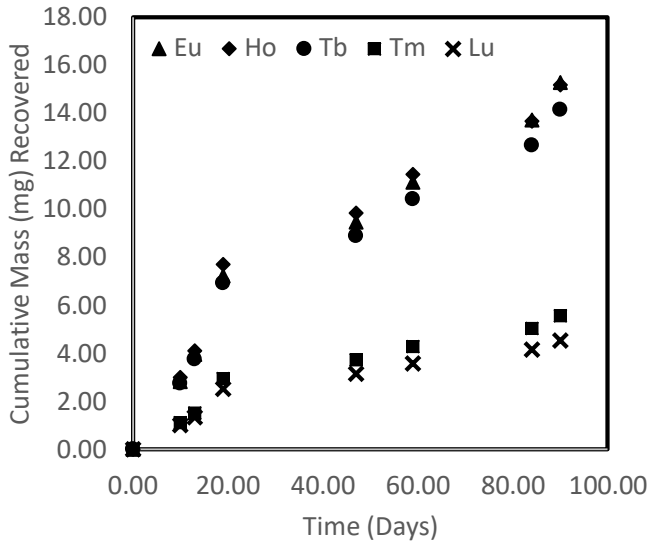

Figure 3 - 32: Column 3 leaching data in terms of cumulative mass recovered in leaching solution versus time for the elements shown based on leaching solution analysis.

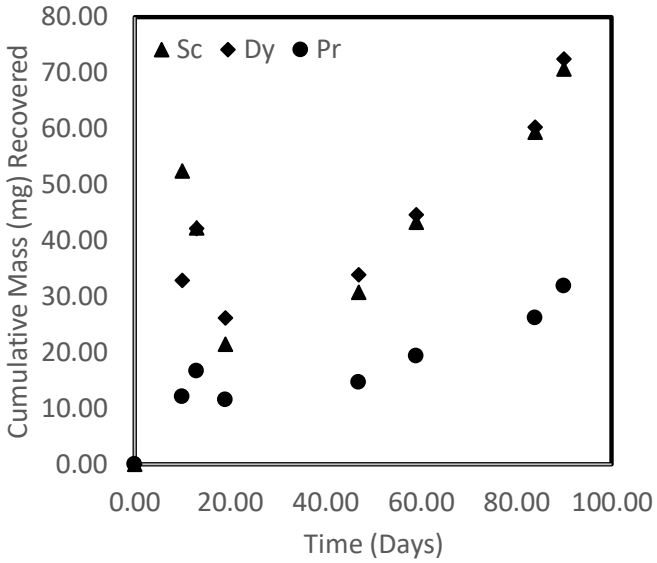

Figure 3 - 33: Column 4 leaching data in terms of cumulative mass recovered in leaching solution versus time for the elements shown based on leaching solution analysis.

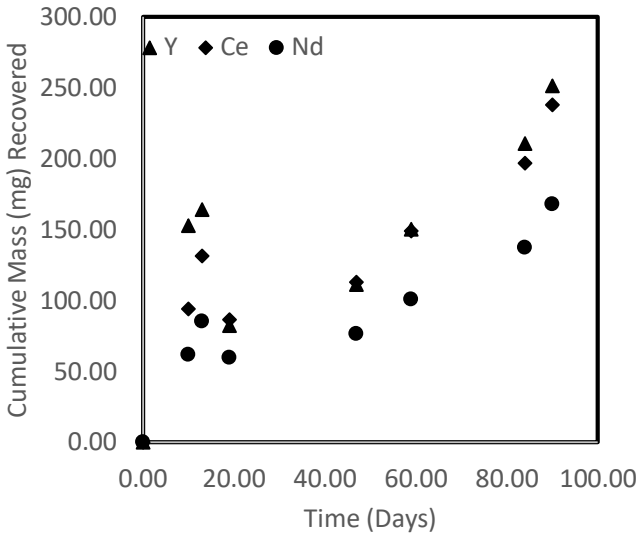

Figure 3 - 34: Column 4 leaching data in terms of cumulative mass recovered in leaching solution versus time for the elements shown based on leaching solution analysis.

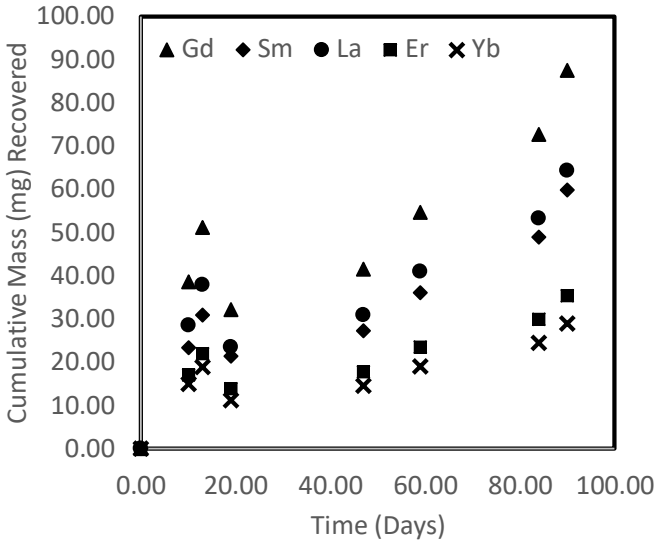

Figure 3 - 35: Column 4 leaching data in terms of cumulative mass recovered in leaching solution versus time for the elements shown based on leaching solution analysis.

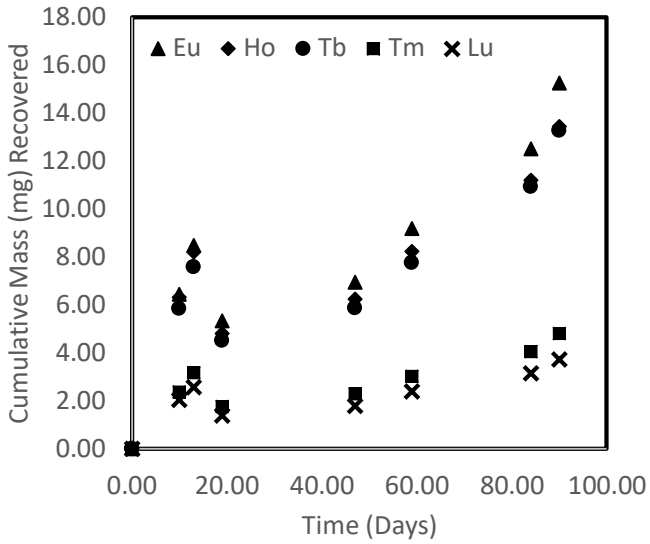

Figure 3 - 36: Column 4 leaching data in terms of cumulative mass recovered in leaching solution versus time for the elements shown based on leaching solution analysis.

The large columns were leached for approximately 120 days. After leaching the columns were disassembled and samples were split from the middle of the columns for analysis. Tables 3 - 10 to 3-13 show the results from the analysis of the solid samples for the feed material as well as the final leached material residue, and the associated values of recovery or consumption are shown.

Table 3 - 10: Column 1 ICP-MS analysis data of solids before and after leaching for 120 days

Element	Feed ppm	Column 1 final ppm	Column 1 (% Extracted)
Aluminum	13800	8570	37.9
Barium	244	155	36.5
Calcium	2750	2980	-8.4
Cerium	60.1	31.6	47.4
Cesium	4.32	2.76	36.1
Chromium	29	18.9	34.8
Cobalt	17.6	11.1	36.9
Dysprosium	4.42	3.14	29.0
Gadolinium	3.55	4.84	-36.3
Gallium	35	23.2	33.7
Iron	41000	34400	16.1
Lanthanum	27.4	14.3	47.8
Lithium	41.9	29.4	29.8
Magnesium	6170	5040	18.3
Manganese	1020	537	47.4
Neodymium	32.9	17	48.3
Potassium	4470	3060	31.5
Praseodymiu	7.33	4.85	33.8
Rubidium	32.3	23.5	27.2
Samarium	6.81	4.98	26.9
Scandium	5.05	5.74	-13.7
Titanium	76.5	31.9	58.3
Vanadium	27.3	18.4	32.6
Yttrium	16.8	11.8	29.8
Zirconium	16.2	9.76	39.8

Table 3 - 11: Column 2 ICP-MS analysis data of solids before and after leaching for 120 days.

Element	Feed ppm	Column 2 Final ppm	Column 2 (% Extracted)
Aluminum	13800	7680	44.3
Barium	244	173	29.1
Calcium	2750	2410	12.4
Cerium	60.1	37.7	37.3
Cesium	4.32	2.75	36.3
Chromium	29	14.1	51.4
Cobalt	17.6	6.07	65.5
Dysprosium	4.42	2.5	43.4
Gadolinium	3.55	3.42	3.7
Gallium	35	25.8	26.3
Iron	41000	22500	45.1
Lanthanum	27.4	16.4	40.1
Lithium	41.9	24.5	41.5
Magnesium	6170	3060	50.4
Manganese	1020	144	85.9
Neodymium	32.9	21.3	35.3
Potassium	4470	3680	17.7
Praseodymium	7.33	5.16	29.6
Rubidium	32.3	24.7	23.5
Samarium	6.81	2.76	59.5
Scandium	5.05	2.5	50.5
Titanium	76.5	61	20.3
Vanadium	27.3	11.2	59.0
Yttrium	16.8	8.12	51.7
Zirconium	16.2	9.1	43.8

Table 3 - 12: Column 3 ICP-MS analysis data of solids before and after leaching for 120 days.

Element	Feed ppm	Column 3 Final ppm	Column 3 (% Extracted)
Aluminum	13800	7010	49.2
Barium	244	120	50.8
Calcium	2750	2730	0.7
Cerium	60.1	35.8	40.4
Cesium	4.32	2.7	37.5
Chromium	29	12.1	58.3
Cobalt	17.6	8.54	51.5
Dysprosium	4.42	2.5	43.4
Gadolinium	3.55	2.5	29.6
Gallium	35	16.7	52.3
Iron	41000	16600	59.5
Lanthanum	27.4	15.3	44.2
Lithium	41.9	21.8	48.0
Magnesium	6170	2540	58.8
Manganese	1020	159	84.4
Neodymium	32.9	19	42.2
Potassium	4470	3820	14.5
Praseodymium	7.33	4.6	37.2
Rubidium	32.3	26.4	18.3
Samarium	6.81	4.74	30.4
Scandium	5.05	2.5	50.5
Titanium	76.5	54.3	29.0
Vanadium	27.3	12	56.0
Yttrium	16.8	8.63	48.6
Zirconium	16.2	12	25.9

Table 3 - 13: Column 4 ICP-MS analysis data of solids before and after leaching for 120 days.

Element	Feed ppm	Column 4 Final ppm	Column 4 (% Extracted)
Aluminum	13800	8580	37.8
Barium	244	119	51.2
Calcium	2750	1930	29.8
Cerium	60.1	44.2	26.5
Cesium	4.32	2.75	36.3
Chromium	29	14.8	49.0
Cobalt	17.6	11.5	34.7
Dysprosium	4.42	3.13	29.2
Gadolinium	3.55	3.78	-6.5
Gallium	35	16.5	52.9
Iron	41000	17900	56.3
Lanthanum	27.4	18.6	32.1
Lithium	41.9	32.4	22.7
Magnesium	6170	3680	40.4
Manganese	1020	222	78.2
Neodymium	32.9	22.6	31.3
Potassium	4470	3820	14.5
Praseodymium	7.33	5.46	25.5
Rubidium	32.3	25.5	21.1
Samarium	6.81	4.83	29.1
Scandium	5.05	3.41	32.5
Titanium	76.5	33.2	56.6
Vanadium	27.3	14.5	46.9
Yttrium	16.8	10.9	35.1
Zirconium	16.2	11.8	27.2

The recoveries as a function of time for Columns 1-4 for selected elements are presented in Figures 3 - 37 to 3 - 48.

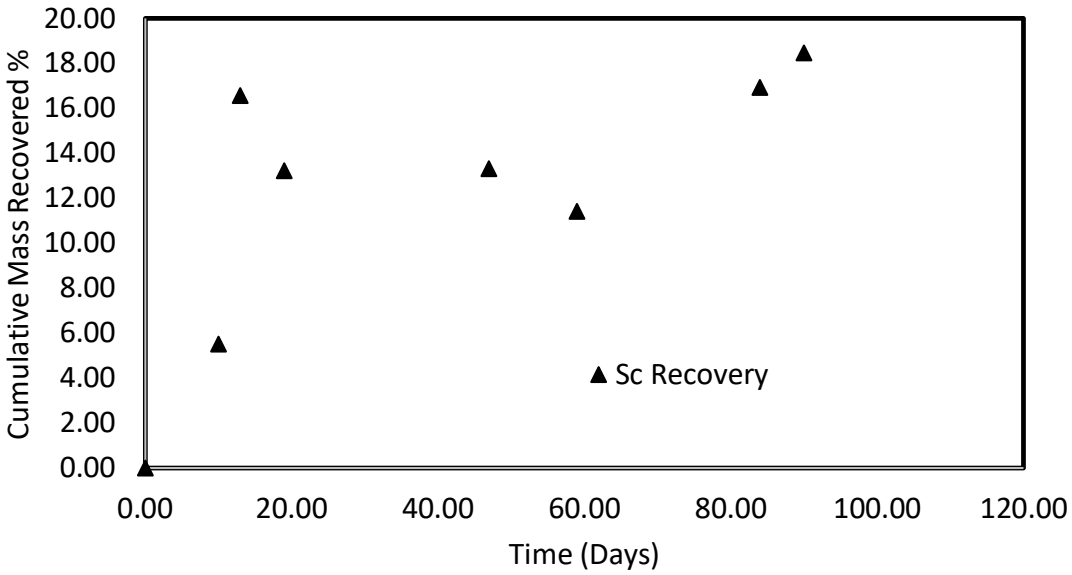

Figure 3 - 37: Comparison of solution based recovery as a function of time for scandium from Column 1.

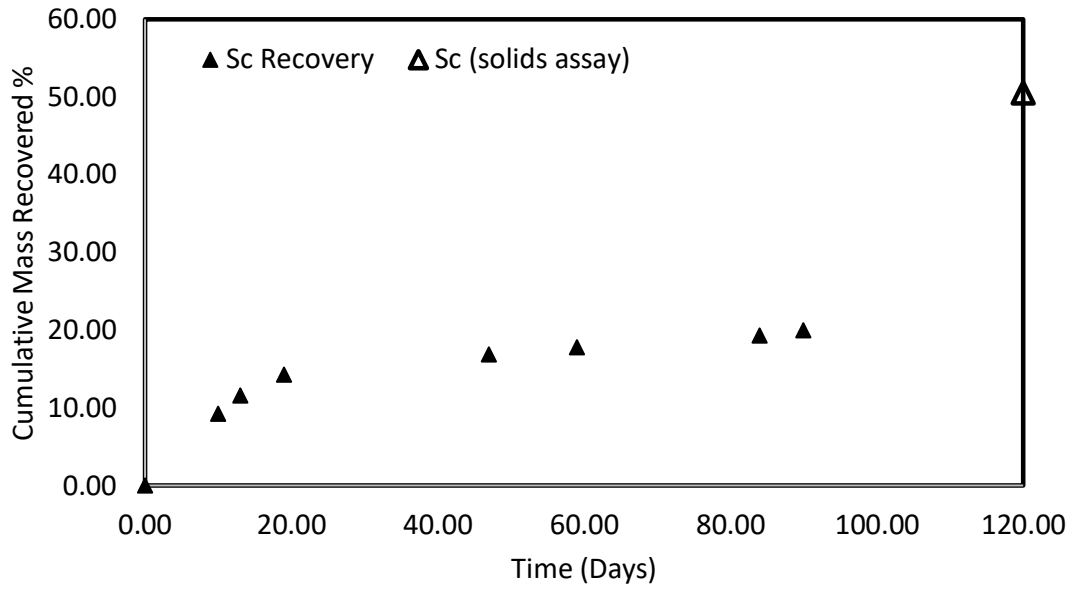

Figure 3 - 38: Comparison of solution based recovery as a function of time for scandium as well as the calculated recovery based on the solids assay before and after 120 days of leaching from Column 2.

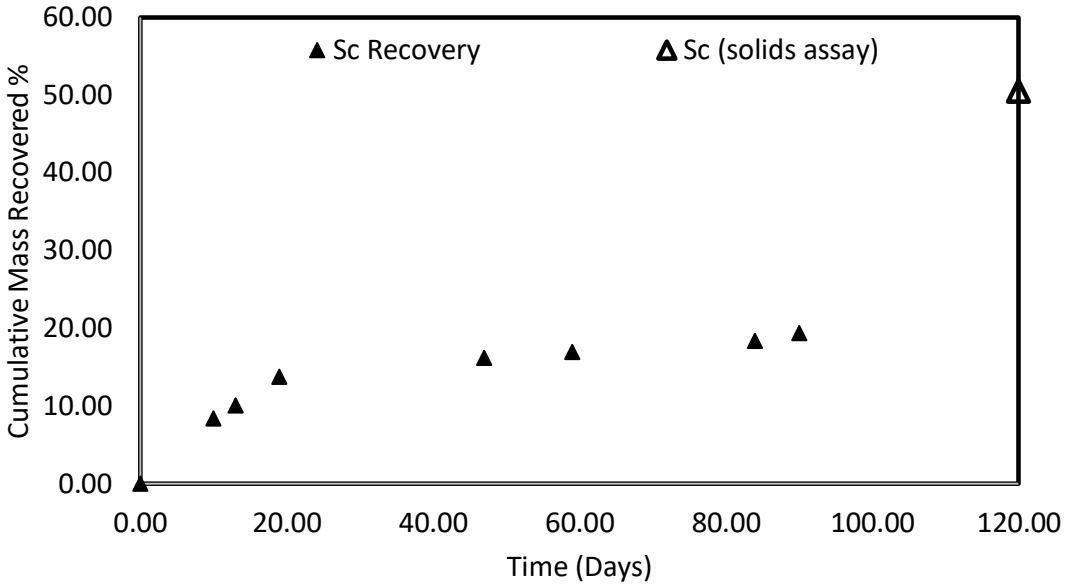

Figure 3 - 39: Comparison of solution based recovery as a function of time for scandium as well as the calculated recovery based on the solids assay before and after 120 days of leaching from Column 3.

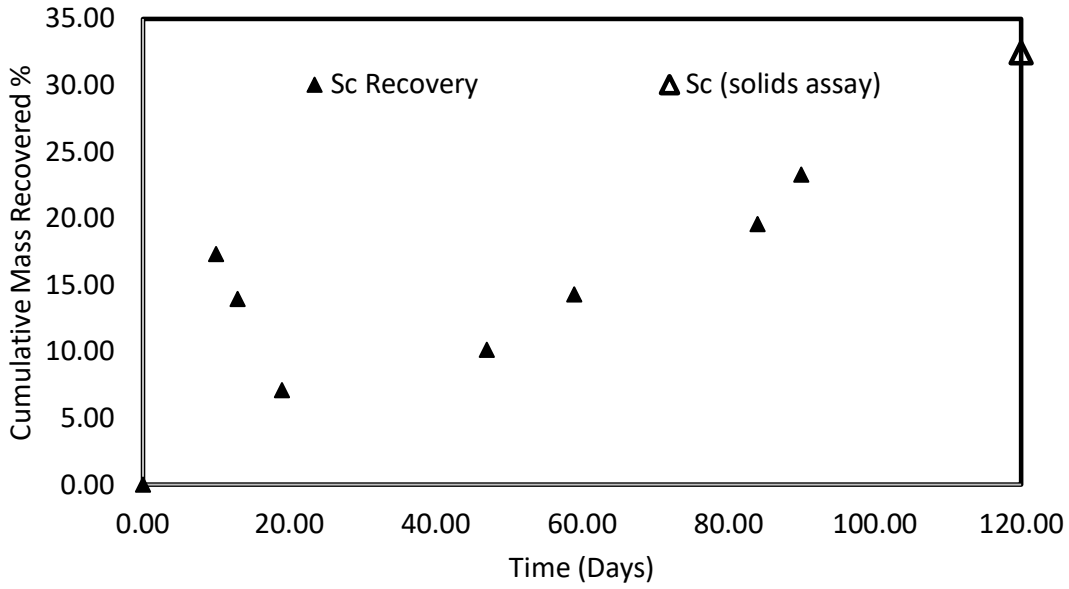

Figure 3 - 40: Comparison of solution based recovery as a function of time for scandium as well as the calculated recovery based on the solids assay before and after 120 days of leaching from Column 4.

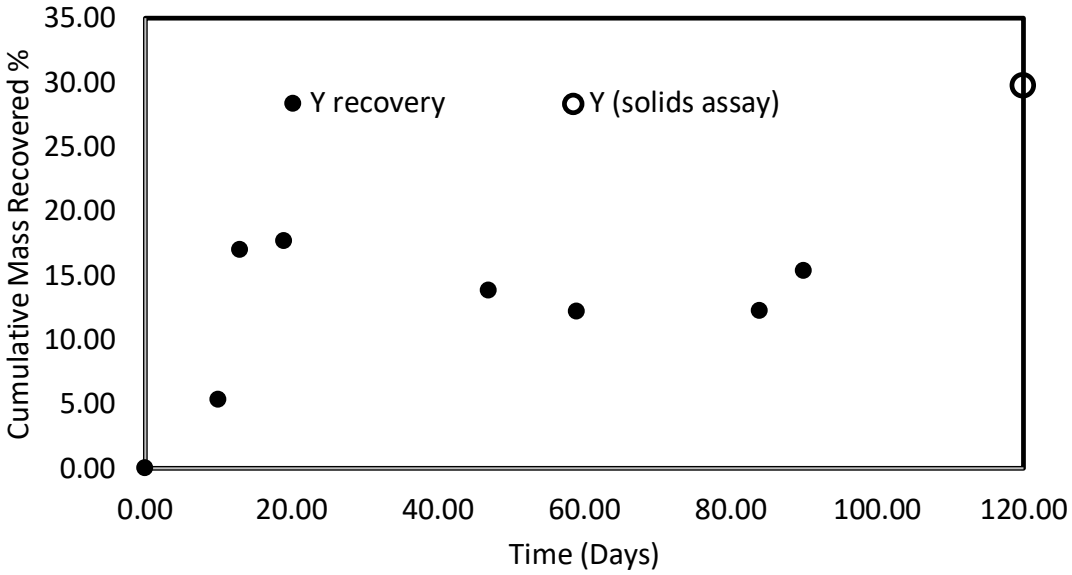

Figure 3 - 41: Comparison of solution based recovery as a function of time for yttrium as well as the calculated recovery based on the solids assay before and after 120 days of leaching from Column 1.

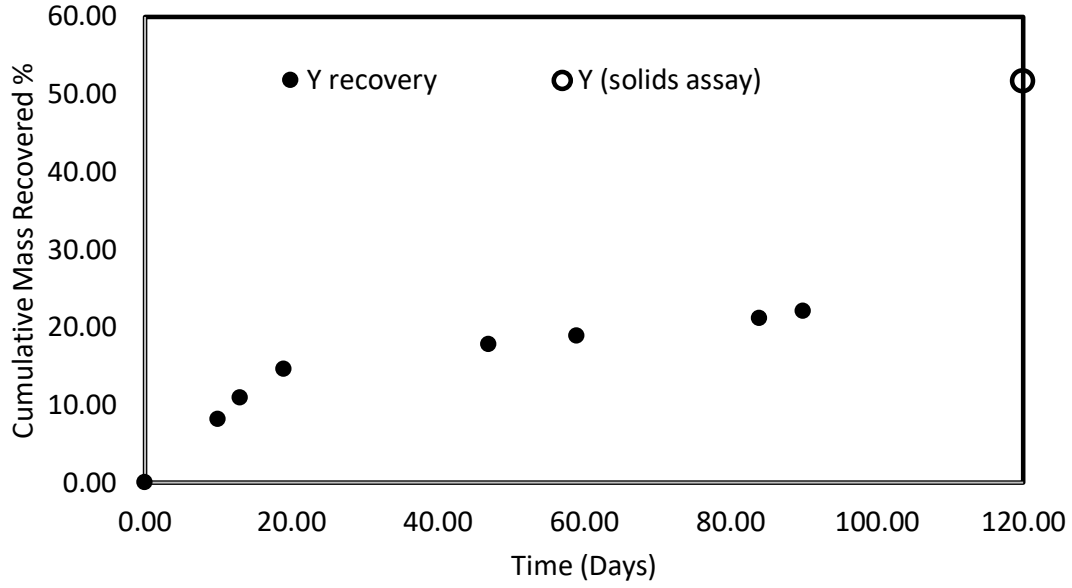

Figure 3 - 42: Comparison of solution based recovery as a function of time for yttrium as well as the calculated recovery based on the solids assay before and after 120 days of leaching from Column 2.

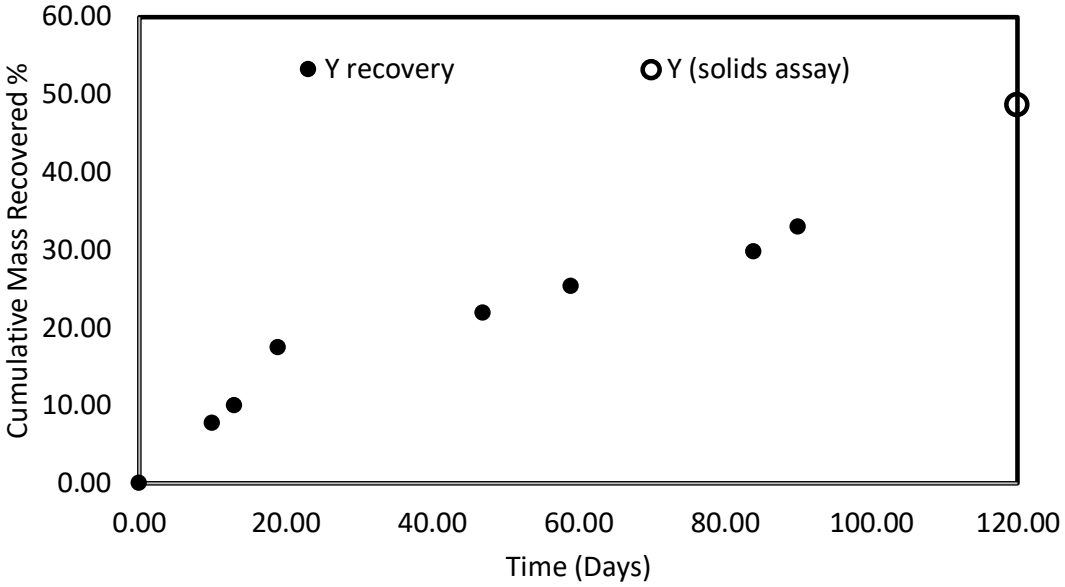

Figure 3 - 43: Comparison of solution based recovery as a function of time for yttrium as well as the calculated recovery based on the solids assay before and after 120 days of leaching from Column 3.

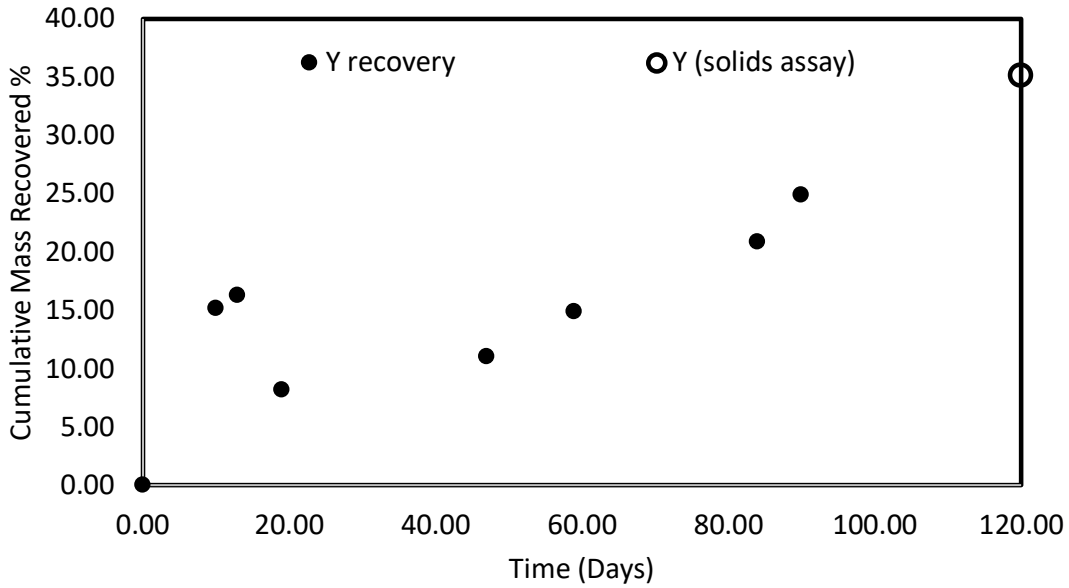

Figure 3 - 44: Comparison of solution based recovery as a function of time for yttrium as well as the calculated recovery based on the solids assay before and after 120 days of leaching from Column 4.

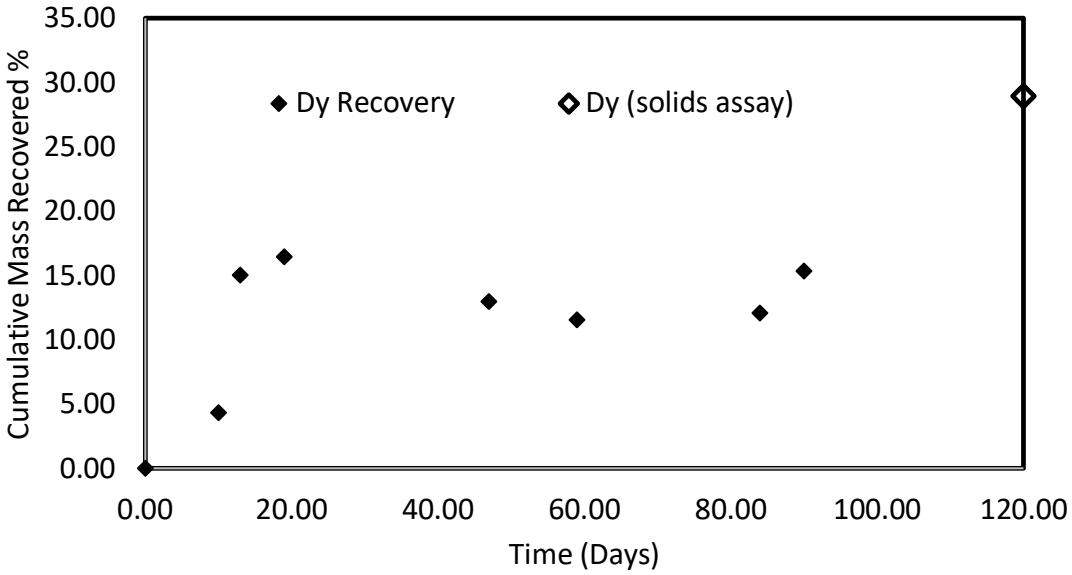

Figure 3 - 45: Comparison of solution based recovery as a function of time for dysprosium as well as the calculated recovery based on the solids assay before and after 120 days of leaching from Column 1.

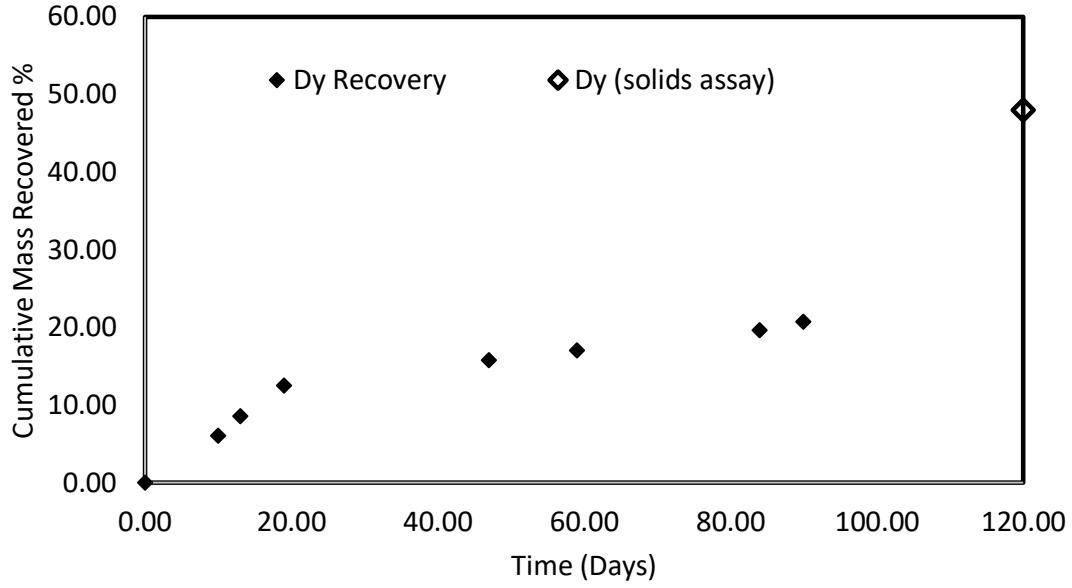

Figure 3 - 46: Comparison of solution based recovery as a function of time for dysprosium as well as the calculated recovery based on the solids assay before and after 120 days of leaching from Column 2.

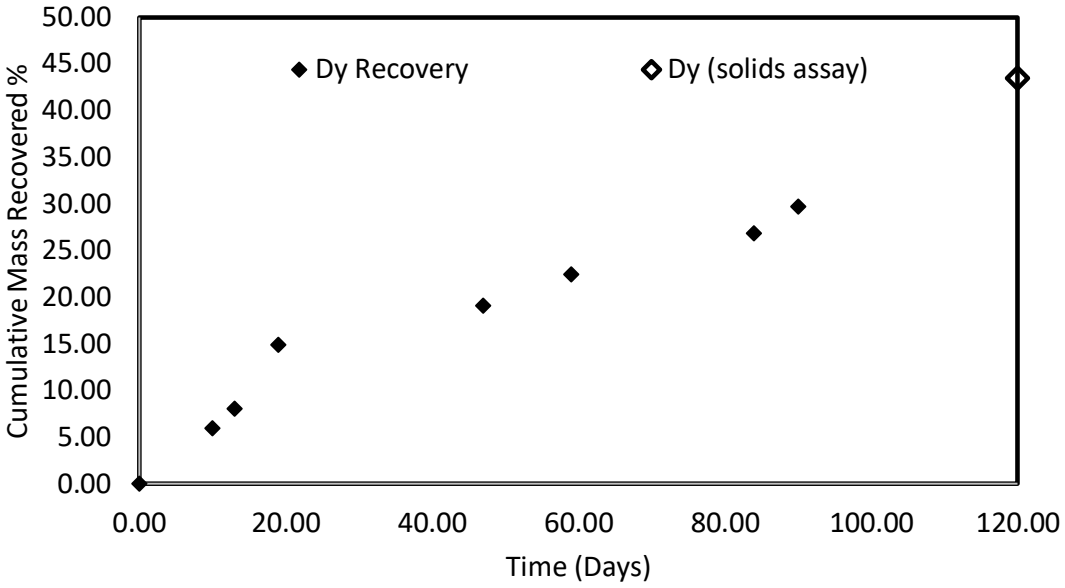

Figure 3 - 47: Comparison of solution based recovery as a function of time for dysprosium as well as the calculated recovery based on the solids assay before and after 120 days of leaching from Column 3.

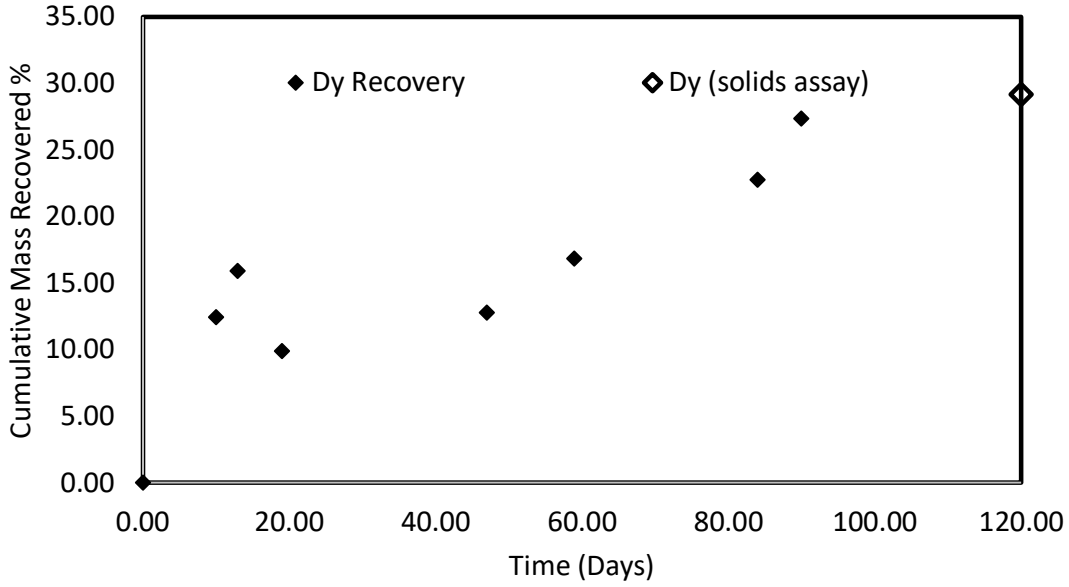

Figure 3 - 48: Comparison of solution based recovery as a function of time for dysprosium as well as the calculated recovery based on the solids assay before and after 120 days of leaching from Column 4.

The column leaching data provides many important insights into the leaching characteristics of the coal waste, the processing that is most effective, and the general viability of the process. Note that in general that the recovery results from Columns 1 and 2 for solution and solids analyses are not very consistent. The recovery results from Columns 3 and 4 for solution and solids analyses are quite consistent, and they show that recoveries of at least 50 % for some elements in 120 days are feasible.

3.3 Overview of column processing method and relationship to results

The leaching data shows that Column 1 generally had the poorest performance overall. It is believed that this is due to the processing method. Column 1 used recirculated solution that was reoxidized by bacteria. As the reoxidation occurred some of the dissolved iron began to precipitate due to the oxidizing environment and high level of iron after a few days of operation. This precipitation likely removed some of the bacteria that were attached to the solid particles as solutions were periodically changed, and some of the other dissolved species such as some of the rare earth elements likely coprecipitated with the iron jarosite compounds that formed. The maximum REE mass recovered in the solutions from Column 1 after about 90 days of leaching was 596 mg based on solution analyses, and the overall recovery of all elements was 28.9 % on average after 120 days of leaching based on the analysis of the solids before and after leaching.

The data for Column 2 show substantially improved results relative to Column 1. The maximum REE mass recovered in the solutions from Column 1 after about 90 days of leaching was 931 mg based on solution analyses, and the overall recovery of all elements was 40.1 % on average after 120 days of leaching based on the analysis of the solids before and after leaching. This column utilized biooxidized solution from a reactor that cultivates bacteria in fresh 9K medium. This approach seemed to work reasonably well.

The data for Column 3 show substantially improved results relative to Column 1. The maximum REE mass recovered in the solutions from Column 1 after about 90 days of leaching was 1082 mg based on solution analyses, and the overall recovery of all elements was 42.5 % on average after 120 days of leaching based on the analysis of the solids before and after leaching. This column utilized biooxidized solution from a reactor that was fed some nutrients and 100 g/l of coal waste with enriched pyrite (7 %). This approach seemed to be the best. Although the solution analyses were slightly higher than Column 2, much of that difference is due to the additional REE-bearing coal waste that is used in the bioreactor to feed the bacteria the needed pyrite. The additional coal waste used in the feeding process for Column 3 ends up in the column and supplies 10 % of the overall material by the end of the 120 days of feeding. However, the analysis of the solids before and after leaching is not impacted by this material. Column 4 generated nearly all of its own acid for leaching.

The data for Column 4 are similar to Column 1. The maximum REE mass recovered in the solutions from Column 4 after about 84 days of leaching was 565 mg based on solution analyses, and the overall recovery of all elements was 35.6 % on average after 120 days of leaching based on the analysis of the solids before and after leaching. This column utilized hydrogen

peroxide to supply the oxidant and fresh acid to provide the needed acid. This approach did not work as well as supplying the acid using the biooxidation of pyrite in the pyrite-enriched coal waste feed material.

Other important information contained in the leaching analysis is that other elements with significant value are also recovered. The cobalt extraction for the four columns varied between 37 and 65 % with the highest recovery from Column 3. Extraction of lithium from the four columns varied between 23 and 48 % with the highest recovery from Column 3. Manganese recovery varied between 47 and 86 %. The vanadium extraction for the four columns varied between 33 and 59 %. Zirconium recovery varied between 26 and 44 %. Thus, there is great potential for recovery of additional elements that have economic value.

Other elements such as calcium were not extracted to a significant extent, which is good. Other elements such as aluminum were extracted significantly and require subsequent precipitation, which is relatively simple for aluminum. Similarly, iron was extracted with recoveries between 16 and 59 %.

3.4 Biooxidation Evaluations

The rate of ferrous ion oxidation by bacteria was measured by adding ferrous sulfate to the solution, followed by measuring the change in oxidation reduction potential (ORP) as a function of time. The Nernst Equation which for the $Fe^{3+} + e^- \leftrightarrow Fe^{2+}$ half-cell reaction is:

$$E = E_o - \frac{2.303RT}{nF} ln \frac{a_{Fe^{2+}}}{a_{Fe^{3+}}} \quad (3\text{-}1)$$

where E is the electrochemical potential, Eo is the standard potential, R is the gas constant, T is the absolute temperature, n is the number of electrons, a is the activity, and F is the Faraday constant. This equation can be rearranged to:

$$E = E_o + \frac{2.303RT}{nF} ln \frac{\gamma_{Fe^{3+}} m_{Fe^{3+}}}{\gamma_{Fe^{2+}} m_{Fe^{2+}}} \quad (3\text{-}2)$$

where the activity coefficient, γ, can be calculated using the Davies Equation:

$$-log\gamma = \frac{Az^2\sqrt{I}}{1+\sqrt{I}} - 0.2I \quad (3\text{-}3)$$

in which z is the charge of the ion considered, and the ionic strength, I, can be estimated by:

$$I = 0.5 \sum_{i=1}^{n} m_i z_i^2 \quad (3\text{-}4)$$

By knowing an initial potential from an ORP probe, and measuring the new ORP value after adding a small amount of ferrous or ferric sulfate, the concentration of ferrous ions initially present can be calculated by deriving an equation using the previous equations to yield:

$$m_{Fe^{2+}_{init}} = \frac{m_{Fe^{2+}_{added}}}{exp\frac{(E_{init} - E_{afterFe2+addition})nF}{RT} - 1} \quad (3\text{-}5)$$

The concentration of free (not complexed) ferric ions initially present can be calculated from the equation similarly derived from the previous expressions:

$$m_{Fe^{3+}_{init}} = exp\frac{(E_{init}-E_o)nF}{RT}\frac{m_{Fe^{2+}_{init}}\,{}^{\gamma}{}_{Fe^{2+}}}{{}^{\gamma}{}_{Fe^{3+}}} \qquad (3\text{-}6)$$

The value of E_o for the ferrous/ferric half-cell reaction is 0.77 V.

By measuring the rate of ferrous ion oxidation, we can determine important information about the bacterial population and activity.

Assuming that all the basic needs are met, the oxidation rate is associated with ferrous ions. The ferrous biooxidation rate can be determined using traditional Michaelis-Menten or Monod kinetics [J. E. Bailey and D. F. Ollis, 1986.]:

$$R_{Fe+2ox.} = \frac{C_{cells}\mu_{\max}C_{Fe+2}}{Y_c(C_{Fe+2}+K_m)} \qquad (3\text{-}7)$$

In this equation, C_{cells} is the cell concentration. μ_{max} is the maximum specific growth rate. Y_c is the cell yield coefficient or cell mass produced per substrate mass consumed. K_m is the Michaelis constant. Michaelis-Menten kinetics is based on the assumption of reaction-limiting site availability. Example values for these variables in stirred reactors with sulfide mineral concentrates are: C_{cells} = 3 g/l, μ_{max} = 0.03 hr^{-1}, Y_c = 0.07, K_m = 0.025 g/l, C_{Fe+2} = 0.03 g/l, [M. L. Free, 1992.]. Values for heap leaching are likely similar, except that the cell concentration is much lower. Heap leaching is also more likely to be controlled by oxygen and carbon dioxide availability. The same form of Equation (3-7) can be used to describe the effect of oxygen on bacterial activity. Because *Acidithiobacillus ferrooxidans* are autotrophic, they utilize carbon dioxide to build cell mass. If carbon dioxide is not readily available, the mass of cells will be limited. In bioreactors, the feed gas can be supplemented with CO_2 (1 % in air) in order to maximize the cell mass, although this was not done in this project.

In most bioleaching operations there are several strains of bacteria that perform different oxidation functions. The most common bacteria associated with mineral leaching are *Leptospirillum ferrooxidans, Acidithiobacillus ferrooxidans, Acidithiobacillus thiooxidans, Acidithiobacillus acidophilus,* and *Sulfolobus*-like bacteria. Typical ferrous oxidation data in a batch test taken from a steady-state bioreactor with a mixed bacterial culture are presented in Figure 3 - 49.

In order to determine the reaction parameters for a given biooxidation scenario, test data can be evaluated. An example of test data was shown in Figure 3 - 49. Equation (3-8) can be best used for data evaluation in a rearranged form:

$$\frac{1}{R_{Fe+2ox}} = \frac{Y_cK_m}{\mu_{\max}C_{cells}C_{Fe+2}} + \frac{Y_c}{\mu_{\max}C_{cells}} \qquad (3\text{-}8)$$

Thus, a plot of $1/R$ versus $1/C_{Fe2+}$ can be used to determine the needed constants. Such a plot, referred to as a Lineweaver-Burke Plot, is shown in Figure 3 - 50. The data from Figure 3 - 49 were used to obtain Figure 3 - 50. The data in Figure 3 - 50 are linearly related as predicted using the Michaelis-Menten or Monod kinetic model. Therefore, it is likely that the bacterial activity is linked to the ferrous ion concentration and associated enzymatic activity within the bacteria.

The rate of bacterial leaching is also affected by the level of nutrients, contaminants, and flow rates. If necessary nutrients are not available, the bacteria will not be able to reproduce or perform at optimal levels. Toxins such as organic compounds and heavy metals can limit or eliminate growth. Finally, if the bacteria-containing medium is exchanged faster than the bacteria can reproduce, the bacterial population will eventually be "washed out". The wash out condition is limisted to low residence time bioreactors.

In our bioreactors, the rate of biooxidation is tracked by monitoring the oxidation reduction potential (ORP), which is reported as the "Eh" or the electrochemical potential of a redox electrode. The measurement is made relative to an internal reference half-cell reaction of silver and silver chloride, which has a potential of 0.199 V relative to the standard hydrogen electrode (SHE). A representative plot of the change in Eh as a function of time for one of our bioreactors is shown in Figure 3 - 51.

In order to evaluate the effect of stirring rate on oxidation, we performed experiments in which we added approximately 0.15 g of ferrous sulfate heptahydrate to a reactor vessel. The results of the tests are presented in Figures 3 - 52 and 3 - 53 for the change in ferrous iron concentration as a function of time based on Equation (3-6) and in Figures 3 - 54 and 3 - 55 for the associated Lineweaver-Burke plots based on Equation (3-8) (see also Figure 3 - 50). Note that the data in Figures 3 - 52 and 3 - 53 show that the rate of ferrous ion biooxidation increased substantially by increasing the stirring rate, which indicates the bacteria are limited by oxygen availability at the lower speed. The bacteria were fed with a 9K medium every 3 hours with a flow rate equivalent to a 7.5-day reactor (1000 ml) residence time.

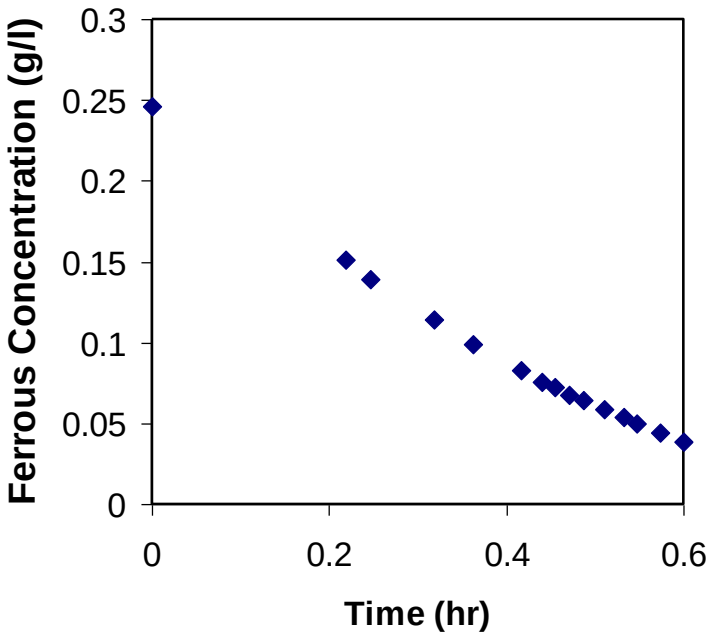

Figure 3 - 49: Batch ferrous ion biooxidation rate test based on measurement of oxidation reduction potential measurements following ferrous sulfate heptahydrate addition.

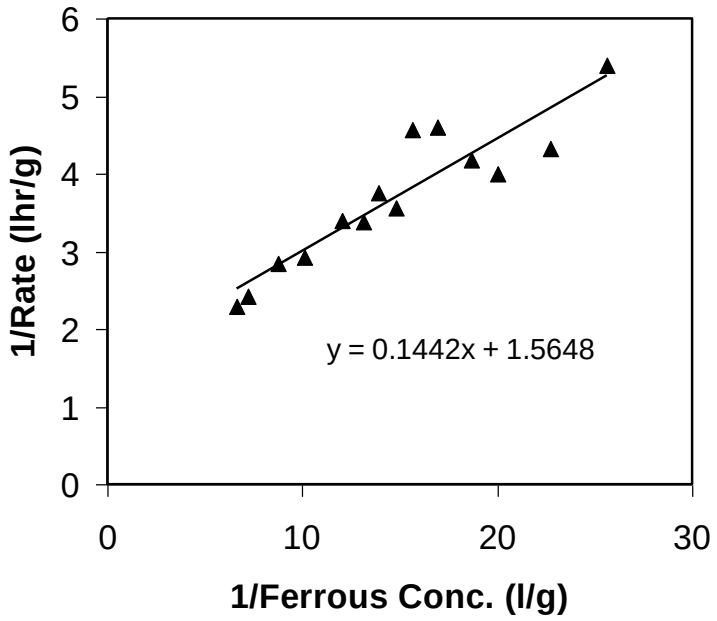

Figure 3 - 50: Lineweaver-Burke plot of batch ferrous biooxidation for the data shown in Figure 3 - 49.

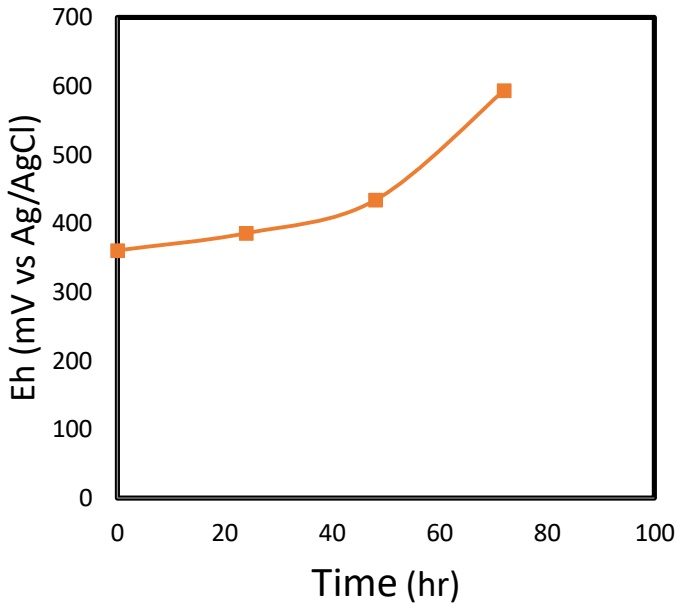

Figure 3 - 51: Comparison of Eh versus time for a typical bioreactor start up with a bacterial inoculum in our lab.

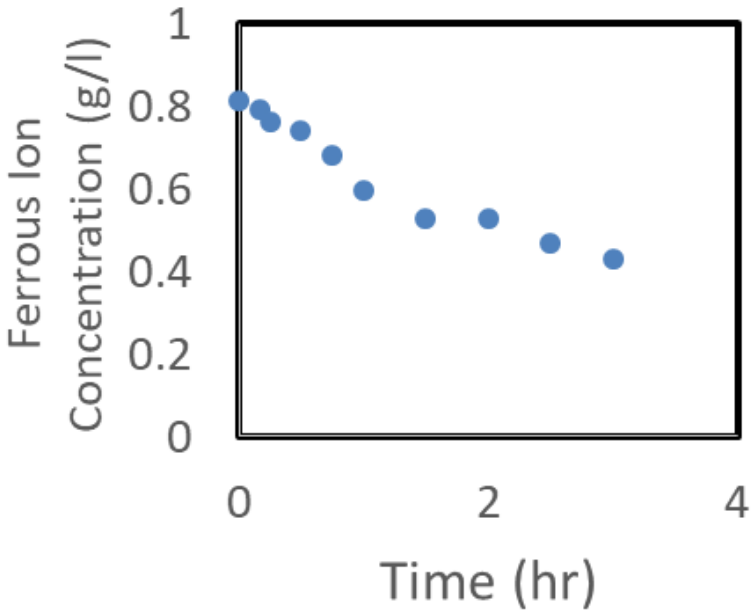

Figure 3 - 52: Batch ferrous ion biooxidation rate test based on measurement of oxidation reduction potential measurements following ferrous sulfate heptahydrate addition in a reactor operating at a rotational speed of 400 RPM.

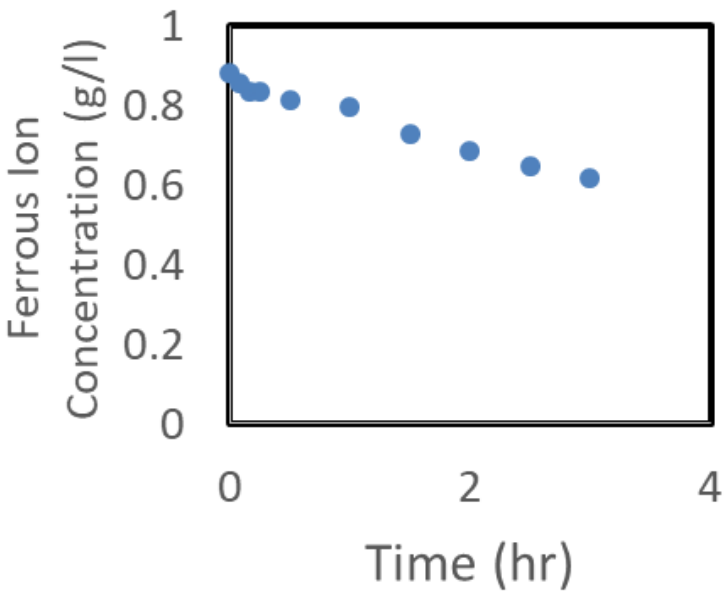

Figure 3 - 53: Batch ferrous ion biooxidation rate test based on measurement of oxidation reduction potential measurements following ferrous sulfate heptahydrate addition in a reactor operating at a rotational speed of 200 RPM.

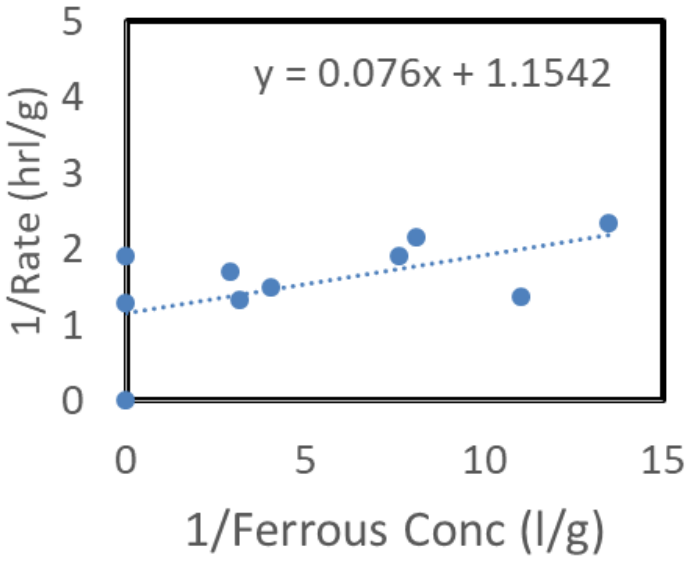

Figure 3 - 54: Lineweaver-Burke plot for a batch ferrous ion biooxidation rate test based on measurement of oxidation reduction potential measurements following ferrous sulfate heptahydrate addition in a reactor operating at a rotational speed of 400 RPM.

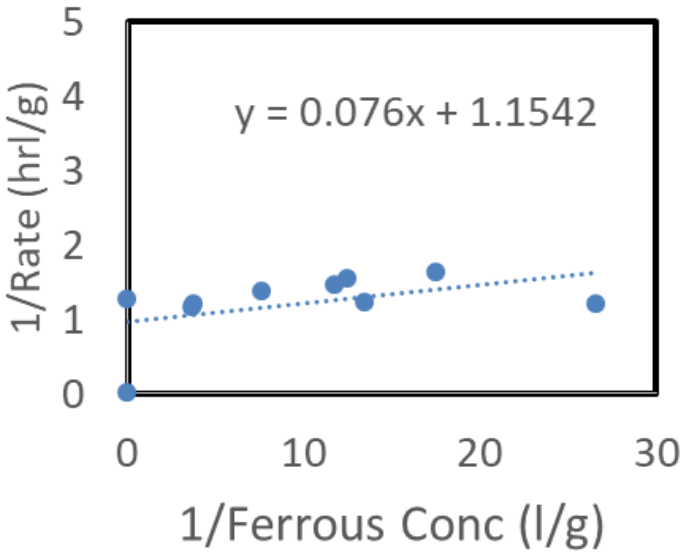

Figure 3 - 55: Lineweaver-Burke plot for a batch ferrous ion biooxidation rate test based on measurement of oxidation reduction potential measurements following ferrous sulfate heptahydrate addition in a reactor operating at a rotational speed of 200 RPM.

3.5 Bacteria Cultivation for the Bioleaching Tests

The Acidothiobacillus ferrooxidans bacteria purchased from the American Type Culture Collectionn (ATCC), mixed with samples from three mines, was cultured by feeding the 9K medium; the device of the bacteria cultivation is shown in Figure 3 - 56. As shown in Figure 3 - 57, bacteria can rapidly oxidize significant levels of ferrous ions in the solution. As a result of biooxidation, the Eh of the solution increased from about 470 mV to 700 mV. After replacing 100 ml solution with 9K medium, the Eh dropped dramatically, then through biooxidation it increased to 700 mV in a few hours. This prepared the bacteria to consume pyrite rather than ferrous sulfate.

Figure 3 - 56: Bacteria cultivation set up.

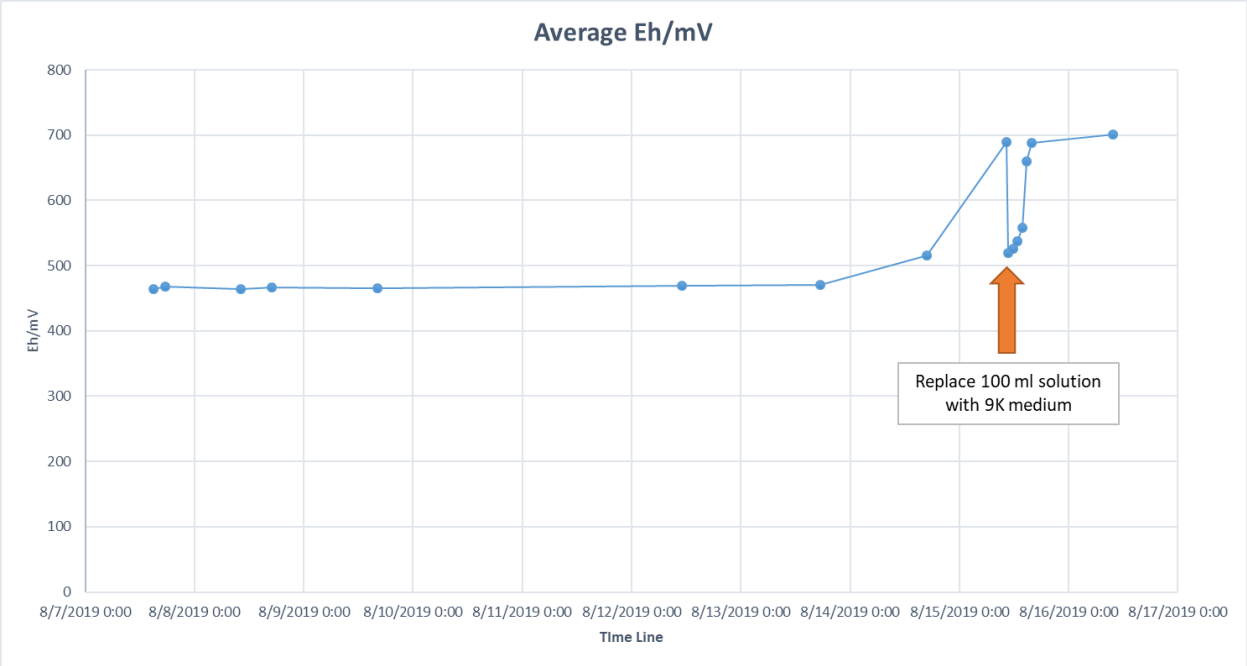

Figure 3 - 57: Eh vs. time when feeding the bacteria with 9K medium.

A new device with a water bath, a gas flow meter, stirring motors, and automatic pyrite and 9K medium (no Fe) feeding system were designed and assembled for the bacteria training to consume pyrite, as shown in Figure 3 - 58.

Figure 3 - 58: Bacteria cultivation device with the pyrite and 9K medium automatic feeding system.

A typical curve of Eh vs. time with pyrite feeding is shown in Figure 3 - 59. Compared with the change of Eh when feeding ferrous ions, the Eh increases more slowly when feeding pyrite, which means it takes more time for the bacteria to consume and oxidize pyrite than it does to oxidize dissolved ferrous ions. From the pH vs. time curve shown in Figure 3 - 60, it can be seen that the pH drops fast when the Eh is in the range of 600 mV to 680 mV. Therefore, the automatic feeding system was set to feed 5 g pyrite per day into the system to maintain the Eh in this range and make sure the bacteria is in an active state. The Eh and pH vs. time curves are shown in Figure 3 - 61 and Figure 3 - 62.

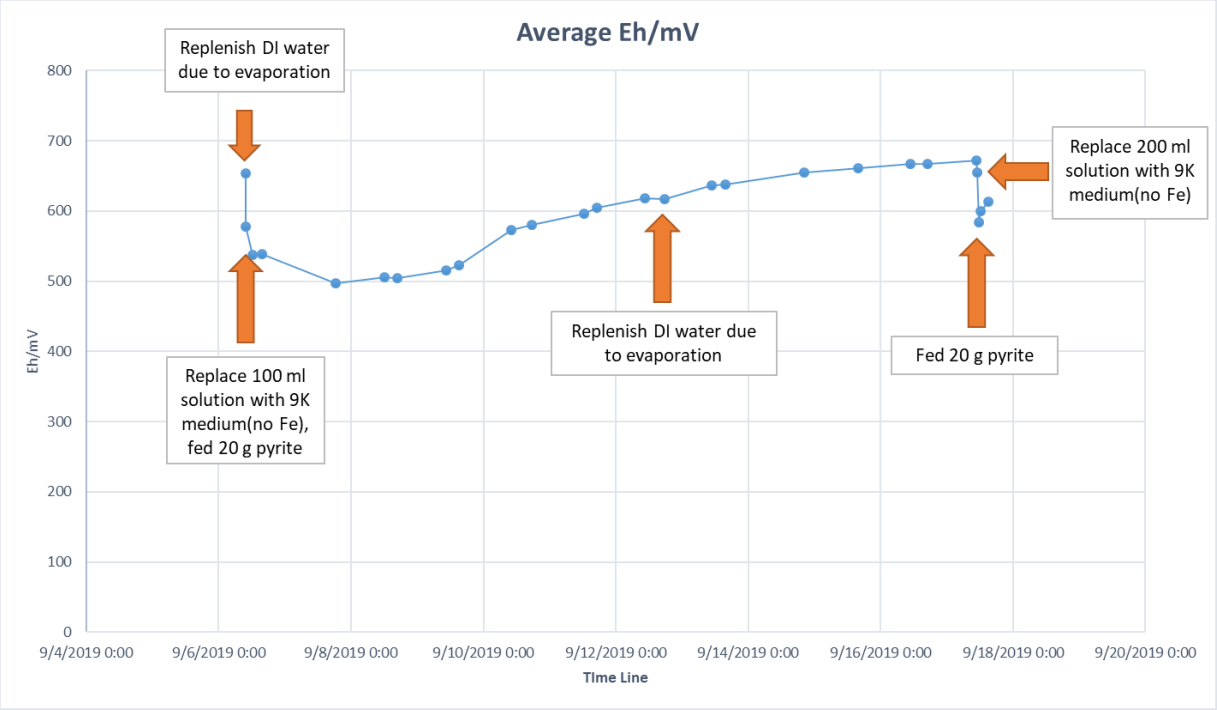

Figure 3 - 59: Eh vs. time with pyrite feeding into the bacteria cultivation device.

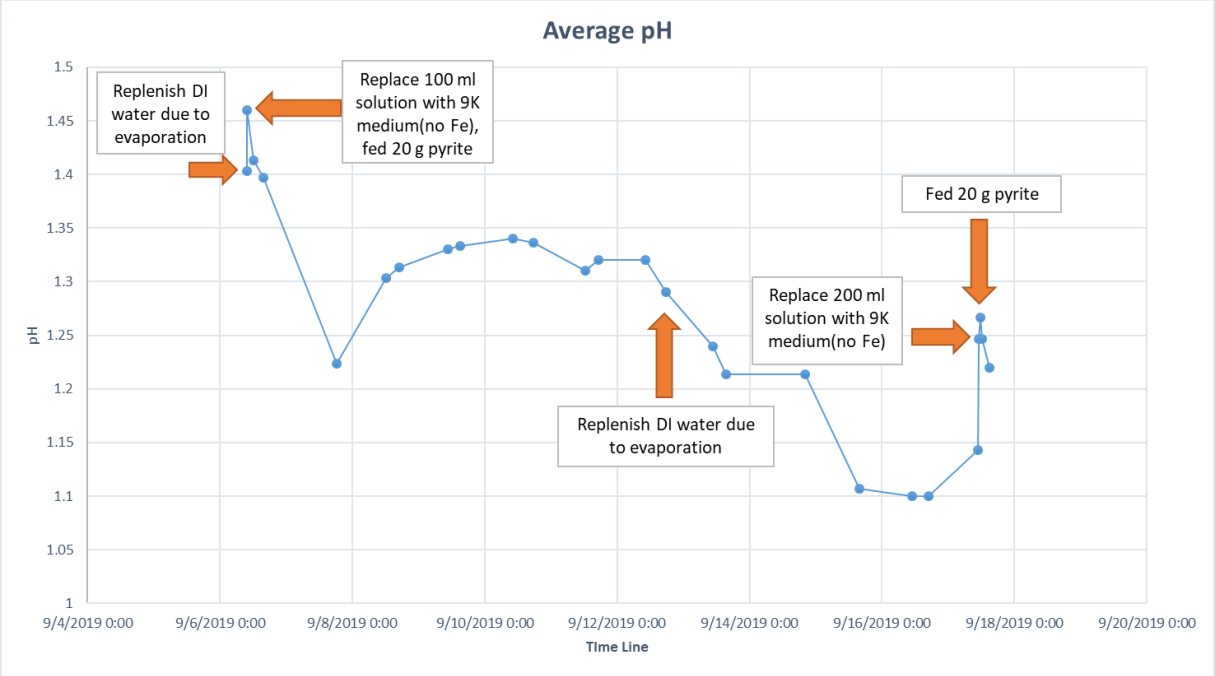

Figure 3 - 60: pH vs. time with pyrite feeding into the bacteria cultivation device.

As can be seen from Figure 3 - 61 and Figure 3 - 62, because of the regular feeding of pyrite, the Eh of the system changed periodically and maintained in the range of 600 mV to 680 mV relative to a silver/silver chloride internal reference electrode. As a result, the pH of the system changed periodically and has an overall trend of decreasing, which means the bacteria are active and generating acid and oxidant necessary for the leaching of rare earth elements leaching.

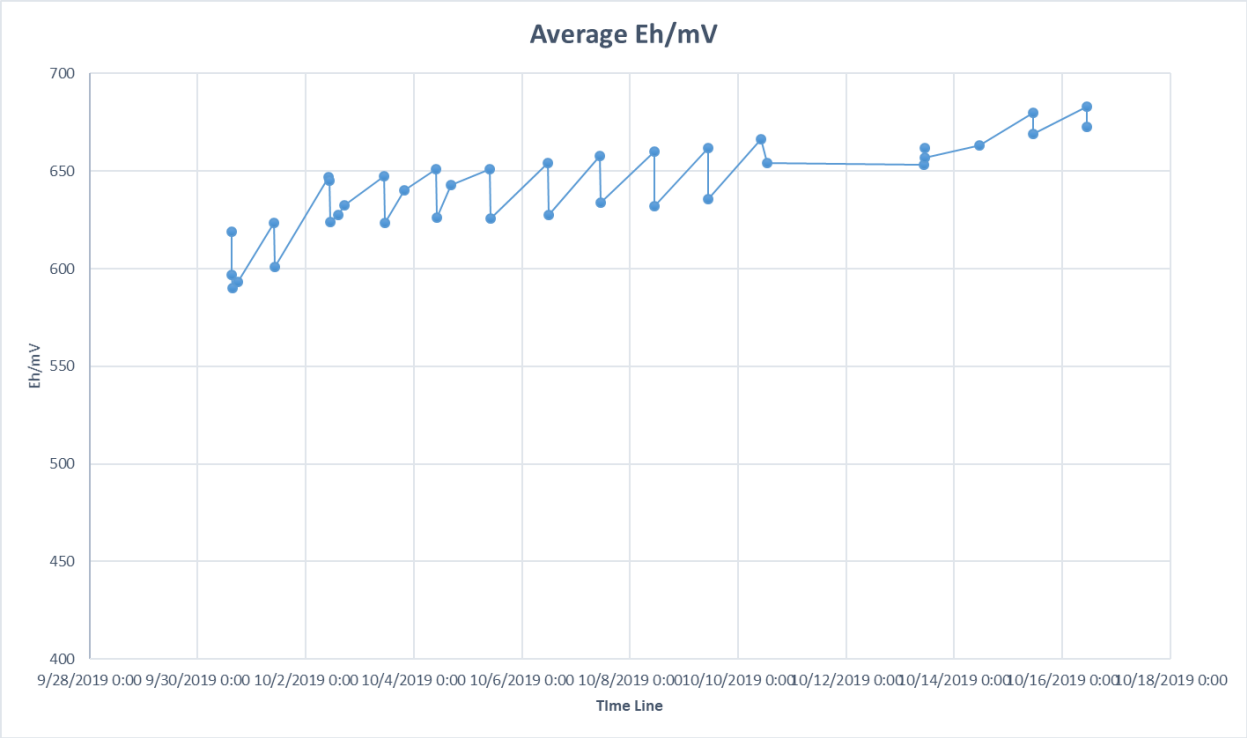

Figure 3 - 61: Eh vs. time with automatic pyrite feeding into the bacteria cultivation device.

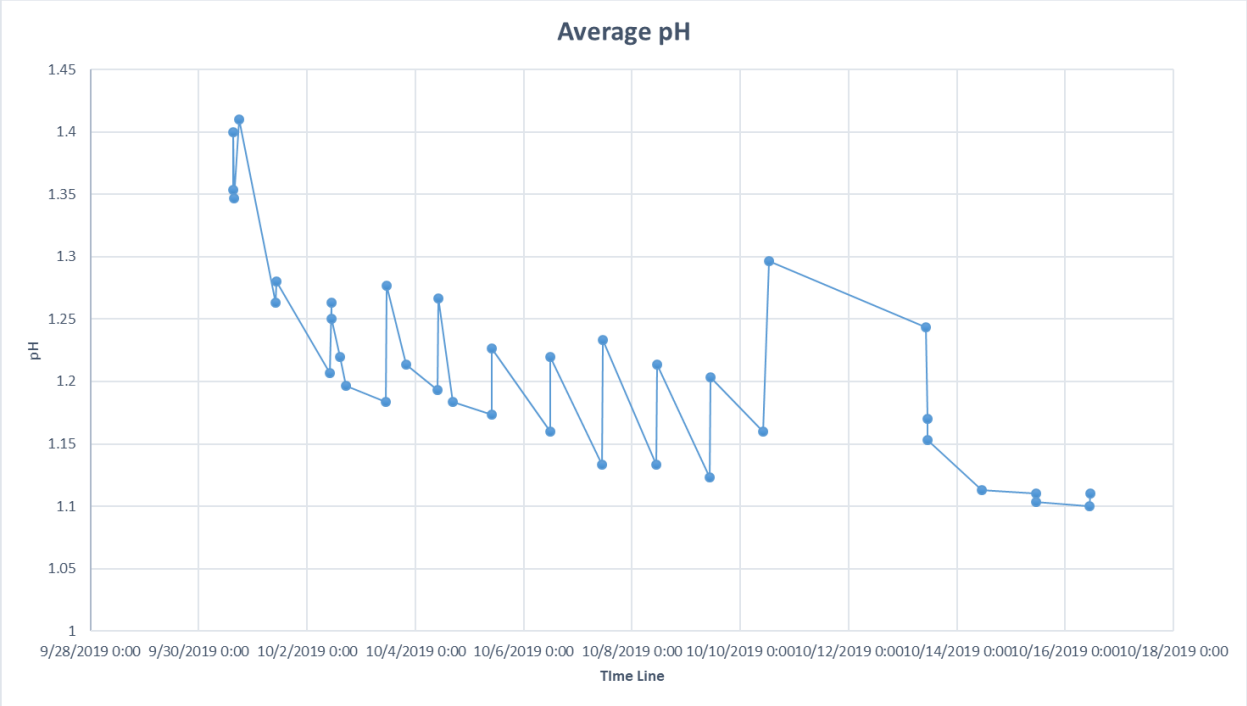

Figure 3 - 62: pH vs. time with automatic pyrite feeding into the bacteria cultivation device.

The automatic feeding system was set up on October 10th, 2019, as shown in Figure 3 - 63. Since then, the bio-oxidation of pyrite has been run automatically by turning on the pumps for 1 min with a timer at 11 am every day. During the running of the pumps, 100 ml of the solutions from the leaching vessel on the right is pumped to the 20 Liter white plastic drum in the front, while 100 ml of the 9K medium (no acid) with 5% of pyrite concentrate was pumped from the feeding vessel on the left-hand side to the leaching vessel. Eh and pH of the leaching solution was tracked regularly. The Eh stays in the ranges of 600-650 mV, and the pH stabilized at around 1.1. This leaching test confirmed the stability of the system on generating acid and ferric ions under the automatic operation.

Figure 3 - 63: Picture of the automated bioleaching system.

The activity of the bacteria is evaluated with a ferrous oxidation test. When the Eh of the solution was at a high level of 604 mV, 5 g of $FeSO_4 \cdot 7H_2O$ was added to the leaching vessel containing 1.5 L leaching solution. The Eh vs. time was measured and recorded. Based on the Eh data, the ferrous concentration vs. time and the ferrous ion consumption rate vs. time curves were plotted and compared with the data we measure three months before, when we first started the leaching test, as shown in Figure 3 - 64 and Figure 3 - 65.

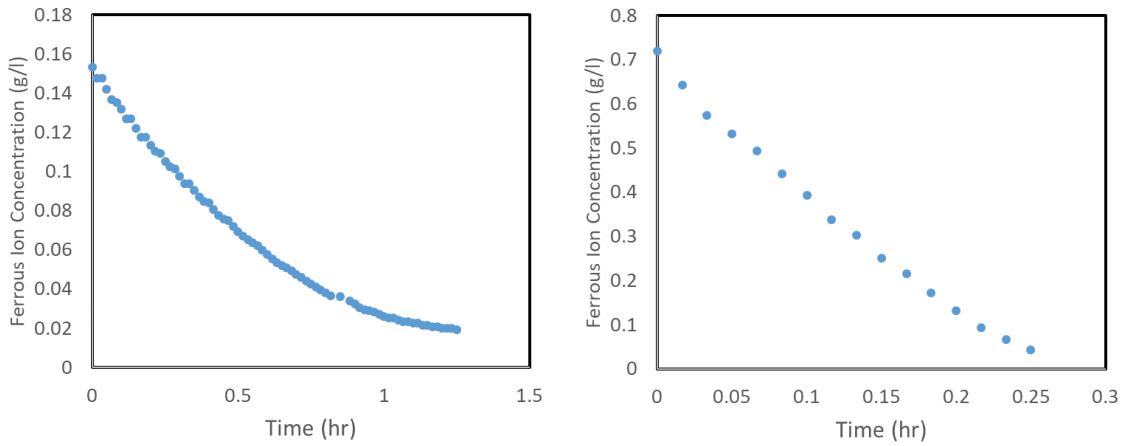

Figure 3 - 64: Ferrous ion concentration vs. time after adding $FeSO_4 \cdot 7H_2O$ before and after three months of cultivation.

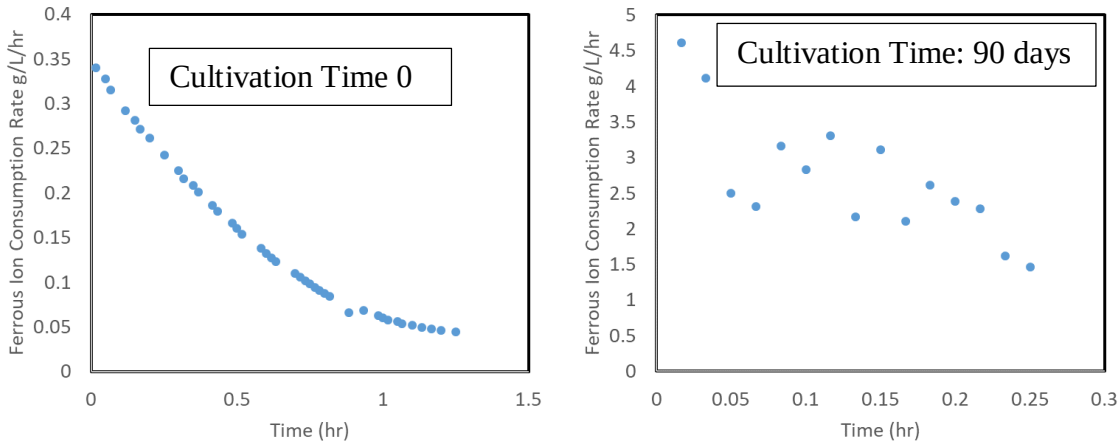

Figure 3 - 65: Ferrous ion consumption rate vs. time after adding $FeSO_4 \cdot 7H_2O$ for early culture and culture after 90 days of cultivation.

As can be seen from the plots, it took less time to oxidize more ferrous ions after 3 months running the leaching tests and selective cultivation of the bacteria. From Figure 3 - 65, we can see that the average ferrous oxidation rate is about 2.5 g/(L·hr), which is more than 10 times the starting oxidation rate 90 days before. The activity of the bacteria has been significantly increased, and the bacteria demonstrated robust activity and a significant population.

Task 4: Solvent Extraction

4.1 Eh and pH controlled tests for bulk solutions for solvent extraction and precipitation

The researchers conducted bulk leaching tests using 4.5 kg of coal refuse samples (CR-D) fines and using 15 liters of 20g/l ferric sulfate solution. The tests were conducted at fixed pH (~ 1.5) and Eh ~650 mV. The tests were conducted for a period of ~ 3 days to prepare solutions for solvent extraction and precipitation.

4.2 Solvent Extraction

Solvent extraction tests were conducted using four different solvent extractants. The team has utilized CYANEX 272, CYANEX 923, D2EPHA, and Versatic 10 as solvent extractants to evaluate. These SX reagents were diluted with kerosene (10% SX and 90% kerosene). 150 ml of leaching solution (collected after appropriate duration after recirculation through large columns) was mixed with 65 ml of each SX reagent (two different tests were conducted for one type of leaching solution) (See Figure 4 - 1). Both loading and stripping was done for a period of ~ 20 minutes. In case of stripping, 20 ml of organic solution (see Figure 4 - 2) was loaded with 50 ml of sulfuric acid of different concentration (0.02 M, 0.06 M, 0.2 M, 0.6 M, 2M, and 6M). Various loading and stripping tests have been performed using a variety of leaching solutions. One of the challenges that was experienced was that the solvent extraction process loads a significant amount of iron due to the high presence of iron in solution.

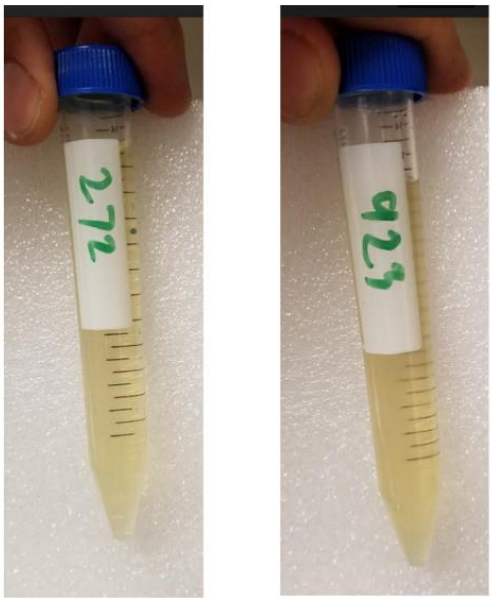

Figure 4 - 1: The snapshots of the collected liquid after loading tests, conducted using Cyanex 272 and Cyanex 923 solvent extractants.

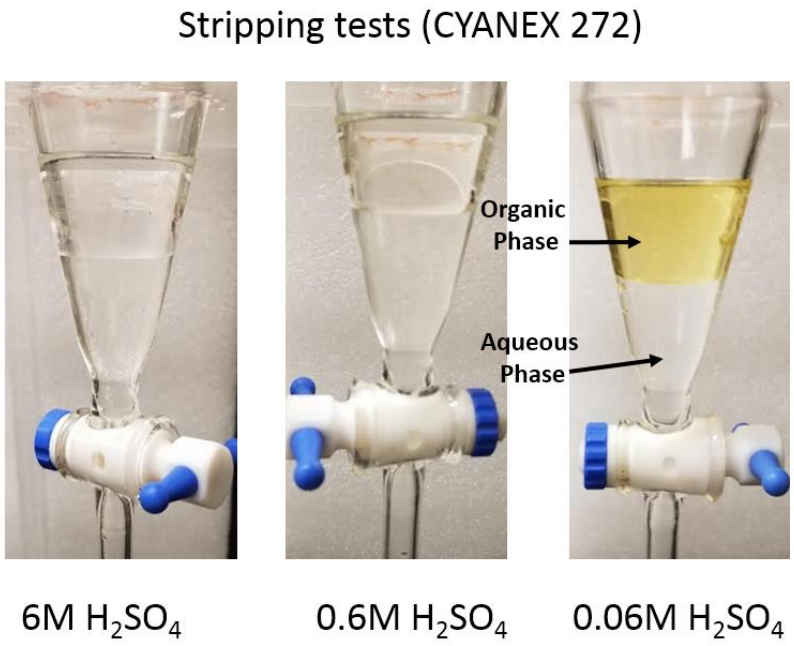

Figure4 - 2: The snapshots of stripping tests conducted using different solvent extractant and different concentration of sulfuric acid. In each separatory funnel, the organic and aqueous phases can be easily distinguished.

The general solvent extraction equation for rare earth elements that is used to describe the solvent extraction loading and stripping, is:

$$Ln^{3+} + 3RH = LnR_3 + 3H^+ \quad (4\text{-}1)$$

In which Ln^{3+} represents lanthanum, but it applies to any rare earth element generally, R represents the organic extractant molecule in an anion form, and H represents the hydrogen. Although this generally applies to two different types of solvent extractants used for rare earth element separations such as carboxylic acids such as versatic acids and phosphorous-bearing acids such as di 2-ethylhexylphosphoric acid (D2EPHA), some acids can form undissociated acids, leading to modified complexes (Feng Xie, Ting An Zhang, David Dreisinger, Fiona Doyle, A critical review on solvent Extraction of rare Earths from Aqueous Solutions, Minerals Engineering, 56, 10-28, 2014.)

The resulting equilibrium constant is:

$$K = \frac{[LnR_3][H^+]^3}{[Ln^{3+}][RH]^3} \quad (4\text{-}2)$$

Rearrangement of this expression, combined with a mass balance for the lanthanum or rare earth element leads to:

$$LnR_3 = \frac{Ln_{Total} K \frac{[RH]^3}{[H^+]^3}}{1 + K\frac{[RH]^3}{[H^+]^3}} \quad (4\text{-}3)$$

Data from a series of solvent extraction tests using D2EPHA, Cyanex 272, and Cyanex 923 are presented in Figures 4 - 3 to 4 - 6.

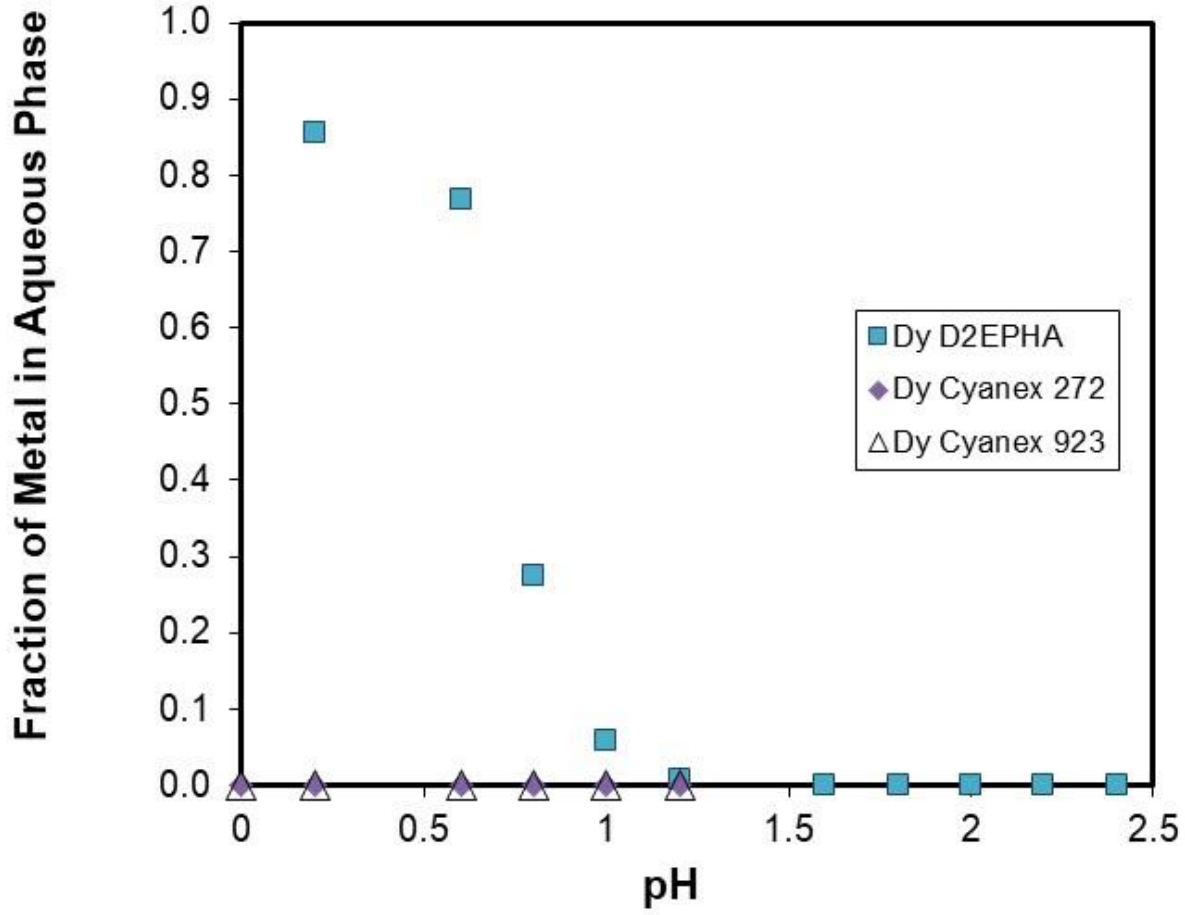

Figure 4 - 3: Comparison of fraction of dysprosium metal in the aqueous phase after equilibration with solvent extractants (D2EPHA, Cyanex 272, and Cyanex 923) as indicated in the legend at room temperature at the specified pH.

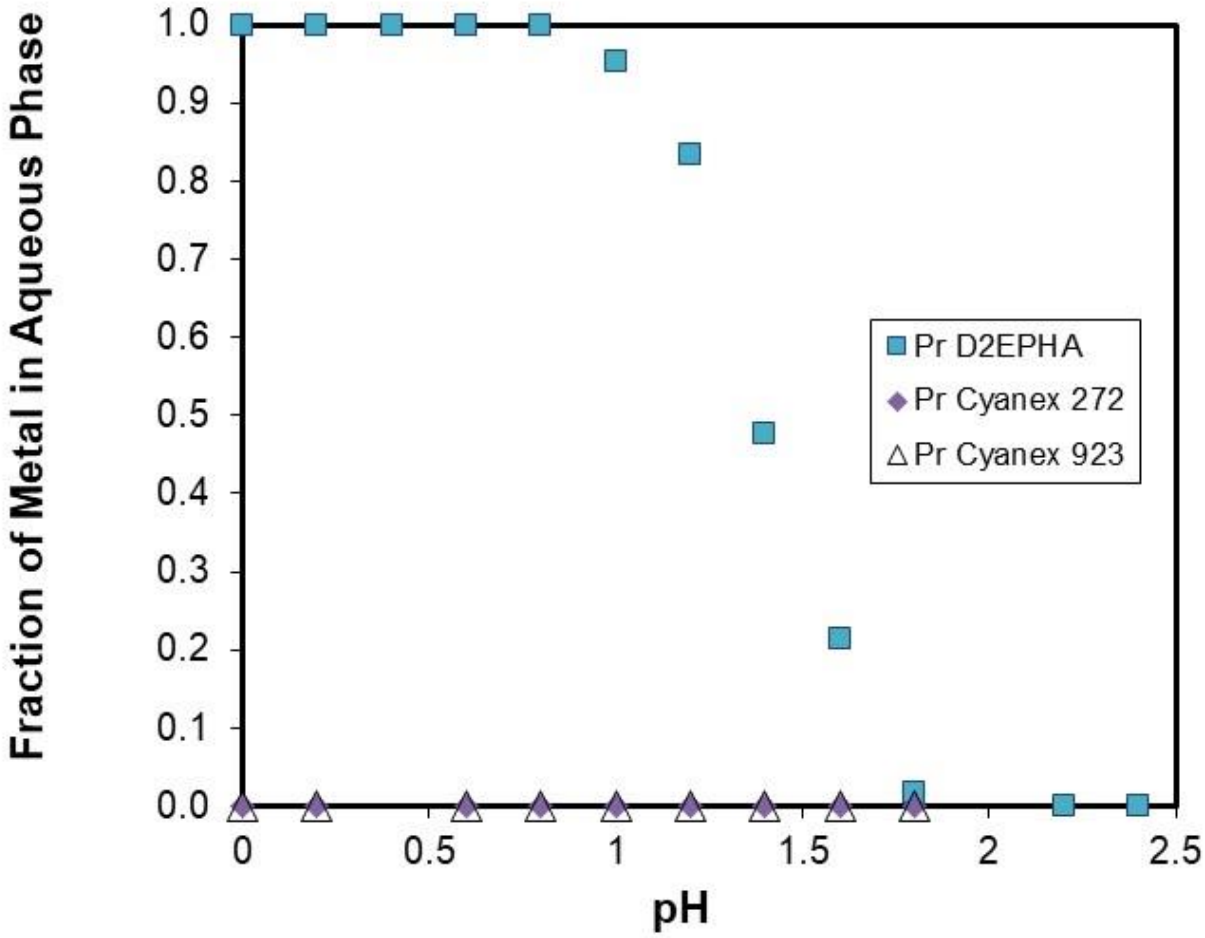

Figure 4 - 4: Comparison of fraction of praesodymium metal in the aqueous phase after equilibration with solvent extractants (D2EPHA, Cyanex 272, and Cyanex 923) as indicated in the legend at room temperature at the specified pH.

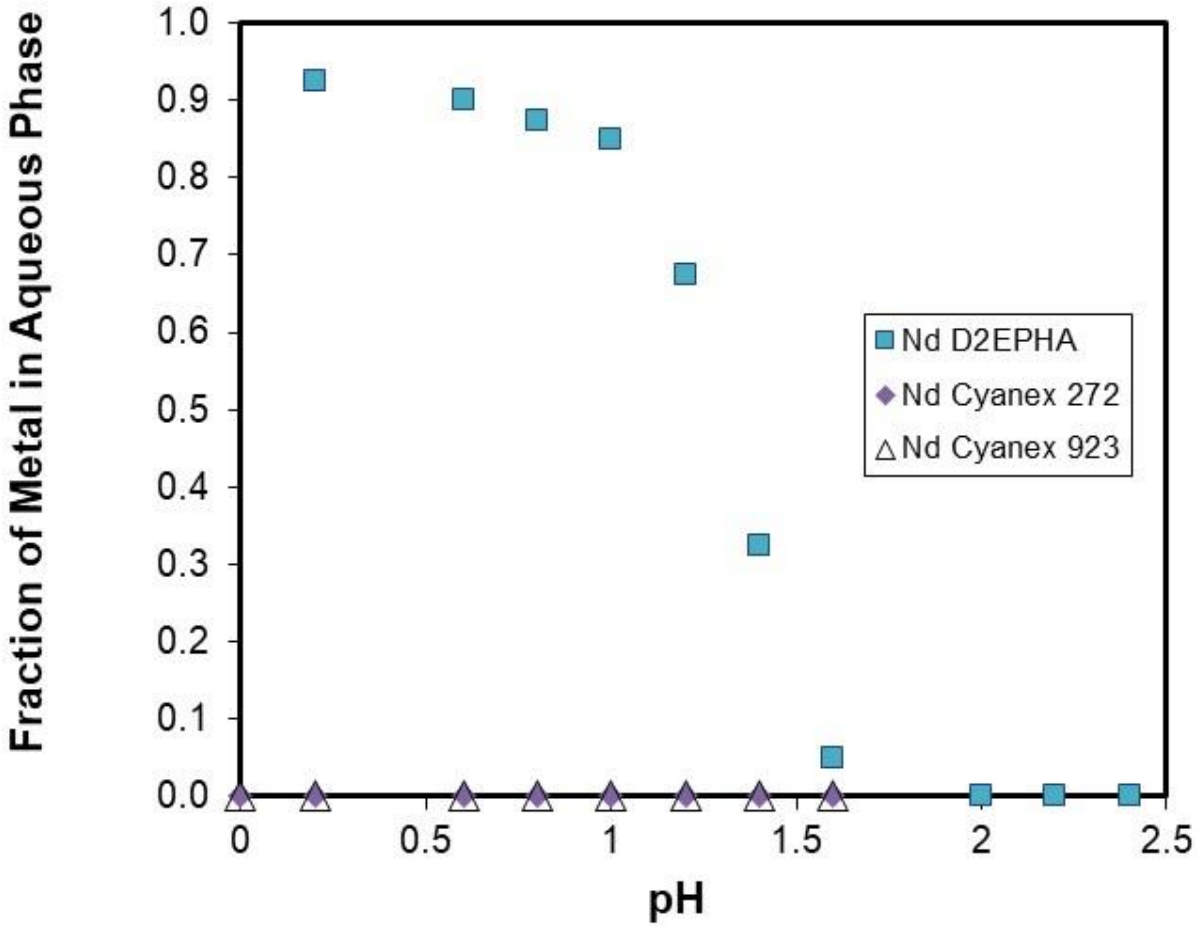

Figure 4 - 5: Comparison of fraction of neodymium metal in the aqueous phase after equilibration with solvent extractants (D2EPHA, Cyanex 272, and Cyanex 923) as indicated in the legend at room temperature at the specified pH.

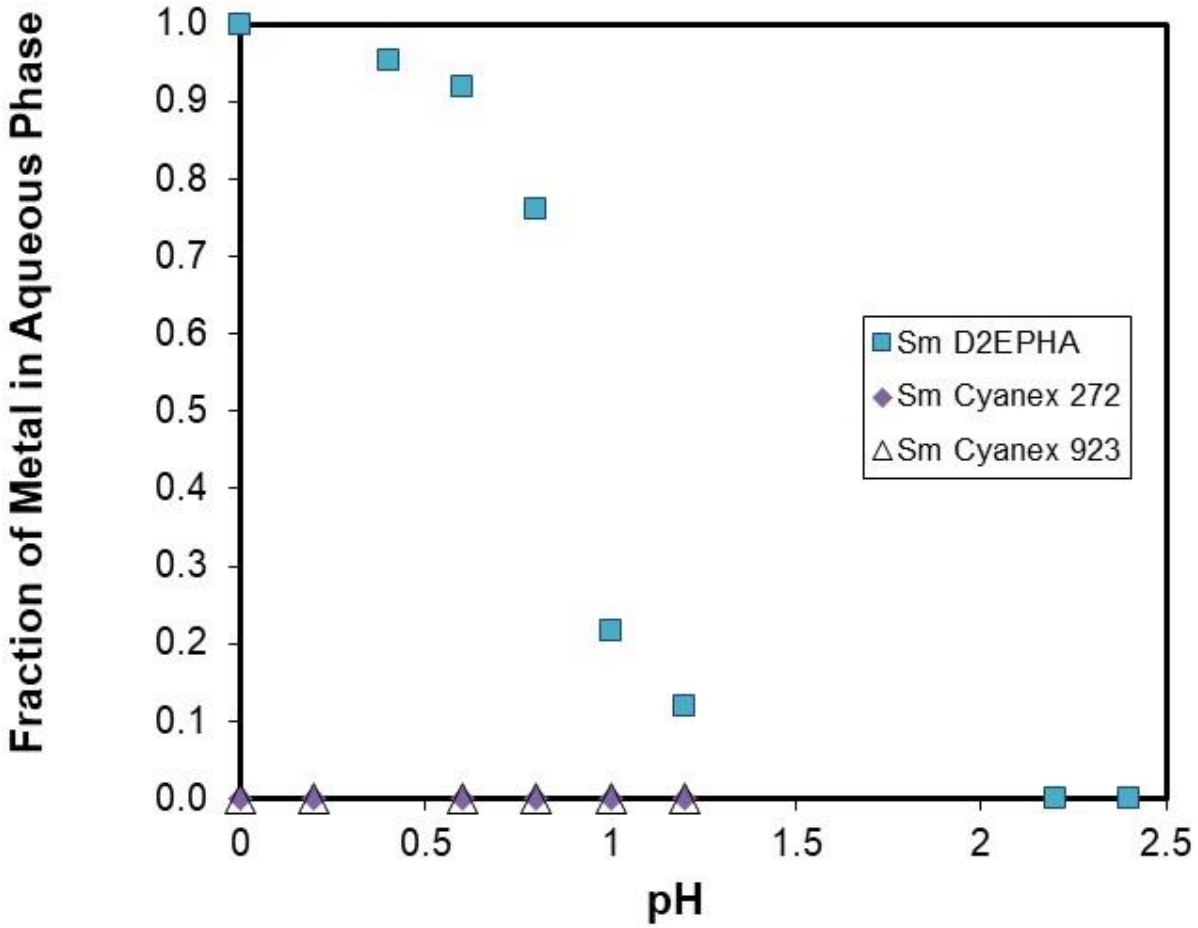

Figure 4 - 6: Comparison of fraction of samarium metal in the aqueous phase after equilibration with solvent extractants (D2EPHA, Cyanex 272, and Cyanex 923) as indicated in the legend at room temperature at the specified pH.

It is readily apparent that the Cyanex 272 and Cyanex 923 bind to the rare earth elements and require a lower pH to perform stripping than is presented.

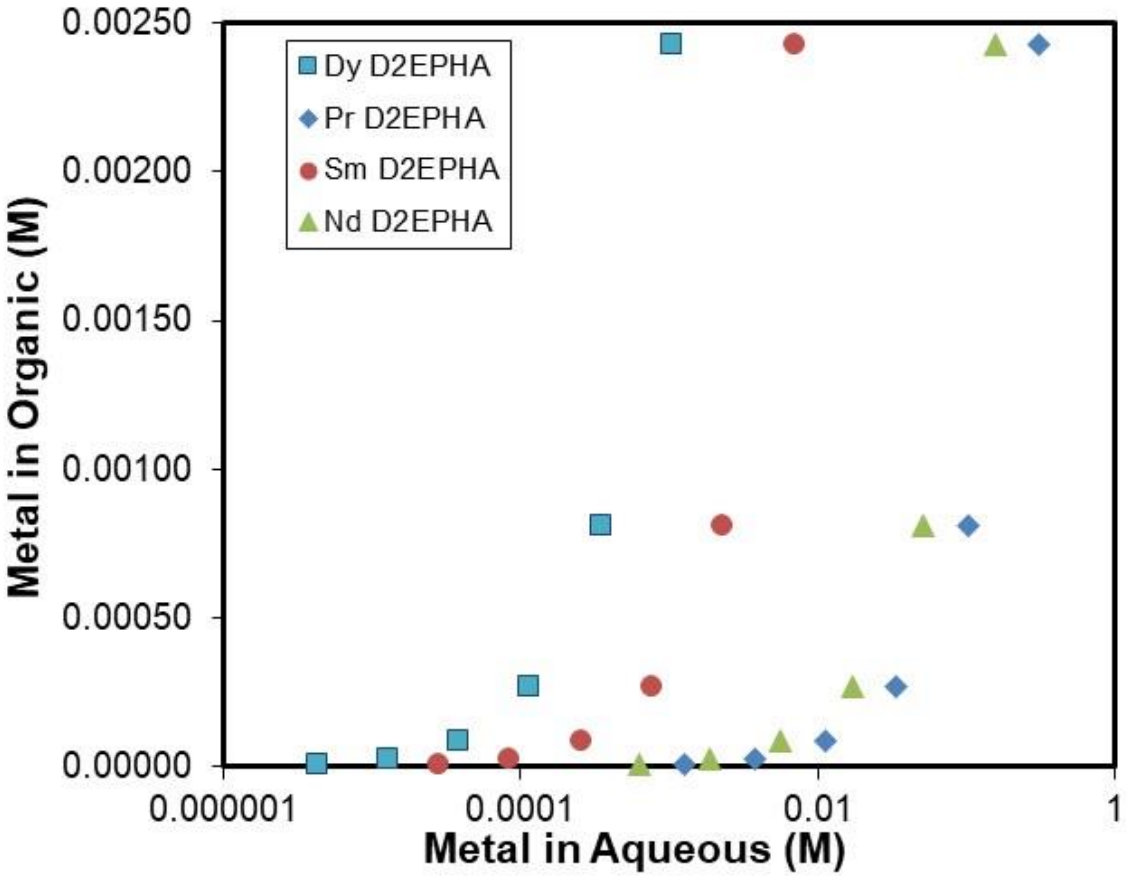

Figure 4 - 7: Comparison of organic and aqueous phase metal concentrations after equilibration with solvent extractant (D2EPHA) for the metals indicated in the legend at room temperature at pH 0.7.

As shown in Figure 4 - 7, the different rare earth elements had different characteristics in terms of their relationship with the organic and aqueous phases, which makes them amenable to separation by solvent extraction using D2EPHA and other organic extractants. Note that Versatic acid did not perform well. It is also important to note that although Cyanex 272 and 923 were excellent at loading the REEs, they were very difficult to strip and required high acid concentrations. Furthermore, all of the solvent extraction reagents were not highly selective relative to iron. Consequently, solutions need to be treated by precipitation to remove iron prior to solvent extraction. The combination of the need to precipitate the iron prior to solvent extraction, combined with the need to use high acid concentrations during stripping, may make a precipitation only process more economically feasible.

4.3 Solvent Extraction Testing and Modeling

Because the concentration of RH is a function of the LnR_3 and pH, solving this equation analytically is not practical, so a numerical solution is useful. Using a numerical solution as the

model fit of the data, the experimental solvent extraction data are presented in Figure 4 - 8 for the rare earth elements evaluated (Dy, Pr, Nd, and Sm), and in Figure 4 - 9 for iron.

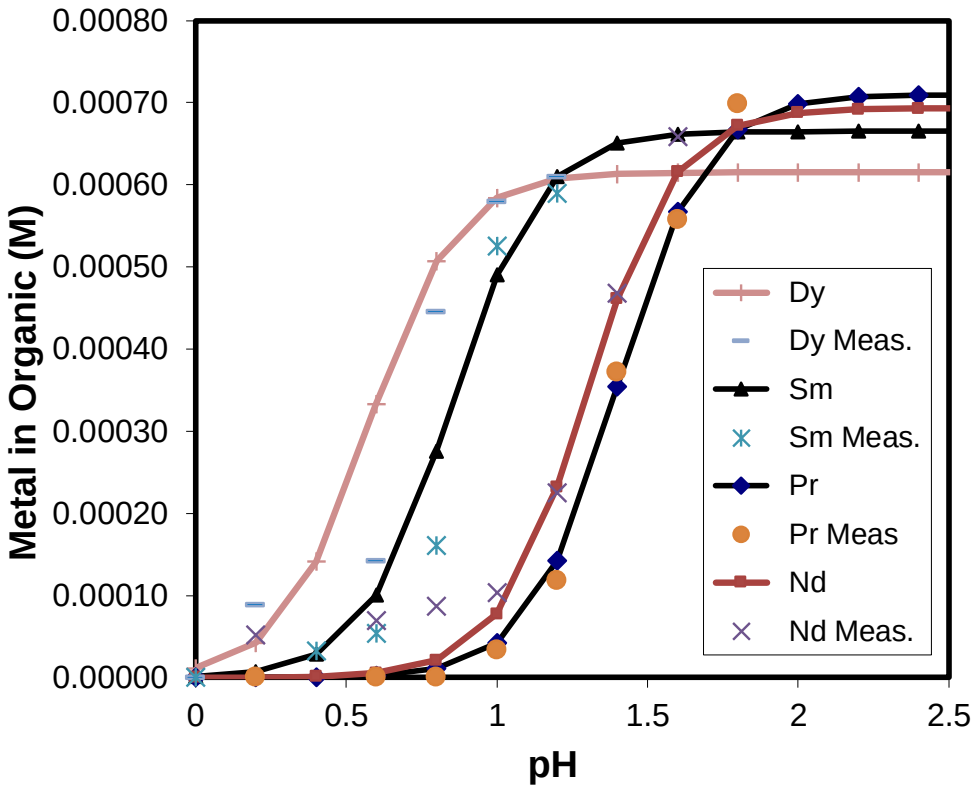

Figure 4 - 8: Comparison of numerically calculated (see Equation (11)) and measured metal concentration in the organic phase di 2-ethylhexylphosphoric acid (1:1 mixture of organic and aqueous phase) as a function of pH for tests involving 100 ppm of each rare earth element shown as well as 2000 ppm iron to simulate initial leaching solutions. Compounds added as metal sulfates.

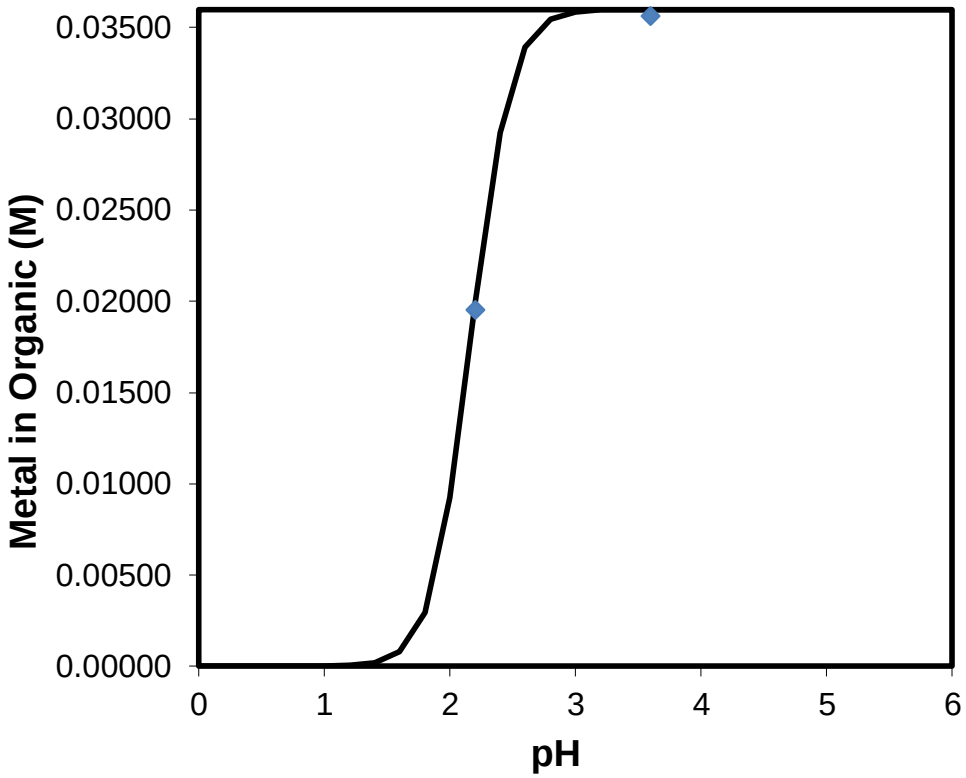

Figure 4 - 9: Comparison of numerically calculated (see Equation (11)) and measured (see diamond markers in the plot) dissolved iron metal in the organic phase di 2-ethylhexylphosphoric acid (1:1 mixture of organic and aqueous phase) as a function of pH for tests involving 100 ppm of Dy, Pr, Nd, and Sm as well as 2000 ppm iron to simulate initial leaching solutions. Compounds added as metal sulfates.

Task 5: Precipitation and REE Product Recovery

5.1 Precipitation tests

Precipitation tests have been conducted for the solutions that were collected from each column after leaching. In many scenarios precipitation testing was conducted using magnesium carbonate while in different tests sodium carbonate was used. Here are the details of the tests:

Test 1: $MgCO_3$/75^o C/pH 2.7

Test 1: Na_2CO_3/60^o C/pH 2.7

Once precipitation tests finished, the filter cake was collected (see Figure 5 - 1) and dried for further elemental analysis. Note that the filter cake mainly contains iron based salts. However, efficient recovery of REEs is essential. The precipitate was also re-dissolve in oxalic acid in order to selectively recover any REEs in filter cake.

Figure 5 - 1: The snapshots of the filtrate after precipitation test, conducted using magnesium carbonate.

Because of the important relationship between carbonate and pH and the potential interaction between carbonate and rare earth elements as pH increases, additional calculations were performed to determine the species present in solution as a function of pH. Table 5 - 1 shows the species calculated for solutions containing the species observed in the leaching solutions based on Visual Minteq software calculations. The information in the table shows that the only relevant species for rare earth elements and iron in the acidic sulfate based solutions used for leaching are the soluble sulfate complexes such as $FeSO_4^+$ $DySO_4^+$, etc. and the dissolved metal ions such as Fe^{3+}, Dy^{3+}, etc. Thus, a more in-depth precipitation analysis was performed that included only these species with varying concentrations of magnesium carbonate, which is used to adjust the pH and cause iron to precipitate. The results are presented in Figures 5 - 2 and 5 - 3. The data in these figures shows that iron can be completely precipitated with magnesium carbonate with approximately a 15 % loss in rare earth elements at pH of 4.5. However, in a real circuit it is desirable to recirculate much of the iron. Thus, at a realistic precipitation pH near pH 3, the losses are predicted to be less than 10 %. Losses can be reduced further by reducing the pH, which will depend on the need for iron recirculation.

Table 5 - 1: Comparison of Visual Minteq species calculations for leaching solutions with added magnesium carbonate for iron removal

Species	Concentration	Activity	Log activity	fraction
Dy(CO3)2-	2.48E-26	1.83E-26	-25.74	0.00%
Dy(SO4)2-	7.11E-06	5.25E-06	-5.28	2.85%
Dy+3	1.09E-04	7.06E-06	-5.15	43.65%
DyCO3+	6.20E-15	4.57E-15	-14.34	0.00%
DyHCO3+2	1.01E-11	2.99E-12	-11.52	0.00%
DyOH+2	1.74E-10	5.14E-11	-10.29	0.00%
DySO4+	1.34E-04	9.87E-05	-4.01	53.51%
Eu(CO3)2-	1.12E-26	8.23E-27	-26.08	0.00%
Eu(SO4)2-	2.43E-05	1.79E-05	-4.75	9.73%
Eu+3	9.37E-05	6.06E-06	-5.22	37.49%
EuCO3+	4.43E-15	3.27E-15	-14.49	0.00%
EuHCO3+2	8.11E-12	2.40E-12	-11.62	0.00%
EuOH+2	1.01E-10	2.98E-11	-10.53	0.00%
EuSO4+	1.32E-04	9.73E-05	-4.01	52.78%
Fe(OH)2+	6.04E-05	4.46E-05	-4.35	0.17%
Fe(OH)3 (aq)	6.70E-12	7.10E-12	-11.15	0.00%
Fe(OH)4-	5.44E-17	4.01E-17	-16.40	0.00%
Fe(SO4)2-	1.20E-03	8.83E-04	-3.05	3.30%
Fe+3	4.83E-03	3.12E-04	-3.51	13.31%
Fe2(OH)2+4	1.30E-03	9.99E-06	-5.00	3.58%
Fe3(OH)4+5	2.03E-04	1.01E-07	-7.00	0.56%
FeOH+2	2.85E-03	8.45E-04	-3.07	7.86%
FeSO4+	2.58E-02	1.91E-02	-1.72	71.22%
Mg+2	8.51E-02	2.52E-02	-1.60	85.14%
Mg2CO3+2	1.49E-16	4.41E-17	-16.36	0.00%
MgCO3 (aq)	3.53E-16	3.74E-16	-15.43	0.00%
MgHCO3+	4.69E-10	3.46E-10	-9.46	0.00%
MgOH+	3.71E-11	2.73E-11	-10.56	0.00%
MgSO4 (aq)	1.49E-02	1.57E-02	-1.80	14.86%
Sc(OH)2+	5.96E-11	4.40E-11	-10.36	0.00%
Sc(OH)3 (aq)	4.71E-17	4.99E-17	-16.30	0.00%
Sc(OH)4-	2.43E-22	1.79E-22	-21.75	0.00%
Sc(SO4)2-	1.72E-05	1.27E-05	-4.90	6.89%
Sc+3	4.19E-05	2.71E-06	-5.57	16.75%
Sc2(OH)2+4	7.77E-11	5.97E-13	-12.22	0.00%
ScOH+2	1.31E-07	3.87E-08	-7.41	0.05%
ScSO4+	1.91E-04	1.41E-04	-3.85	76.30%
Y(CO3)2-	1.44E-26	1.06E-26	-25.98	0.00%
Y(SO4)2-	1.98E-05	1.46E-05	-4.84	7.90%
Y+3	1.21E-04	7.80E-06	-5.11	48.25%
Y2(OH)2+4	4.06E-18	3.12E-20	-19.51	0.00%
YCO3+	5.70E-15	4.20E-15	-14.38	0.00%
YHCO3+2	7.39E-12	2.19E-12	-11.66	0.00%
YOH+2	1.18E-10	3.50E-11	-10.46	0.00%
YSO4+	1.10E-04	8.09E-05	-4.09	43.85%

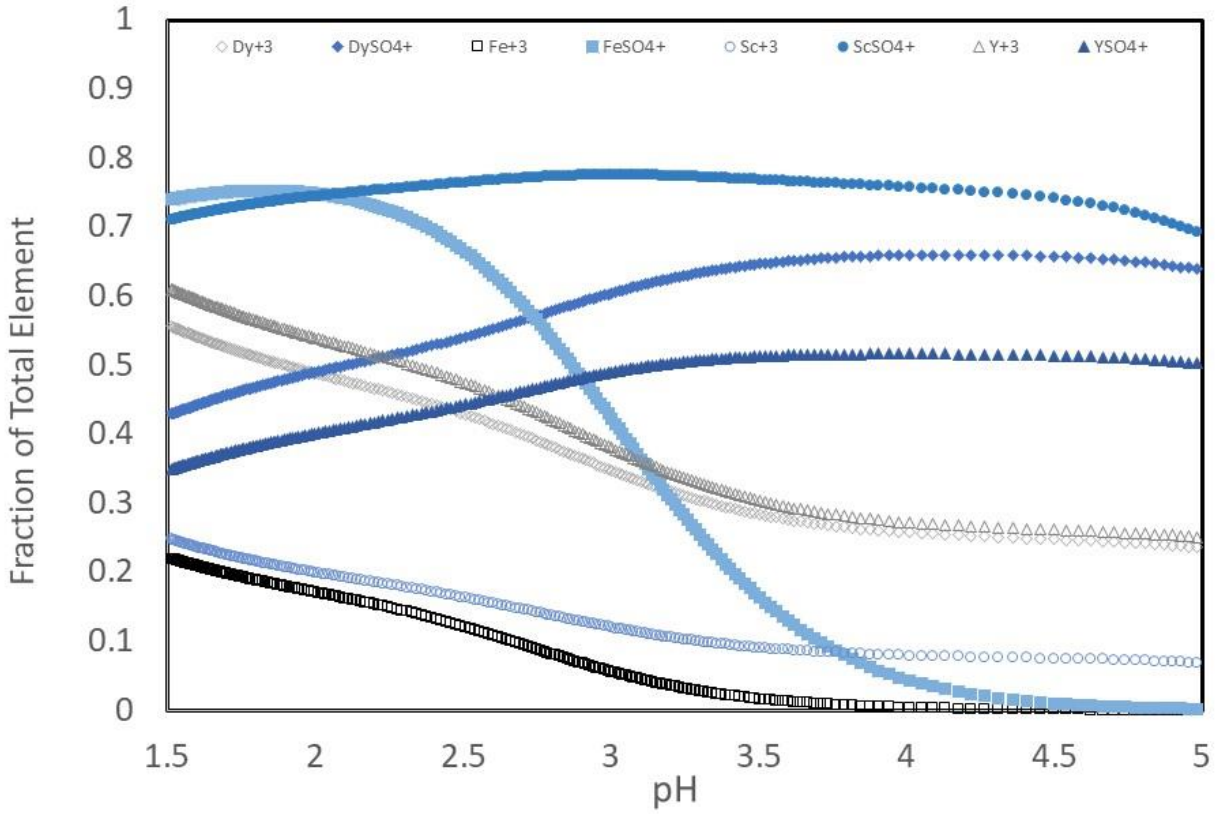

Figure 5 - 2: Visual Minteq calculated speciation for solutions using magnesium carbonate to precipitate iron based on 20 g/l ferric sulfate heptahydrate beginning at pH 1.5 with rare earth concentrations of approximately 10 ppm.

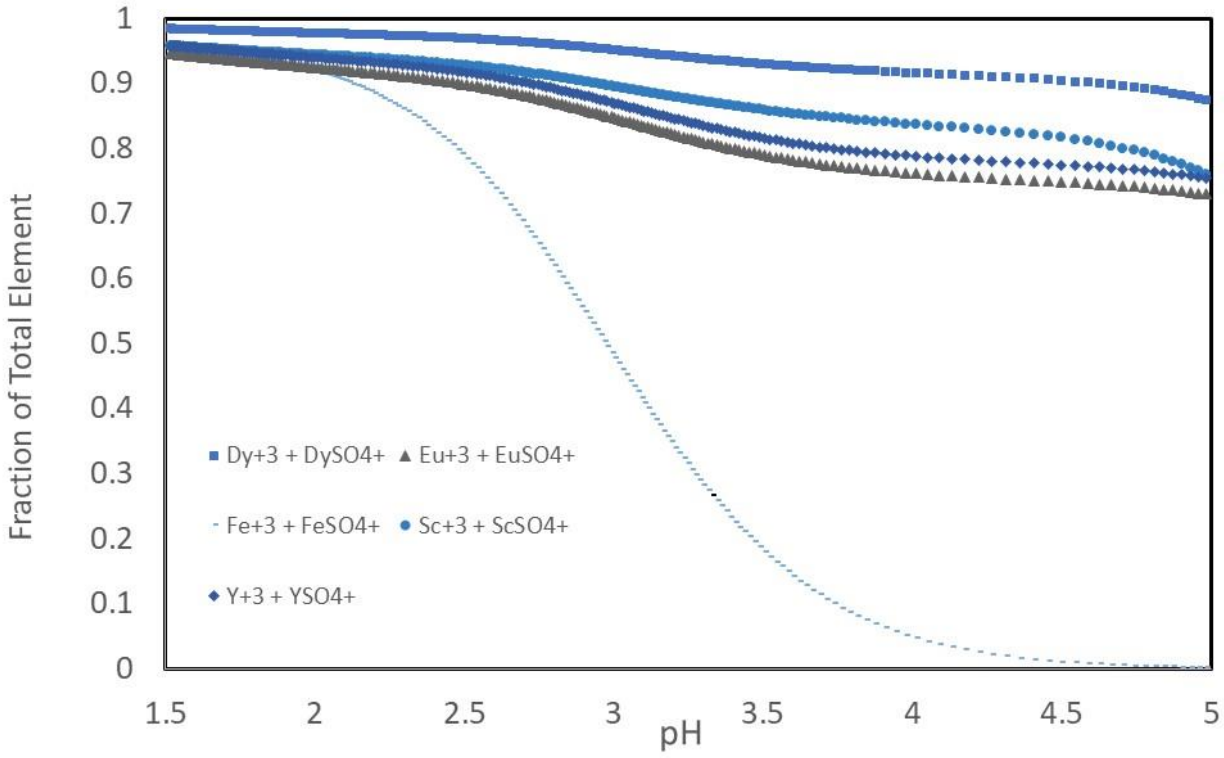

Figure 5 – 3: Visual Minteq calculated soluble sum of sulfate and metal ion fractions for solutions using magnesium carbonate to precipitate iron based on 20 g/l ferric sulfate heptahydrate beginning at pH 1.5 with rare earth concentrations of approximately 10 ppm.

Calculations show that various precipitates begin to form in iron rich solutions above approximately pH 2 that are relevant to our leaching solutions. These precipitation events can be helpful in selectively removing iron compounds such as goethite, ferrihydrite, jarosite, hematite, and magnetite. Calculated saturation indexes for these compounds as a function of pH are shown in Figures 5 - 4 and 5 - 5.

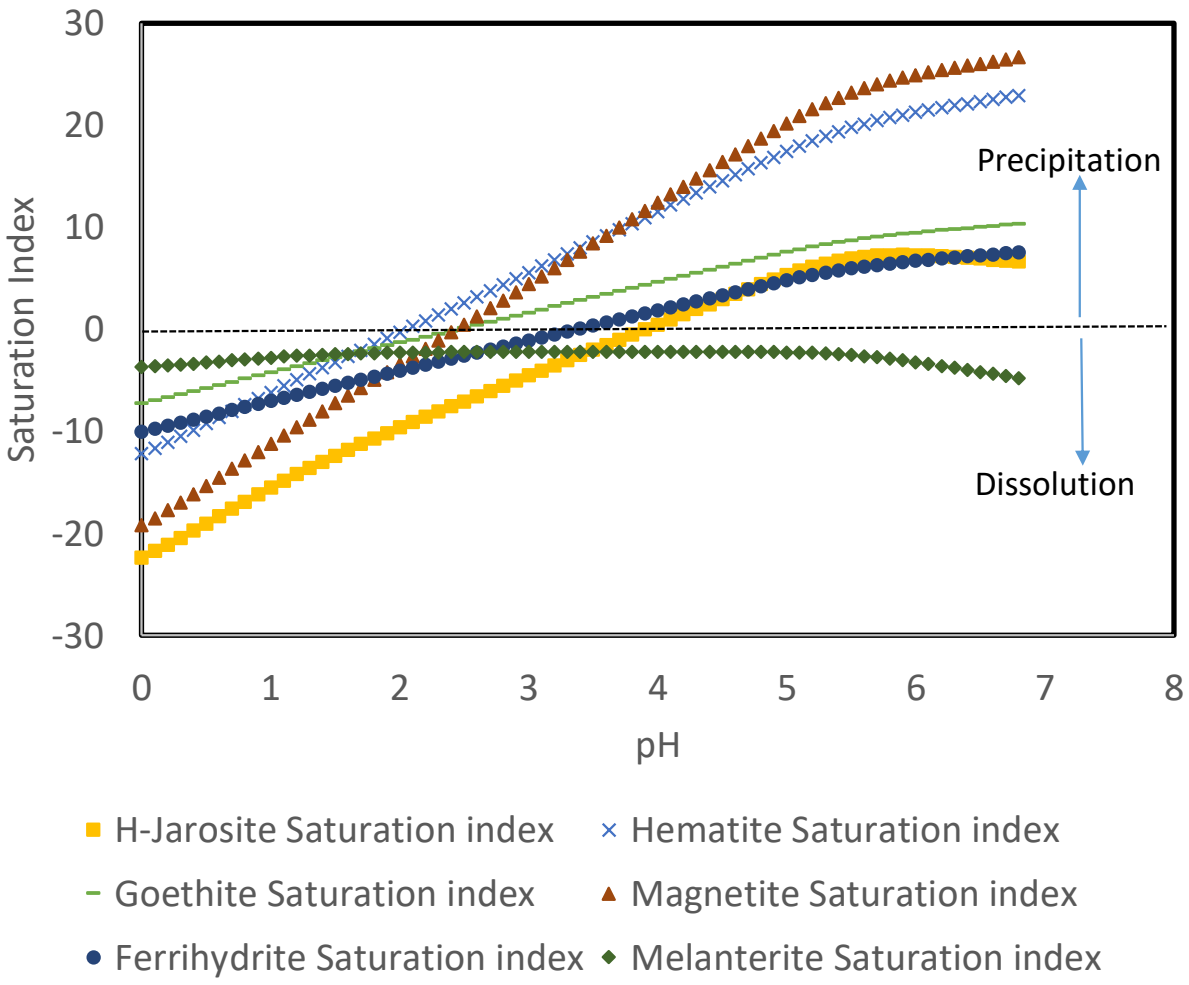

Figure 5 - 4: Comparison of saturation index values, which indicate precipitate formation is feasible if above zero, as a function of pH for a solution containing 2 grams per liter of iron as iron sulfate (50 % ferric iron and 50 % ferrous iron). (Visual Minteq 3.1 calculations)

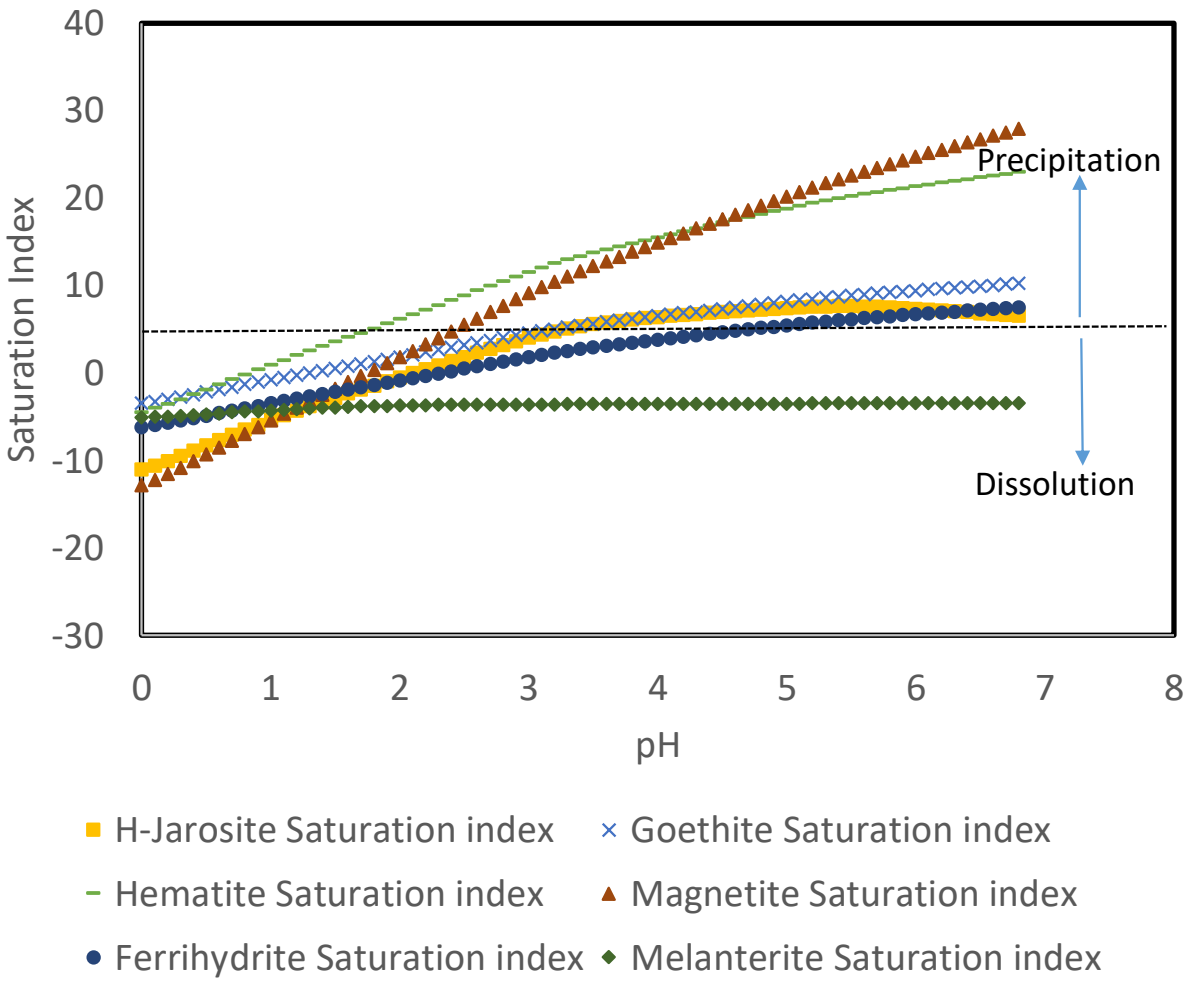

Figure 5 - 5: Comparison of saturation index values, which indicate precipitate formation is feasible if above zero, as a function of pH for a solution containing 2 grams per liter of iron as iron sulfate (94 % ferric iron and 6 % ferrous iron). (Visual Minteq 3.1 calculations)

The data in these saturation index based calculations show that hematite begins to precipitate at about pH 2 when there is an equal ratio of ferrous and ferric iron in solution, whereas the pH decreases to about 1.8 when the ratio of ferric to ferrous iron is increased to 94 % ferric iron and 6 % ferrous iron. Thus, these figures suggest that some iron precipitation is feasible at moderate pH and that the higher ratio of ferric to ferrous iron facilitates precipitation at lower pH levels.

The calculation of the soluble species for the same scenarios shown previously indicate a drop in solubility near a pH of 5.5 if the ratio of ferrous iron to ferric iron is 19:1 as shown in Figure 5 - 6. However, if the ferrous iron to ferric iron is reversed to 1:19, the pH for reduced solubility is decreased to pH 4 as shown in Figure 5 - 7.

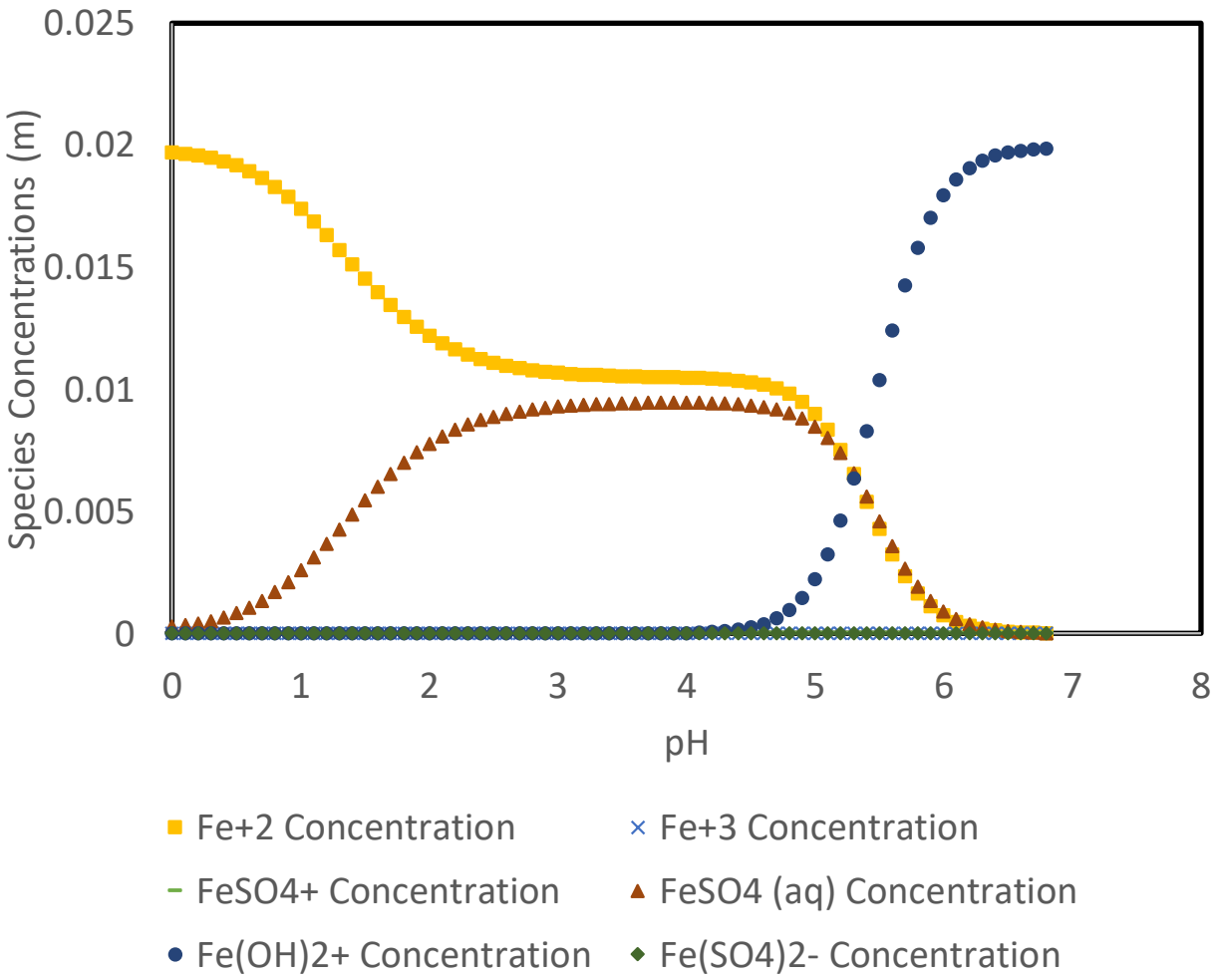

Figure 5 - 6: Comparison of species solution concentrations as a function of pH for a solution containing 2 grams per liter of iron as iron sulfate (6 % ferric iron and 94 % ferrous iron). (Visual Minteq 3.1 calculations)

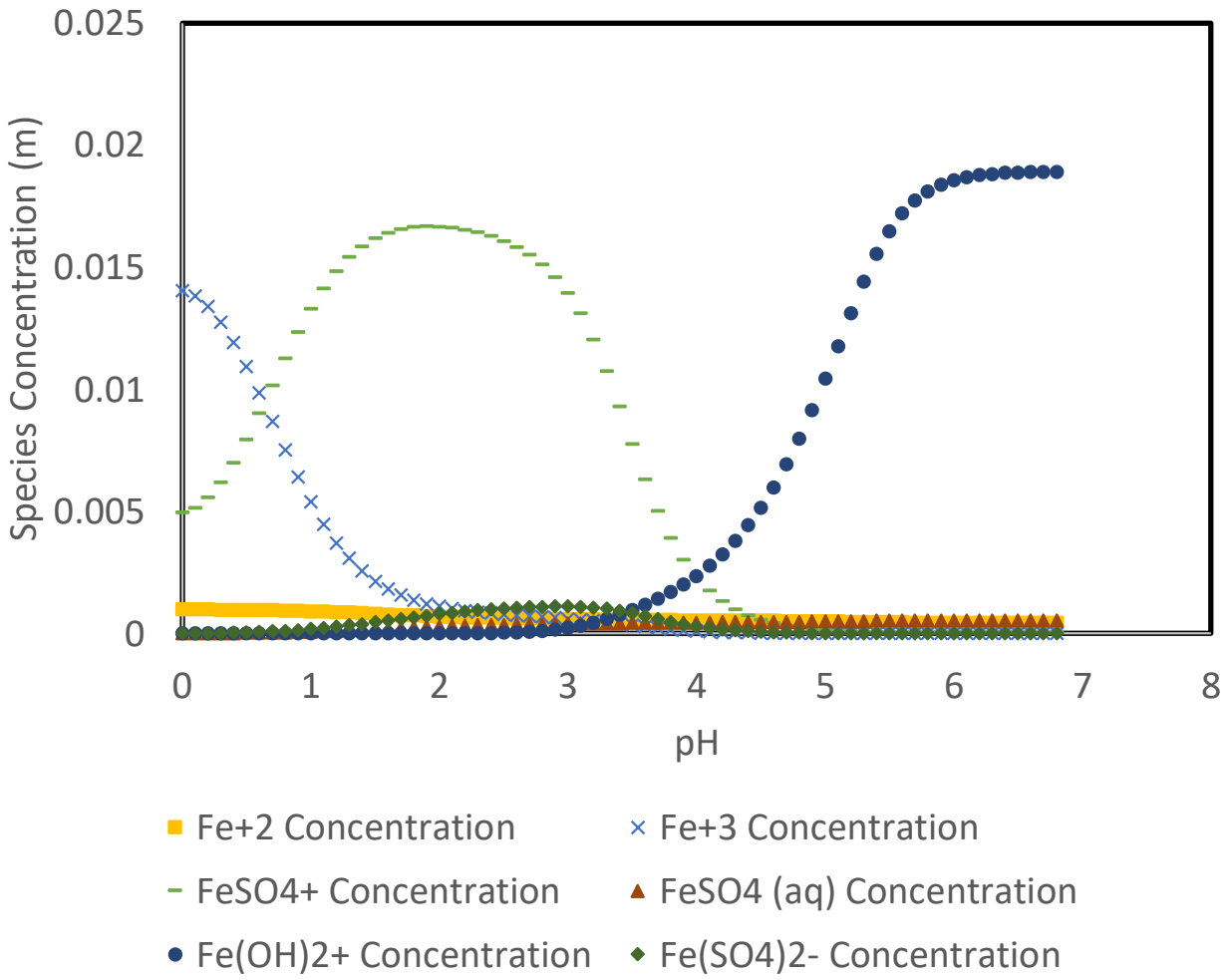

Figure 5 - 7: Comparison of species solution concentrations as a function of pH for a solution containing 2 grams per liter of iron as iron sulfate (94 % ferric iron and 6 % ferrous iron). (Visual Minteq 3.1 calculations)

In order to test the theoretical calculations and evaluate the potential for loss of REEs, precipitation tests were performed on leaching solutions from column 1 and column 3.

Leachate from column 3 was adjusted to an Eh of 650mv, and the resulting solution was centrifuged and the solution obtained. 100ml of leaching solution was used for Test 1 in which magnesium carbonate was added to adjust the pH. Test 2 involved calcium dihydroxide as the pH adjusting species. During the pH adjustment tests, the solutions were heated up to 50°C, then 10 mL of a 1 M solution was added followed by pH measurement before another dose of 10 mL of 1 M alkali solution was added. The resulting samples were allowed to settle and the final pH values were recorded as noted in Figures 5 - 8 and 5 - 9 which show the resulting solutions and precipitates.

	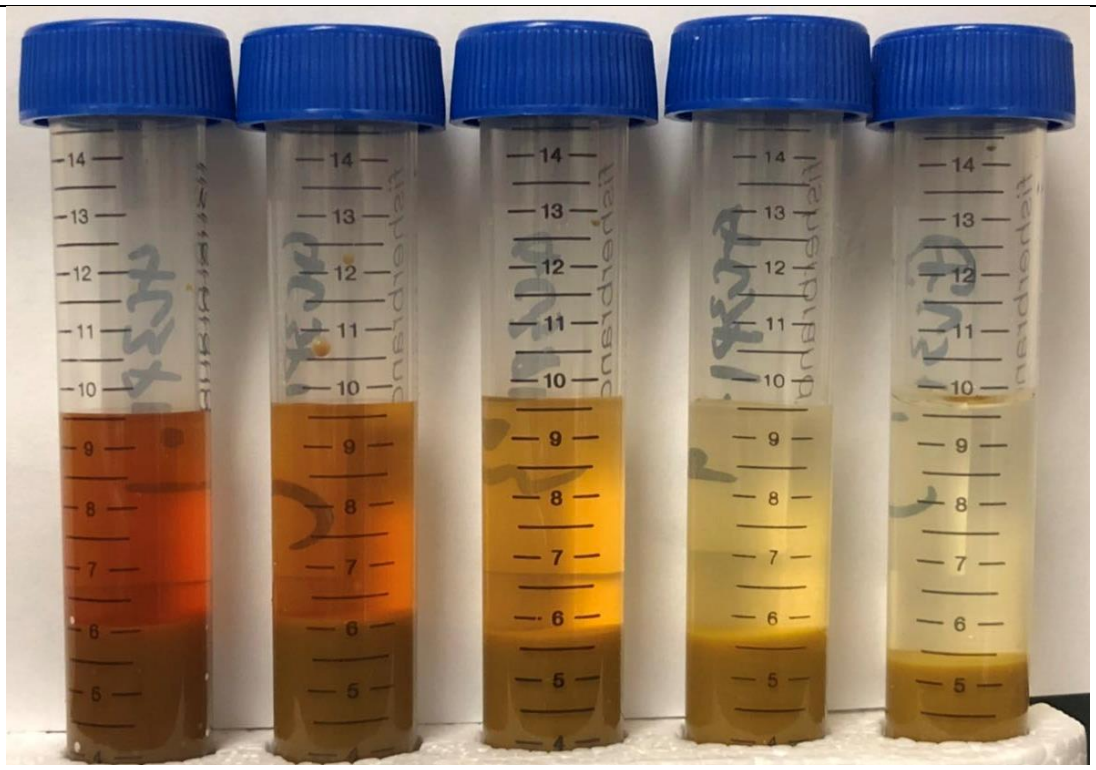				
pH-50°C	1.952	1.875	2.142	2.281	3.283
pH-25°C	2.14	2.14	2.22	2.43	3.82

Figure 5 - 8: Precipitates and solutions formed by the addition of varying amounts of magnesium carbonate to leaching solution from column 3 to adjust the pH to the level shown.

Test 2	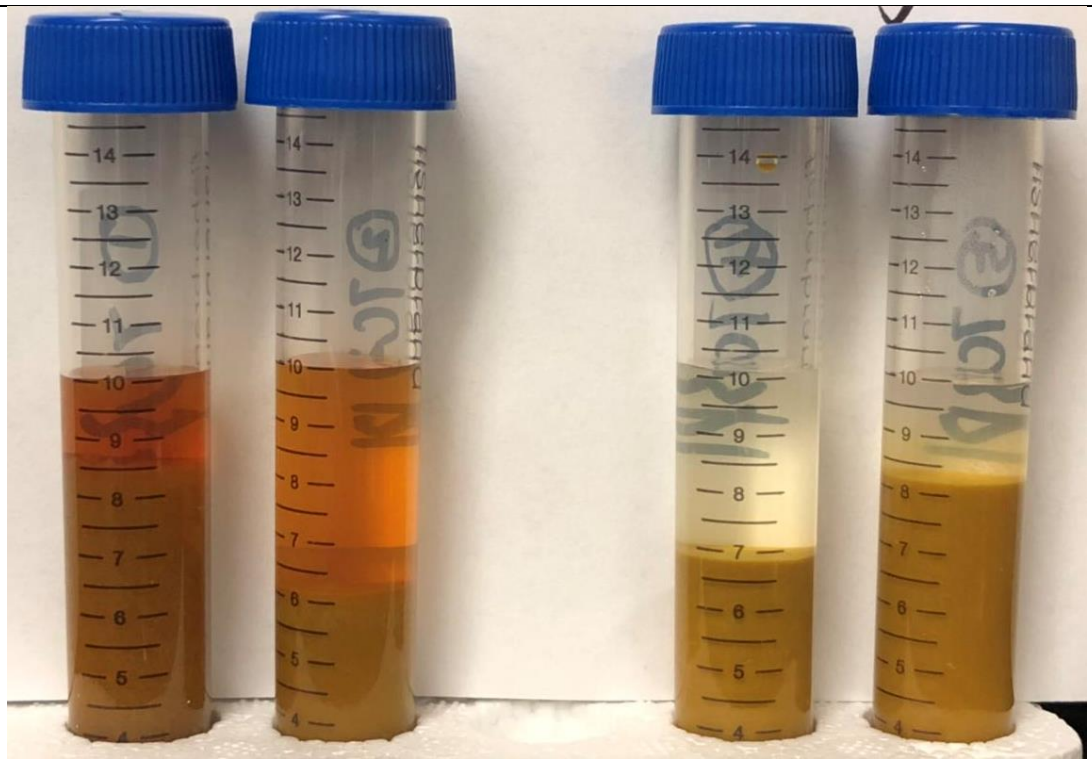				
pH-50°C	1.930	2.033	2.118	2.809	4.189
pH-25°C	2.21	2.32	Na	3.44	5.50

Figure 5 - 9: Precipitates and solutions formed by the addition of varying amounts of calcium dihydroxide to leaching solution from column 3 to adjust the pH to the level shown.

After column leaching, leachate was oxidized using bacteria to increase the Eh of the solution to 600 mV (relative to a silver/silver chloride reference). As the Eh increased, a precipitate formed as shown in Figure 5 - 10.

Figure 5 - 10: - Precipitate formed by biooxidation of leachate from large column 1.

The precipitate that formed was analyzed to determine if rare earth elements were precipitated and to determine the compounds that formed. Inductively Coupled Plasma Mass Spectroscopy (ICP-MS) analysis of the solutions before and after precipitation indicated that the rare earth content was only 2.9 ppm in solution, and the total REEs lost to this precipitate amounted to only 0.48 % of the total REEs in the column leachate, which shows excellent recovery of the rare earth elements in the solution phase after iron precipitation. An X-Ray Diffraction (XRD) analysis of the precipitate, shown in Figure 5 - 11, indicates the precipitate is a jarosite compound. The general composition of jarosite is $NaFe_3(SO_4)_2(OH)_6$, although it should be noted that significant substitution of elements such as K for Na often takes place. It is important to note that jarosite removes both iron and sulfate without increasing the pH substantially. Thus, this approach seems viable for removal of excess iron and sulfate without significant loss of REEs.

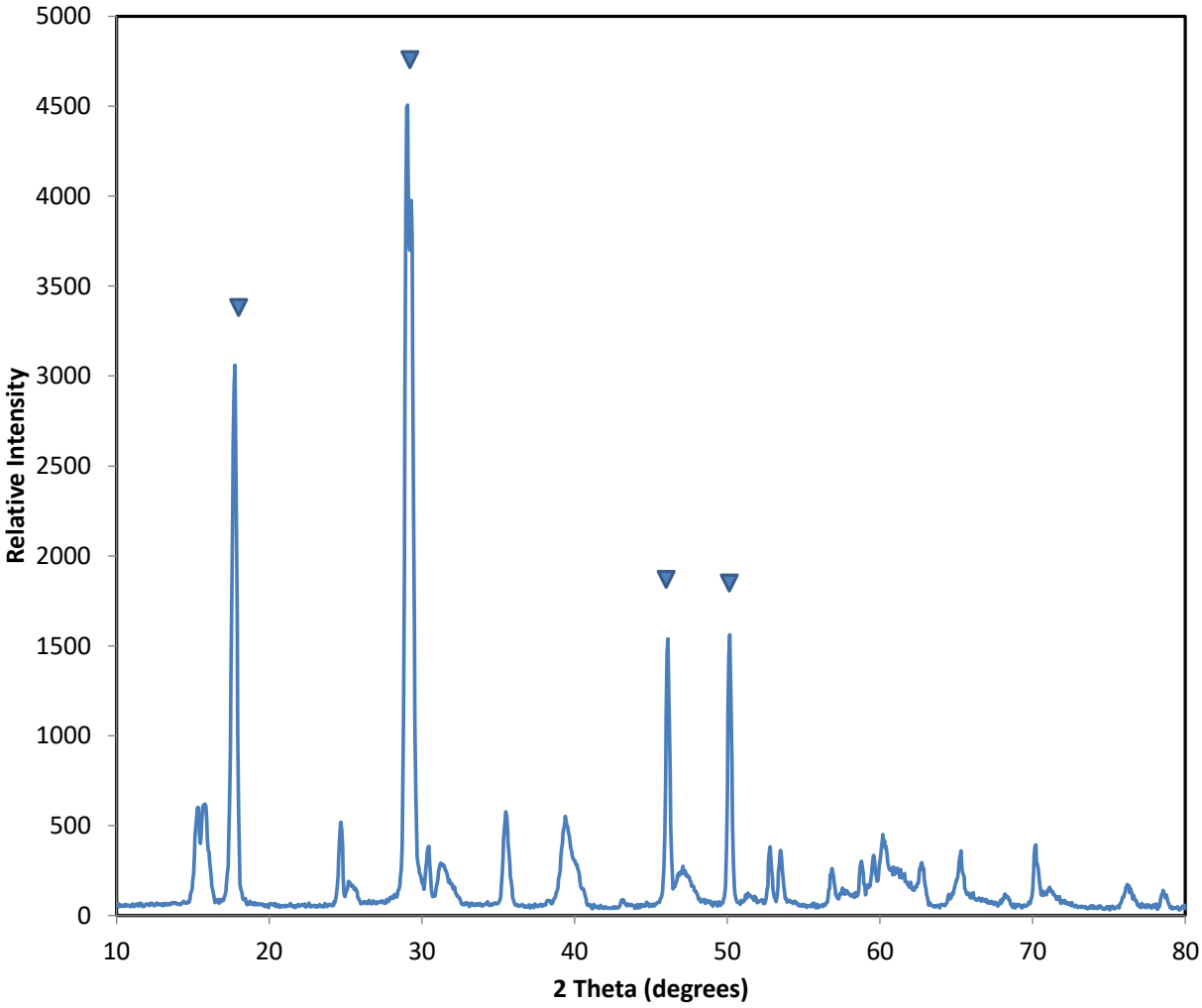

Figure 5 - 11: XRD data for precipitate from column 1 after biooxidation to 600 mV Eh level. The triangles represent major peaks for jarosite type compounds.

The analysis of the remaining solution after precipitation at pH 2.4, which followed biooxidation to 600 mV showed no significant loss of REEs from solution.

5.2 Precipitation Modeling Information

Modeling of precipitation behavior of rare earth elements in solutions containing ferric sulfate from the biooxidation of pyrite was performed using Visual Minteq 3.1. The model was based on an input of 10 g/l of ferric sulfate heptahydrate and 50 ppm of lanthanum and 50 ppm of dysprosium to simulate the effect of pH on precipitation of iron and rare earth elements. The software calculated the following species existing at the concentrations shown in Table 5 - 2 at a pH of zero. It should be noted that the high concentration of dissolved constituents can make the model less accurate, so the accuracy of the results is likely to be impacted by a few percent. Also, it should be noted that only a few of the most common species in the model database were

considered, and it is possible that other species exist and could alter the results from model predictions.

As indicated in the data in Table 5 - 2, the primary soluble species with significant concentration levels at pH 0 are metal ions and metal sulfate ions (Fe^{3+}, $FeSO_4^+$, Dy^{3+}, $DySO_4^+$, La^{3+}, $LaSO_4^+$). As the pH rises, the reducing concentration of H^+ ions, makes sulfate more available to complex with the metal ions as indicated in Eq. (5-1):

$$H^+ + SO_4^{2-} \leftrightarrow HSO_4^- \qquad (5\text{-}1)$$

It shows that as H^+ is removed, HSO_4^- separates into H^+ and SO_4^{2-}. The excess SO_4^{2-} is then available to form soluble metal sulfate complexes as illustrated in Figures 5 - 12 to 5 - 16. As shown in Figure 5 - 12, soluble ferric iron is generally removed from solution beginning at a pH of around 2.5 and finishing at a pH of around 4.3. However, it should also be noted that for iron, some precipitates such as jarosite and hematite can precipitate between a pH of 1 and 2 as shown in Figure 5 - 15 by the saturation index, which indicates precipitation is thermodynamically favorable above a value of 0, although in practice it is higher. Figures 5 - 13 and 5 - 14 show that rare earth compounds remain soluble or do not begin to precipitate until a much higher pH of around 8 is achieved. Figure 5 - 16 shows that if the iron is in the form of ferrous ions, it will remain as either soluble $FeSO_4(aq)$ or Fe^{2+} until the pH reaches about 9. Therefore, if the ferrous iron is not oxidized to Fe^{3+} completely, it will precipitate with the rare earth elements. However, if the dissolved iron is oxidized to Fe^{3+} the large differences in speciation and precipitation of iron and rare earth elements make it is possible to easily remove iron from solution by precipitation without substantial losses of rare earth elements.

However, in practice, precipitation requires the use of a basic compound such as sodium hydroxide. In industry it is common to use a very low cost base such as calcium oxide to perform precipitation reactions. When calcium oxide is used to perform the precipitation in sulfate solutions, the resulting product is a mixture of gypsum, which also removes the sulfate, and iron hydroxide/oxide solids. Because the gypsum removes the sulfate, which is the main complexing agent for the rare earth elements, some of the rare earth elements precipitate with the gypsum and iron hydroxide/oxide solids. The coprecipitation of the desired rare earth element product with the waste material reduces the product yield. Because the magnesium sulfate solubility product is approximately 500,000 times larger than that of calcium sulfate (0.00009), the sulfate remains in solution and is able to stabilize rare earth solubility through complexation. Consequently, the use of magnesium carbonate can result in a higher recovery of the rare earth elements. Thus, from a commercial viability perspective, we have used magnesium carbonate as our pH adjustment medium for removing iron. Figures 5 - 17 to 5 - 20 show the speciation associated with changing the pH using magnesium carbonate rather than hydroxide. Figure 5 - 20 confirms that the increasing addition of magnesium carbonate increases magnesium availability while also increasing sulfate availability by removing acid, which normally complexes with sulfate to make it less available. Thus, magnesium carbonate helps to maintain rare earth element solubility during

precipitation of iron, which is nearly completely removed using magnesium carbonate at a pH approaching 4 as shown in the figures.

Table 5 - 1: Speciation of iron, lanthanum, and dysprosium using an input of 10 g/l of ferric sulfate heptahydrate and 50 ppm of lanthanum and 50 ppm of dysprosium at pH = 0 based on Visual Minteq 3.1 calculations.

Species	Concentration (m)
$Dy(SO_4)^{2-}$	1.95E-07
Dy^{+3}	2.70E-04
$DyOH^{+2}$	1.73E-12
$DySO_4^{+}$	3.94E-05
$Fe(OH)_2^{+}$	4.43E-09
$Fe(OH)_3$ (aq)	1.55E-18
$Fe(OH)_4^{-}$	4.79E-26
$Fe(SO_4)_2^{-}$	6.35E-05
Fe+3	2.32E-02
$Fe_2(OH)_2^{+4}$	3.81E-07
$Fe_3(OH)_4^{+5}$	3.43E-12
$FeOH^{+2}$	5.52E-05
$FeSO_4^{+}$	1.47E-02
H^{+1}	1.32E+00
HSO_4^{-}	4.11E-02
$La(SO_4)^{2-}$	7.09E-07
La^{+3}	3.11E-04
$LaOH^{+2}$	1.20E-13
$LaSO_4^{+}$	4.85E-05
OH-	1.30E-14
SO_4^{-2}	9.57E-04

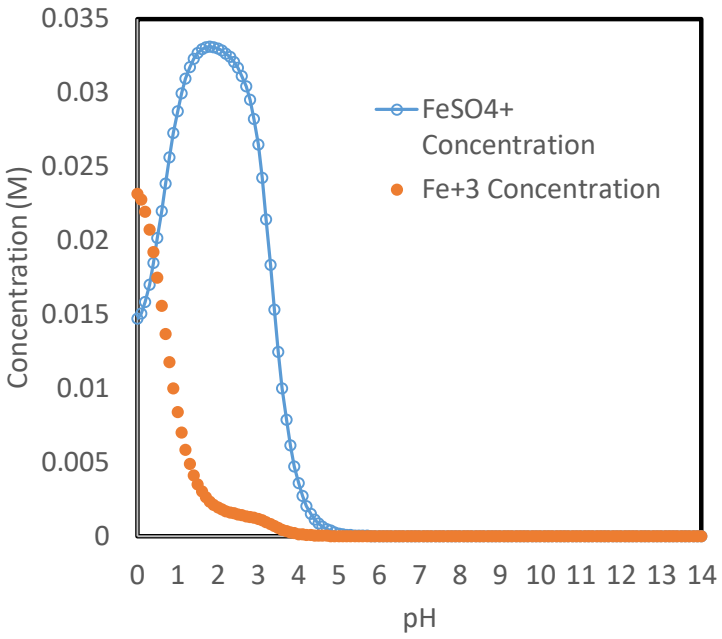

Figure 5 - 12: Comparison of Visual Minteq 3.1 calculated Fe^{3+} and $FeSO_4^+$ concentrations as a function of pH for a system containing 10 g/l of ferric sulfate heptahydrate and 50 ppm of lanthanum and 50 ppm of dysprosium.

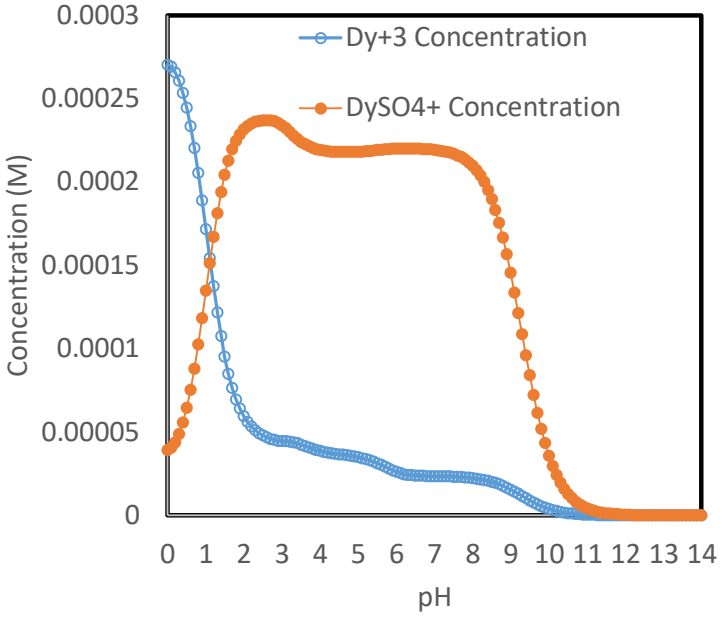

Figure 5 - 13: Comparison of Visual Minteq 3.1 calculated Dy^{3+} and $DySO_4^+$ concentrations as a function of pH for a system containing 10 g/l of ferric sulfate heptahydrate and 50 ppm of lanthanum and 50 ppm of dysprosium.

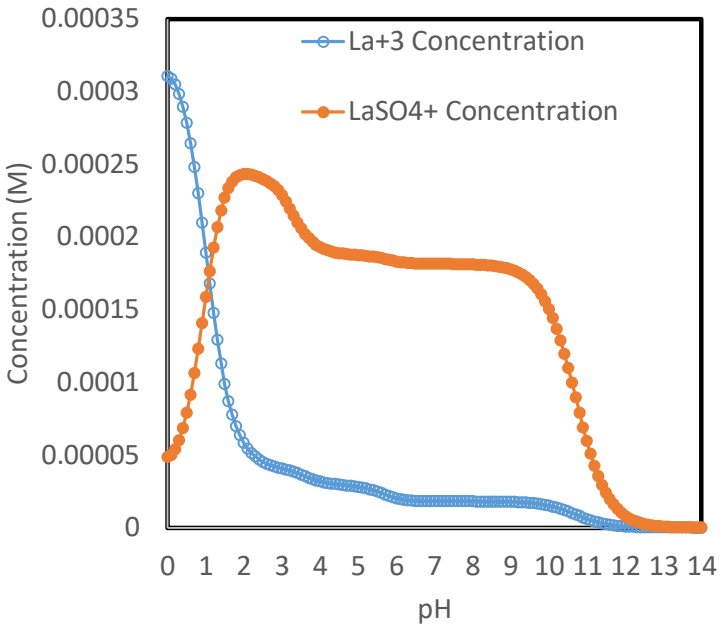

Figure 5 - 14: Comparison of Visual Minteq 3.1 calculated La^{3+} and $LaSO_4^+$ concentrations as a function of pH for a system containing 10 g/l of ferric sulfate heptahydrate and 50 ppm of lanthanum and 50 ppm of dysprosium.

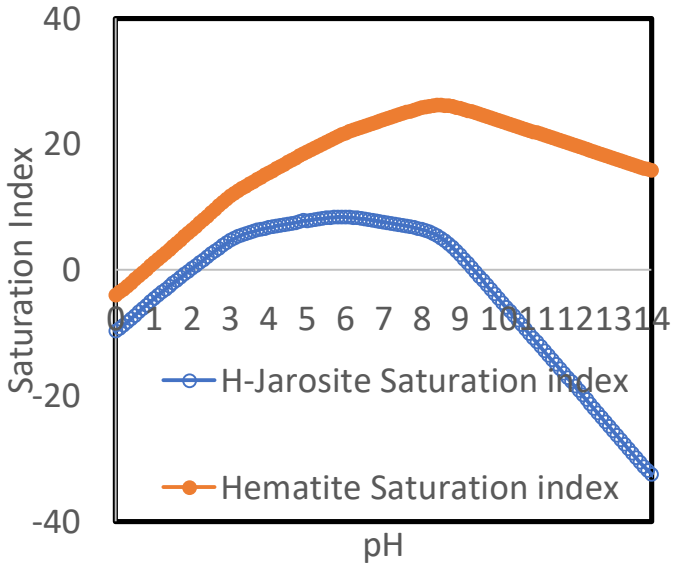

Figure 5 - 15: Comparison of Visual Minteq 3.1 calculated hematite and jarosite saturation index values as a function of pH for a system containing 10 g/l of ferric sulfate heptahydrate and 50 ppm of lanthanum and 50 ppm of dysprosium.

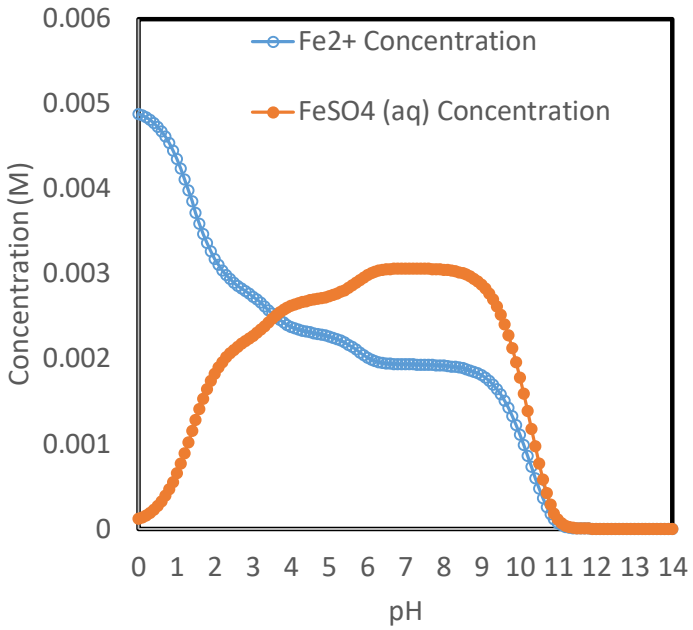

Figure 5 - 16: Comparison of Visual Minteq 3.1 calculated ferrous and ferrous sulfate concentrations es as a function of pH for a system containing 10 g/l of ferric sulfate heptahydrate and 50 ppm of lanthanum and 50 ppm of dysprosium, as well as 0.005 M Fe^{2+}.

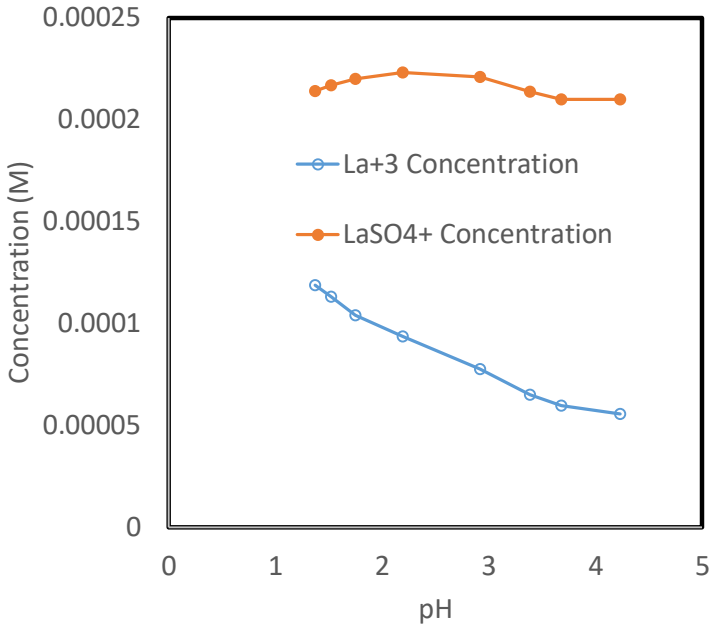

Figure 5 - 17: Comparison of Visual Minteq 3.1 calculated Fe^{3+} and $FeSO_4^+$ concentrations as a function of pH for a system containing 10 g/l of ferric sulfate heptahydrate and 50 ppm of lanthanum and 50 ppm of dysprosium with magnesium carbonate used to adjust the pH.

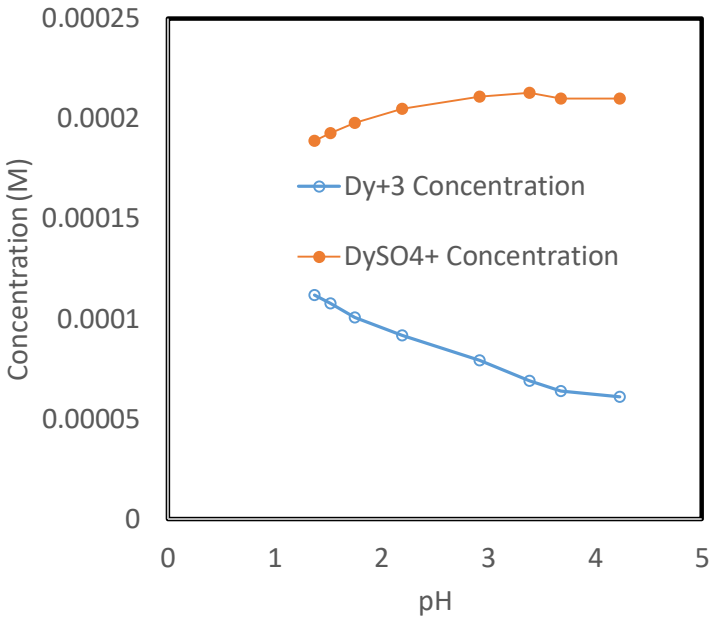

Figure 5 - 18: Comparison of Visual Minteq 3.1 calculated Dy^{3+} and $DySO_4^{+}$ concentrations as a function of pH for a system containing 10 g/l of ferric sulfate heptahydrate and 50 ppm of lanthanum and 50 ppm of dysprosium with magnesium carbonate used to adjust the pH.

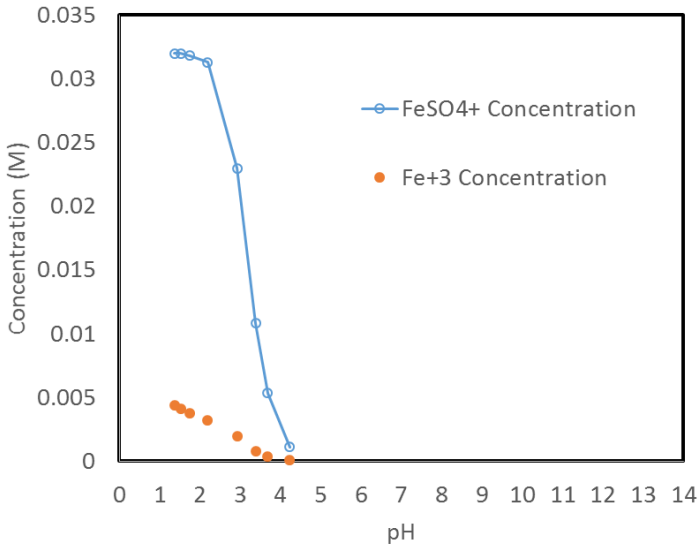

Figure 5 - 19: Comparison of Visual Minteq 3.1 calculated La^{3+} and $LaSO_4^{+}$ concentrations as a function of pH for a system containing 10 g/l of ferric sulfate heptahydrate and 50 ppm of lanthanum and 50 ppm of dysprosium with magnesium carbonate used to adjust the pH.

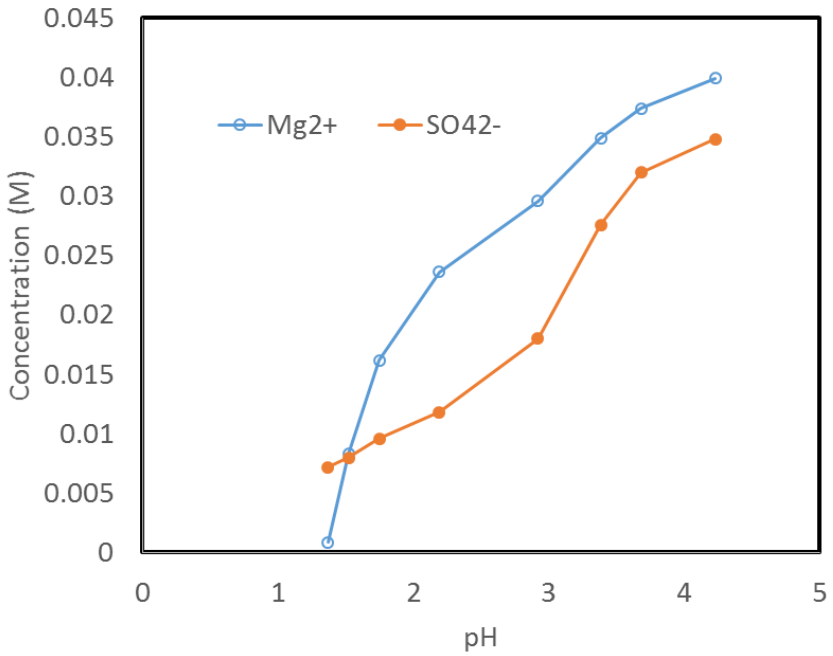

Figure 5 - 20: Comparison of Visual Minteq 3.1 calculated Mg^{2+} and SO_4^{2-} concentrations as a function of pH for a system containing 10 g/l of ferric sulfate heptahydrate and 50 ppm of lanthanum and 50 ppm of dysprosium with magnesium carbonate used to adjust the pH.

5.3 Selected Data from Precipitation Experiments

$Fe_2(SO_4)_3$(Mallinckrodt AR) and/ $La_2(SO_4)_3$ (Alorich ≥99.99%) were used to prepare the solution of $La_2(SO_4)_3$ with 1000 PPM of La^{3+} and $Fe_2(SO_4)_3$ with 20000 PPM of Fe^{3+}, respectively. Then, 20mL of various solutions described above was used in each sample of the precipitation experiments and for pH adjustment either of HCl, NaOH or $MgCO_3$, was added to the solution samples to change the pH value. Sufficient time ~ up to 48 hours was allowed for complete precipitation. The pH and Eh of various samples were measured by a pH Meter (Thermo Scientific Orion Star 211) and a pH Electrode (Oakton WD-35805-05) or a ORP ATC Combination Triode Electrode (Thermo Scientific Orion 9179BNMD). The pH Electrode was calibrated by the pH 4.01, 7.00, and 10.01 Buffer solution (Hach) and the ORP ATC Combination Triode Electrode was calibrated by an a standard $Fe(NH_4)_2(SO_4)_2$ - $Fe(NH_4)(SO_4)_2$ redox solution before each measurement. The precipitate of each sample was filtered through a filter funnel. Then, the filter paper was dried and weighted. As a result, the amount of each precipitate was obtained.

The relationships between the amount of precipitate and pH for $Fe_2(SO_4)_3$ and $La_2(SO_4)_3$ solution when used HCl and NaOH solution to change pH are shown in Figure 5 - 21.

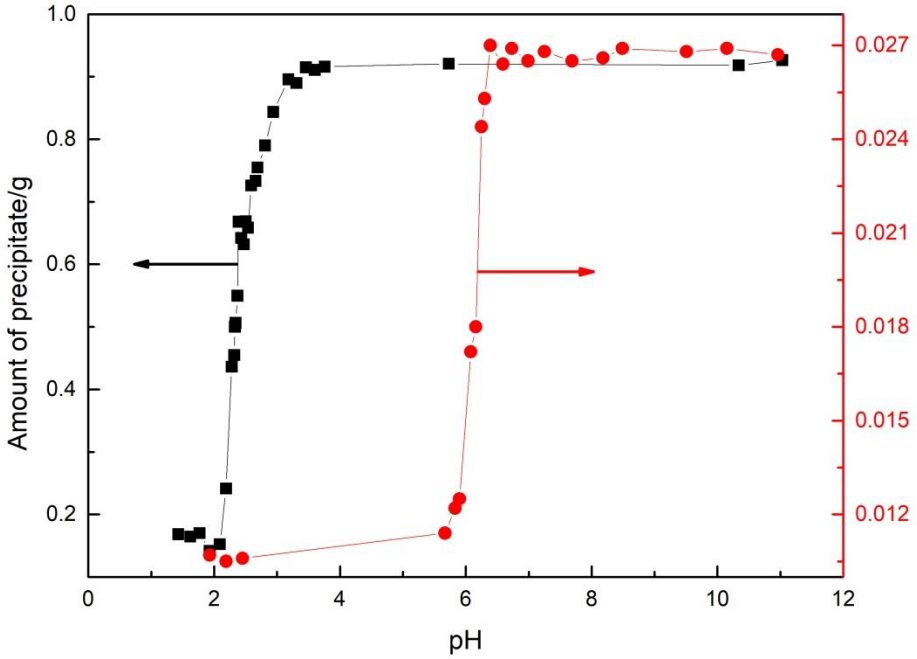

Figure 5 - 21: Amount of precipitate versus pH value for different solution with using HCl and NaOH solution to change pH value (■- $Fe_2(SO_4)_3$ solution; ●- $La_2(SO_4)_3$ solution)

As can be seen in Figure 5 - 21, precipitation of iron began at pH of about 2, and at about 3.5, the precipitation was mostly completed. Meanwhile, lanthanum started to precipitate at pH of ~ 5.5 and most precipitation completed at a pH of 6.4. On the base of above analysis, if in order to separate La^{3+} from Fe^{3+} through precipitation by using NaOH solution, the pH value of 3.5-5.5 is recommended. The project team also conducted precipitation tests using $MgCO_3$. The relationships between the amount of precipitate and pH for $Fe_2(SO_4)_3$ solution when used HCl solution and $MgCO_3$ emulsion to change pH are shown in Figure 5 - 22.

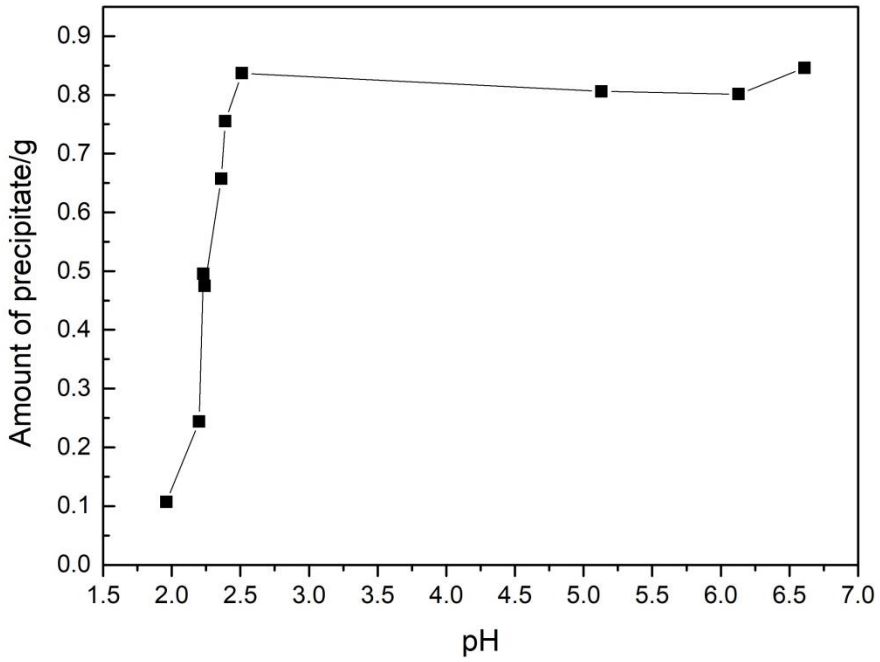

Figure 5 - 22: Amount of precipitate versus pH value for different solution with using sulfuric acid solution and $MgCO_3$ emulsion to change pH values.

Figure 5 – 22 shows that if $MgCO_3$ emulsion was used to increase the pH value of $Fe_2(SO_4)_3$ instead of NaOH solution, iron starts to precipitate at pH of about 2 and total precipitation occurs at pH of 2.5. It was thus it is thought that if precipitation was used to separate La^{3+} from Fe^{3+} with using $MgCO_3$ emulsion, the pH value could be lower.

5.4 Precipitation result from coal waste leaching material

The previous tests were modeled and tested using artificial solutions used to simulate the leaching environment. Tests have been performed on leaching solutions from coal waste. Results from these leaching solutions are shown in Figures 5 - 23 and 5 - 24. Results from testing of precipitation of iron using magnesium carbonate are presented in Figure 5 – 23. After precipitation of iron, the solution becomes clear as shown in Figure 5 - 24, further precipitation to remove REEs is shown in the next figure, followed by the dried precipitate in the final right-hand-side pictures in Figure 5 - 24. Initial analysis results of energy dispersive spectroscopy of the rare earth element bearing powder shown in Figure 5 - 24 are shown in the figures presented in Figure 5 - 25. Figure 5 - 25 shows that elements such as europium, dysprosium, and erbium are present in significant quantities in the powder.

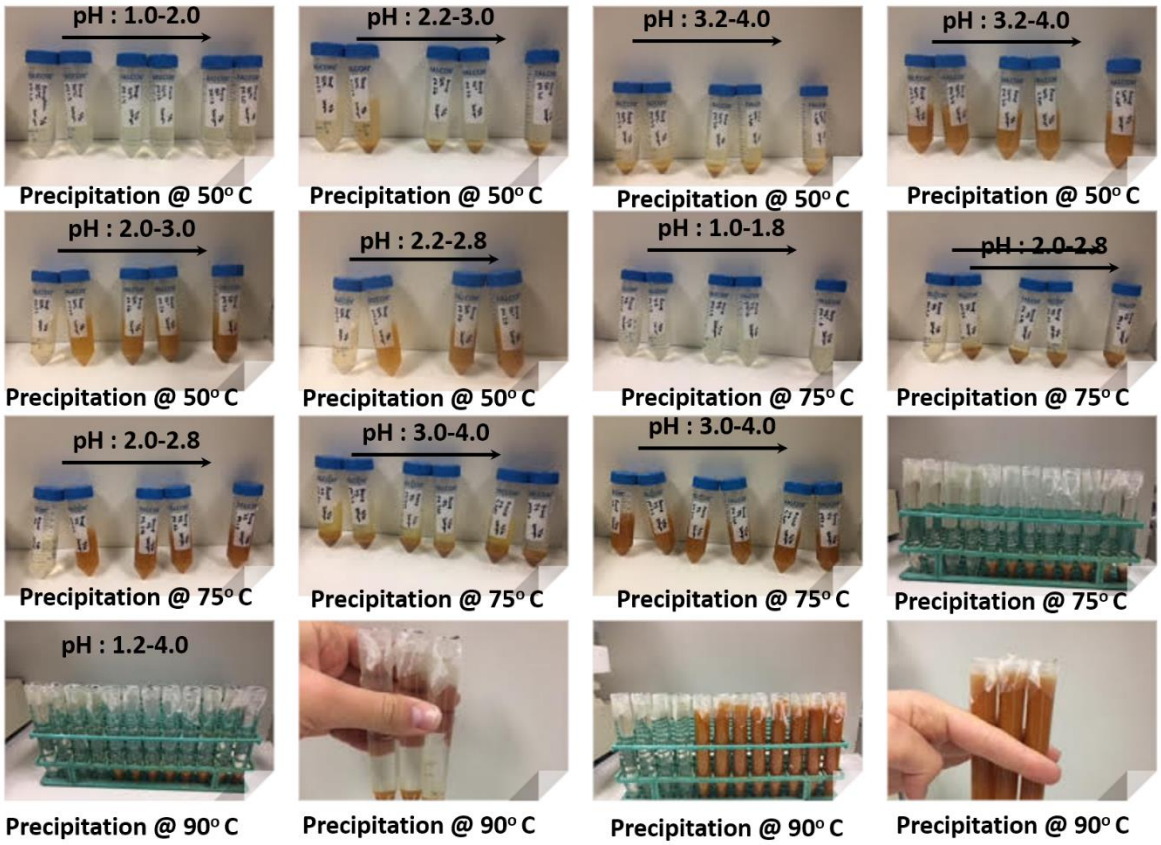

Figure 5 - 23: Comparison of precipitation products produced using magnesium carbonate from leaching solutions at different temperatures and pH levels.

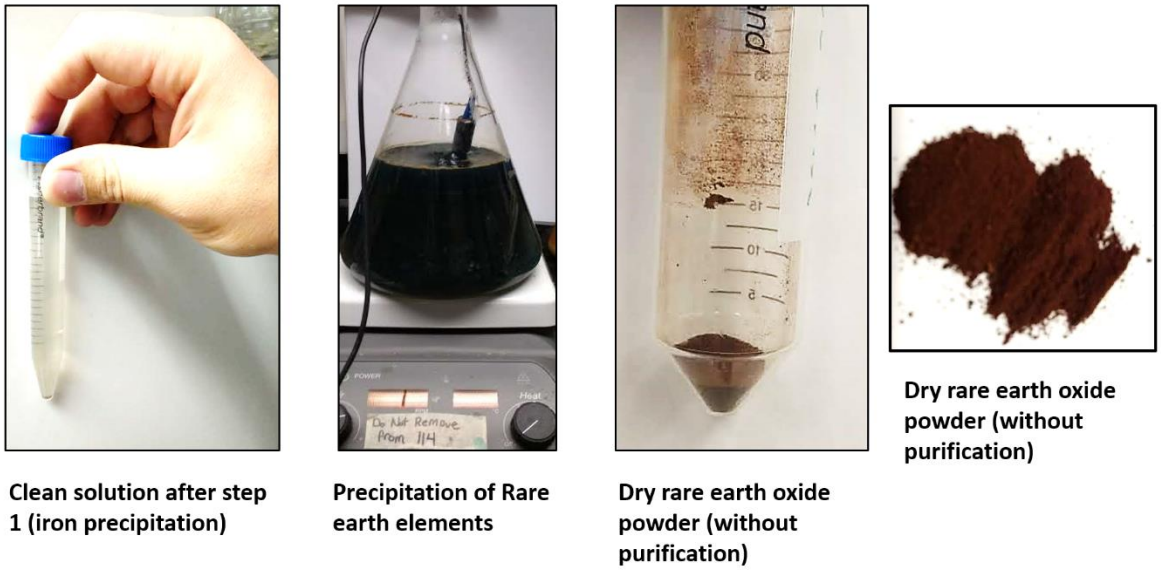

Figure 5 - 24: Pictures of precipitation products produced after removal of iron from leaching solutions at 75ºC using magnesium carbonate illustrating additional precipitation of powder containing rare earth elements.

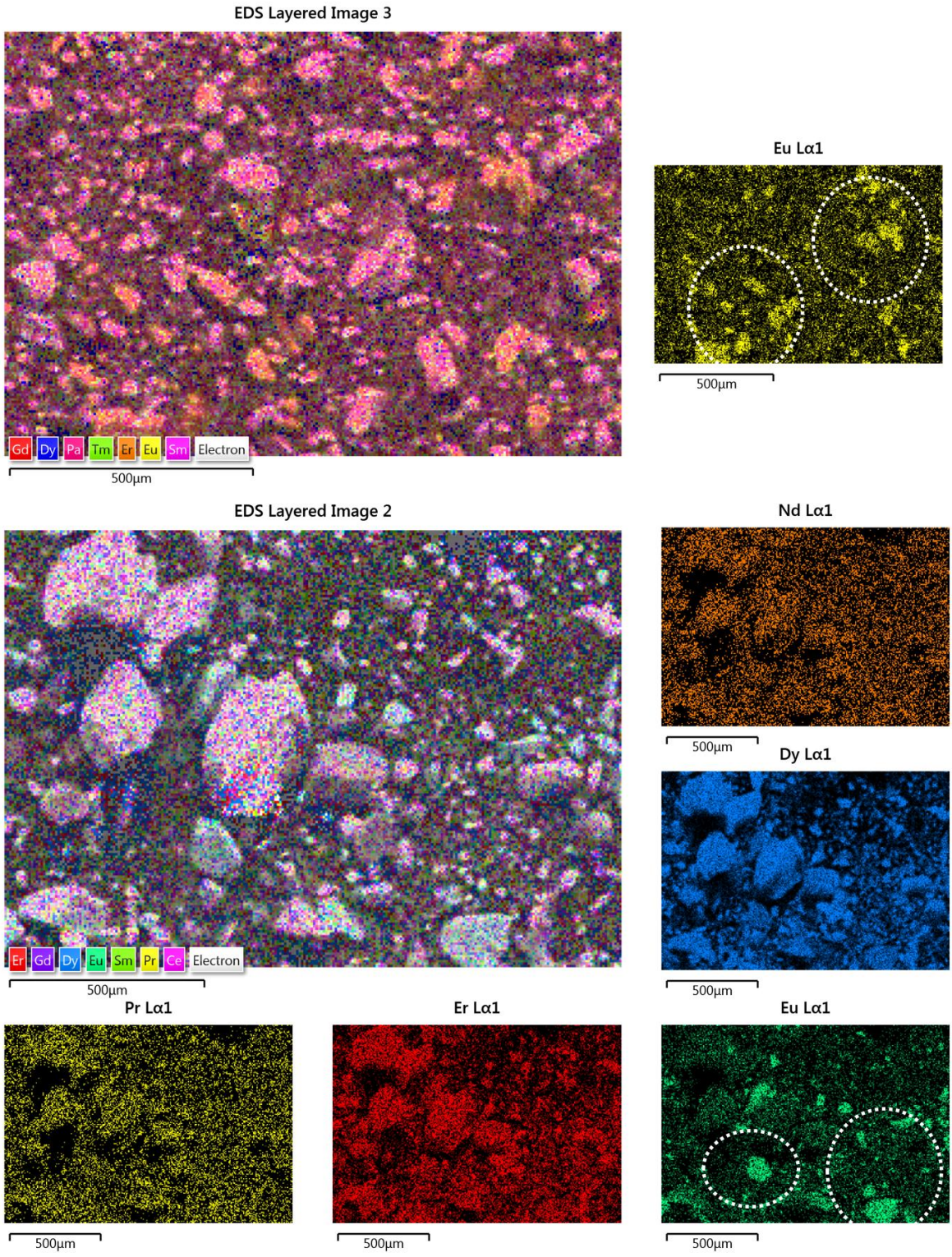

Figure 5 - 25: EDS elemental map of rare earth oxide powder (without purification) shown in the far right image of Figure 5 - 24. The presence of europium is significant among all rare earth element based oxide as can be seen in map (see white circle) in both images. The presence of Pr is also evident as can be seen in map.

5.5 Additional Rare Earth Element Precipitation Tests

Additional testing was performed to enchance the rare earth element extraction and recovery from coal waste. First, a rare earth element precipitation test was conducted with the leaching solution from coal waste. The composition of the solution in each step was measured and tracked. Second, the bacteria cultivation device was designed and used to culture the Acidothiobacillus ferrooxidans bacteria. The bacteria were adapted to oxidize sulfide ore, such as pyrite. Third, in order to simulate the acidic and oxidizing conditions of the bacteria leaching solution, a leaching test was conducted to study the kinetics of the leaching process for extracting rare earth elements from coal waste. The details of these three aspects of the research were discussed below. Fourth, the resulting leaching solutions were used to recover REEs through three precipitation steps.

5.5.1 Experimental Procedures

The test started with 3 L of the rare earth bearing leaching solution from the coal waste. The solution was marked as 7C3S0. The pH of this solution was 1.76, and the Eh was 414.5. To get a decent amount of the rare earth elements precipitation, 0.0858 g of $LaCl_3 \cdot 7H_2O$ was dissolved to the leaching solution 7C3S0 to bring up the concentration of La in the solution by ~10 ppm. This solution after adding extra amount of La was marked as 7C3S1. Then the pH of the solution was adjusted to 4.00 by adding 1 M $MgCO_3$ suspension and around 1.13 L of $MgCO_3$ suspension was added to the 7C3S1 solution. The purpose of this step is to remove the iron in the solution, which was brought into the solution as the oxidant. Then the solution was filtered to remove the precipitates. The solution after filtration had a volume of around 3.3 L and was marked as 7C3S2. The precipitate was airdried to get 207.28 g solid and was marked as 7C3F2. After that, 1 M NaOH solution was added to 7C3S2 to adjust the pH to 7.00. After this step, 21.97 g of precipitate was acquired, which should be the rare earth elements bearing material, marked as 7C3F3. The remaining solution was marked as 7C3S3. Lastly, the 7C3F3 precipitate was re-dissolved by HNO_3 with a volume of 100 ml, and the final pH was adjusted to 2.5. After the other filtration, the final solution was marked as 7C3S4. Part of the solution was taken for ICP analysis, which was marked as 7C3S412. Samples were taken from each of the process solutions and diluted for rare earth element concentration analysis with the Inductively coupled plasma mass spectrometry (ICP-MS, Agilent 7900).

5.5.2 REE Precipitation Results and Discussion

The concentrations of the rare earth elements in the process solution 7C3S0, 7C3S1, 7C3S2, 7C3S3, and 7C3S412 are shown in Figure 5 - 26, and a close-up for the first four solutions is shown in Figure 5 - 27. As can be seen, Y, Ce, and Nd have higher initial concentration in sample 7C3S0, with concentrations higher than 3 ppm. After adding La salt into the original solution, The La concentration increased to more than 10 ppm. After the first precipitation and filtration, the concentration of all the rare earth elements decreased to some extent because of the loss in the precipitated solids. As shown in Figure 5 - 28, for most of the elements, the yield from 7C3S1 to 7C3S2 is about 60%, which means around 40% of the rare earth elements were lost during the first precipitation and filtration.

However, from concentration of rare earth elements in S2 and S3, we can clearly see that the second precipitation and filtration process collected most of the rare earth elements into the precipitates because the rare earth element concentrations in 7C3S3 are really low and for most of the elements, the concentration in this solution is below the detection limits of the ICP-MS.

Finally, the rare earth elements in the precipitate were dissolved to 100 ml solution, which means the rare elements were concentrated. From the concentration data, it can be seen that concentration in S4 is about 30 times higher than S2. From figure 5 - 29, it is confirmed that for most of the elements, a yield rate higher than 95% is possible in the second precipitation and re-dissolving steps.

Overall, this initial process is sufficient for the precipitation and concentration of the rare earth elements in the leaching solution.

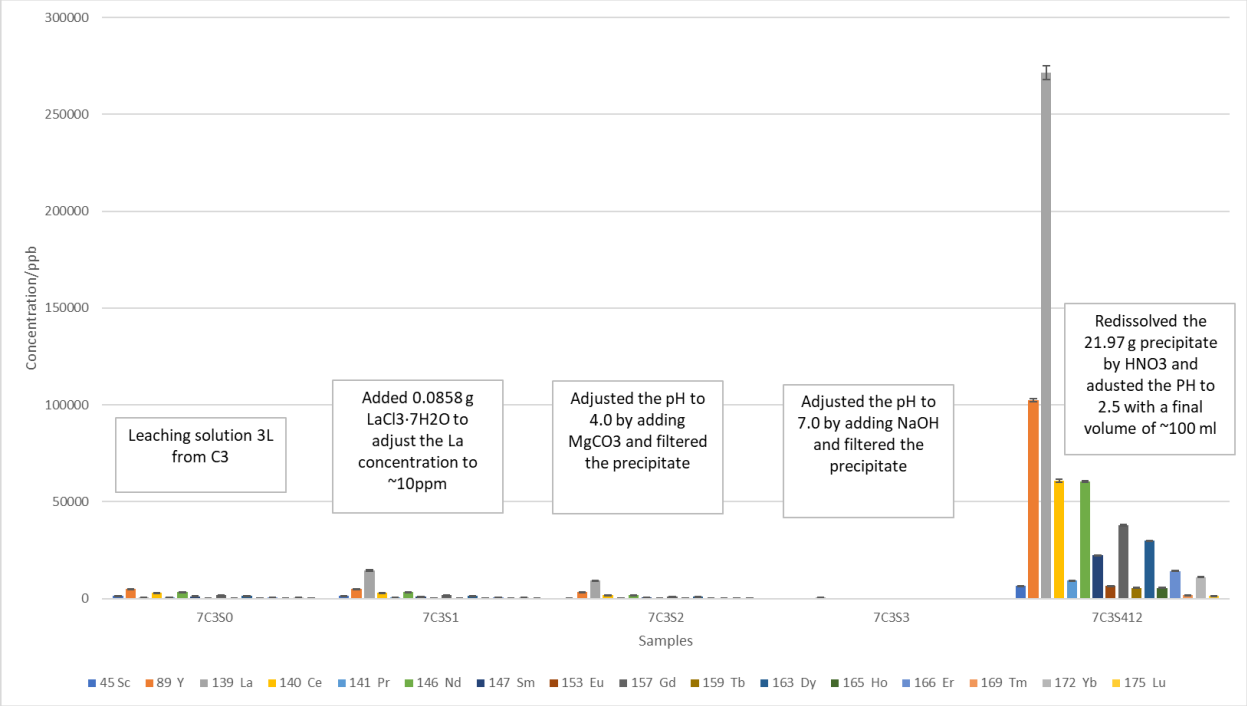

Figure 5 - 26: Rare earth elements concentrations in the process solutions.

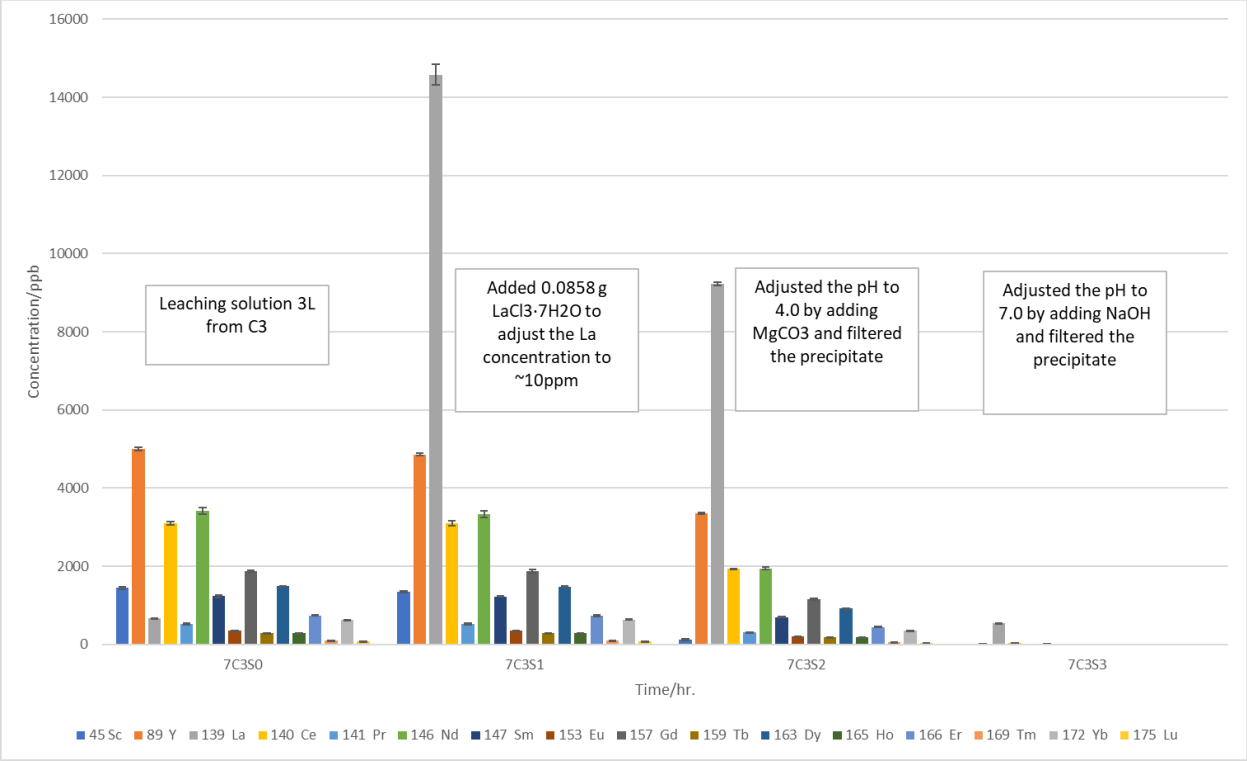

Figure 5 - 27: Rare earth elements concentrations in first four process solutions.

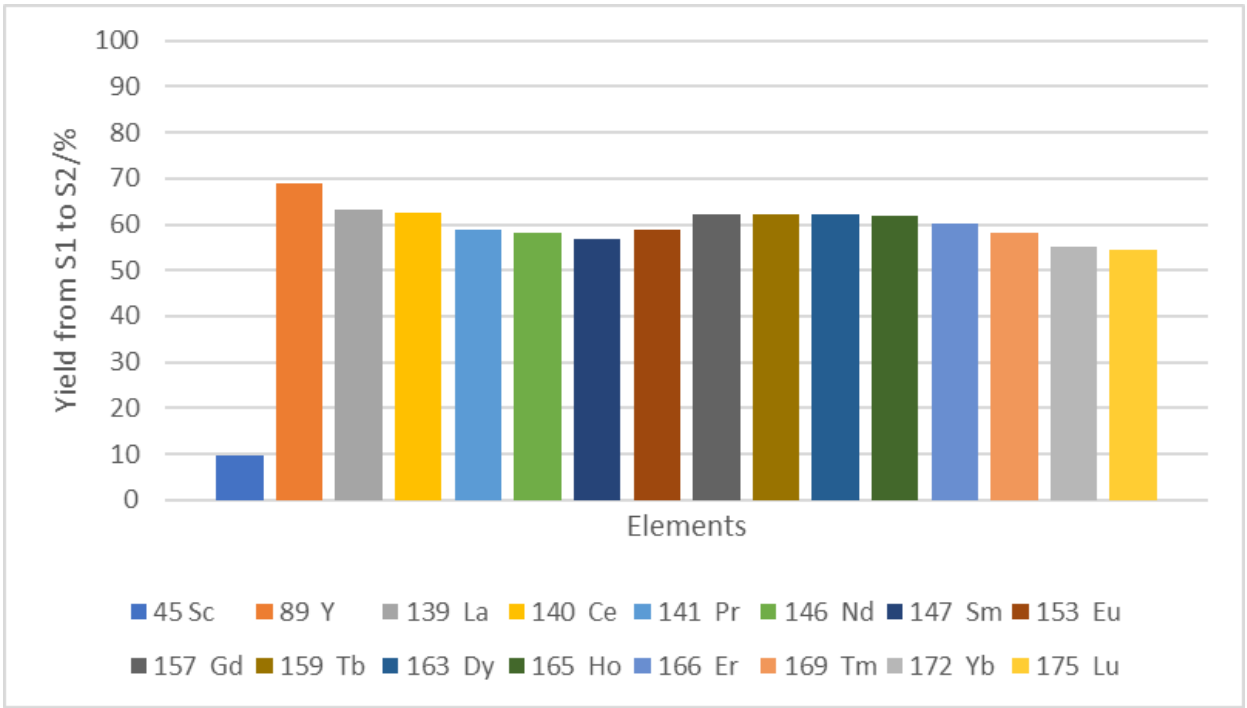

Figure 5 - 28: Rare earth elements yields from S1 to S2.

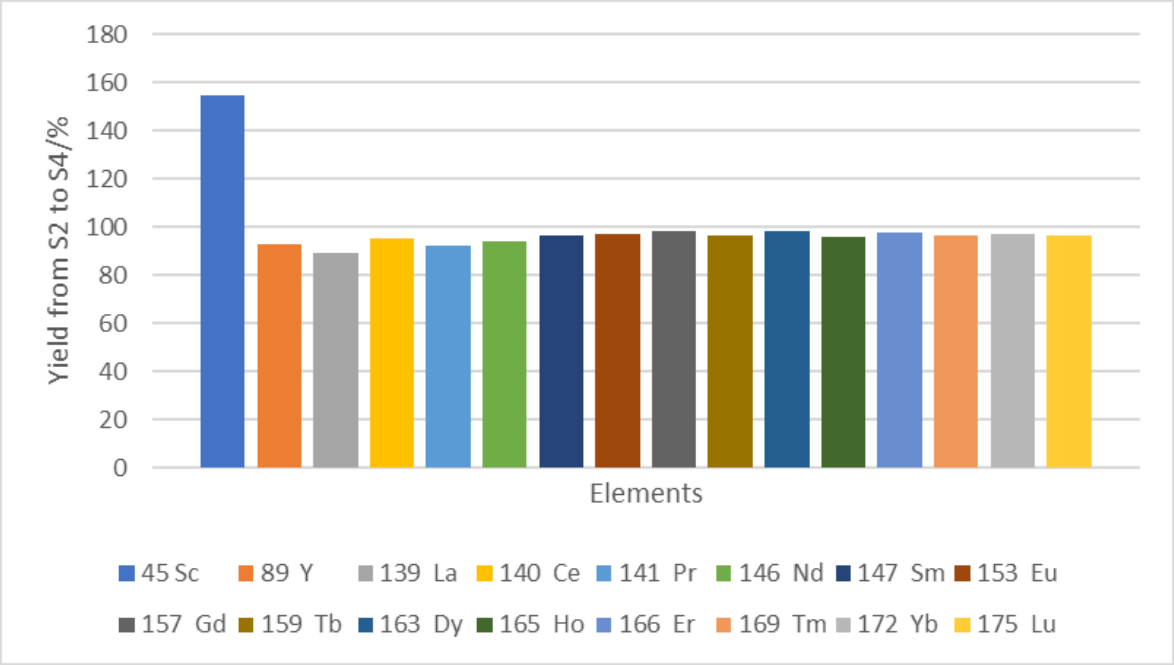

Figure 5 - 29: Rare earth elements yields from S2 to S4.

5.6 Coal Waste Rare Earth Leaching Tests to Achieve 8% Rare Earth in The Final Products

To achieve the goal of 8% rare earth in the final product of the leaching and precipitation test, two new leaching tests were conducted and followed with the precipitation tests. The reason for conducting these two tests is that the REE concentration in the leaching solution from the Beckley coal waste is too low to get a reasonable amount of precipitate in the precipitation tests. In the new leaching tests, the coal waste used for the column leaching tests, which have realized higher REE concentrations, was utilized in the bioleaching simulating tests.

5.6.1 Experimental

The leaching tests were conducted using the typical Eh and pH conditions of the bacteria cultivation solution. In the first leaching test, 90 g of the coal waste under 200 mesh was separated from the large column leaching coal waste material. A total volume of 300 ml of the leaching solution containing 10 g/L $Fe_2(SO_4)_3$ was prepared. The pH of the solution was adjusted to 1.30. Then the coal waste solid and the leaching solution were mixed, and the mixed slurry was stirred with a magnetic stirrer to keep a uniform composition of the slurry and increase the leaching rate. Hydrogen peroxide was added throughout the test to maintain the Eh>550 mV. Diluted H_2SO_4 was added to keep the pH around 1.30 during the test. The leaching vessel was placed on a hot plate to keep the solution temperature at ~ 35 ℃. The leaching test was conducted for 48 hrs., and it was followed by the precipitation test. The leaching solution was filtered to remove the coal waste residue. Then the pH of the solution was adjusted to 4.3 with 1M NaOH solution to remove the iron in the solution as a precipitate, which was subsequently filtered from solution. Further, the pH of the remaining solution filtrate was adjusted to 7.0 with 1M NaOH solution to collect the REE into a precipitate. The precipitate from this step was dried and re-dissolved into a HNO_3 solution

with a final pH of 2.5. Finally, oxalic acid was added to this solution to generate the final REE oxalate. Solutions from each step of this process were sampled and analyzed by ICP-MS for REE concentration. This test was marked as B4-1.

To increase the amount of final precipitate, another leaching and precipitation test was conducted with the same procedures mentioned above. The leaching test was conducted with 1200 g of coal waste under 10 mesh and with 2.8 L of the leaching solution. The leaching test was conducted for 72 hrs. Samples were collected at 0 hr., 1 hr., 2 hr., 1 hr., 4 hr., 8 hr., 24 hr., 48 hr., and 72 hr. The final volume of solution for REE precipitate dissolution is 60 ml. 30 ml of this solution was taken for the oxalic acid precipitation test. This test was marked as B4.

5.6.2 Results and discussion for enriched precipitation product

5.6.2.1 REE concentration analysis with ICP-MS

The REE concentrations of the leaching solution and the process solutions during the enriched precipitation tests are shown in Figure 5 - 30. As it shows, Y, Ce, Nd, and Dy show a higher concentration than other elements. After the pH 4.3 precipitation test, all the concentrations dropped significantly, which means the pH of 4.3 might be too high for the iron removal step. Based on the previous results, pH 4.0 should be a good condition for this step. As expected, the REE concentration in the pH 7.0 solution is very low, which means most of the REE went to the precipitate. After re-dissolving, the concentration increased. Based on the concentrations before and after the oxalic acid precipitation, about 33.22% of the REE went to the precipitate.

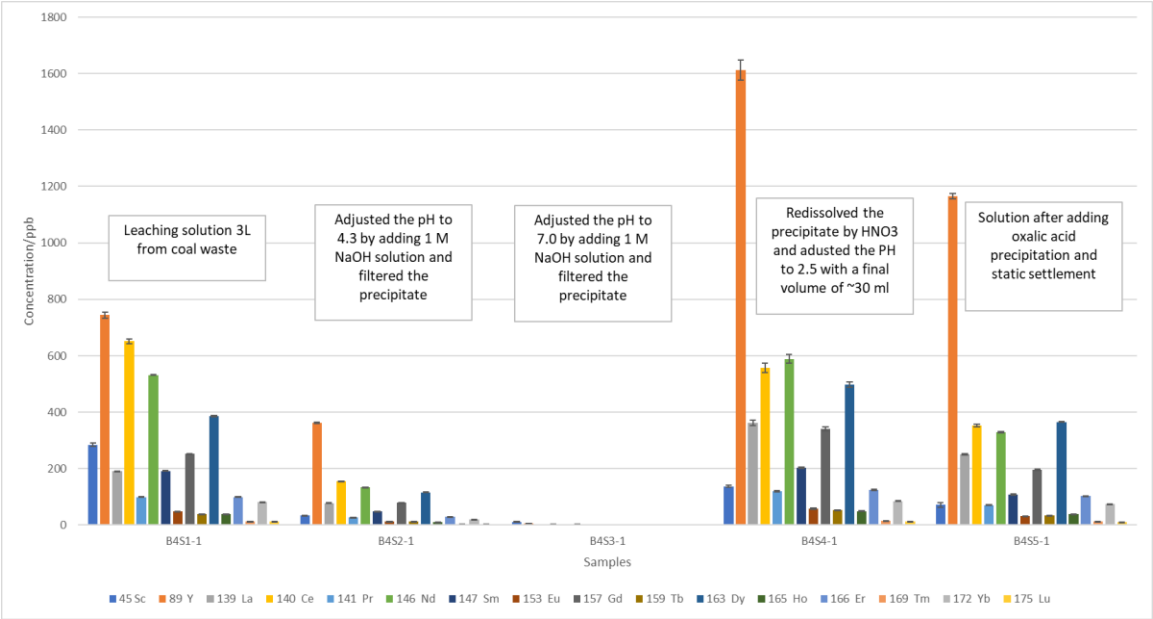

Figure 5 - 30: Rare earth element concentrations in the process solutions of B4-1 test.

The yield rate of REE from each step is shown in Figure 5 - 31 and Figure 5 - 32. As indicated above. Too much REE was lost in the first precipitation, with an average yield of around 30% from S1 to S2. From S2 to S4, the average yield is around 42.8%.

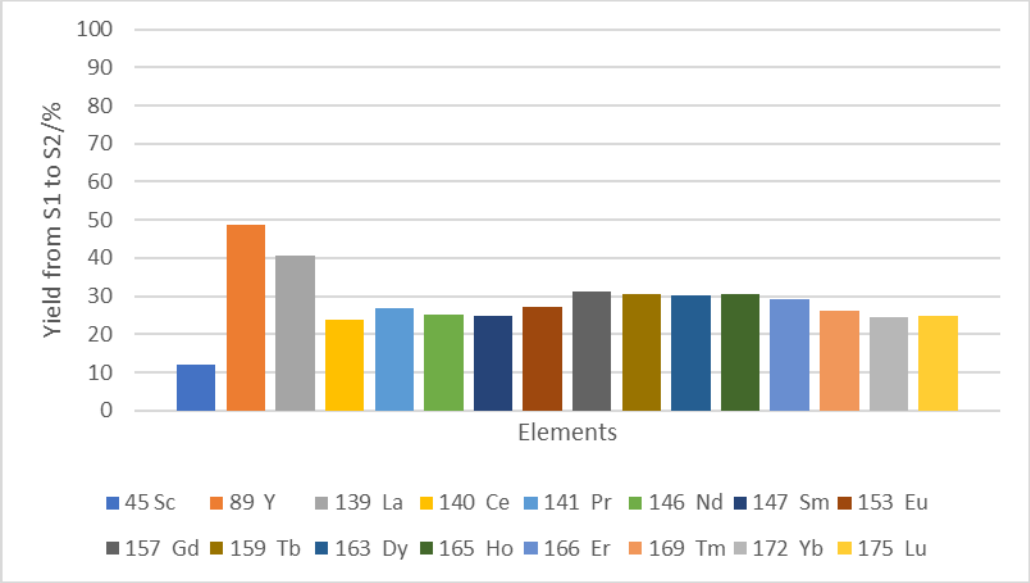

Figure 5 - 31: Rare earth elements yield from S1 to S2 of B4-1 test.

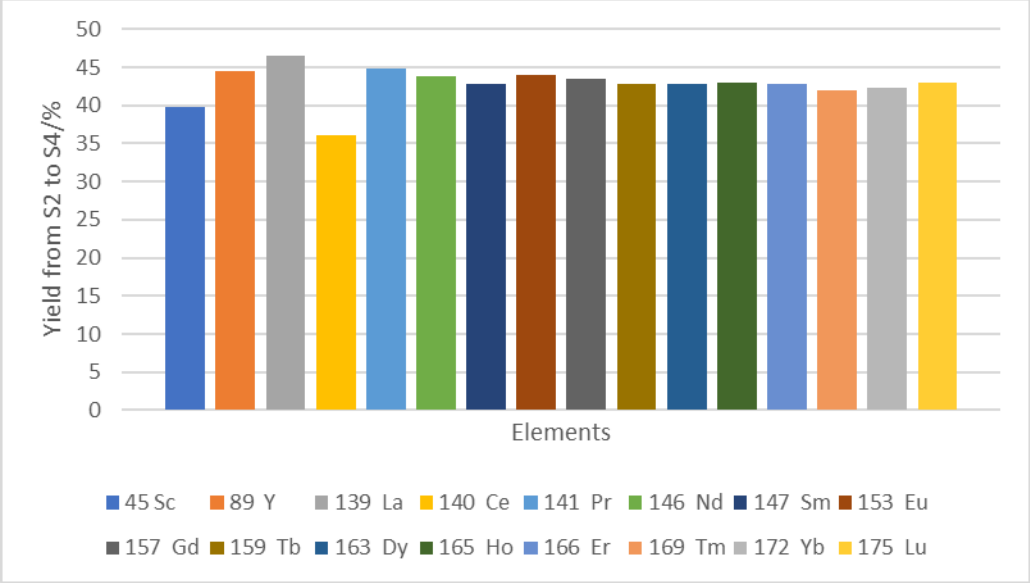

Figure 5 - 32: Rare earth elements yield from S2 to S4 of B4-1 test.

The concentrations of the rare earth elements in the leaching solution after different leaching times in the B4 test are shown in Figure 5 - 33. The concentrations of all the elements increase with the leaching time but may appear different leaching rates.

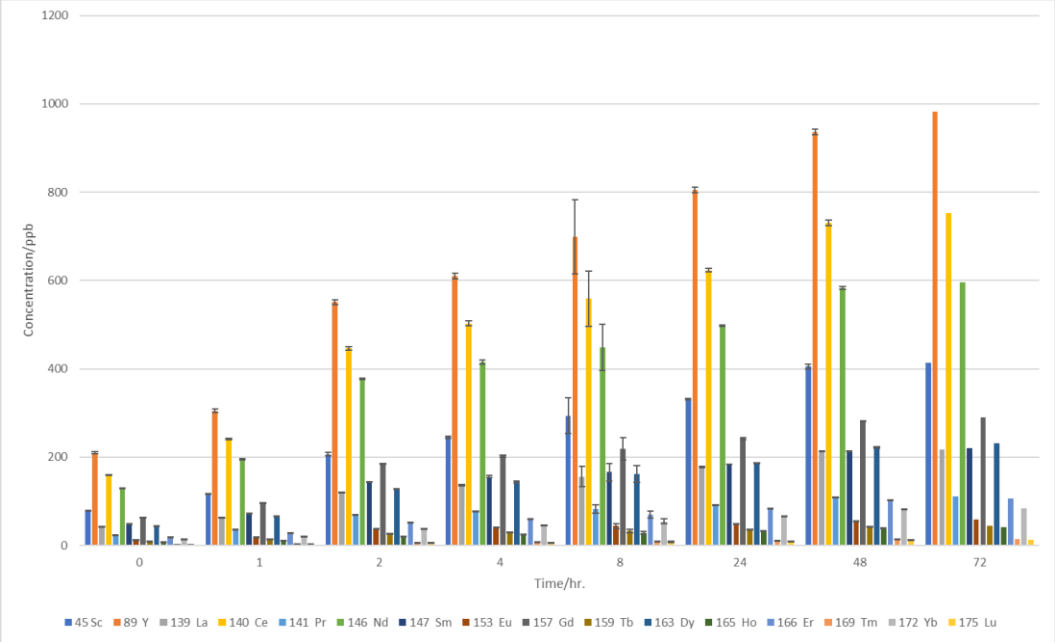

Figure 5 - 33: Rare earth elements concentrations vs. leaching time of B4 test.

The total concentration of all the rare earth elements was calculated by summing all the concentrations. The total concentration of the rare earth elements as a function time is shown in Figure 5 - 34. This curve is basically a kinetic curve of the leaching process. It shows that the rate of leaching is high in the first few hours of the test; after that, it becomes slower. During the third day of the leaching test, the concentration did not change very much, which means the leaching is almost finished in the first two days even with the large rare earth coal waste particles.

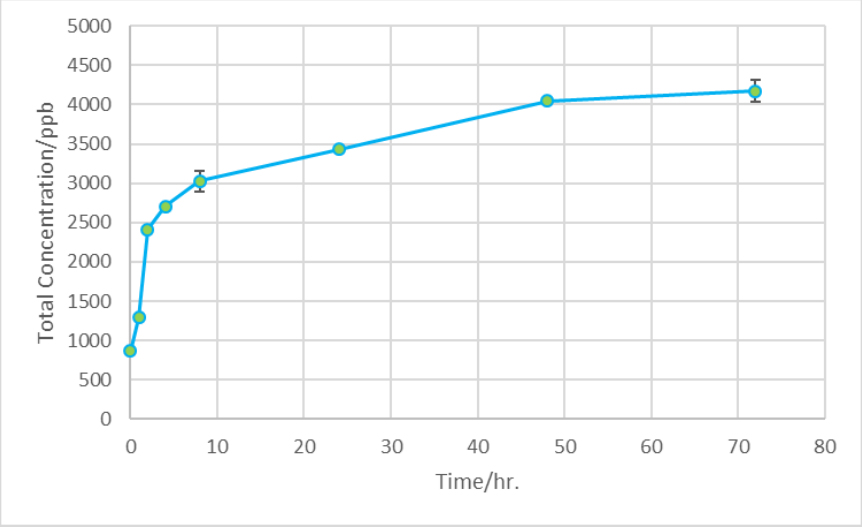

Figure 5 - 34: Total rare earth elements concentration vs. time in the leaching process of B4 test.

The REE concentrations of the process solutions during the precipitation tests for B4 test are shown in Figure 5 - 35. As it shows, similar precipitation behavior is shown for this test.

However, because of the high REE concentration in the concentrated solution, a higher percentage of 63.68% of the REE went to the precipitate.

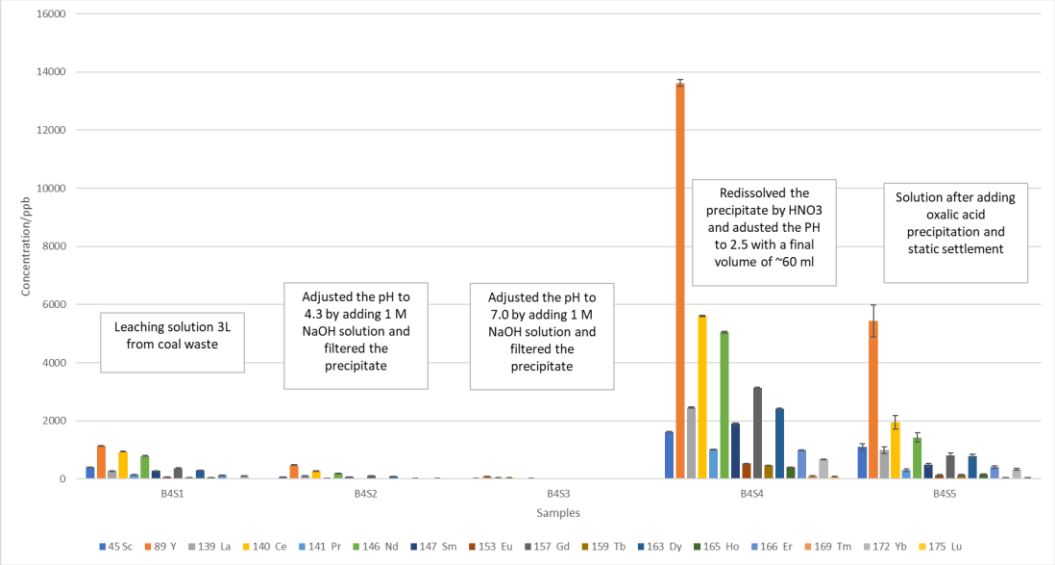

Figure 5 - 35: Rare earth element concentrations in the process solutions of B4 test.

The yield rate of REE from each step in the B4 test is shown in Figure 5 - 36 and Figure 5 - 37. For this test the yield rate is similar to the B4-1 test, with an average yield of around 20.38% from S1 to S2. From S2 to S4, the average yield is around 51.00%.

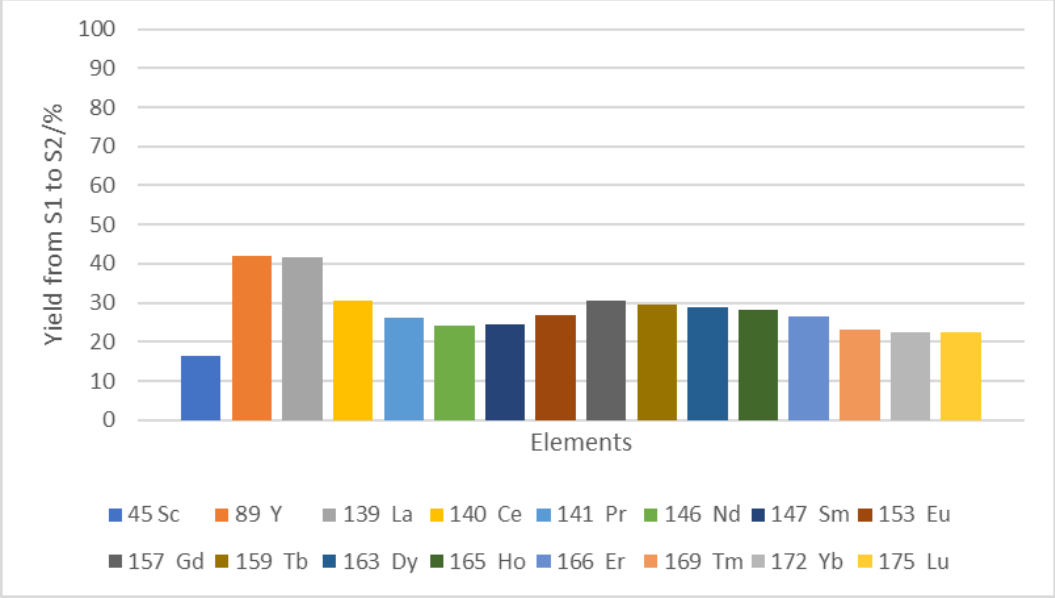

Figure 5 - 36: Rare earth elements yield from S1 to S2 of B4 test.

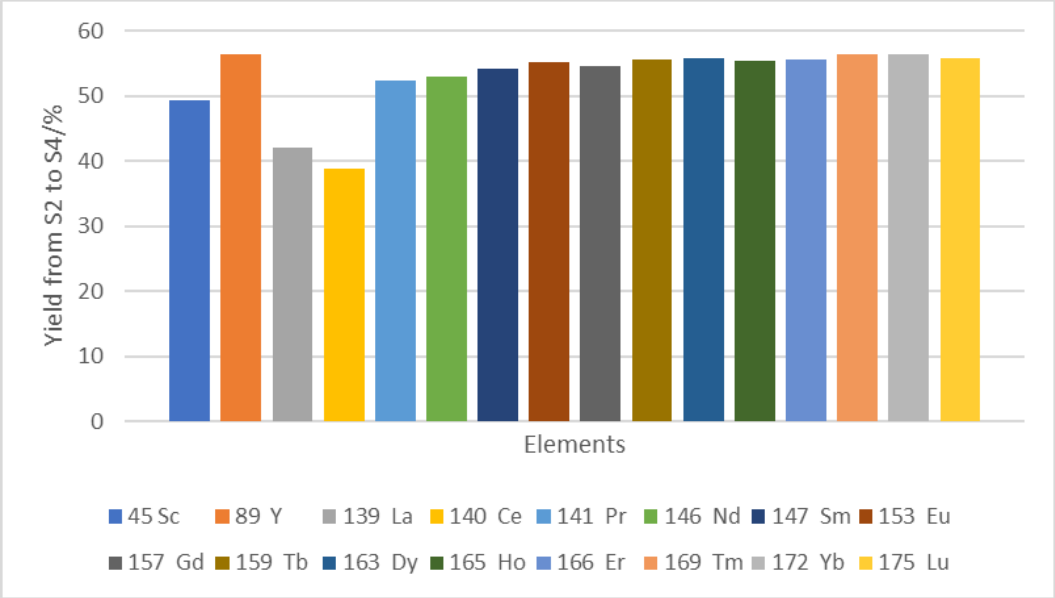

Figure 5 - 37: Rare earth elements yield from S2 to S4 of B4 test.

5.6.2.2 SEM and EDS analysis

The precipitate from the oxalic acid precipitation test is shown in Figure 5 - 38. The precipitate is a white crystal, and its amount increased with the amount of leaching solution. SEM and EDS were conducted on the rare earth precipitate.

Figure 5 - 38: Rare earth precipitate from the leaching test.

The SEM images of the REE precipitate are shown in Figure 5 - 39. It shows the rare earth precipitate is composed of small flakes of the solid with a shape of a shell. The size is of the flake is quite uniform and is about 10-15 microns.

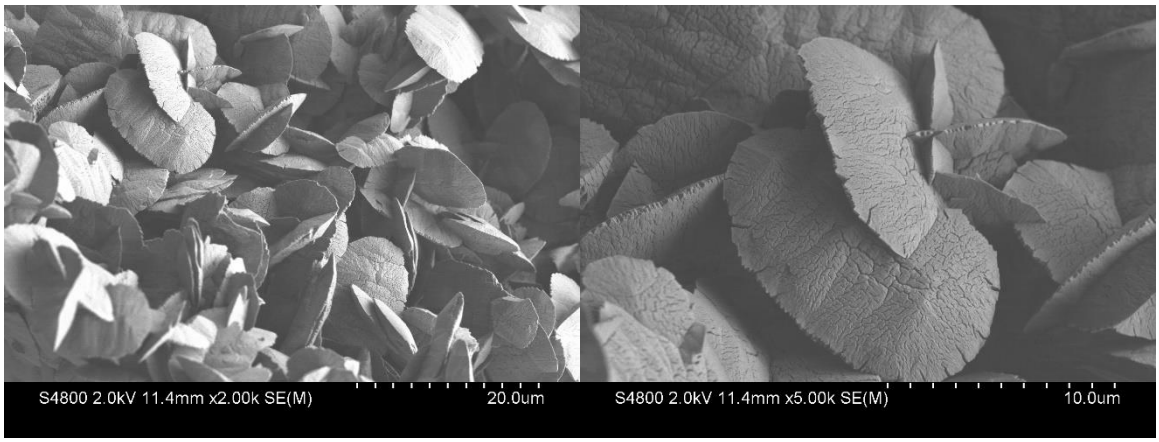

Figure 5 - 39: SEM images of the REE precipitate.

An EDS analysis has been done on one of the flakes in the precipitate, as shown in Figure 5 - 40. As can be seen, in the range of the flake, there is a very high concentration of O and C, which is consistent with the composition of the precipitate, REE oxalate ($Ree(C_2O_4)_3$). As indicated by the density of the dots in the EDS map, the concentration of Pm, Nd, Sm, La, Y, Pr, and Ce are high in the precipitate. As an impurity, there is a considerable amount of Zn in the precipitate.

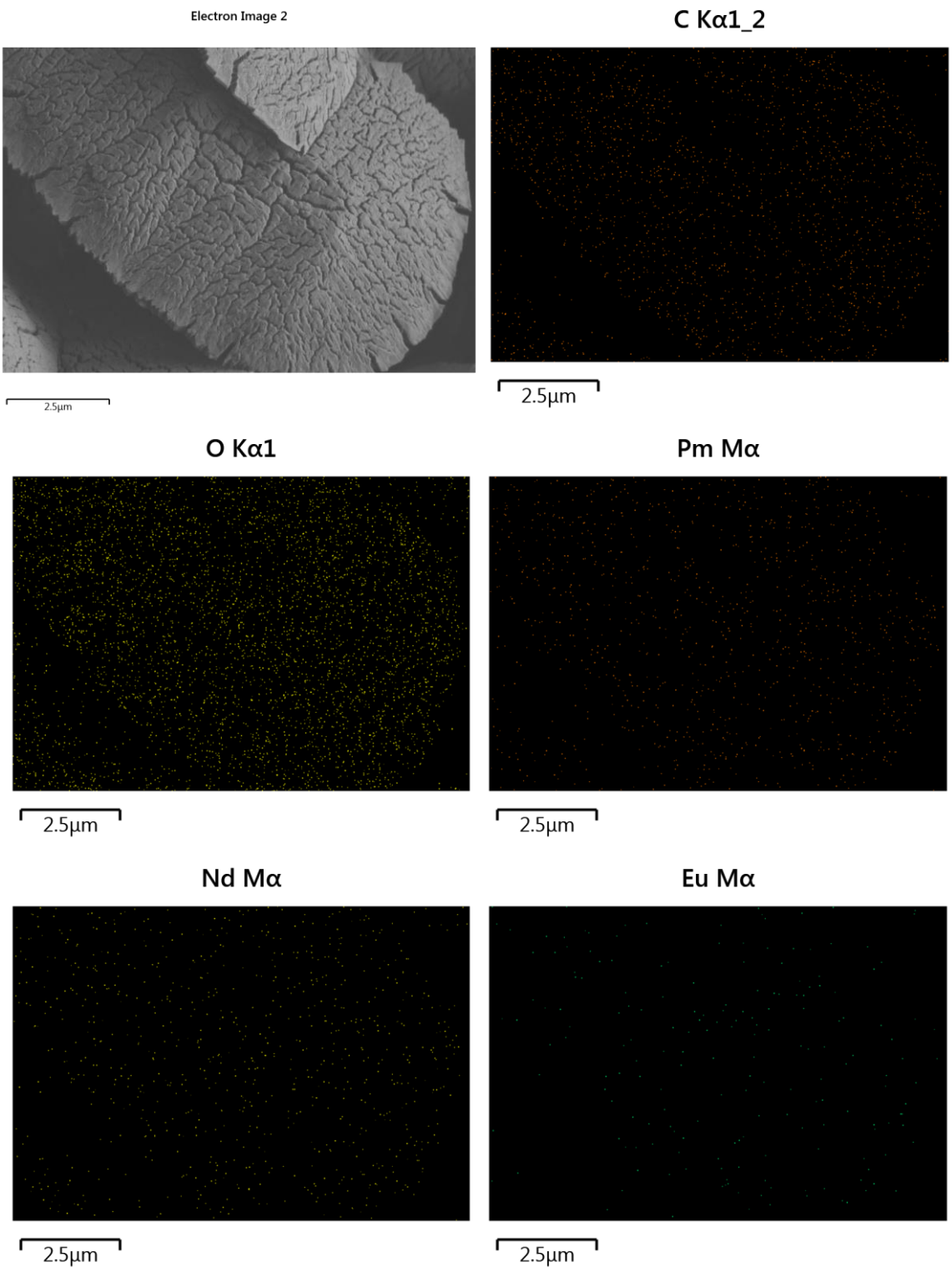
Electron Image 2
2.5µm
C Kα1_2
2.5µm
O Kα1
2.5µm
Pm Mα
2.5µm
Nd Mα
2.5µm
Eu Mα
2.5µm

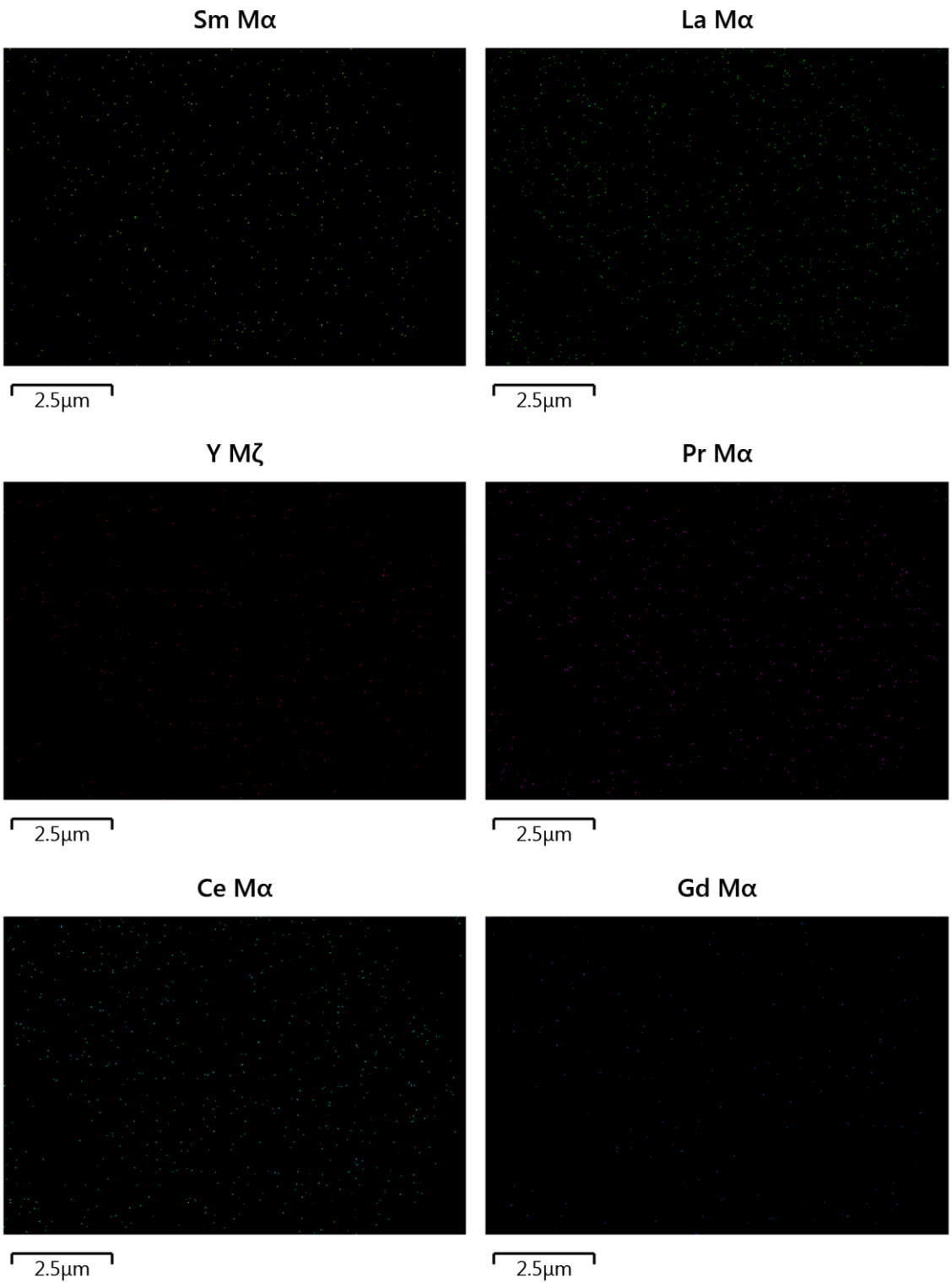
Sm Mα
La Mα
2.5µm
2.5µm
Y Mζ
Pr Mα
2.5µm
2.5µm
Ce Mα
Gd Mα
2.5µm
2.5µm

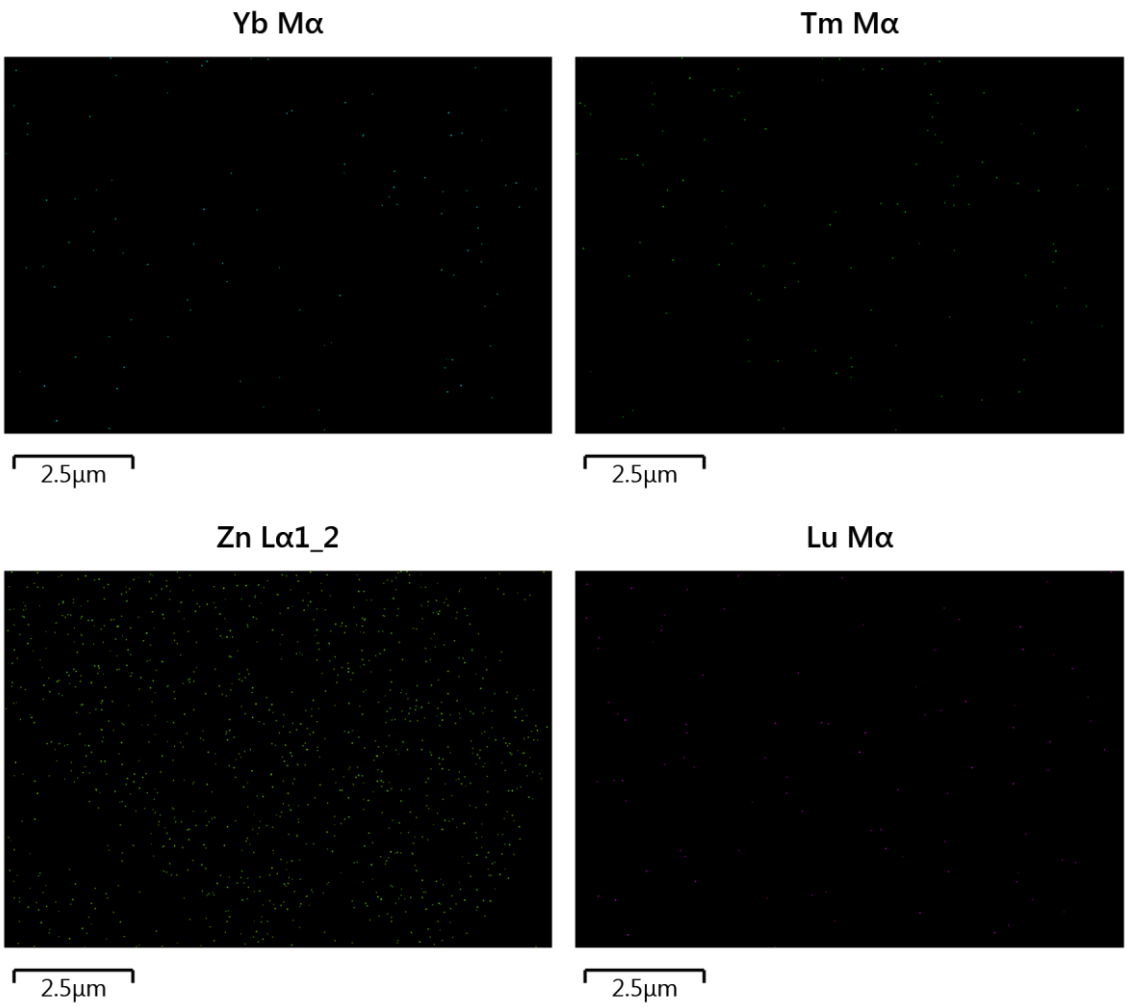
Yb Mα
Tm Mα
2.5µm
2.5µm
Zn Lα1_2
Lu Mα
2.5µm
2.5µm

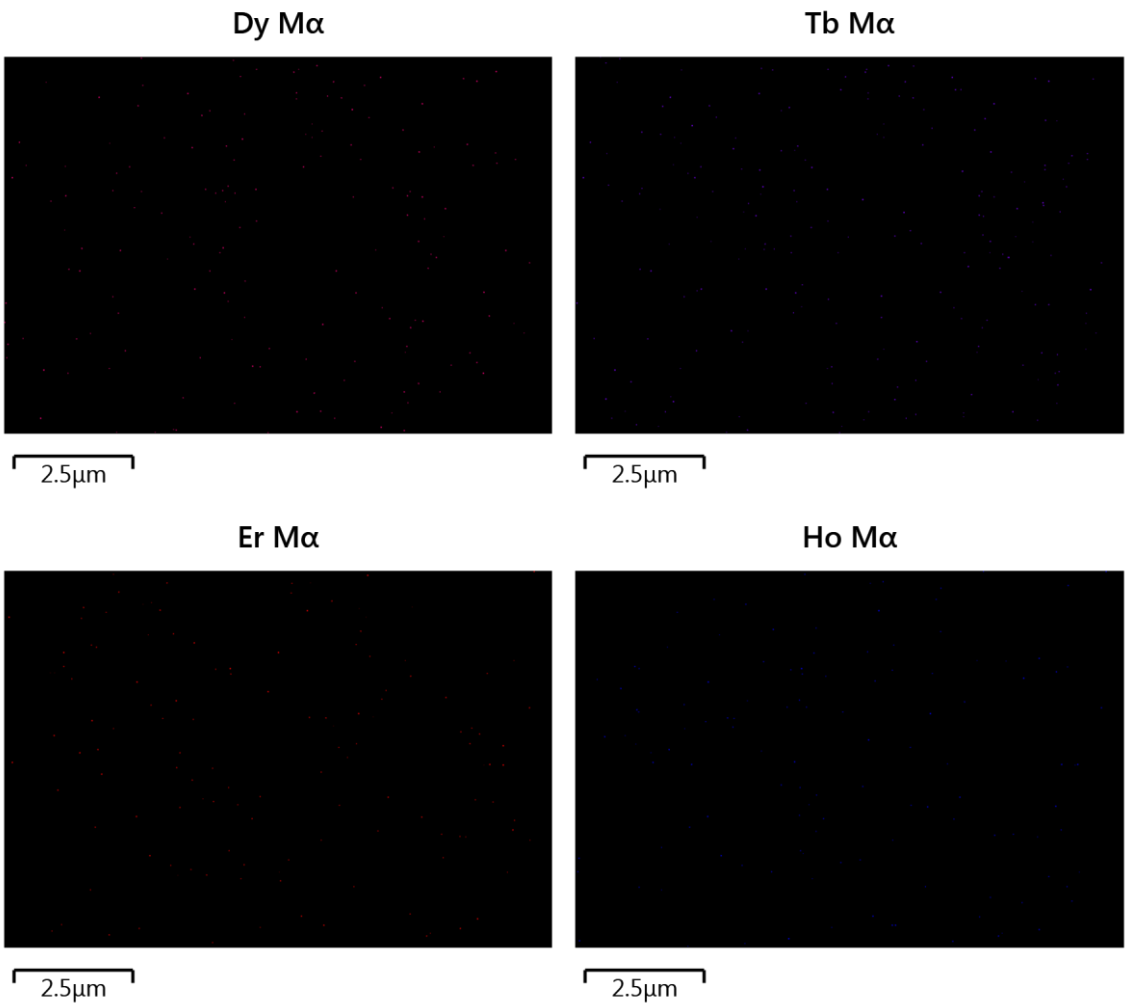

Figure 5 - 40: EDS map images of the REE precipitate.

5.6.2.3 REE concentration in the precipitate

The REE concentration in the precipitate is calculated based on the data acquired in the leaching and precipitation tests. For the 4 L leaching and precipitation test, the amount of the precipitate formed in the oxalic acid precipitation step is 4.3 mg. Based on the REE concentration change before and after adding oxalic acid and the volume of the solution, the amount of REE went to the precipitate as REE oxalate is calculated as:

$$m_{REE\ xoalate} = \frac{\left(C_{inital} - C_{final}\right) \times V}{Aw_{REE\ average}} \times Aw_{REE\ oxalate\ average}$$

$$= \frac{\left(40.15 - 14.58\right)(mg/L) \times 0.03L}{124.64(g/mol)} \times 256.64(g/mol)$$

$$= 1.58\,mg$$

Therefore, the percentage of REE oxalate in the precipitate is:

$$\eta(\%) = \frac{m_{REE\ xoalate}}{m_{precipitate}} \times 100\%$$
$$= \frac{1.58\,mg}{4.3\,mg} \times 100\%$$
$$= 36.7\%$$

Therefore, the final REE oxalate salt concentration in the final product is 36.7%.

5.6.2.4 Precipitate composition analysis

To have a better understanding of the composition of the precipitate, more tests and analysis were carried out on the solutions before and after oxalic acid precipitation. The concentrations of the major elements were analyzed by a third party analytical lab. These elements include: Y, La, Ce, Co, Li, Fe, Mn, Zn, and Ni. Rare earth elements Y, La, and Ce were included in this list because they have relative high concentrations in the solution and the concentrations of Y, La, and Ce can be used to cross check the accuracy of the concentration of other rare earth elements not included in this test. The solution before oxalic acid precipitation (B4S4) was diluted by a factor of 50 because of its little volume saved for analysis. The solution after oxalic acid precipitation (B4S5) was diluted by a factor of 5 before sending for analysis.

The measured concentrations of these elements are shown in Table 5 - 2. As can be seen from this table Zn shows a significant change in concentration, so it is one of the main impurities. Mn, Co, and Ni each show modest recoveries in the precipitate based on the changes in concentrations before and after precipitation. Iron shows little change, and is therefore clear it is not a major contaminant. The concentrations of Y, La, and Ce are very close to the concentrations reported in Figure 5 - 35, which validates the accuracy of the previous results.

Table 5 - 2: Concentrations of the major elements in the solutions before (B4S4) and after (B4S5) oxalic acid precipitation.

Elements	B4S4/ppm	B4S5/ppm
Zn	198.5	83
Mn	60	46.85
Co	21.3	10.75
Y	13.95	3.555
Ni	10.2	4.355
Ce	6.25	0.915
La	3.055	0.675
Fe	<25	14

Based on Table 5 - 2, the concentrations of all the elements show some decrease in the solution after oxalic acid precipitation. However, because of the difference in the oxalate salt solubilities of these elements, it is clear that for some elements, the percentage yield in the precipitate is a lot higher than other elements, especially for the rare earth elements.

It is clear that for the rare elements Y, La, and Ce, the yield is as high as 75% to 85%, which indicates most of the rare earth elements have been precipitated into the precipitation phase. Other elements such as Zn, Ni, and Co have a moderate yield, however, Zn concentration in the initial solution is 10 – 20 times higher than Ni and Co. Also, this is consistent with the EDS mapping in Figure 5 - 40. It is worth noting that no Na, Al, and Mn were detected in the EDS mapping.

Task 6: Techno-economic Analysis

Key Findings

- High sulfur refuse will require long-term acid mine drainage treatment, and x-ray sorting can significantly concentrate acid generating materials.
- Solely purchasing pyrite may not be cost effective in a bioreactor plant when compared to buying acid directly, although it is variable with prices.
- An X-ray sorted pyrite product can reduce process costs by supplementing purchased pyrite in a bioreactor plant for internal acid production.
- An X-ray sorted and spiral concentrated pyrite product may entirely eliminate the need for additional purchased pyrite in a bioreactor plant and has the greatest cost savings compared to directly purchasing acid.
- The highest level of preconcentration of pyrite material may be the most tolerant to reduced acid conversion ratios and acid requirements of the heap leach.

Detailed Results

6.1 Model Design

The techno-economic model was generated to evaluate various scenarios of processing options:

1. "Do-nothing" Scenario – Coarse refuse is not processed for REE's and requires lifetime acid drainage treatment
2. External acid/pyrite Scenario – Coarse refuse is processed for REE extraction leaching of coarse refuse, but external acid or pyrite is purchased for leaching
3. Pyrite Recovery Scenario – Coarse refuse is processed for REE extraction and associated pyrite is concentrated from refuse stream for an internal acid source
    i. 3a. A coarse ore X-ray sorting process enriches REE and pyrite material.
    ii. 3b. An x-ray sorting process along with an additional spiral concentration circuit enriches pyrite material.

The analysis is organized in sections by unit operations of the heap leaching process, including;

1. physical preconcentration plant
2. pyrite bioreactor for acid production
3. heap leach
4. solvent extraction/selective precipitation plant.

The specifics of the unit operations, such as the physical plant and bioreactor, will vary between the proposed scenarios. The unit inputs include technical data and basic cost estimation components. Technical inputs include REE and pyrite content (converted sulfur values obtained

from laboratory analysis). The physical plant unit involves the most detailed cost estimation, including two different flowsheet options of varying levels of pre-concentration, specifically for pyrite material that may be used for acid production.

6.2 Model Assumptions

6.2.1 Feedstock Information

For this analysis, a feed rate of 500 tonnes per hour with a TREE concentration of 300 ppm is assumed. Based on the sulfur content of CR-B and an assumed composition of completely pyritic sulfur, the feed pyrite grade is approximately 7%. Figure 6 - 1 shows the feedstock information of the economic analysis.

Feedstock Information			Key
			Input
Feed Rate	mtph	500	Calculated
Feed REE	ppm	300	Linked
Total Sulfur	%	4%	
Pyritic Sulfur	%	4%	
Feed Pyrite Content	%	7%	
Feed Acid Generation	mg/L CaCO3	247.21	

Figure 6 - 1: Feedstock inputs for technoeconomic analysis

6.2.2 Physical Plant Assumptions

Capital and operating costs for the physical plant are based on InfoMine cost guides, Mohanty, et al. (2006), and industry estimates. Table 6 - 1 shows the equipment for the list for the largest physical plant option (Scenario 3b), as the smaller option is contained within the same list. The table includes the approximate capacities given the 500 mtph feed rate, along with the capital costs and operating costs per hour. Operating costs per ton of material are calculated using the total capacity of the plant. The capital costs do not include installation, therefore a Lang factor of three is assumed in the total installed CAPEX calculation. Additionally, the CAPEX values in the table represent 2016 prices, but are converted to 2019 prices in the total CAPEX summation. The x-ray sorters are assumed to be leased, and therefore only reflect operating costs at a lease agreement of $0.50 per ton ejected.

6.2.3 Heap Leach Assumptions

The heap leach unit of the analysis depends on multiple assumptions. For cost assumptions, the capital cost to construct the leach pad includes a dual clay-lined pad that costs $0.42 per ton ($0.46 per tonne) leached. The total tonnage leached is assumed for a 10 year life at 500 mtph and $1.00 per tonne ore operating cost. The acid requirement for leaching is assumed to be 0.05 tonnes acid per tonne of material leached. The assumed REE recovery from the leach is 30%.

Table 6 - 1: Physical preconcentration plant equipment list with capacity, CAPEX, and OPEX

Equipment List	Solids Capacity (mtph)	CAPEX	OPEX ($/hr)
Grizzly Scalper	500	$103,800.00	$2.87
Grizzly Oversize Belt	400	$61,702.40	$1.92
Grizzly Undersize Belt	100	$47,605.10	$1.08
Crusher Feeder	488	$18,682.21	$0.14
Cone Crusher	488	$773,356.83	$29.38
2.5x0.5" Screen Deck	588		
Fines Product Belt	88	$47,052.26	$1.04
Sorter Feed Belt	412	$13,427.22	$0.41
Oversize Recirculating Belt	88	$47,052.26	$1.04
X-ray Sorter 1	412		$10.29
Organic Waste Belt	21	$43,873.46	$0.85
Sorter 2 Feed Belt	391	$13,174.48	$0.39
X-ray Sorter 2	391		$20.59
Heap Product Belt	350	$59,352.85	$1.78
Pyrite Product Belt	41	$44,840.92	$0.91
Roll Crusher Feeder	75	$13,989.24	$0.09
Roll Crusher	75	$123,634.65	$3.14
Roll Crusher Product Belt	75	$9,292.77	$0.14
1/4" x 1mm Screen Deck	75	$145,000.00	$1.50
+1mm Recirculating Belt	34	$44,494.14	$0.89
-1mm Cyclone Feed Belt	41	$8,877.88	$0.12
Slurry Mixer	41	$35,000.00	$0.49
Cyclone Feed Pump	41	$13,536.99	$0.51
Hydrocyclone (150 micron cut)	41	$15,827.90	$0.00
Overflow Slurry Pump	9	$10,662.26	$0.15
Spiral Feed Pump	32	$12,744.88	$0.41
Spiral Bank	32	$28,379.04	$0.02
Spiral Concentrate Pump	16	$11,321.90	$0.23
Spiral Tailings Pump	16	$11,277.27	$0.23
Spiral Concentrate Dewatering Screen	16	$21,525.36	$1.36
Spiral Tailings Dewatering Screen	16	$20,870.74	$1.32

6.2.4 Bioreactor Assumptions

The focus of this technoeconomic analysis is to compare the REE recovery process when using internal acid as opposed to externally purchasing acid, therefore the bioreactor unit of the analysis is very important overall. Calculations in the bioreactor unit depend on the conversion ratio of pyrite to acid, which is assumed to be 1.64 based on the stoichiometric relationship of the conversion of pyrite to sulfuric acid. This value will be subjected to sensitivity analysis later in the

report. Additional external pyrite needed is also calculated based on the pyrite output of the physical plant and acid requirements of the heap leach.

The capital cost of the bioreactor is based on a value of $33,000 per ton per day ($36,376.26/mtpd) and $17/ton ($18.74/tonne) operating cost. The cost of the total acid required is also calculated in this unit to compare purchasing acid directly to producing acid from the bioreactor.

6.2.5 Solvent Extraction/Selective Precipitation Assumptions

Since this analysis is more heavily focused on the upstream concentration efforts of the process, the assumptions and analysis of the solvent extraction and selective precipitation unit are simpler. This unit relies on an assumed recovery of 95%, a capital cost of $20,000,000 for the plant, and an operating cost of $25/kg of REE product.

6.2.6 Global Economic Assumptions

Factors used to evaluate the economic performance of the proposed scenarios include capital costs, operating costs, net present value, internal rate of return, and cost savings when comparing internal acid production to external acid supply. To calculate revenue, a basket price based on REE concentration data of CR-B-g (the heap leach feed material) was generated. The percent composition of REEs, prices, and conversions from REO to REE values are given in Table 6 - 2.

Other inputs for economic calculations include the interest rate and period. The interest rate is assumed to be 12% and the period is 10 years. 10 operating hours per day and 2080 operating hours per year are used.

Table 6 - 2: Basket value of heap leach feed material CR-B-g

Leaching Feed Material	Sc	Y	La	Ce	Pr	Nd	Sm	Eu	Gd	Tb	Dy	Ho	Er	Tm	Yb	Lu
CR-B-g (% TREE)	7.40%	8.90%	16.92%	35.31%	4.15%	15.92%	3.27%	0.66%	2.76%	0.38%	2.02%	0.37%	0.95%	0.13%	0.76%	0.11%
Mkt Value REO ($/kg)	$4,200.00	$6.00	$2.00	$2.00	$52.00	$42.00	$7.00	$150.00	$32.00	$400.00	$230.00	--	$34.00	--	$34.00	--
REO/REE Ratio	65%	79%	85%	81%	83%	86%	86%	86%	87%	85%	87%	87%	88%	88%	88%	88%
Mkt Value REE ($/kg)	$6,441.72	$7.62	$2.34	$2.46	$62.80	$49.01	$8.12	$173.61	$36.87	$470.59	$264.06	$0.00	$38.86	$0.00	$38.72	$0.00
Basket Value ($/kg REE)	**$499.23**															

6.3 Scenario 1

In this scenario, there is no process to recover rare earth elements from coarse coal refuse. The material is sent through the coal preparation plant and into refuse piles. These piles must be monitored for environmental impact in perpetuity as natural weathering will continuously expose fresh rock surfaces and introduce mineral substances, such as pyrite, into solutions of water that will be transported to the surrounding environment. The head sample CR-B and all x-ray sorted blue (iron-enriched) samples were subjected to long-term static leaching tests. Small amounts of solid samples were introduced to pure water and left to rest for approximately two months. Two samples, CR-B and CR-B-b had acidic solutions after the leaching while the rest were relatively neutral. The solutions were also tested for major cations and REEs. Table 6 - 3 shows the cation and REE concentrations in the leach solutions, as well as the final pH of the solutions.

Table 6 - 3: Static leach solution REE and major cation concentrations in ppb, and solution final pH

**all values in ppb*

Sample	TREE	Fe	Al	Mn	pH
CR-B	842	114	2,025	204	3.76
CR-B-b	2550	76,789	15,859	793	2.49
CR-C1-b	6	24	LOD	1,415	6.34
CR-C2-b	4	LOD	LOD	LOD	7.13
CR-D1-b	6	24	LOD	172	7.91
CR-D2-b	4	LOD	LOD	LOD	8.21

The following equation (Hedin, 2006) was used to estimate acid generating potential (in mg/L as $CaCO_3$) of the solid materials that generated acidic leach solutions.

$$Acid_{calc} = 50 * \left(2 * \frac{Fe^{2+}}{56} + 3 * \frac{Fe^{3+}}{56} + 3 * \frac{Al}{27} + 2 * \frac{Mn}{55} + 1000 * 10^{-pH}\right) - alkalinity \quad (6\text{-}1)$$

Iron concentration used for the calculation was assumed to be completely ferric due to mechanical and natural oxidation of the refuse material. Alkalinity was assumed to be negligible as the pH of the acidic solutions was naturally lower than the endpoint of a complete titration (pH = 4.2). The calculated acidities for CR-B and CR-B-b were 247.2 mg/L $CaCO_3$ and 6066.4 mg/L $CaCO_3$, respectively.

The acidities of these solutions represent the acid generating potential of the coarse refuse and the equivalent base treatment required for the runoff material from the refuse piles of these materials. The acidity of CR-B would indicate the treatment needed for drainage from the coarse refuse pile if the material were not re-mined for REE production. The acidity of CR-B-b represents the treatment needed for the heavy mineral product of x-ray sorting that would be

generated in Scenario 2: coarse refuse extracted and x-ray sorted for REE enrichment and pyrite/iron depletion.

6.4 Scenario 2

In scenario 2, coarse refuse is processed for REE recovery. The material is processed by an x-ray sorting circuit shown in Figure 6 - 2. The coarse refuse stream is scalped by a coarse grizzly, and material finer than 2.5” is fed to a screen where the 2.5x0.5” fraction is produced as the ideal sorting size range. Grizzly oversize is fed to a cone crusher to undergo size reduction targeted for the sorting size range. The crusher product joins the grizzly undersize in the screen feed. The +2.5” material is recirculated to the crusher. Material finer than 0.5” is the first waste stream of the process. The sorter feed enters the first sorter where the smallest mass fraction of light, carbon rich material is ejected. The ejected material is a waste stream and the accepted material passes to the second sorter. In the second sorter, the heavy mineral (in this case pyritic) material is ejected as the pyrite product and the accepted material is the REE-enriched heap leach feed. In the case of CR-B, which these processes are based on as high-sulfur refuse, the REE content of the sorted heap leach feed material is enriched by approximately 11%, and the sorting removes most of the carbon and nuisance pyrite.

In this scenario, the pyrite is a waste product and has a higher acid producing potential than the initial refuse material. From the acidities given in Scenario 1, the sorted pyrite product has almost 25x the acid producing potential of the unsorted refuse.

This scenario directly compares the difference between using only externally purchased pyrite in the bioreactor versus purchasing acid and bypassing the bioreactor unit completely. Figure 6 - 3 to Figure 6 - 5 show the complete analysis for this scenario. Values are either inputs, calculations, or links from the other sheets in the workbook where more extensive calculations or estimations were made.

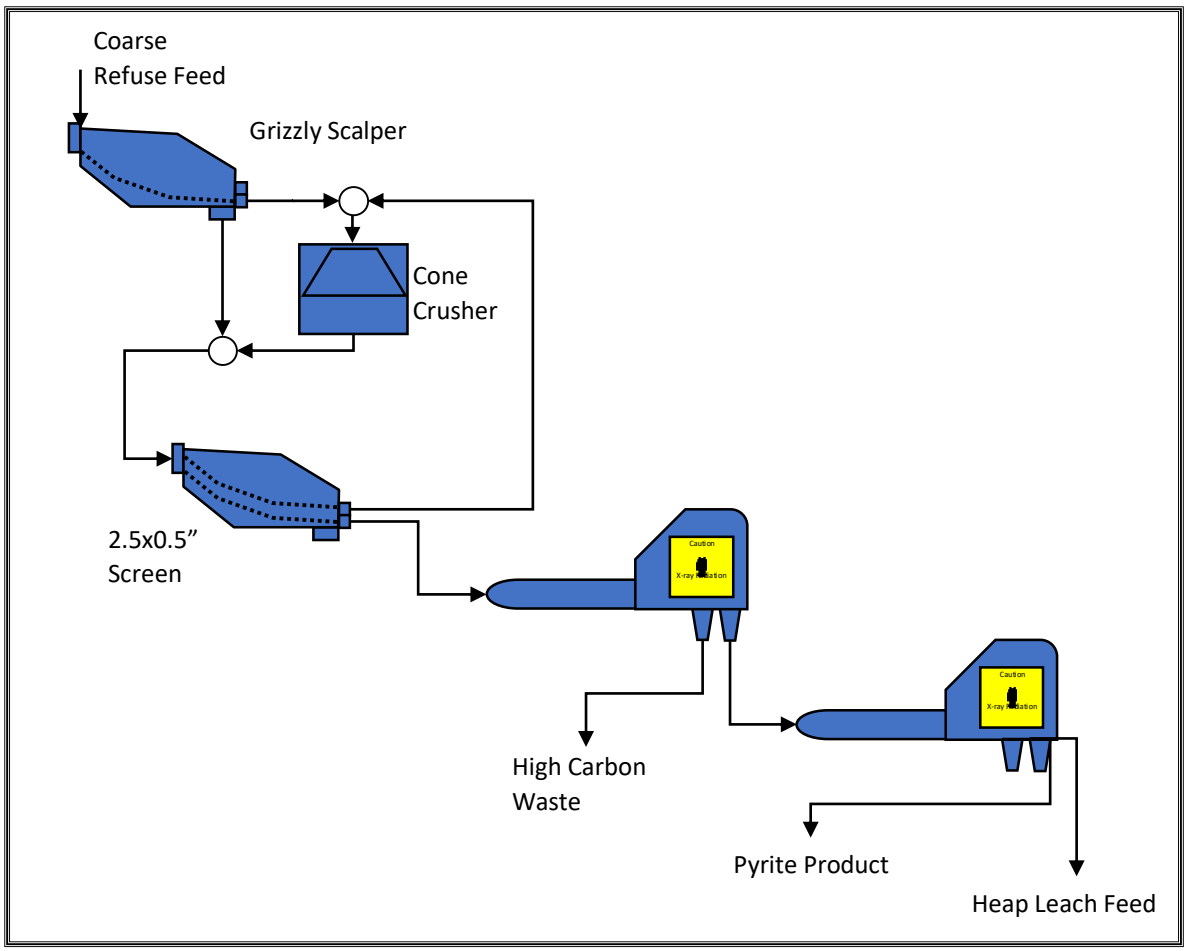

Figure 6 - 2: Flowsheet A for coarse refuse physical preconcentration

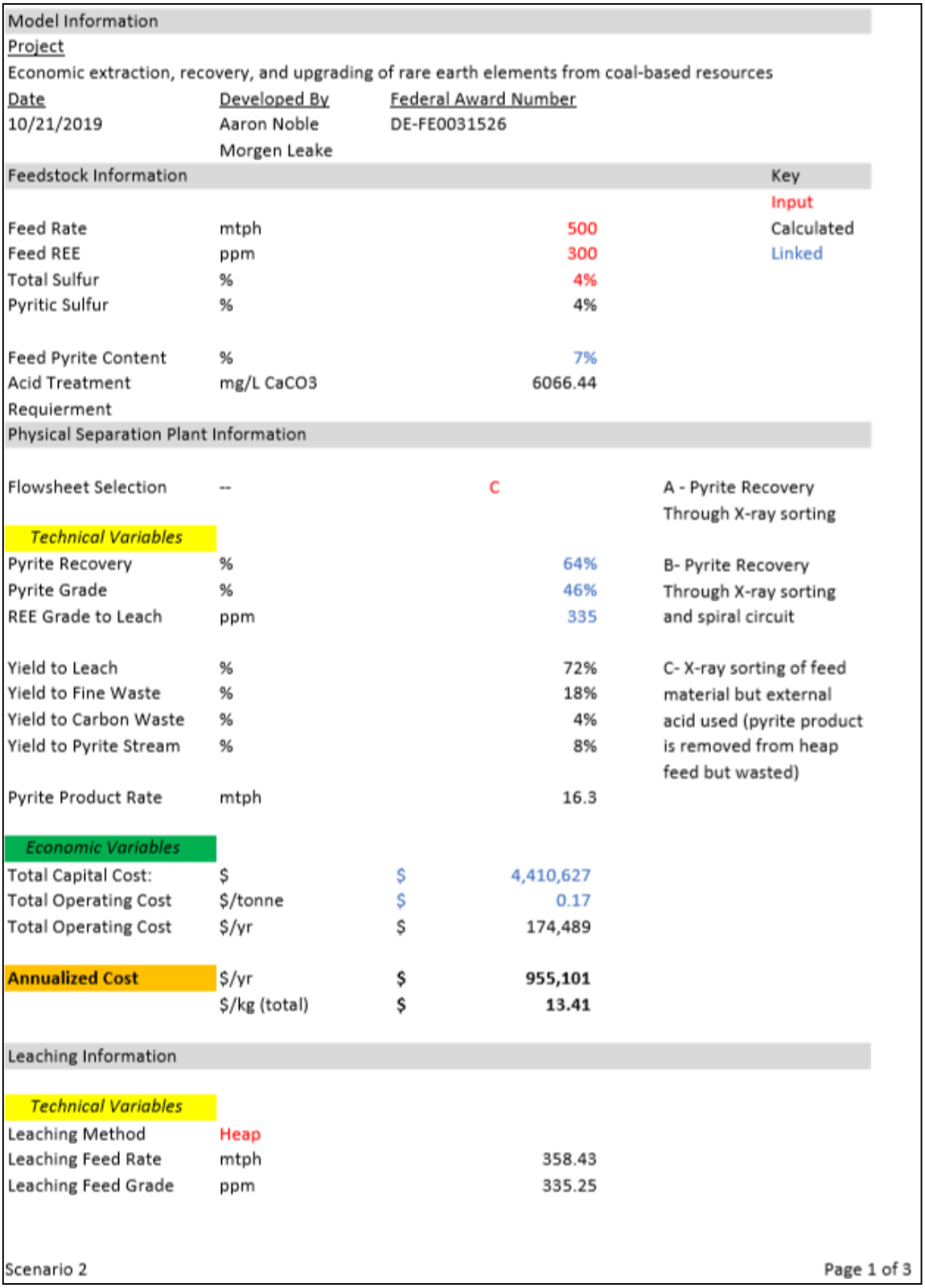

Model Information

Project

Economic extraction, recovery, and upgrading of rare earth elements from coal-based resources

Date	Developed By	Federal Award Number
10/21/2019	Aaron Noble Morgen Leake	DE-FE0031526

Feedstock Information				Key
				Input
Feed Rate	mtph		500	Calculated
Feed REE	ppm		300	Linked
Total Sulfur	%		4%	
Pyritic Sulfur	%		4%	
Feed Pyrite Content	%		7%	
Acid Treatment Requierment	mg/L CaCO3		6066.44	
Physical Separation Plant Information				
Flowsheet Selection	--		C	A - Pyrite Recovery Through X-ray sorting
Technical Variables				
Pyrite Recovery	%		64%	B- Pyrite Recovery Through X-ray sorting and spiral circuit
Pyrite Grade	%		46%	
REE Grade to Leach	ppm		335	
Yield to Leach	%		72%	C- X-ray sorting of feed material but external acid used (pyrite product is removed from heap feed but wasted)
Yield to Fine Waste	%		18%	
Yield to Carbon Waste	%		4%	
Yield to Pyrite Stream	%		8%	
Pyrite Product Rate	mtph		16.3	
Economic Variables				
Total Capital Cost:	$	$	4,410,627	
Total Operating Cost	$/tonne	$	0.17	
Total Operating Cost	$/yr	$	174,489	
Annualized Cost	$/yr	**$**	**955,101**	
	$/kg (total)	**$**	**13.41**	
Leaching Information				
Technical Variables				
Leaching Method	Heap			
Leaching Feed Rate	mtph		358.43	
Leaching Feed Grade	ppm		335.25	

Scenario 2 Page 1 of 3

Figure 6 - 3: Technoeconomic analysis of Scenario 2 - REE recovery from coarse refuse with an X-ray sorting preconcentration and external acid source (page 1 of 3)

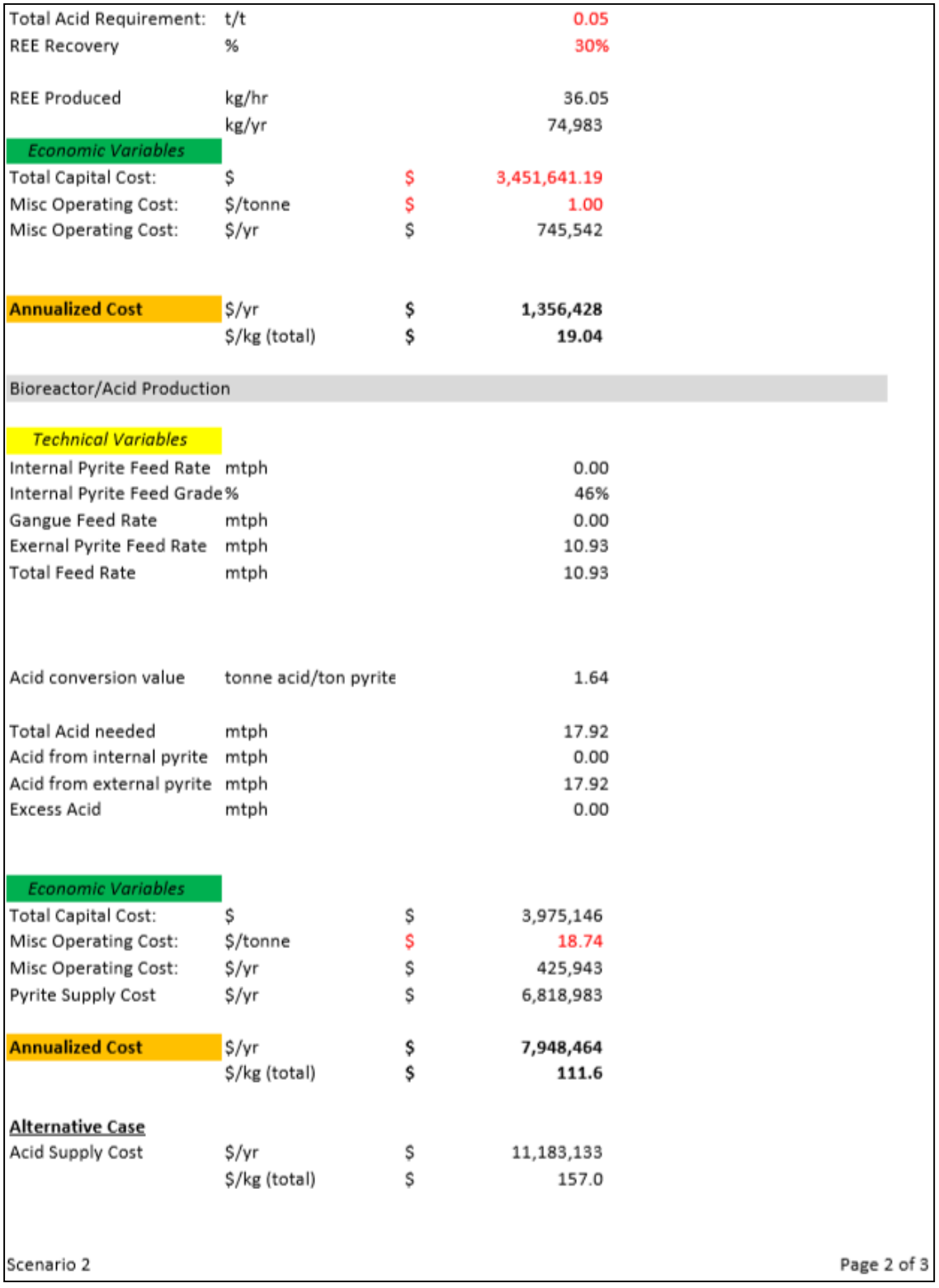

Total Acid Requirement:	t/t		0.05
REE Recovery	%		30%
REE Produced	kg/hr		36.05
	kg/yr		74,983
Economic Variables			
Total Capital Cost:	$	$	3,451,641.19
Misc Operating Cost:	$/tonne	$	1.00
Misc Operating Cost:	$/yr	$	745,542
Annualized Cost	$/yr	$	**1,356,428**
	$/kg (total)	$	**19.04**
Bioreactor/Acid Production			
Technical Variables			
Internal Pyrite Feed Rate	mtph		0.00
Internal Pyrite Feed Grade	%		46%
Gangue Feed Rate	mtph		0.00
Exernal Pyrite Feed Rate	mtph		10.93
Total Feed Rate	mtph		10.93
Acid conversion value	tonne acid/ton pyrite		1.64
Total Acid needed	mtph		17.92
Acid from internal pyrite	mtph		0.00
Acid from external pyrite	mtph		17.92
Excess Acid	mtph		0.00
Economic Variables			
Total Capital Cost:	$	$	3,975,146
Misc Operating Cost:	$/tonne	$	18.74
Misc Operating Cost:	$/yr	$	425,943
Pyrite Supply Cost	$/yr	$	6,818,983
Annualized Cost	$/yr	$	**7,948,464**
	$/kg (total)	$	**111.6**
Alternative Case			
Acid Supply Cost	$/yr	$	11,183,133
	$/kg (total)	$	157.0

Scenario 2 Page 2 of 3

Figure 6 - 4: Technoeconomic analysis of Scenario 2 - REE recovery from coarse refuse with an X-ray sorting preconcentration and external acid source (page 2 of 3)

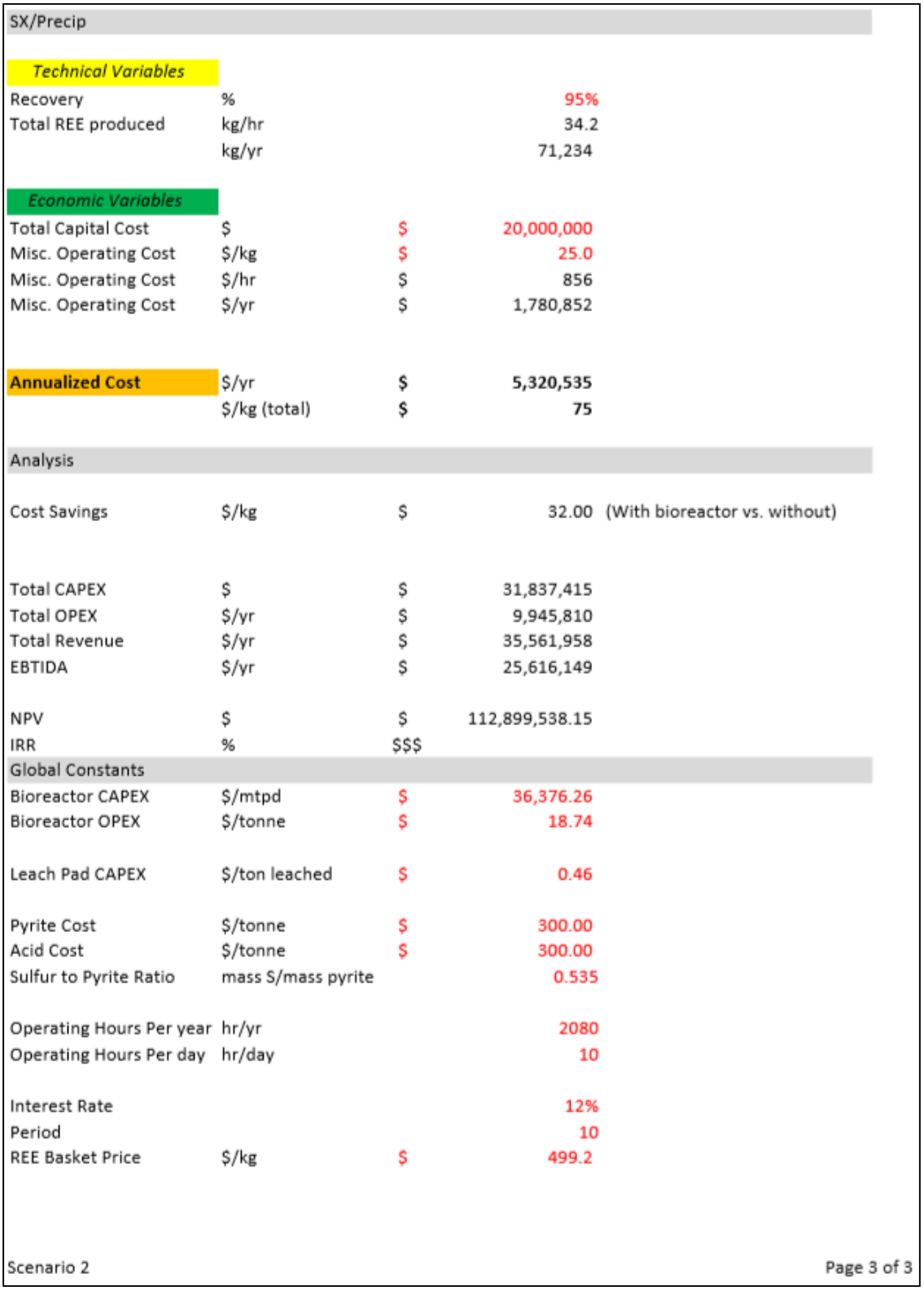

SX/Precip				
Technical Variables				
Recovery	%		95%	
Total REE produced	kg/hr		34.2	
	kg/yr		71,234	
Economic Variables				
Total Capital Cost	$	$	20,000,000	
Misc. Operating Cost	$/kg	$	25.0	
Misc. Operating Cost	$/hr	$	856	
Misc. Operating Cost	$/yr	$	1,780,852	
Annualized Cost	$/yr	**$**	**5,320,535**	
	$/kg (total)	**$**	**75**	
Analysis				
Cost Savings	$/kg	$	32.00	(With bioreactor vs. without)
Total CAPEX	$	$	31,837,415	
Total OPEX	$/yr	$	9,945,810	
Total Revenue	$/yr	$	35,561,958	
EBTIDA	$/yr	$	25,616,149	
NPV	$	$	112,899,538.15	
IRR	%	$$$		
Global Constants				
Bioreactor CAPEX	$/mtpd	$	36,376.26	
Bioreactor OPEX	$/tonne	$	18.74	
Leach Pad CAPEX	$/ton leached	$	0.46	
Pyrite Cost	$/tonne	$	300.00	
Acid Cost	$/tonne	$	300.00	
Sulfur to Pyrite Ratio	mass $/mass pyrite		0.535	
Operating Hours Per year	hr/yr		2080	
Operating Hours Per day	hr/day		10	
Interest Rate			12%	
Period			10	
REE Basket Price	$/kg	$	499.2	

Scenario 2 Page 3 of 3

Figure 6 - 5: Technoeconomic analysis of Scenario 2 - REE recovery from coarse refuse with an X-ray sorting preconcentration and external acid source (page 3 of 3)

6.5 Scenario 3a

This scenario involves the same physical concentration plant as Scenario 2; however the pyrite product is used in the bioreactor as opposed to only externally purchased pyrite. From lab testing data, this pyrite bioreactor feed material contains approximately 64% of the feed pyrite at a grade of 46%. The full technoeconomic analysis for this scenario is given in Figure 6 - 6 to Figure 6 - 8.

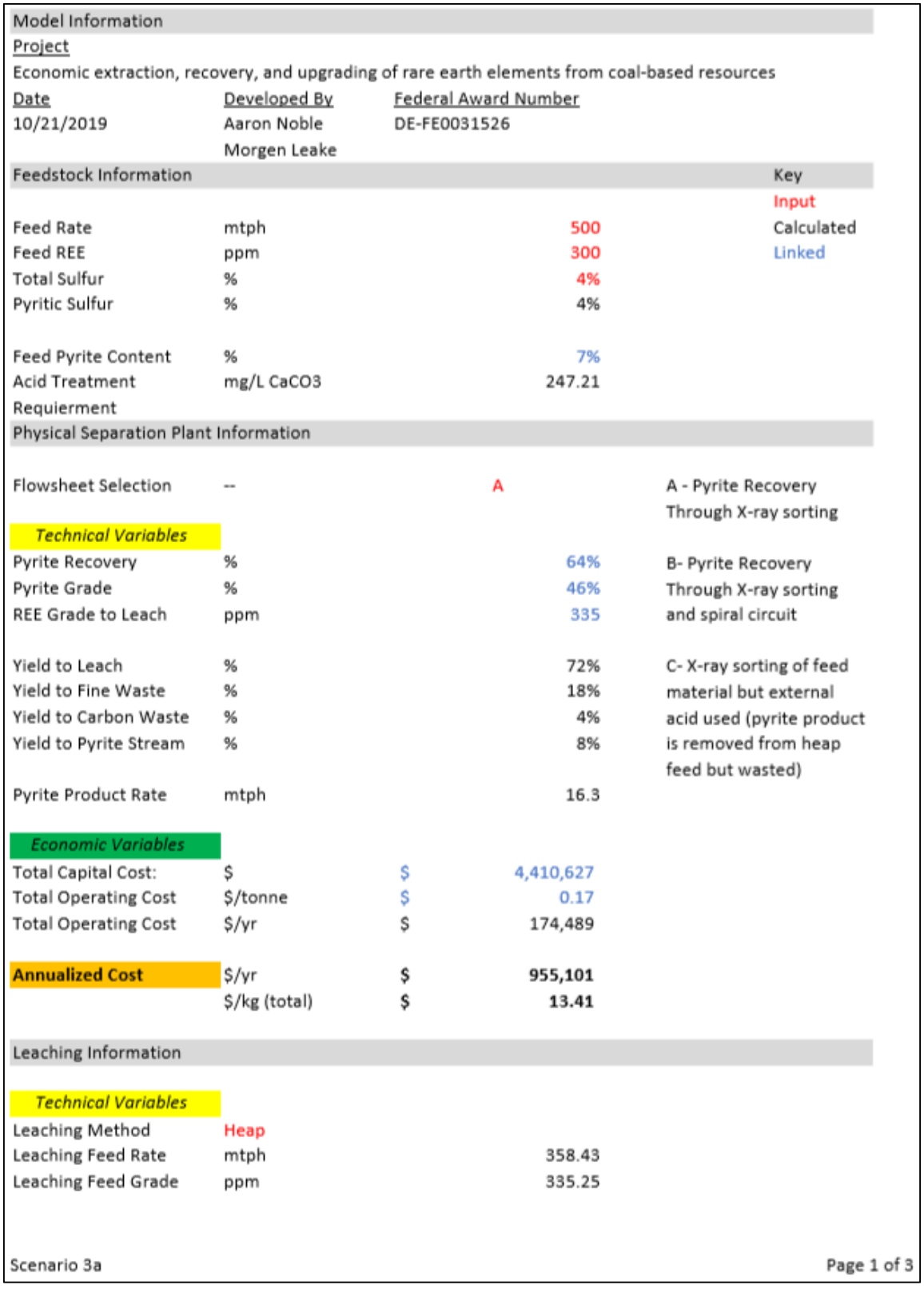

Model Information

Project

Economic extraction, recovery, and upgrading of rare earth elements from coal-based resources

Date	Developed By	Federal Award Number
10/21/2019	Aaron Noble Morgen Leake	DE-FE0031526

Feedstock Information				Key
				Input
Feed Rate	mtph		500	Calculated
Feed REE	ppm		300	Linked
Total Sulfur	%		4%	
Pyritic Sulfur	%		4%	
Feed Pyrite Content	%		7%	
Acid Treatment Requierment	mg/L CaCO3		247.21	

Physical Separation Plant Information				
Flowsheet Selection	--		A	A - Pyrite Recovery Through X-ray sorting
Technical Variables				
Pyrite Recovery	%		64%	B- Pyrite Recovery Through X-ray sorting and spiral circuit
Pyrite Grade	%		46%	
REE Grade to Leach	ppm		335	
Yield to Leach	%		72%	C- X-ray sorting of feed material but external acid used (pyrite product is removed from heap feed but wasted)
Yield to Fine Waste	%		18%	
Yield to Carbon Waste	%		4%	
Yield to Pyrite Stream	%		8%	
Pyrite Product Rate	mtph		16.3	
Economic Variables				
Total Capital Cost:	$	$	4,410,627	
Total Operating Cost	$/tonne	$	0.17	
Total Operating Cost	$/yr	$	174,489	
Annualized Cost	$/yr	$	**955,101**	
	$/kg (total)	$	**13.41**	

Leaching Information		
Technical Variables		
Leaching Method	Heap	
Leaching Feed Rate	mtph	358.43
Leaching Feed Grade	ppm	335.25

Scenario 3a

Page 1 of 3

Figure 6 - 6: Technoeconomic analysis of Scenario 3a - REE recovery from coarse refuse with an X-ray sorting preconcentration and internal acid source (page 1 of 3)

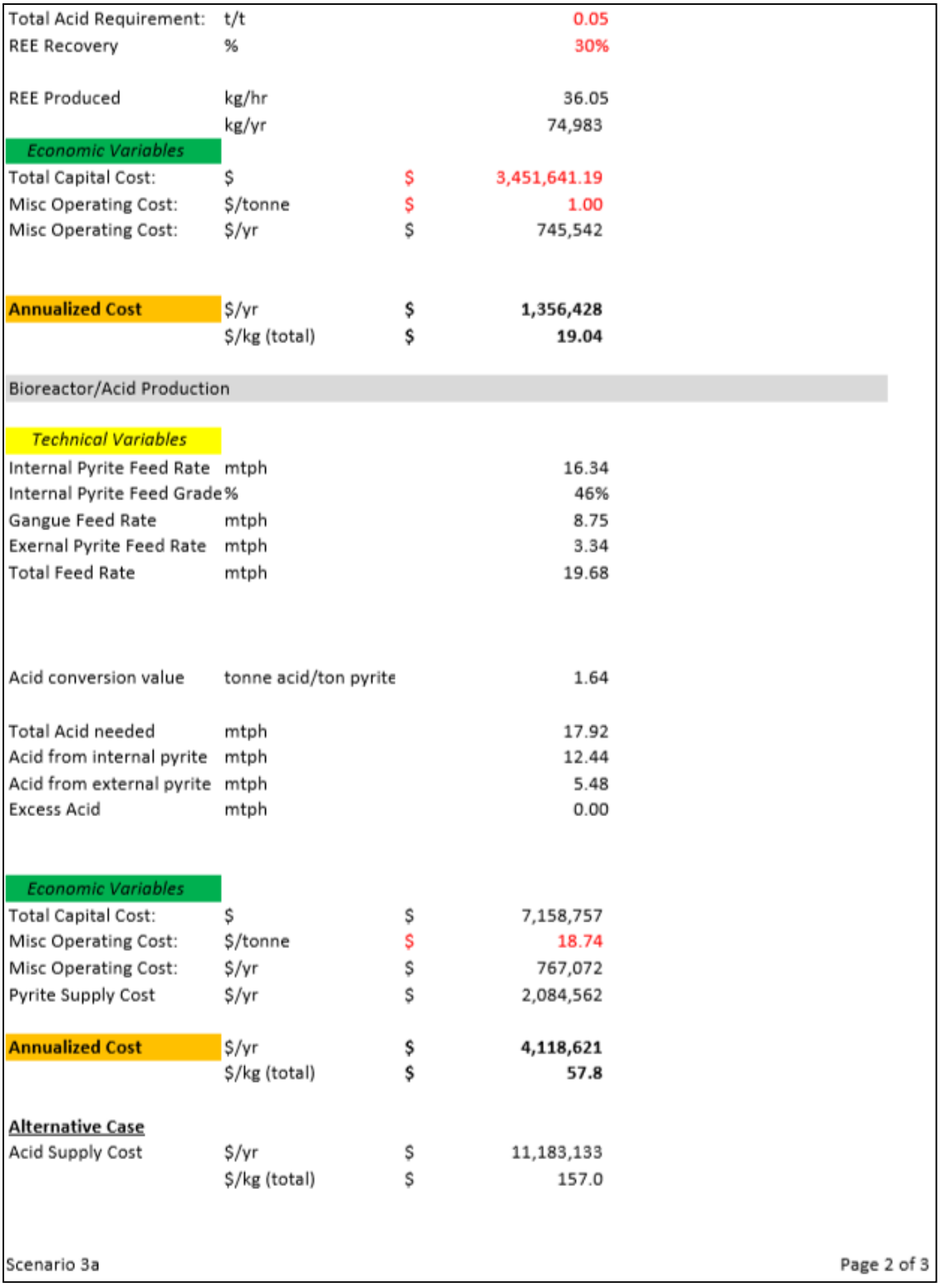

Total Acid Requirement:	t/t		0.05
REE Recovery	%		30%
REE Produced	kg/hr		36.05
	kg/yr		74,983
Economic Variables			
Total Capital Cost:	$	$	3,451,641.19
Misc Operating Cost:	$/tonne	$	1.00
Misc Operating Cost:	$/yr	$	745,542
Annualized Cost	$/yr	$	**1,356,428**
	$/kg (total)	$	**19.04**
Bioreactor/Acid Production			
Technical Variables			
Internal Pyrite Feed Rate	mtph		16.34
Internal Pyrite Feed Grade	%		46%
Gangue Feed Rate	mtph		8.75
Exernal Pyrite Feed Rate	mtph		3.34
Total Feed Rate	mtph		19.68
Acid conversion value	tonne acid/ton pyrite		1.64
Total Acid needed	mtph		17.92
Acid from internal pyrite	mtph		12.44
Acid from external pyrite	mtph		5.48
Excess Acid	mtph		0.00
Economic Variables			
Total Capital Cost:	$	$	7,158,757
Misc Operating Cost:	$/tonne	$	18.74
Misc Operating Cost:	$/yr	$	767,072
Pyrite Supply Cost	$/yr	$	2,084,562
Annualized Cost	$/yr	$	**4,118,621**
	$/kg (total)	$	**57.8**
Alternative Case			
Acid Supply Cost	$/yr	$	11,183,133
	$/kg (total)	$	157.0

Scenario 3a Page 2 of 3

Figure 6 - 7: Technoeconomic analysis of Scenario 3a - REE recovery from coarse refuse with an X-ray sorting preconcentration and internal acid source (page 2 of 3)

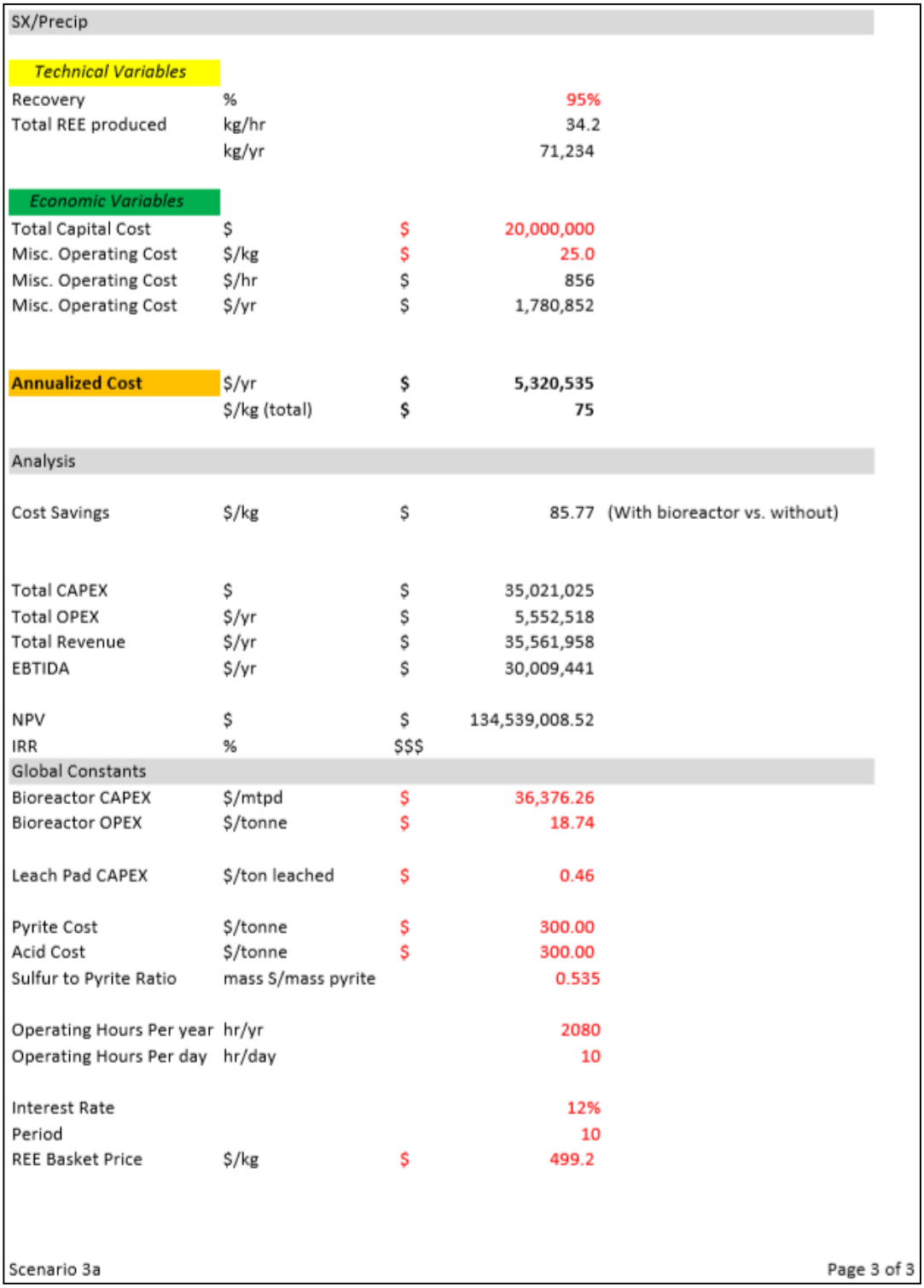

SX/Precip				
Technical Variables				
Recovery	%		95%	
Total REE produced	kg/hr		34.2	
	kg/yr		71,234	
Economic Variables				
Total Capital Cost	$	$	20,000,000	
Misc. Operating Cost	$/kg	$	25.0	
Misc. Operating Cost	$/hr	$	856	
Misc. Operating Cost	$/yr	$	1,780,852	
Annualized Cost	$/yr	**$**	**5,320,535**	
	$/kg (total)	**$**	**75**	
Analysis				
Cost Savings	$/kg	$	85.77	(With bioreactor vs. without)
Total CAPEX	$	$	35,021,025	
Total OPEX	$/yr	$	5,552,518	
Total Revenue	$/yr	$	35,561,958	
EBTIDA	$/yr	$	30,009,441	
NPV	$	$	134,539,008.52	
IRR	%	$$$		
Global Constants				
Bioreactor CAPEX	$/mtpd	$	36,376.26	
Bioreactor OPEX	$/tonne	$	18.74	
Leach Pad CAPEX	$/ton leached	$	0.46	
Pyrite Cost	$/tonne	$	300.00	
Acid Cost	$/tonne	$	300.00	
Sulfur to Pyrite Ratio	mass S/mass pyrite		0.535	
Operating Hours Per year	hr/yr		2080	
Operating Hours Per day	hr/day		10	
Interest Rate			12%	
Period			10	
REE Basket Price	$/kg	$	499.2	

Scenario 3a Page 3 of 3

Figure 6 - 8: Technoeconomic analysis of Scenario 3a - REE recovery from coarse refuse with an X-ray sorting preconcentration and internal acid source (page 3 of 3)

6.6 Scenario 3b

The final scenario builds from Scenario 3a by adding a spiral concentration circuit for the pyrite material ejected by the x-ray sorter. Figure 6 - 9 shows the expanded flowsheet. The sorted pyrite material is fed through a roll crusher to prepare it for spiral concentration. The crushed material passes over a dry 1mm screen where the oversize is recirculated to the crusher and the undersize is fed to a cyclone bank. The cyclone bank makes a cut at 150 microns and the underflow proceeds to a spiral bank. The overflow from the cyclones is a fine slurry waste.

The spiral bank concentrates the material at approximately 2.95 SG, producing an approximately 71% grade pyrite product, recovering 44% of the pyrite from the initial coarse refuse feed. The full techno-economic analysis is given in Figure 6 - 10 to Figure 6 - 12.

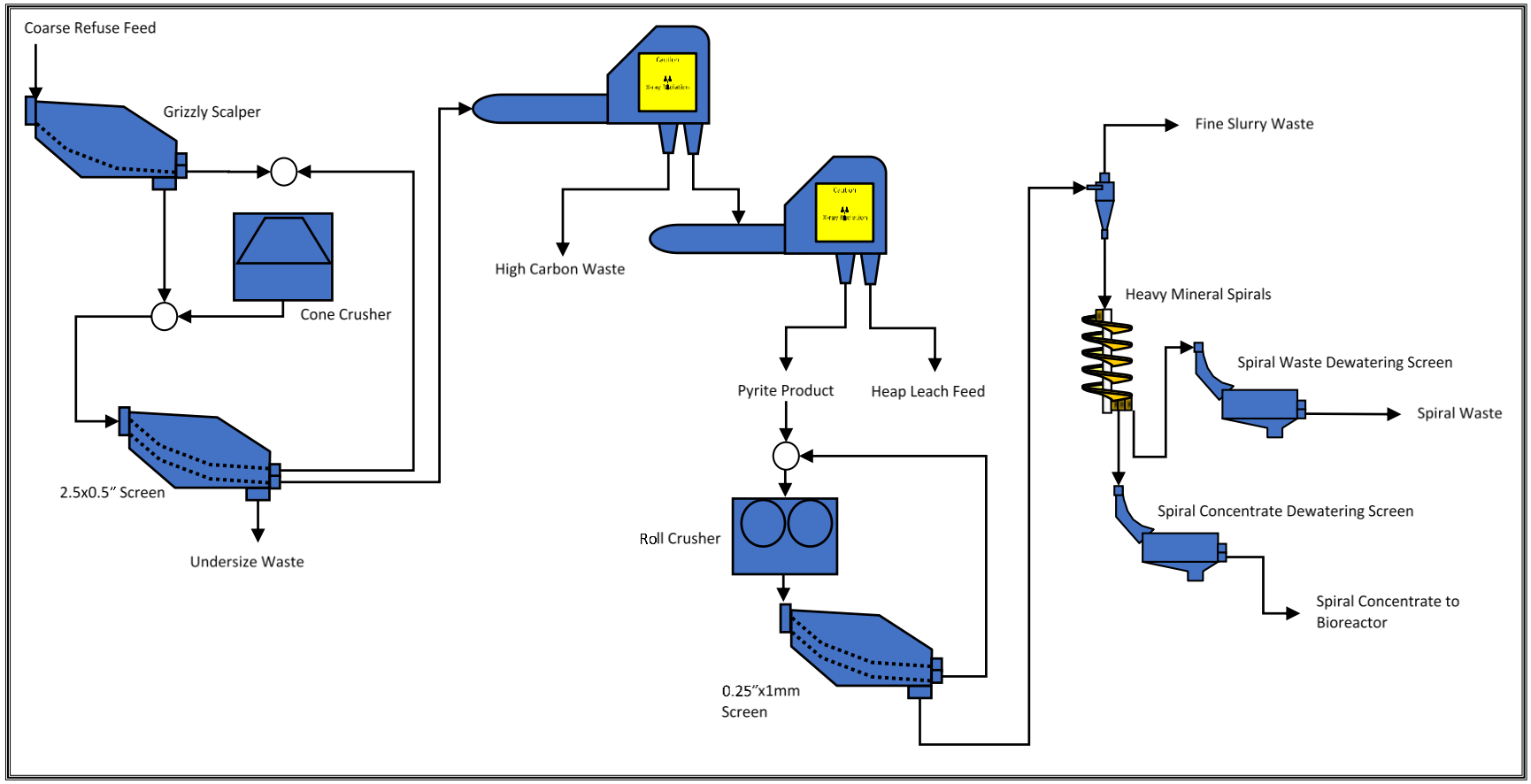

Figure 6 - 9: Process flowsheet for Scenario 3b - Physical preconcentration of heap leach feed material by x-ray sorting and spiral concentration

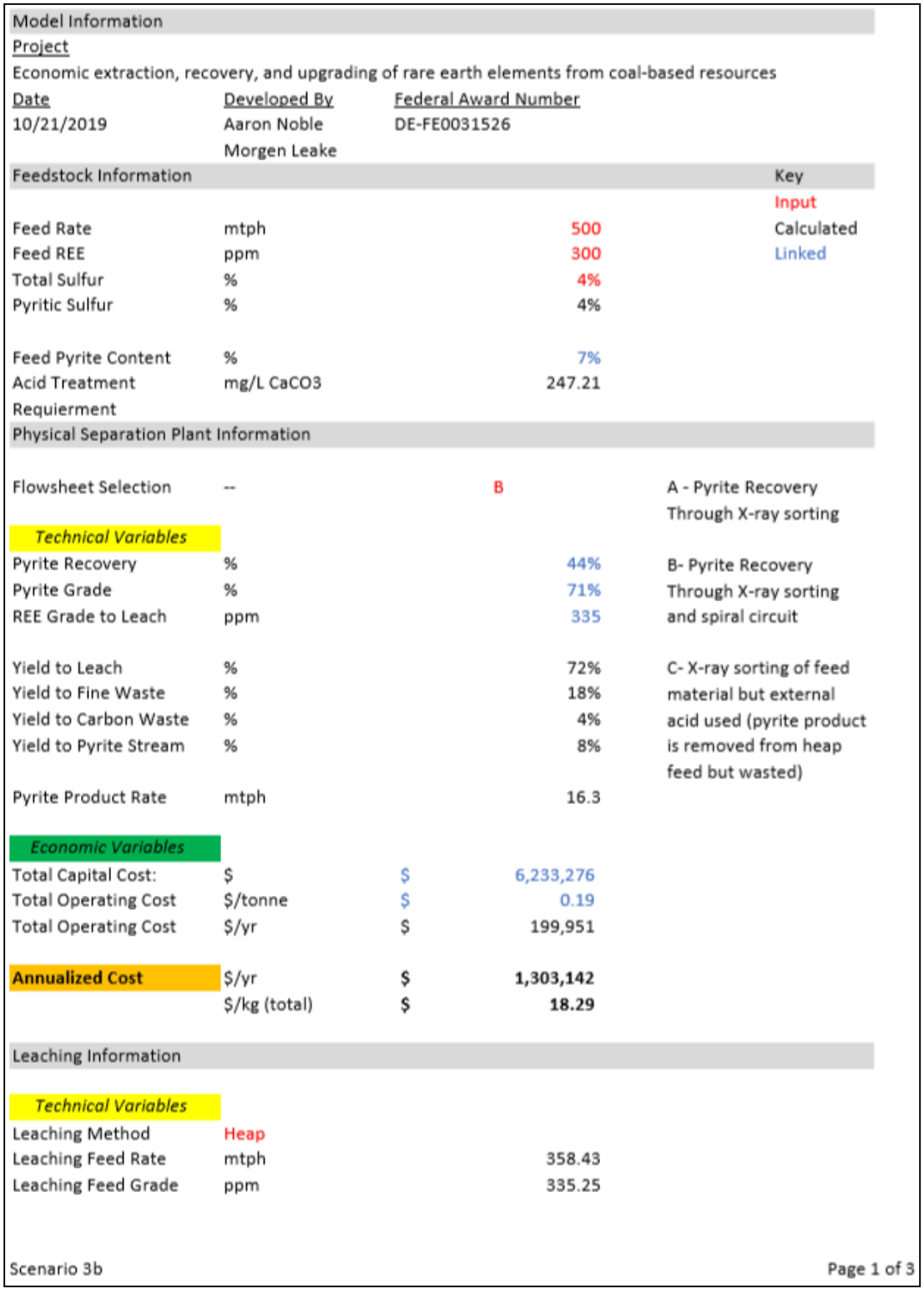

Model Information				
Project				
Economic extraction, recovery, and upgrading of rare earth elements from coal-based resources				
Date	Developed By	Federal Award Number		
10/21/2019	Aaron Noble Morgen Leake	DE-FE0031526		
Feedstock Information				Key
				Input
Feed Rate	mtph		500	Calculated
Feed REE	ppm		300	Linked
Total Sulfur	%		4%	
Pyritic Sulfur	%		4%	
Feed Pyrite Content	%		7%	
Acid Treatment Requierment	mg/L CaCO3		247.21	
Physical Separation Plant Information				
Flowsheet Selection	--		B	A - Pyrite Recovery Through X-ray sorting
Technical Variables				
Pyrite Recovery	%		44%	B- Pyrite Recovery Through X-ray sorting and spiral circuit
Pyrite Grade	%		71%	
REE Grade to Leach	ppm		335	
Yield to Leach	%		72%	C- X-ray sorting of feed material but external acid used (pyrite product is removed from heap feed but wasted)
Yield to Fine Waste	%		18%	
Yield to Carbon Waste	%		4%	
Yield to Pyrite Stream	%		8%	
Pyrite Product Rate	mtph		16.3	
Economic Variables				
Total Capital Cost:	$	$	6,233,276	
Total Operating Cost	$/tonne	$	0.19	
Total Operating Cost	$/yr	$	199,951	
Annualized Cost	$/yr	$	**1,303,142**	
	$/kg (total)	$	**18.29**	
Leaching Information				
Technical Variables				
Leaching Method	Heap			
Leaching Feed Rate	mtph		358.43	
Leaching Feed Grade	ppm		335.25	

Scenario 3b

Page 1 of 3

Figure 6 - 10: Technoeconomic analysis of Scenario 3b – REE recovery from coarse refuse with x-ray sorting preconcentration and additional spiral concentration of pyrite material for internal acid production (page 1 of 3)

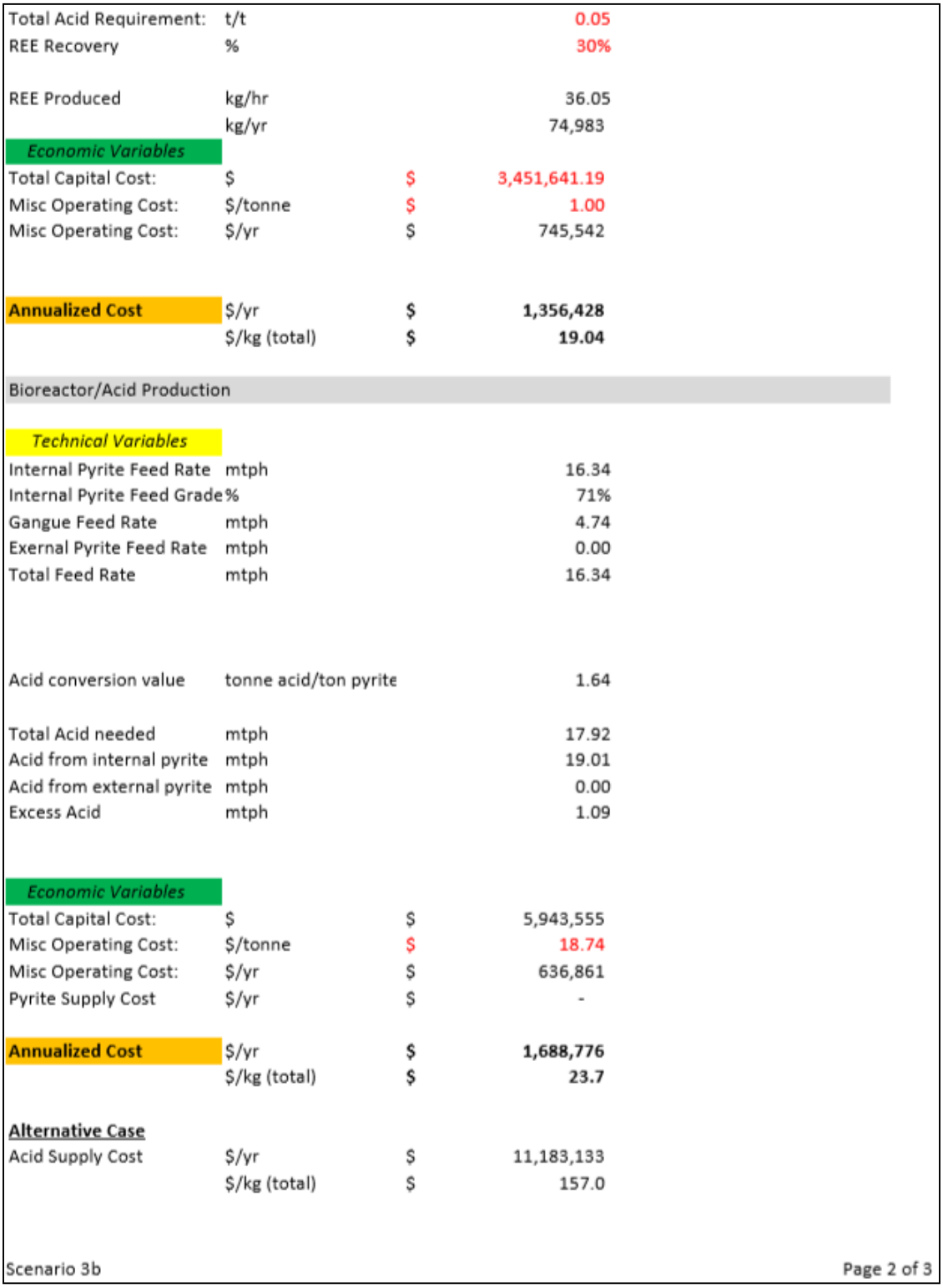

Total Acid Requirement:	t/t		0.05
REE Recovery	%		30%
REE Produced	kg/hr		36.05
	kg/yr		74,983
Economic Variables			
Total Capital Cost:	$	$	3,451,641.19
Misc Operating Cost:	$/tonne	$	1.00
Misc Operating Cost:	$/yr	$	745,542
Annualized Cost	$/yr	$	**1,356,428**
	$/kg (total)	$	**19.04**
Bioreactor/Acid Production			
Technical Variables			
Internal Pyrite Feed Rate	mtph		16.34
Internal Pyrite Feed Grade	%		71%
Gangue Feed Rate	mtph		4.74
Exernal Pyrite Feed Rate	mtph		0.00
Total Feed Rate	mtph		16.34
Acid conversion value	tonne acid/ton pyrite		1.64
Total Acid needed	mtph		17.92
Acid from internal pyrite	mtph		19.01
Acid from external pyrite	mtph		0.00
Excess Acid	mtph		1.09
Economic Variables			
Total Capital Cost:	$	$	5,943,555
Misc Operating Cost:	$/tonne	$	18.74
Misc Operating Cost:	$/yr	$	636,861
Pyrite Supply Cost	$/yr	$	-
Annualized Cost	$/yr	$	**1,688,776**
	$/kg (total)	$	**23.7**
Alternative Case			
Acid Supply Cost	$/yr	$	11,183,133
	$/kg (total)	$	157.0

Scenario 3b Page 2 of 3

Figure 6 - 11: Technoeconomic analysis of Scenario 3b – REE recovery from coarse refuse with x-ray sorting preconcentration and additional spiral concentration of pyrite material for internal acid production (page 2 of 3)

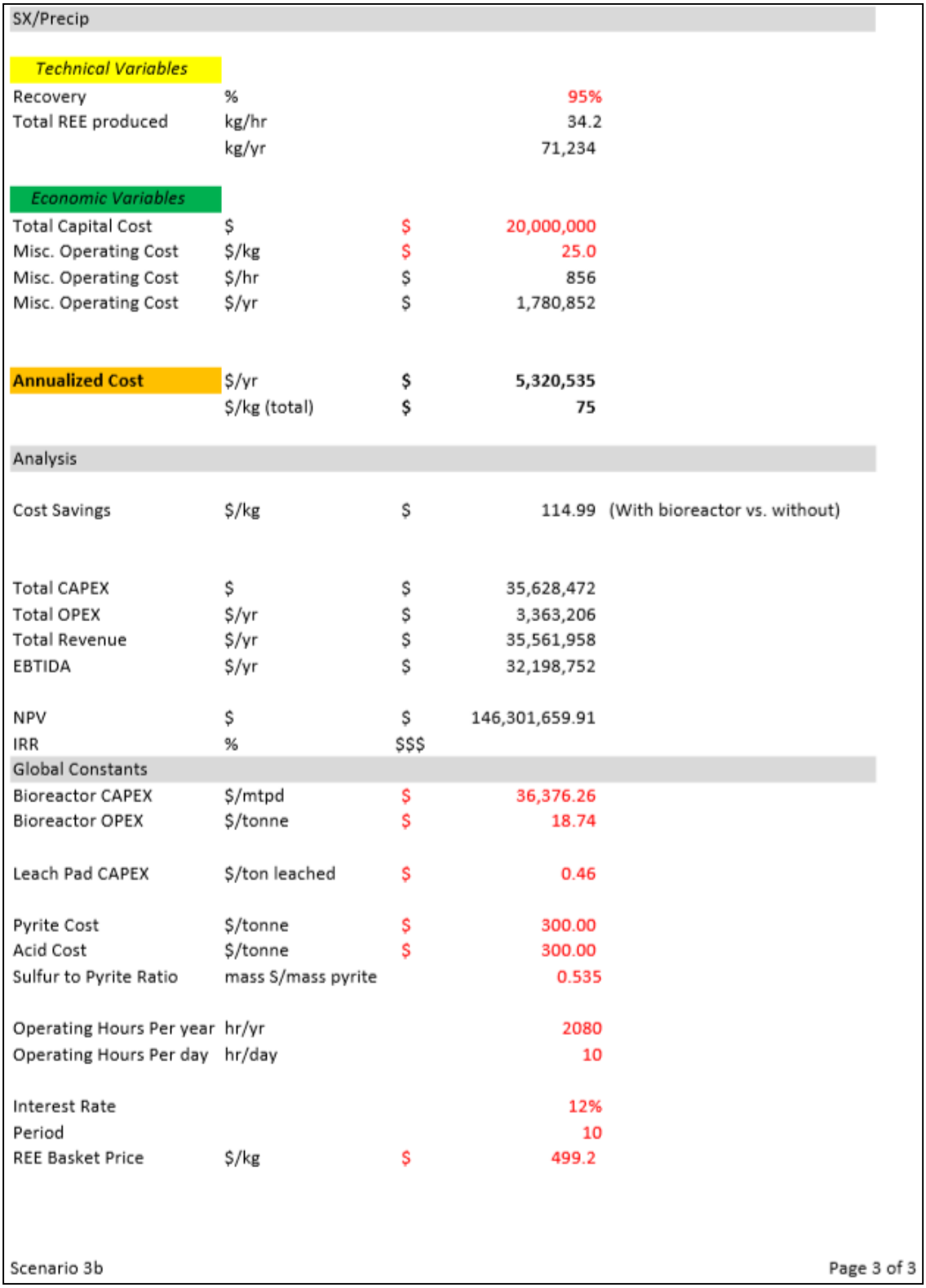

SX/Precip				
Technical Variables				
Recovery	%		95%	
Total REE produced	kg/hr		34.2	
	kg/yr		71,234	
Economic Variables				
Total Capital Cost	$	$	20,000,000	
Misc. Operating Cost	$/kg	$	25.0	
Misc. Operating Cost	$/hr	$	856	
Misc. Operating Cost	$/yr	$	1,780,852	
Annualized Cost	$/yr	$	**5,320,535**	
	$/kg (total)	$	**75**	
Analysis				
Cost Savings	$/kg	$	114.99	(With bioreactor vs. without)
Total CAPEX	$	$	35,628,472	
Total OPEX	$/yr	$	3,363,206	
Total Revenue	$/yr	$	35,561,958	
EBTIDA	$/yr	$	32,198,752	
NPV	$	$	146,301,659.91	
IRR	%	$$$		
Global Constants				
Bioreactor CAPEX	$/mtpd	$	36,376.26	
Bioreactor OPEX	$/tonne	$	18.74	
Leach Pad CAPEX	$/ton leached	$	0.46	
Pyrite Cost	$/tonne	$	300.00	
Acid Cost	$/tonne	$	300.00	
Sulfur to Pyrite Ratio	mass S/mass pyrite		0.535	
Operating Hours Per year	hr/yr		2080	
Operating Hours Per day	hr/day		10	
Interest Rate			12%	
Period			10	
REE Basket Price	$/kg	$	499.2	

Scenario 3b Page 3 of 3

Figure 6 - 12: Technoeconomic analysis of Scenario 3b – REE recovery from coarse refuse with x-ray sorting preconcentration and additional spiral concentration of pyrite material for internal acid production (page 3 of 3)

6.7 Results and Discussion

Table 6 - 4 shows the three scenarios compared by cost savings, CAPEX, OPEX, and NPV. Scenario 2 shows the fewest savings when comparing bioreaction of pyrite for acid production compared to purchasing acid outright. These savings are considering equal cost of pyrite and acid per ton. Savings increase with increasing internal pyrite used for acid production. The additional physical concentration of the pyrite material also contributes to decreasing operating costs due to the price of purchasing pyrite, while only slightly increasing capital costs. The individual analyses show the increased grade of bioreactor feed can reduce the capacity and therefore reduce capital costs.

Figure 6 - 13 shows the sensitivity of NPV to changes in TREE feed grade and heap leach recovery. The data shows that increasing recoveries are slightly more sensitive with increasing feed grade. NPV also appears to be more sensitive to changes in recovery from 30-60%. Figure 6 - 14 represents the sensitivity of NPV to REE basket price and feed grade for Scenario 2. NPV is also very sensitive to the basket price, ranging from -$50 million to +200 million within a $400/kg price range. This trend is the same for the other scenarios, shifted slightly in the positive direction.

Figure 6 - 15 – Figure 6 - 17 show the sensitivities of cost savings to bioreactor feed grade and acid conversion ratio for the three scenarios. For Scenario 2, the pyrite feed grade is constant, but it is obvious that the acid conversion ratio significantly affects the cost savings of producing acid versus purchasing acid. Scenarios 3a and 3b show the same trends, however the cost savings for the x-ray sorter only scenario are consistently less along the same scales when compared to the x-ray sorter accompanied by the spiral concentration.

Sensitivity of cost savings to pyrite and acid bulk prices for Scenarios 2 and 3a are compared in Figure 6 - 18 and Figure 6 - 19, respectively. Scenario 2 is the most sensitive due to the entire pyrite source being purchased in that scenario, while cost savings remain positive in Scenario 3a for the range of prices used. Scenario 3b does not rely on any external pyrite or acid for the acid requirement of leaching.

Finally, Figure 6 - 20 – Figure 6 - 22 compare the sensitivity of cost savings to the leaching acid requirement and the acid conversion ratio for all three scenarios. When observing decreasing rations, approximately between 1.15-1.2, the higher acid requirements have greater negative effects on cost savings. Acid conversion ratios less than one will have increasingly negative effects on cost savings with increasing acid requirements, as the opposite is true for ratios greater than 1. Additionally, Scenario 3b that contains the most extensive physical preconcentration appears to have the highest tolerance to decreasing acid conversion ratios before reaching negative cost savings.

Table 6 - 4: Summary of economic parameters of various proposed processing scenarios

Summary Table			
	Scenario 2	Scenario 3a	Scenario 3b
Cost Savings ($/kg)	$32.00	$85.77	$114.99
CAPEX	$31,837,415.00	$35,021,025.00	$35,628,472.00
OPEX ($/yr)	$9,945,810.00	$5,552,518.00	$3,363,206.00
NPV	$112,899,538.00	$134,539,008.52	$146,301,659.00

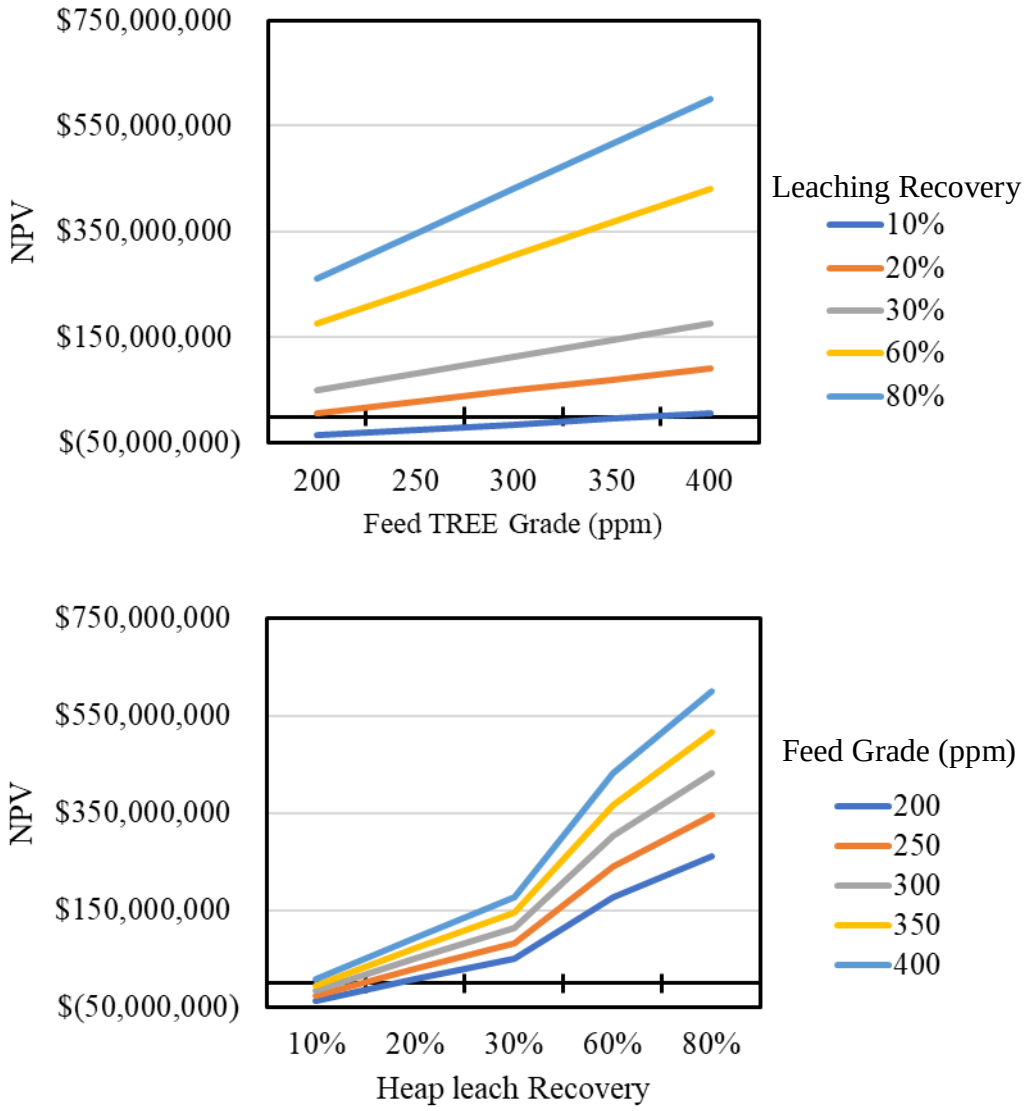

Figure 6 - 13: Sensitivity of NPV to changes in TREE feed grade (ppm) and heap leach recovery for Scenario 2

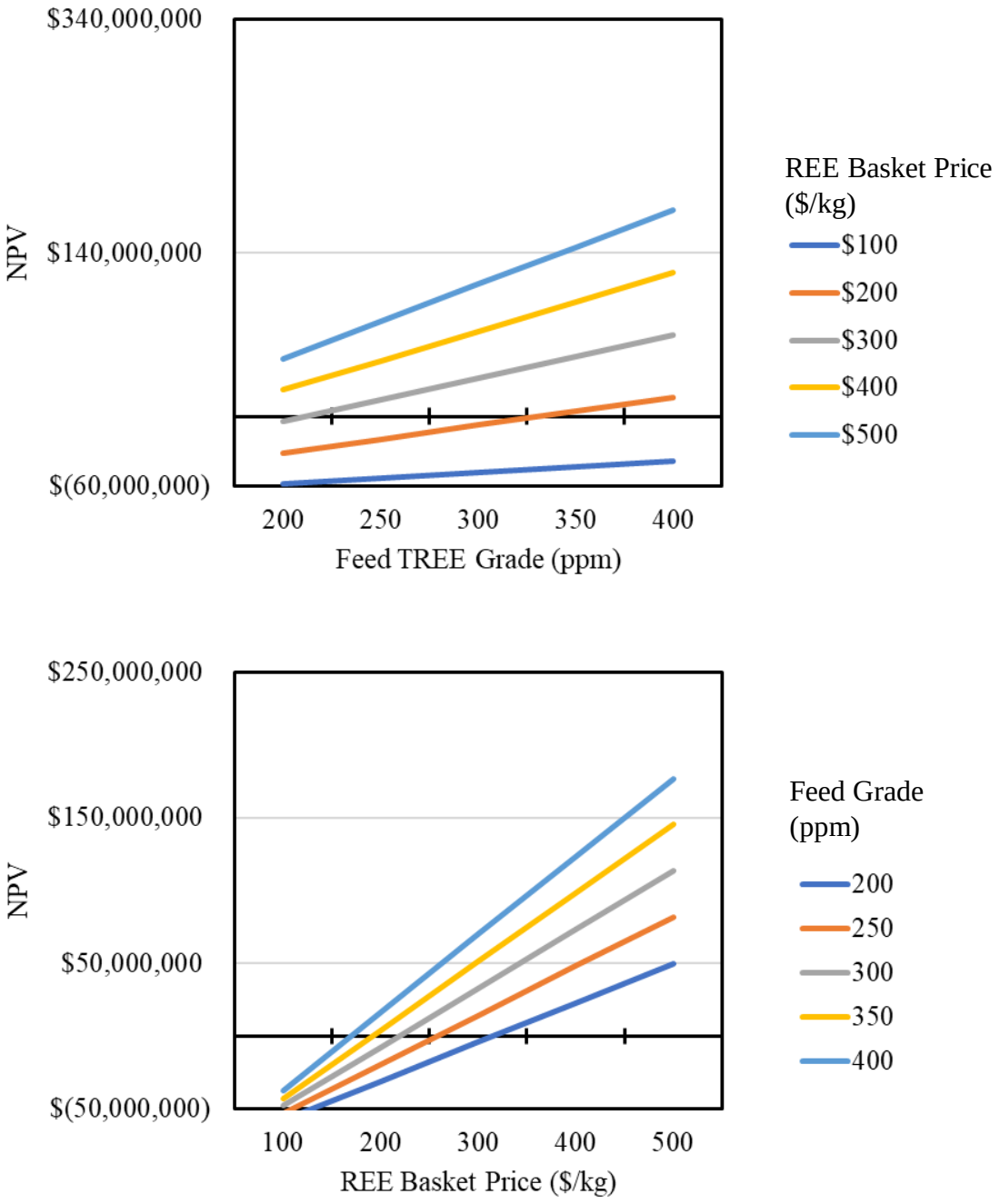

Figure 6 - 14: Sensitivity of NPV to REE basket price ($/kg) and TREE feed grade (ppm) for Scenario 2

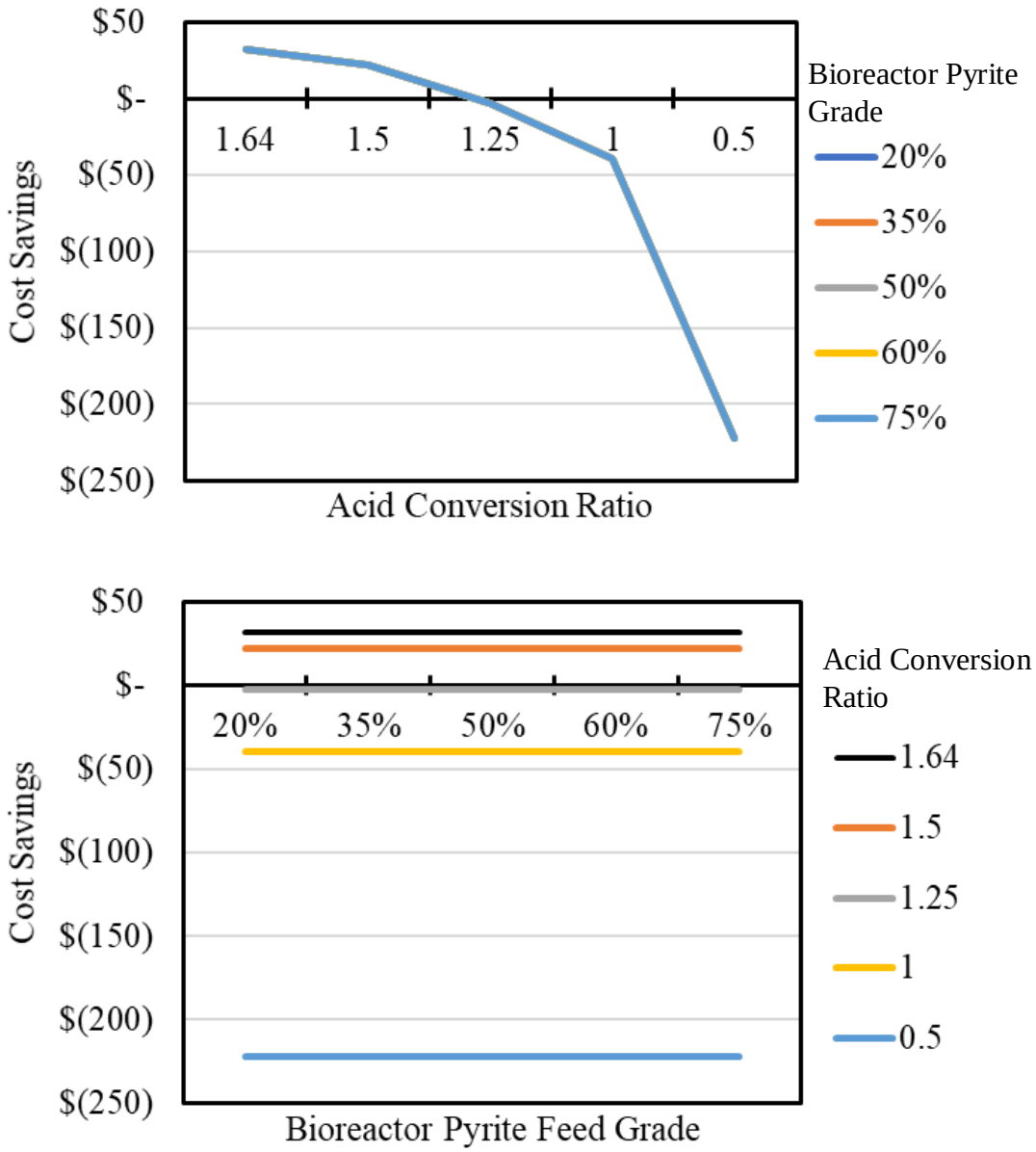

Figure 6 - 15: Sensitivity of cost savings to bioreactor pyrite feed and acid conversion ratio for Scenario 2

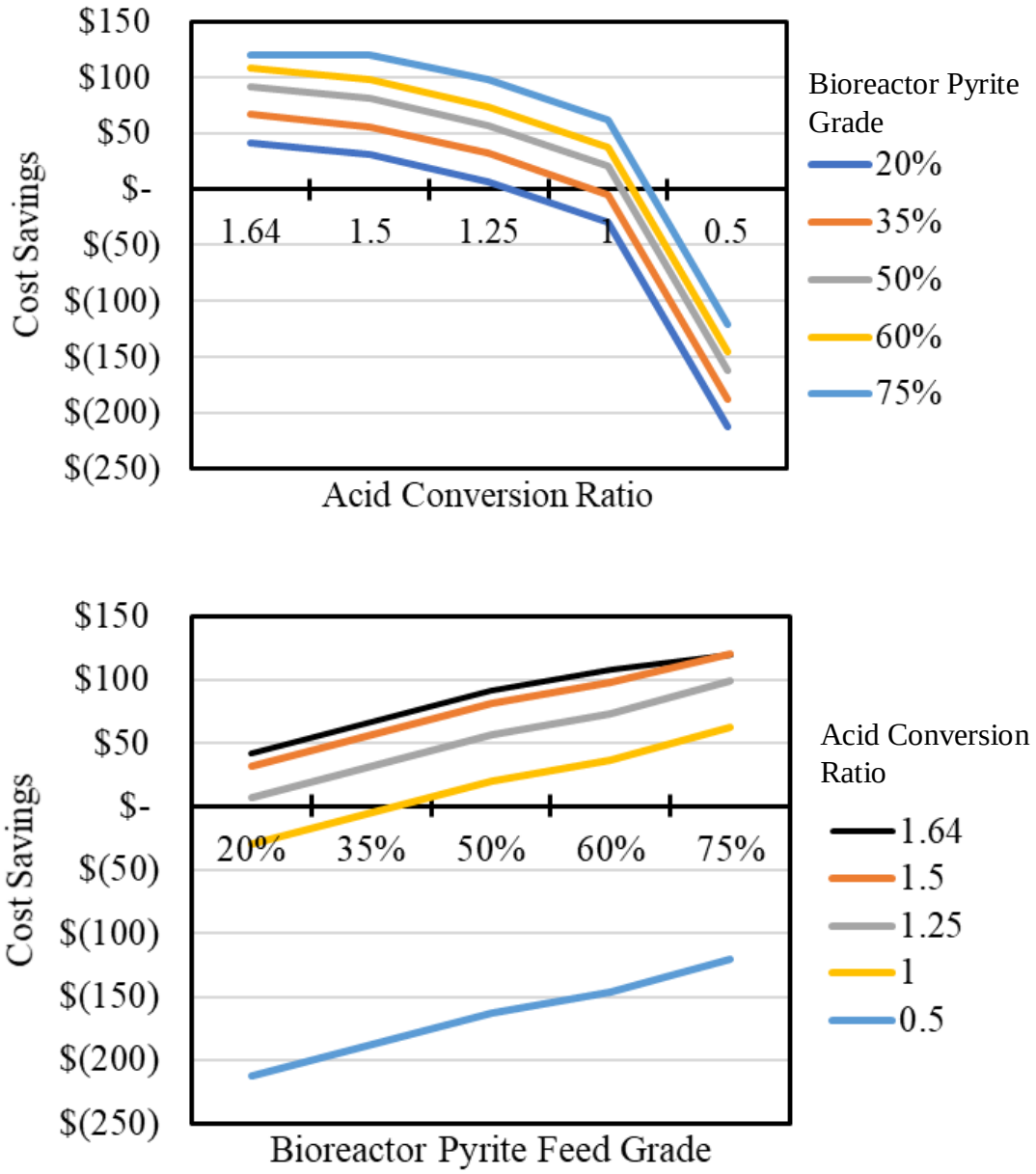

Figure 6 - 16: Sensitivity of cost savings to bioreactor pyrite feed and acid conversion ratio for Scenario 3a

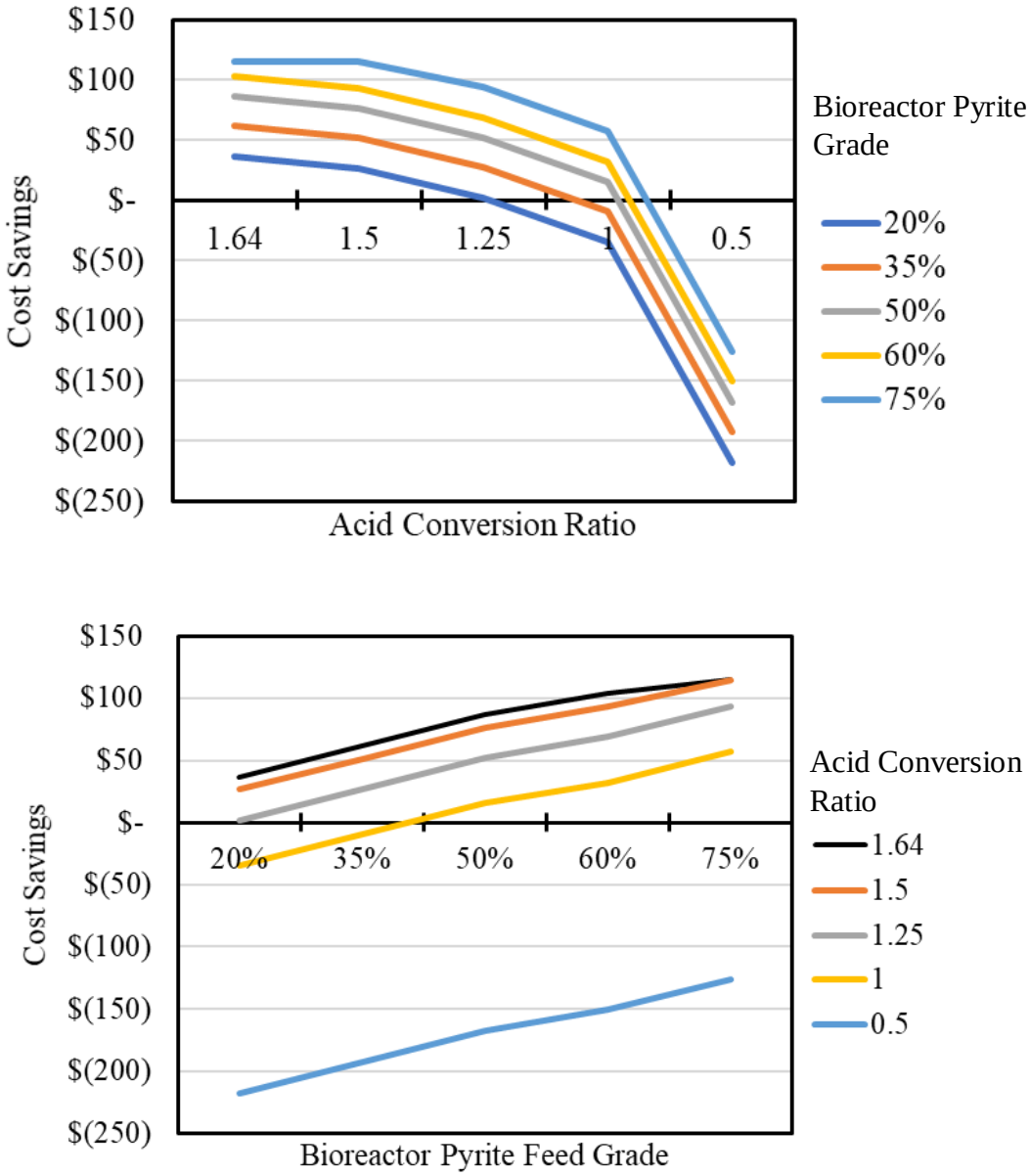

Figure 6 - 17: Sensitivity of cost savings to bioreactor feed and acid conversion ratio for Scenario 3b

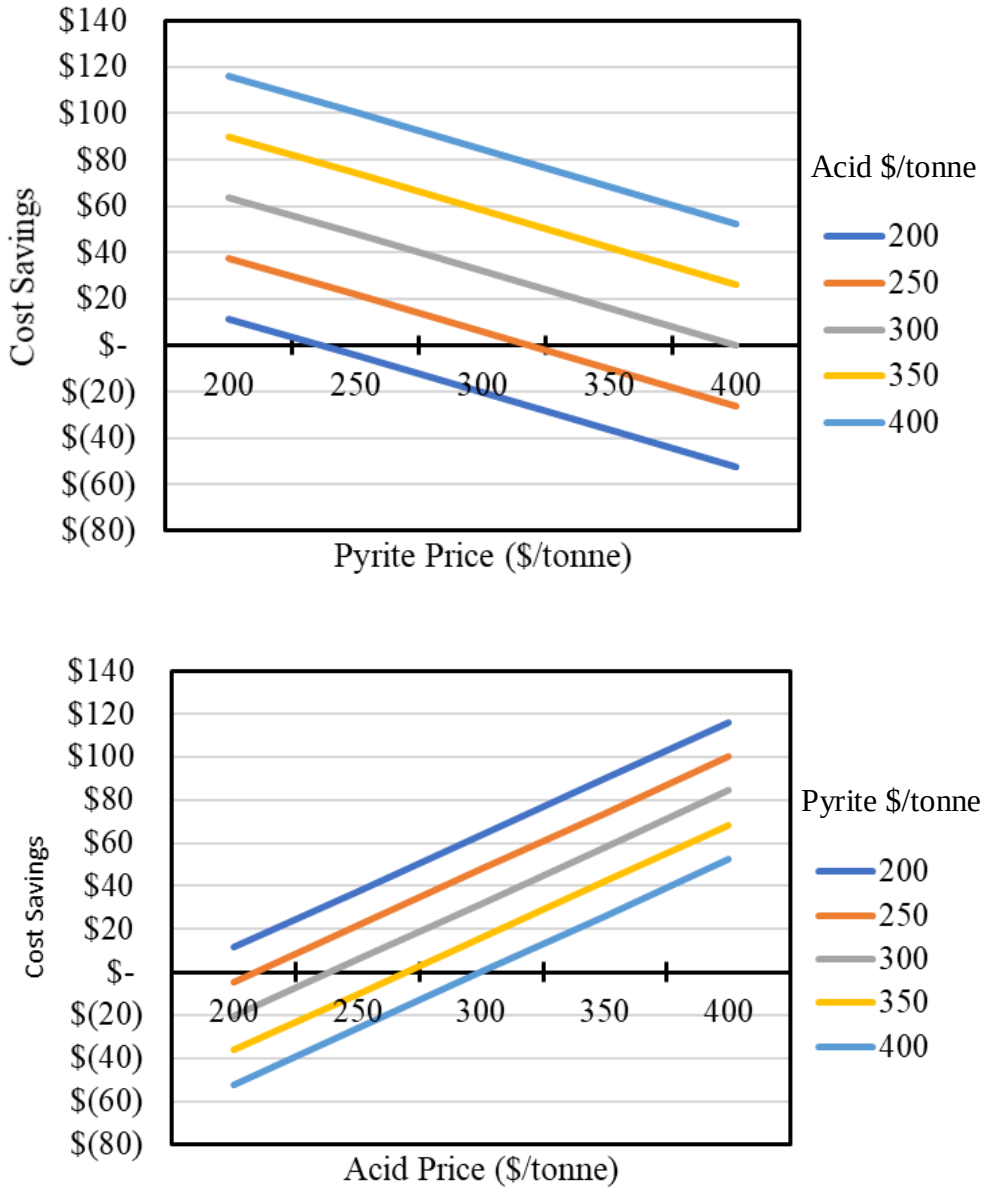

Figure 6 - 18: Sensitivity of cost savings to pyrite and acid bulk prices for Scenario 2

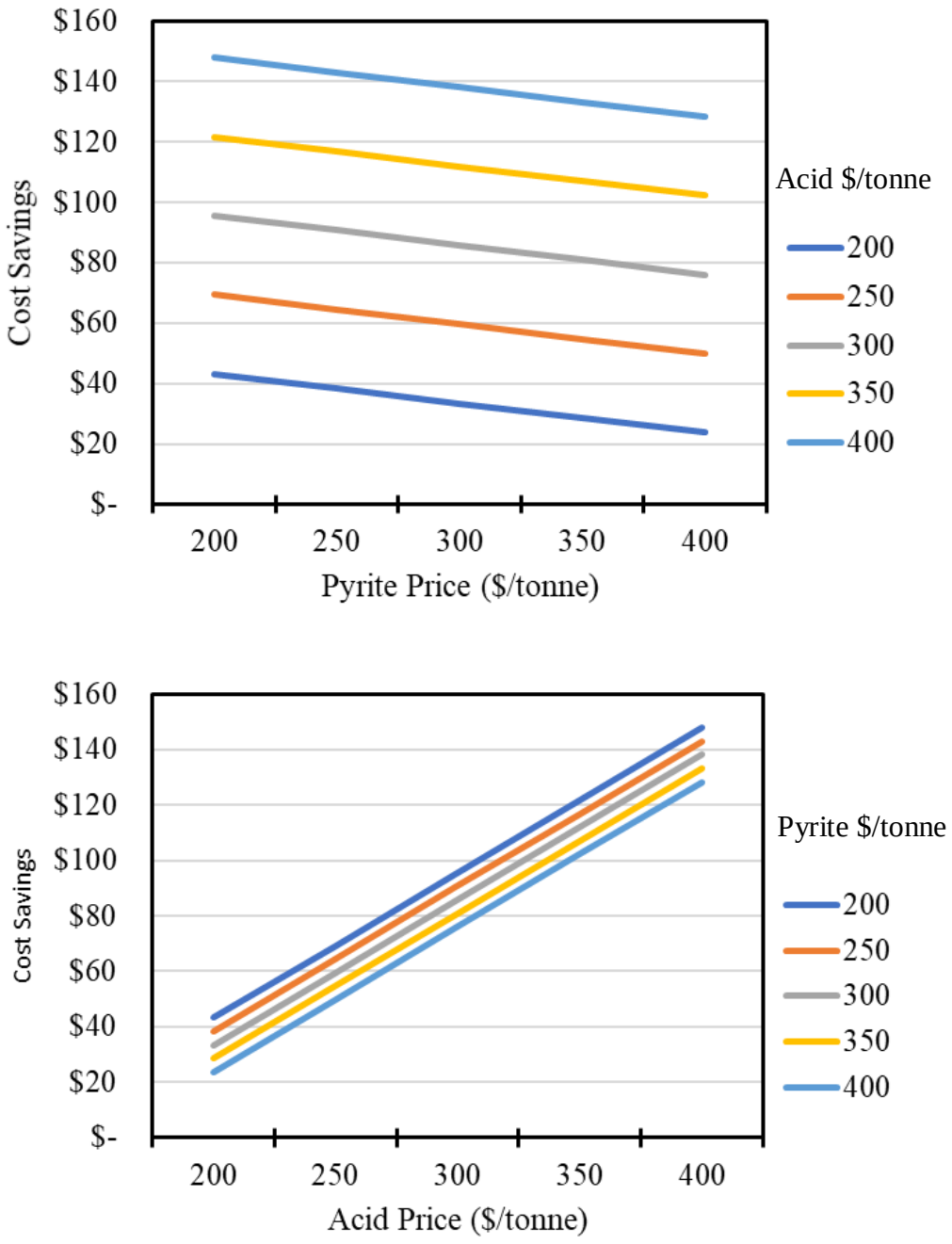

Figure 6 - 19: Sensitivity of cost savings to pyrite and acid bulk prices for Scenario 3a

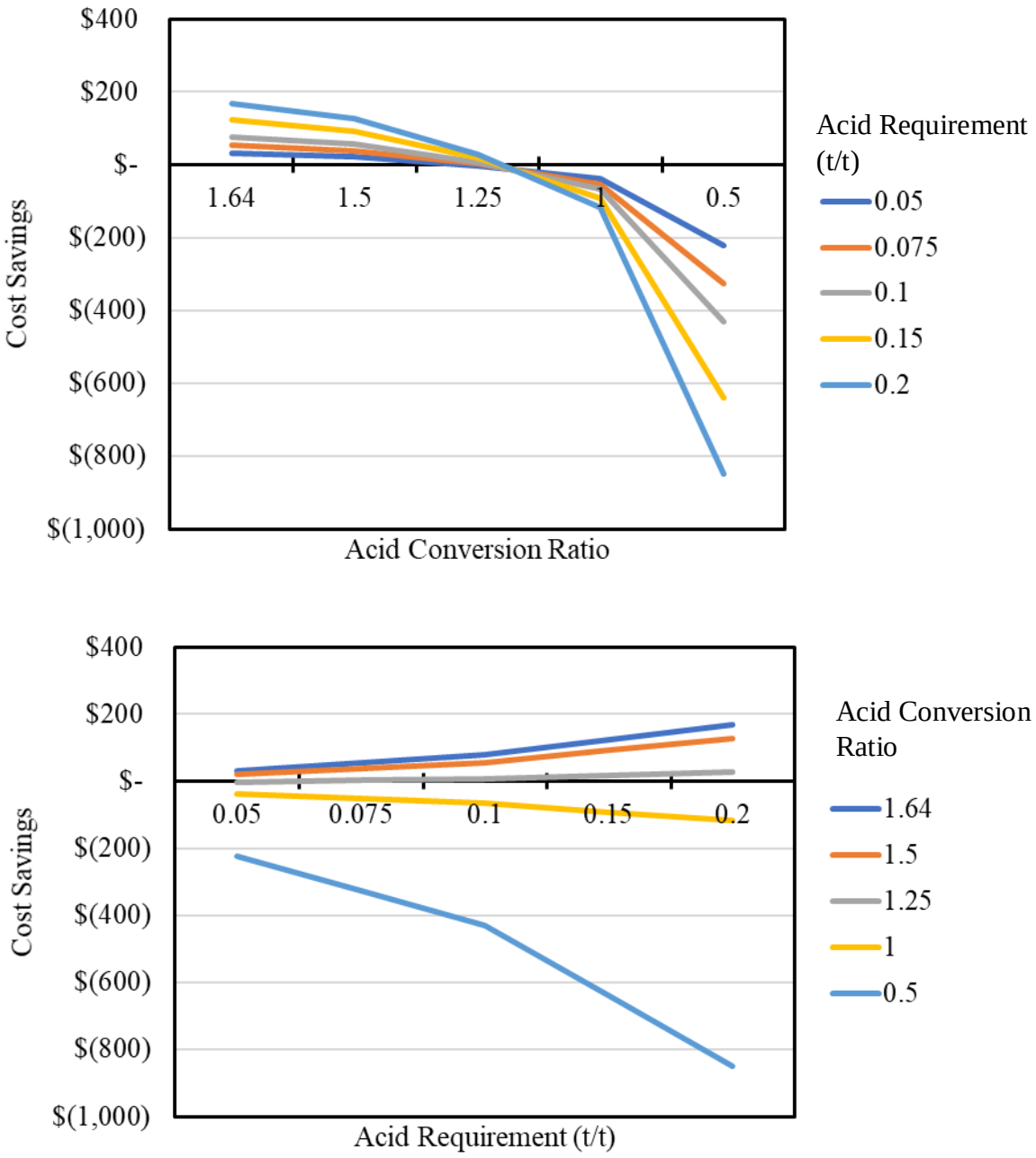

Figure 6 - 20: Sensitivity of cost savings to acid conversion ratio and acid requirements (tonnes acid/tonnes leached) for Scenario 2

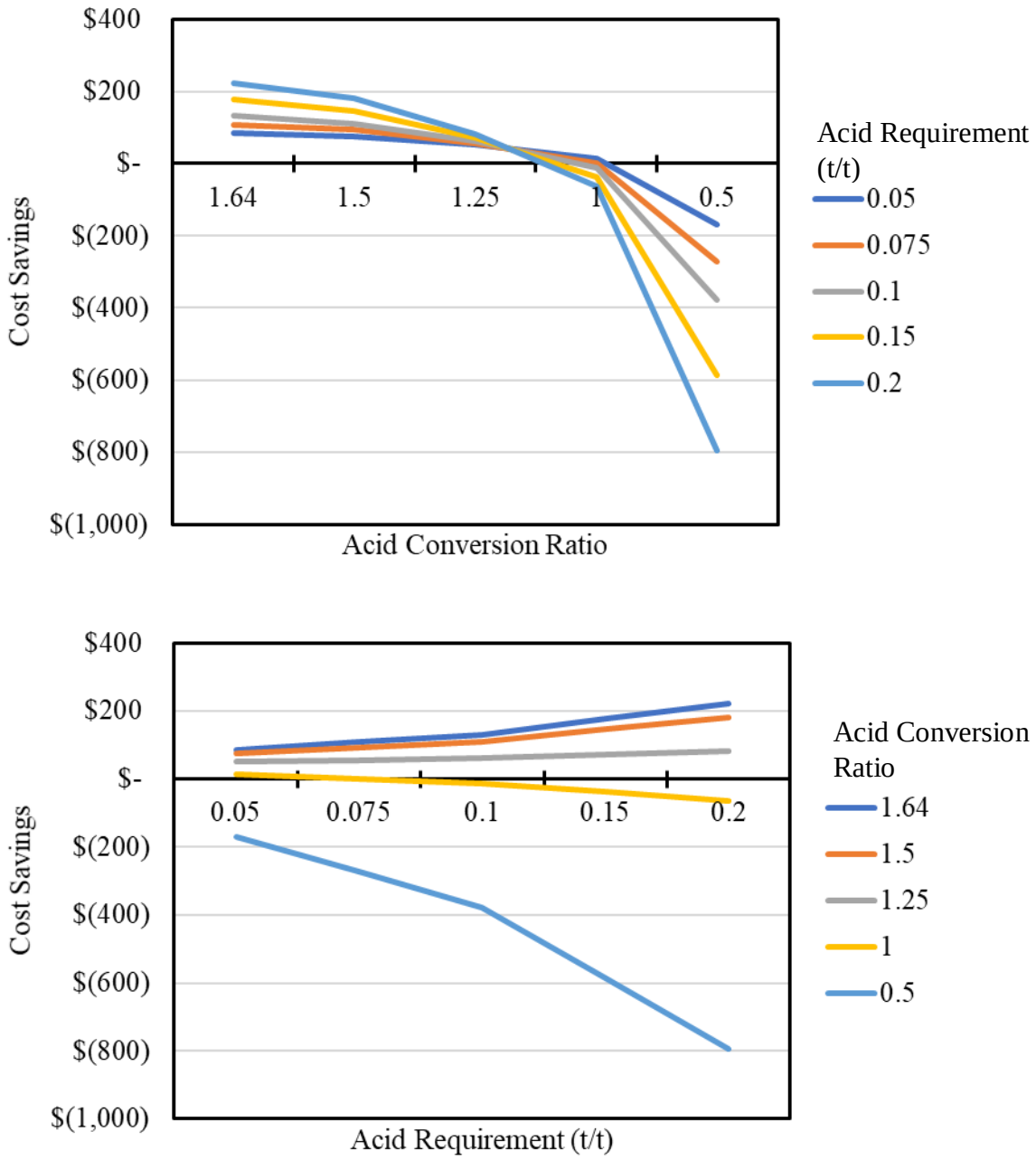

Figure 6 - 21: Sensitivity of cost savings to acid conversion ratio and acid requirements (tonnes acid/tonnes leached) for Scenario 3a

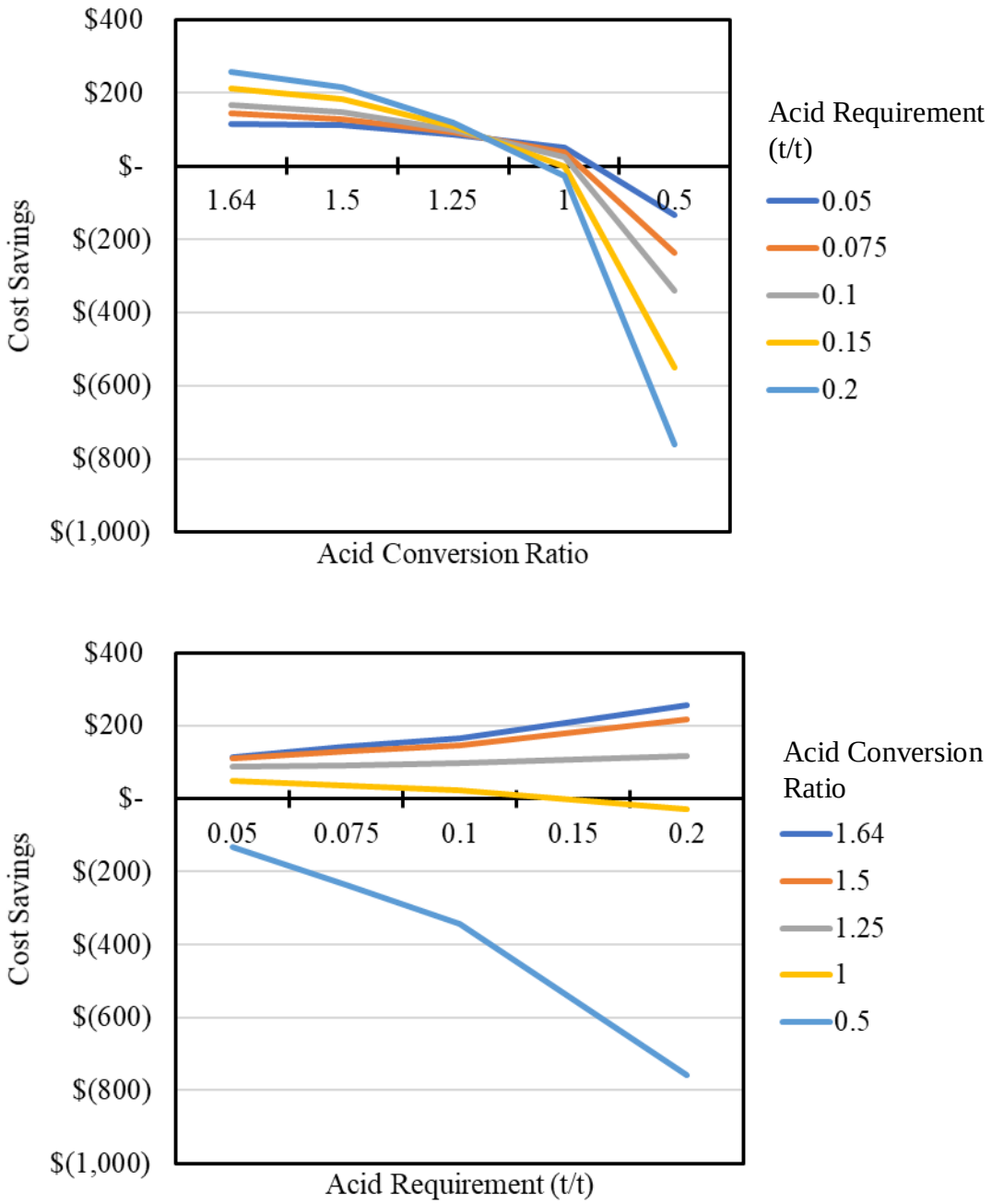

Figure 6 - 22: Sensitivity of cost savings to acid conversion ratio and acid requirements (tonnes acid/tonnes leached) for Scenario 3b

Summary of Key Findings

Task 2 Sample Acquisition and Characterization

- Size analysis showed that all samples have a similar size distribution with little variability in the GGS parameters.
- Primary mineral constituents of the samples include silica, iwakite, illite, siderite, and pyrite in one sample.
- A sodium peroxide fusion method resulted in the greatest TREE concentrations for the CR head samples, compared to hydrofluoric and reverse aqua regia digestions.
- X-ray sorting has the capacity to produce a high yield, REE-enriched product, along with an iron-enriched (pyrite if present) fraction and a middling ash carbon fraction.
- On a whole mass basis, the green sub samples from the x-ray sorting process (i.e. high-ash, low-iron) have the highest TREE concentrations. On a whole ash basis, the orange sub samples (i.e. low-ash) contain the greatest TREE concentrations.
- A standard coal flotation showed ability to enrich REE-bearing material in a tailings product.
- Through x-ray sorting, size classification, and density separation, an approximately 40% sulfur material can be produced from a feed material containing only 4-5% sulfur.
- Pyrite framboids have been found in both the high-ash and low-ash x-ray sorted sub samples. This finding could complicate efforts to concentrate pyrite through density or flotation methods alone. Additionally, pyrite can be identified in most of the sub samples but the abundance of pyrite in CR-B Blue far surpasses all others.
- This product is derived from a byproduct stream in an REE-concentrating process, so two favorable material streams can be produced by a single separation process.
- The XRF results showing higher sulfur content in CR-B and CR-B-b have been supported by greater acid producing potential observed in a simple static leaching trial of blue x-ray sorted products
- Progressions in the development of density separation and flotation methods led to a minor improvement in attainable sulfur concentration, with an increase to 10% S in a float fraction of a 1.65 SG separation, and over 8% in a single stage flotation as opposed to 8% in the previous quarter from a two-stage flotation. Neither surpassed the almost 18% S achieved by x-ray hand sorting.
- Sulfur may be depleted from the heap leach feed by gravity separation in a size class suitable for spiral concentration; however, this step will need to be considered against the comminution required for a high yield of material to be processed.

Task 3 Leaching

- The distributions of the rate earth elements show that the main rare earth elements being leaching from the small column leaching tests are: Y, Ce, Nd, Sc, and La.
- The increased ferric ion concentration had a small negative effect on the extraction, increasing flow rate had a modest positive effect on extraction, increasing pH had a

negative effect on extraction, the combination of ferric ion concentration and flow rate had no significant effect, increasing both ferric ion concentration and pH had a positive effect, increasing flow rate and pH had a positive effect, and increasing all three parameters had a very small positive impact.

- Large column leaching tests show that the scandium is leached at least as well as or better than the other elements evaluated. Other more valuable REEs such as Y, Nb, and Dy are also leached as well as or better than other REEs.
- The overall accumulation of REEs in leaching solutions approaches an overall recovery of around 15-30 % after 90 days based on solution analyses and 30-50 % after 120 days based on solids analyses. It is anticipated that with no optimization of process variables approximately 50 % recovery can be achieved in approximately one year.
- Typical curves of Eh and pH vs. time with pyrite feeding were taken for the bioleaching test, and they are consistent with typical biooxidation scenarios.
- The activity of the bacteria has been significantly increased, and the bacteria can be maintained in a productive condition (2-3 g/l/hr of iron oxidation) with automatic feeding.

Task 4 Solvent Extraction

- The Cyanex 272 and Cyanex 923 bind to the rare earth elements selectively which can facilitate subsequent separation, although they require a lower pH to perform stripping than is desirable.
- Different rare earth elements had different characteristics in terms of their relationship with the organic and aqueous phases, which makes them amenable to separation by solvent extraction using D2EPHA and other organic extractants.

Task 5 Precipitation and REE Product Recovery

- The only relevant species for rare earth elements and iron in the acidic sulfate based solutions used for leaching are the soluble sulfate complexes such as $FeSO_4^+$ $DySO_4^+$, etc. and the dissolved metal ions such as Fe^{3+}, Dy^{3+}, etc.
- Calculations show that various precipitates begin to form in iron rich solutions above approximately pH 2 that are relevant to our leaching solutions.
- Hematite begins to precipitate at about pH 2 when there is an equal ratio of ferrous and ferric iron in solution, whereas the pH decreases to about 1.8 when the ratio of ferric to ferrous iron is increased to 94 % ferric iron and 6 % ferrous iron.
- An X-Ray Diffraction (XRD) analysis of the precipitate, shown in Figure 5 - 11, indicates the precipitate is a jarosite compound. The general composition of jarosite is $NaFe_3(SO_4)_2(OH)_6$, although it should be noted that significant substitution of elements often takes place.
- The precipitation process is sufficient for the precipitation and concentration of the rare earth elements in the leaching solution. However, the yield rate of the first precipitation step is too low and will cause a significant loss of rare earth elements.

- The rate of leaching is high in the stages of leaching; after that, it becomes slower.
- EDS mapping shows that there is a very high concentration of O and C, which is consistent with the composition of the precipitate, REE oxalate ($Ree(C_2O_4)_3$). As indicated by the density of the dots in the EDS map, the concentration of Pm, Nd, Sm, La, Y, Pr, and Ce are high in the precipitate.
- Precipitation of iron can be facilitated by reoxidizing the leaching solution to convert iron to Fe^{3+} form, which is much easier to precipitate than Fe^{2+} at lower pH levels.
- With a mass balance calculation based on the experimental measurement data, the REE oxide equivalent concentration in the final precipitate is about 36.7%, which exceeds the goal of the project. The final precipitate contains very little iron and significant amounts of Zn.
- Three stage precipitation of REEs from leaching solutions (pH 4 using sodium hydroxide or calcium oxide/calcium dihydroxide), filtration, (pH 7 using sodium hydroxide), followed by redissolution of the pH 7 precipitate in nitric acid at pH 2.5, followed by precipitation using oxalic acid, was found to produce the highest grade product.

Task 6 Techno-Economic Analysis

- High sulfur refuse will require long-term acid mine drainage treatment, and x-ray sorting can significantly concentrate acid generating materials.
- Solely purchasing pyrite may not be cost effective in a bioreactor plant when compared to buying acid directly, although it is variable with prices.
- An X-ray sorted pyrite product can reduce process costs by supplementing purchased pyrite in a bioreactor plant for internal acid production.
- An X-ray sorted and spiral concentrated pyrite product may entirely eliminate the need for additional purchased pyrite in a bioreactor plant and has the greatest cost savings compared to directly purchasing acid.
- The highest level of preconcentration of pyrite material may be the most tolerant to reduced acid conversion ratios and acid requirements of the heap leach.

Although the overall project and associated analyses were performed based on the initial projection of concentrating the REE rich coal waste and concentrating pyrite for the bioreactors, followed by leaching, solvent extraction, and precipitation, the results of this project suggest that a better overall process flow sheet might include the steps shown in Figure 6 – 23.

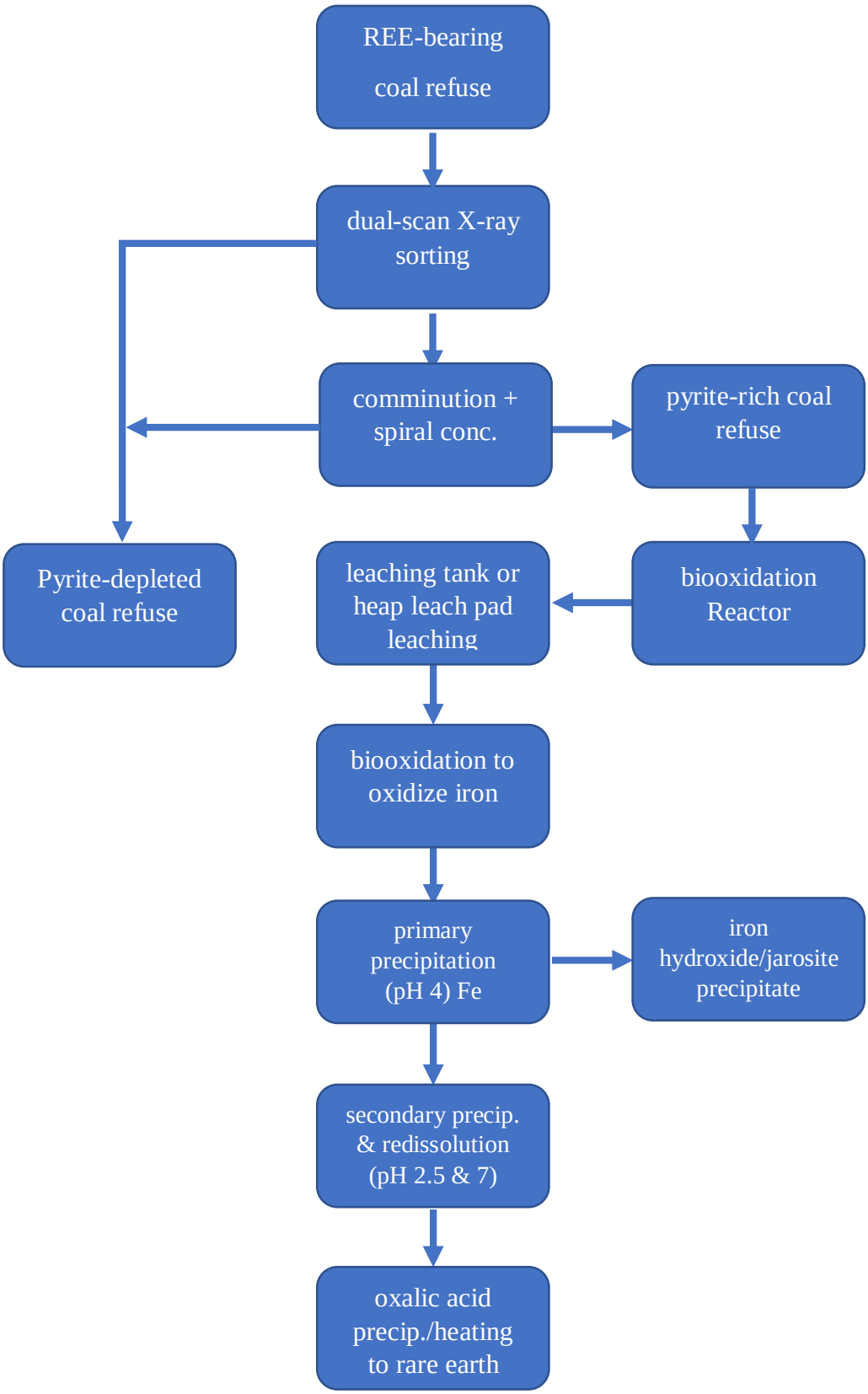

Figure 6-23. Likely scenario for an overall flow sheet based on project results.

Disclaimer:

This report was prepared as an account of work sponsored by an agency of the United States government. Neither the United States government nor any agency thereof, nor any of their employees, make any warranty, express or implied, or assumes any legal liability or responsibility for the accuracy, completeness, or usefulness of any information, apparatus, product, or process disclosed, or represents that its use would not infringe privately owned rights. Reference to any specific commercial product, process, or service by trade name, trademark, manufacturer, or otherwise does not necessarily constitute or imply its endorsement, recommendation, or favoring by the United States government or any agency there. The views and opinions of author's expressed herein do not necessarily state or knows of the United States government or any agency thereof.

References

CostMine Division (2016). Mine & Mill Equipment Costs, an Estimator's Guide. InfoMine, USA.

M. L. Free, "Bioleaching of a Sulfide Ore Concentrate - Distinguishing Between the Leaching Mechanisms of Attached and Nonattached Bacteria," M. S. Thesis, University of Utah, 1992

Hedin, R. S. (2006). The use of measured and calculated acidity values to improve the quality of mine drainage datasets. *Mine Water and the Environment*, *25*(3), 146-152.

Mohanty, M., S. Hassan, AM. Mahajan, Z. Huang (2006). Use of Artificial Intelligence for Developing a Novel Coal Preparation Plant Simulator. Final Technical Report. Illinois Clean Coal Institute. 40 pp.

J. E. Bailey and D. F. Ollis (1986). Biochemical Engineering Fundamentals. 2nd ed., McGraw-Hill Publishing Company, New York, 473-476,

Products

1. Free, Michael, Prashant Sarswat, Gerald H. Luttrell, Aaron Noble, Xianwei Hu, Landen Allen, M. McNeill, Daejin Kim^, and Isaias Arce. (2018). "Economic Extraction, Recovery, and pgrading of Rare Earth Elements from Coal-Based Resources," Poster Presentation, Project Review Meeting for Rare Earth Elements (REE) Program, Pittsburgh, PA, April 10, 2018.

2. Sarswat, Prashant, Michael Free, Aaron Noble, and Gerald Luttrell. (2018). "Efficient Recovery of Rare Earth Elements from Coal Based Resources," Poster Presentation, Extraction 2018, Ottawa, Canada, August 29, 2018.

3. Free, Michael, Prashant Sarswat, Landen Allen, X. Hu, Aaron Noble, Gerald H. Luttrell, and Daejin Kim. (2018). "Economic Extraction, Recovery and Upgrading of Rare Earth Elements from Coal-Based Resources," Presentation, 2018 AIChE Annual Meeting. Pittsburgh, PA, November 1, 2018.

4. Leake, Morgen and Aaron Noble. (2019). "Enrichment of Rare Earth Element-bearing Coarse Coal Refuse by X-ray Transmission Sorting." Mineral Processing Division – Student Poster Session: 2019 SME Annual Meeting & Exhibit. Denver, CO. February 27, 2019.

5. Free, Michael, Prashant Sarswat, Landon Allen, Wei Liu, Kara Sorensen, Aaron Noble, Gerald Luttrell, Daejin Kim, Morgen Leake. (2019). "Economic Extraction, Recovery, and Upgrading of Rare Earth Elements from Coal-Based Resources." 2019 Crosscutting Research & Rare Earth Elements Portfolios Review Meeting. Department of Energy. Pittsburgh, PA. April 9 – 11, 2019.

6. Free, Michael, Prashant K. Sarswat, Landon Allen, Aaron Noble, and Gerald Luttrell. (2019). "Low-Cost Methods for Rare Earth Elements Extraction and Recovery from Coal-Waste" 36th Annual International Pittsburgh Coal Conference. Pittsburgh, PA, September 3 – 6, 2019.

7. Free, Michael, Prashant K. Sarswat, Landon Allen, Aaron Noble, and Gerald Luttrell. (2019). "Utilizing Biooxidation in a Flow Sheet to Facilitate Low-Cost Rare Earth Elements Extraction from Coal-Based Resources and Eliminate Future Acid Mine Drainage." 2019 AIChE Annual Meeting. Orlando, FL. November 10 – 15, 2019.

8. Leake, Morgen, Aaron Noble, and Michael Free (2020). "Physical Pre-Concentration of Coarse Coal Refuse for a Heap Leaching Approach to Rare Earth Element Extractions." 2020 SME Annual Meeting and Exhibit. Phoenix, AZ. February 24 – 26, 2020.

9. Free, Michael, Aaron Noble, Morgen Leake, Landon Allen, Prashant Sarswat, and Gerald H. Luttrell. “Utilizing Biooxidation to Facilitate Low-Cost Rare Earth Elements Extraction from Coal-Based Resources and Eliminate Future Acid Mine Drainage.” 2020 SME Annual Meeting and Exhibit. Phoenix, AZ. February 24 – 26, 2020.

10. Sarswat, Prashant, Morgen Leake, Landon Allen, Michael Free, Xianwei Hu, Daejin Kim, Aaron Noble, Gerald H. Luttrell. (in press). “Efficient Recovery of Rare Earth Elements from Coal Based Resources: A Bioleaching Approach.” *Materials Today Chemistry, 16, 100246, 2020.*